Magnetic Reconnection:

3D Magnetic Null Points

Peter Wyper

Department of Mathematics

University of Sheffield

A thesis submitted for the degree of

Doctor of Philosophy

December, 2012

Acknowledgements

The work presented within this thesis would have not been possible had it not been for the help and guidance I have received not only in the last three years but in those years leading up to the start of my PhD. There are many who have inspired me in different ways so I shall just say a brief thank you to a few of you.

Firstly, I'd like to say a huge thank you to my supervisor Rekha Jain. The first time we met she had me sat down at the computer in her office and applying online to become her PhD student within less than an hour. Little did I appreciate at the time how such enthusiasm and speed would be play a role in my immediate future... I have very much enjoyed our chats in her office over the last few years, occasionally they even deviated toward the work I was doing. It's rare that you meet someone with such a fascination for their subject area and with such a pure and well meant drive to improve the quality of the research they produce. If I've picked up anything, I hope it's a little of that.

Secondly, the numerical work produced within this manuscript would never have been possible had it not been for the extreme patience and good natured Scottish humour of David Pontin. Why he put up with me I'll never know, but I'm eternally grateful for the help he gave me in understanding and putting to good use what could have been a very daunting numerical code. I should also thank Klaus Galsgaard for writing it and allowing me to use it and the access granted to me by Alan Hood to run it on the St. Andrews cluster. It certainly helped test a few ideas...

Although she knows I love her, I think it's only fair that I acknowledge the support I've had from my wife Sarah. Thank you for bringing a bit of silliness to my life whenever I seem too serious and quite convincingly seeming as if you care what happens to magnetic fields and plasmas when I tell you about my day. And of course, thank you for saying yes!

Lastly, a big thank you to everyone else. That is, my brother Alex, sister Sarah, mum, dad, Martin, Val, Laura, James and everyone else of the two families I now belong to, as well as to my friends and drinking buddies over the last few years in the many countries I've been with you in and the professors and teachers who thought it wise to encourage my occasionally stubborn personality into the area of solar physics. In one way or another you've helped make this work (and myself) what it is.

Abstract

Three dimensional magnetic null points are now accepted as important topological features at which magnetic reconnection occurs. However, the understanding of the processes involved is still far behind the well developed field of 2D X-point reconnection. Therefore, the aim of this thesis is to present realistic extensions of the known ways in which 3D null point reconnection occurs.

The Torsional (twisting) regimes of 3D null point reconnection are investigated using analytical models with, for the first time, localised current structures that qualitatively match those seen in simulation studies. These solutions show a wealth of possible scenarios in which new connections can form as a result of twisting perturbations near 3D nulls.

Analytical solutions for fan and spine reconnection are presented with asymmetric current sheets as this scenario is thought to be commonplace in astrophysical plasmas. The asymmetry in each solution has a profound and rather different effect in each case. This analysis is then complimented by a series of numerical experiments studying the self consistent formation of similar current structures for the spine-fan mode in response to transient driving. Time dependent effects, such as the movement of the null position and the applicability of scaling laws derived from analyses with symmetric current sheets, are discussed. These results suggest that, in typical astrophysical plasmas, 3D null points may be continuously shifting position with a flow of plasma at the null point itself.

Lastly, as instabilities are thought to play an important role in astrophysical reconnection dynamics, a series of numerical experiments investigating the self consistent formation and subsequent instability of a current-vortex layer at the fan plane of a 3D null point is presented. The results suggest that separatrix surfaces are great potential sites for current-vortex sheet formation and, therefore, the additional heating and connection change associated with instabilities of this layer.

Contents

List of Figures

1 Introduction

Elwood: "*It's 106 miles to Chicago. We've got a full tank of gas, half a pack of cigarettes, it's dark and we're wearing sunglasses.*"
Jake: "*Hit it.*"
The Blues Brothers

1.1 The Importance of Magnetic Reconnection

Magnetically dominated plasmas are found everywhere throughout the universe and so understanding their nature and evolution is incredibly important for our understanding of the universe as a whole. Many different effects occur in such plasmas, but few with more dramatic consequences than magnetic reconnection. Broadly speaking magnetic reconnection is the fundamental physical process that allows stressed magnetic fields to relax through a reordering of the field connectivity. This reordering liberates the stored magnetic energy in such fields expelling it as heat, particle acceleration and bulk fluid motion. The success of magnetic reconnection, and why it continues to be of interest long after its initial conception in the 1950's, is that it is an elegant mechanism which is adaptable to explain many astrophysical phenomena.

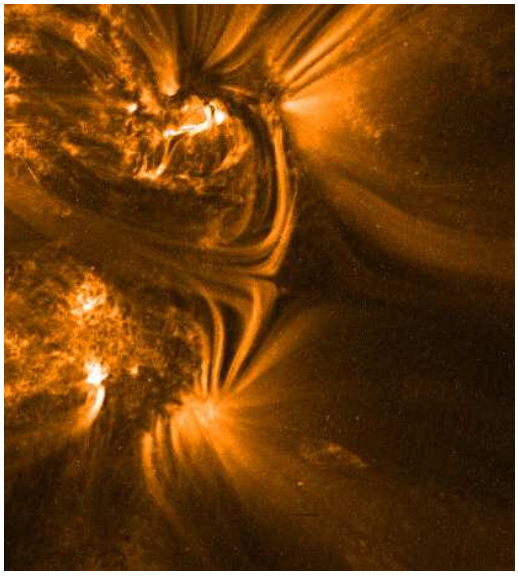

Figure 1.1: Could the hyperbolic loop structure in the center of the image be a coronal null point? Observation from the TRACE (Transition Region And Coronal Explorer) satellite.

With its strong magnetic fields and hot plasma the Sun's Corona (outer atmosphere) provides the perfect conditions for magnetic reconnection to occur. The expanding loops of a solar flare occur as a result of a reconnection region which moves up through the solar corona as the loops form [Forbes, 1997]. The rapid expulsion of magnetic field and plasma from the solar atmosphere known as coronal mass ejections (CME's) are modelled using reconnection (such as the magnetic breakout [Antiochos et al., 1999] and CSHKP models [Carmichael, 1964; Hirayama, 1974; Kopp and Pneuman, 1976; Sturrock, 1966]). Additionally, smaller scale events such as solar jets (short lived jets of plasma assumed to be from magnetic slingshot due to reconnection) [e.g. Gontikakis et al., 2009], X-ray bright points (knots of intense X-ray emission appearing randomly in the corona) [e.g. Brown et al., 2001] and Ellerman bombs (micro-flares commonly observed in H-alpha) [Archontis and Hood, 2009; Pariat et al., 2004] are also believed to be driven by it.

The solar corona is also known to be significantly hotter ($\sim$ 1 million Kelvin) than the observable solar surface below it (5000-6000 Kelvin). How the solar corona maintains its hot temperature is unclear, but one possibility is that reconnection could provide the answer through multiple heating events (*nanoflares*) associated with the untangling of braided field within coronal loops [Parker, 1988; Wilmot-Smith and Hornig, 2011].

Further out from the corona, the solar wind (which is continually streaming away from the sun) carries with it significant magnetic fields (especially during CME's). When these

fields interact with the earth's magnetosphere they often lead to violent reconnection. Such violent interactions are what drive magnetospheric substorms near the bow shock in the Earth's magnetosphere [Baker et al., 1996] and also reconnects magnetic field in the Earth's magnetotail leading to a rapid acceleration of particles which ultimately form the aurora [Angelopoulos et al., 2008]. Additionally, along the flanks of the earth's magnetosphere the strong shear flow created as the solar wind streams past excites the Kelvin-Helmholtz instability which in turn drives reconnection [Miura, 1984; Nykyri et al., 2006]. Thus, magnetic reconnection provides a fundamental link between the Earth's magnetosphere and the solar wind.

However, the Earth's magnetosphere is not the only magnetosphere in our solar system that experiences reconnection with the magnetic field carried by the solar wind. Aurorae have been observed on Jupiter, Saturn and Neptune all suggesting that similar reconnective processes are occurring there. Reconnection within the solar wind has also been put forward to explain features of other objects within the solar system without their own intrinsic magnetic fields, such as the sudden disconnection of comet tails [Shi et al., 2011; Vourlidas et al., 2007] and the aurora observed on Venus [Volwerk et al., 2009].

Outside of the solar system, reconnection is believed to be involved with accretion disks around black holes [e.g. de Gouveia dal Pino and Lazarian, 2005] and other galaxies. It is also believed to be responsible for saw tooth crashes in Tokamaks [Hastie, 1997] and self organisation in reversed field pinch devices [Sarff et al., 2005].

1.2 Magnetohydrodynamics

A useful mathematical framework for investigating magnetic reconnection is magnetohydrodynamics (MHD). A non-relativistic MHD framework treats the plasma as an electrically conducting quasi-neutral fluid, assumed to be travelling at velocities much less than the speed of light ($v^2 \ll c^2$). It is applicable, therefore, to slowly varying plasma scenarios with a typical length scale much larger than the length scale of kinetic effects (such as the ion skin depth or ion gyro radius). Derivations of the MHD equations can be found in, for instance, Priest [1984] or Choudhuri [1998]. A system under these approximations may be fully described by the following equations:

Mass conservation:

$$\frac{\partial \rho}{\partial t} + \boldsymbol{\nabla} \cdot (\rho \mathbf{v}) = 0, \tag{1.1}$$

Equation of Motion:

$$\rho \frac{\partial \mathbf{v}}{\partial t} + \rho(\mathbf{v} \cdot \boldsymbol{\nabla})\mathbf{v} = -\boldsymbol{\nabla} P + \mathbf{J} \times \mathbf{B} + \mathbf{F}, \tag{1.2}$$

Faraday's equation:

$$\boldsymbol{\nabla} \times \mathbf{E} = -\frac{\partial \mathbf{B}}{\partial t}, \tag{1.3}$$

Gauss's law:

$$\boldsymbol{\nabla} \cdot \mathbf{B} = 0, \tag{1.4}$$

Ampère's law:

$$\boldsymbol{\nabla} \times \mathbf{B} = \mu_0 \mathbf{J}, \tag{1.5}$$

Ohm's law:

$$\mathbf{E} + \mathbf{v} \times \mathbf{B} = \mathbf{R}, \tag{1.6}$$

and an energy equation that closes the MHD equations. Here ρ is density, P pressure, $\mathbf{v}$ plasma velocity, $\mathbf{B}$ magnetic field, $\mathbf{E}$ electric field, $\mathbf{J}$ electric current, μ_0 the permeability of free space, $\mathbf{F}$ the sum of all other forces on the system and $\mathbf{R}$ represents some non-ideal term. In this work it is assumed that the plasma is sufficiently collisional so that the non-ideal term is well described by

$$\mathbf{R} = \eta \mathbf{J},$$

where η is the electrical resistivity and is related to the electrical conductivity (σ) through $\eta = 1/\sigma$.

Combining Faraday's equation and Ampère's law with Ohm's law and using this form of the non-ideal term (with η assumed to be constant) gives the
Induction equation

$$\frac{\partial \mathbf{B}}{\partial t} = \boldsymbol{\nabla} \times (\mathbf{v} \times \mathbf{B}) + \eta_d \nabla^2 \mathbf{B}, \tag{1.7}$$

where $\eta_d = \eta/\mu_0$ is the magnetic diffusivity. This equation shows that changes to the magnetic field can occur through bulk motions of the fluid (first term on the right hand side) or magnetic diffusion (second term on the right hand side). The order of magnitude ratio of the two terms

$$Re_m = \frac{\boldsymbol{\nabla} \times (\mathbf{v} \times \mathbf{B})}{\eta_d \nabla^2 \mathbf{B}} \approx \frac{L_0 V_0}{\eta_d}, \tag{1.8}$$

gives the relative importance of each effect and is known as the magnetic Reynolds number. In the majority of astrophysical plasmas $Re_m \gg 1$ and so diffusion effects are negligible. Taking the Solar Corona as an example, a typical length scale (of say a coronal loop) is $\sim 10^8\,\mathrm{m}$, typical velocities can be of the order of $10^6\,\mathrm{m\,s^{-1}}$ and $\eta_d \sim 1\,\mathrm{m^2\,s^{-1}}$ at a temperature of $10^6\,\mathrm{K}$ [Priest and Forbes, 2000] leading to $Re_m \sim 10^{14} \gg 1$. In such

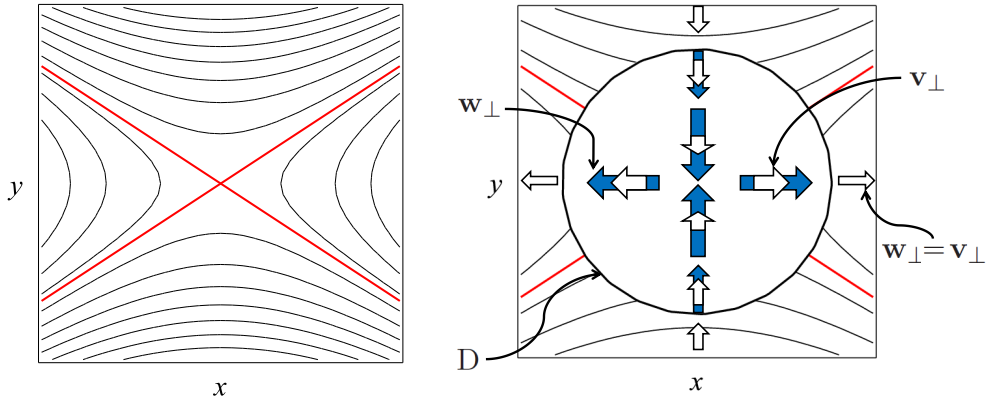

Figure 1.2: Left: The field line structure near an hyperbolic 2D null point (X-point). The domain is split into four topological regions by the separatrices (shown in red). Right: a diagram showing the difference between the flux transporting velocity (blue arrows) and the plasma velocity (white arrows; sitting on top of the blue arrows for flux transport) inside a localised non-ideal region (D).

regimes the induction equation can be approximated by

$$\frac{\partial \mathbf{B}}{\partial t} = \boldsymbol{\nabla} \times (\mathbf{v} \times \mathbf{B}),$$

which is known as the *ideal* limit. When the fluid is described by such an ideal induction equation Alfvén's theorem [Alfvén, 1942] states that the plasma and the magnetic field become 'frozen' to one another and reconnection can not take place. However, considering the observations of flares and CME's reconnection is clearly occurring in the Solar Corona so that this approximation cannot hold in all regions of the Coronal plasma. The only exceptions to the frozen in condition are thin regions (such as current sheets) where the length scale is small enough that $Re_m \leq 1$ and diffusion effects become important. Therefore, reconnection can only take place in localised regions of intense current. As most astrophysical plasmas have extremely high magnetic Reynolds numbers these regions must be incredibly small (relative to a global length scale at which the resulting topology change is seen) and the current flow within them very intense. Reconnection is, therefore, a process of extremes.

1.3 2D Reconnection

Any model of reconnection should ideally include a strong electric field to accellerate particles, an intense current sheet to ohmically heat the plasma and break the frozen in

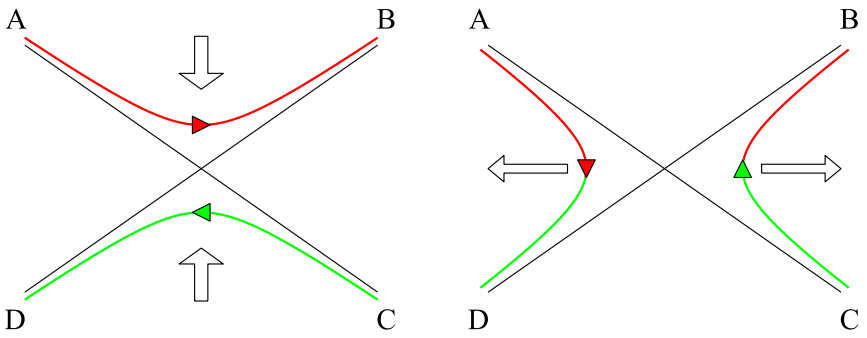

Figure 1.3: Field lines from two topologically distinct regions changing their connectivity from AB and CD to AD and CB where the black lines are the separatrix lines (separatrices) between the regions.

flux condition, jets of bulk plasma motion and a change in the connectivity of the magentic field. In two dimensions (2D) reconnection only occurs at hyperbolic null points of the magnetic field and so these stuctures are the only paces where such a scenario may occur. The linear field near these nulls is given, in general, by

$$\mathbf{B} = \frac{B_0}{L_0}(y, \alpha^2 x), \tag{1.9}$$

where B_0 and L_0 are some typical field strength and length scale respectively. An example of the field this produces is shown in Figure 1.2. This field is separated into 4 topologically distinct regions of magnetic field, i.e. there are four regions where magnetic field lines approach and then recede away from the null in the same fashion.

The special field lines (shown in red) which separate these topological regions (described by the lines $y = \pm\alpha x$) are known as separatrices and the point at which they cross is known as the X-point. The current developed by this magnetic field is given using Equation (1.5) as $\mathbf{J} = B_0(\alpha^2 - 1)/L_0\mu_0\hat{\mathbf{z}}$. Therefore, when $\alpha = 1$ the null is current free (or potential). In the potential state the separatrices are exactly perpendicular to each other. However, in general, this configuration is unstable so that if the foot points of the field are free to move (parallel to the edges of the domain of consideration) and the field is perturbed so that $\alpha \neq 1$ the combination of magnetic pressure in the 'opened out' regions and magnetic tension in the 'scissored up' regions strengthens the perturbation (making $(\alpha^2 - 1)$ and, therefore, the current larger). As this 'X-point collapse' increases a strong

current layer forms at the null and diffusion effects become important. This is just one example of how current sheets form dynamically at X-points and was first put forward by Dungey [1953]. Another particularly relevant case to the solar atmosphere (where the foot points of the magnetic field are effectively tied to the solar surface by a rapid increase in density) is when an initially linear non-potential ($\alpha \neq 1$) X-point field is placed in a domain where the field line foot points are held rigidly to the boundaries (or line-tied) and then allowed to ideally relax. In this case, a similar 'scissoring effect' occurs and the global stress in the field congregates toward the null forming a strong non-linear current sheet. As the relaxation is ideal, the current strength builds indefinitely, becoming singular after and infinite time [see, for instance, Pontin and Craig, 2005]. The fact that null points form these singular current sheets during line tied ideal relaxations is one of the greatest indicators that reconnection must occur at coronal nulls since, as the current strength grows toward infinity, dissipation always becomes important so that Alfvén's frozen in flux condition breaks down and the field lines can reconnect.

The reconnection within these strong current sheets occurs in the pairwise fashion shown in Figure 1.3 where field lines 'break' and then 're-connect' in a symmetric way. Hornig and Schindler [1996] showed that (when the current sheet is localised) this pairwise connection change can be described mathematically through the definition of a flux conserving velocity

$$\mathbf{w} = \frac{\mathbf{E} \times \mathbf{B}}{B^2}, \tag{1.10}$$

satisfying the idealised Ohm's law

$$\mathbf{E} + \mathbf{w} \times \mathbf{B} = 0.$$

This idealised velocity is the same as the plasma velocity outside of the current sheet but travels as if the magnetic field were frozen into it within the current sheet. It is, therefore, only a conceptual quantity but provides a useful framework for understanding reconnection. From this definition, Hornig and Schindler [1996] showed that $\mathbf{w}$ becomes singular only at the null and, therefore, the system behaves as if the magnetic field is cut and pasted at only this point.

This becomes clearer if we consider a simple illustrative example (which is an extension of that presented in Priest et al. [2003]). Consider the linear magnetic field above with the globally constant electric current density: $J_z = B_0(\alpha^2 - 1)/L_0\mu_0$. Imagine localising the non-ideal region (within which $\eta\mathbf{J} \neq 0$) near to the null point with a spatially localised resistivity: $\eta = \eta_0 f(x, y)$, where $f(x, y)$ is zero outside of a region (D) close to the null point (shown in Figure 1.2 as a circular region, although the shape can be of any finite

form as long as the magnetic field only enters and leaves the region once). Taking the electric field to be $\mathbf{E} = \eta_0 \mathbf{J}$ the perpendicular components of the plasma velocity can then be found as

$$\mathbf{v}_\perp = \frac{\eta_0}{\mu_0}(\alpha^2 - 1)(1 - f(x,y)) \left(-\frac{\alpha^2 x}{y^2 + \alpha^4 x^2}, \frac{y}{y^2 + \alpha^4 x^2} \right), \tag{1.11}$$

from the vector product of Ohm's law with the magnetic field. When $f(x,y)$ is chosen so that $(1 - f(0,0))$ goes to zero faster than $\sqrt{x^2 + y^2}$, this is well behaved everywhere. The associated perpendicular component of the flux transport velocity is given by

$$\mathbf{w}_\perp = \frac{\eta_0}{\mu_0}(\alpha^2 - 1) \left(-\frac{\alpha^2 x}{y^2 + \alpha^4 x^2}, \frac{y}{y^2 + \alpha^4 x^2} \right), \tag{1.12}$$

which is equal to $\mathbf{v}_\perp$ outside of D and around its boundary (where $f(x,y) = 0$) but differs inside of D where it behaves as if the magnetic field is frozen to the plasma (shown diagrammatically by the blue arrows in the right panel of Figure 1.2). As a singularity in $\mathbf{w}_\perp$ exists at the null point, this shows that, although the field and plasma are moving at different rates within the non-ideal region (quantified by $\mathbf{w}_\perp - \mathbf{v}_\perp$), the magnetic field behaves as if it is effectively only changing connectivity at the null in a pairwise fashion since it is only here that $\mathbf{w}_\perp$ can not be defined. The rate at which magnetic flux ($\Psi = \int \mathbf{B} \cdot d\mathbf{a}$) is reconnected (per unit length in the z-direction), $d^2\Psi/dzdt$, is then given directly by the electric field at this point ($E_{null}\hat{\mathbf{z}}$).

The early models for 2D reconnection took this pairwise connection change for granted but, as we will see in the next section, beyond two dimensions this is not generally the case. The first to model this process were Sweet [1958] and Parker [1957] who showed that, in steady state, a relative reconnection rate (given by the ratio of the plasma inflow speed to the inflow Alfvén velocity) can be defined, which for their model is proportional to $Re_m^{-\frac{1}{2}}$. For the proposed application of this mechanism to solar flares this rate was found to be too slow at realistic magnetic Reynolds numbers. Many other variations have stemmed from this original model which attempt to speed up this process, the most notable of which is the Petcheck model [Petschek, 1964] which incorporates slow shocks to reduce the current sheet length leading to a reconnection rate proportional to $(\ln Re_m)^{-1}$. Most recent 2D reconnection research now focuses on speeding up the reconnection rate by considering non-MHD effects on the very smallest scales in plasmas where collisional MHD is not applicable (see for instance Zweibel and Yamada [2009] for a review).

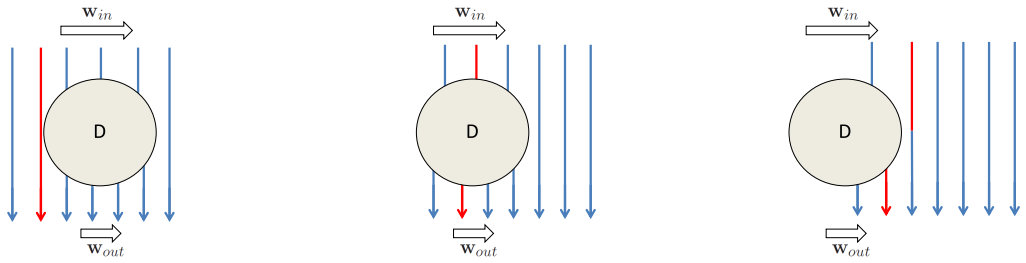

Figure 1.4: Cartoon of the three dimensional slipping reconnection that occurs when $\mathbf{E} \cdot \mathbf{B} \neq 0$ within some finite 3D non-ideal volume D. The ends of the red field line which thread into (from the top) and out (from the bottom) of the non-ideal region are transported at different rates and so one end is seen to slip relative to the other on to a neighbouring field line.

1.4 3D Reconnection

In three dimensional (3D) reconnection, the manner in which the connections are changed is considerably more varied. Within the framework of resistive MHD, reconnection (or more formally, changes of connectivity) may occur anywhere where a strong current parallel to the magnetic field develops. Much effort in recent years has therefore been put into understanding where in three dimensional fields strong current sheets form.

Bungey et al. [1996] and Priest et al. [1997] were amongst the first to show that any complex three dimensional magnetic field (for example the lower coronal magnetic field of the quiet sun) can be characterised by its magnetic skeleton. This skeleton divides up the differently connected regions of magnetic field (topological regions) and is made up of the region's 3D magnetic nulls, separators (field lines joining two nulls) and separatrix surfaces (surfaces lying between different topological regions, which are the 3D extension of separatrices in 2D). These three different structures are known as the topological features of the region of magnetic field under consideration. Priest and Démoulin [1995] showed that, in general, in 3D intense thin current sheets develop in regions where the magnetic field line mapping diverges strongly, i.e. when two field lines are traced from two points initially close to one another the distance between them rapidly increases. At the separators and nulls of the magnetic skeleton the field line mapping is discontinuous making these two topological features likely sites of reconnection. In addition, regions of field with the same connectivity containing no nulls or separators can also generate strong currents if the field line mapping is sufficiently distorted in regions known as Quasi-Separatrix Layers (QSLs) (for a review of magnetic topology see, for instance, Longcope [2005]).

In separators and QSLs the reconnection that occurs is quiet different from the tradi-

tional image of the breaking and rejoining of field lines that occurs in 2D. In particular, there is no magnetic null point associated with this kind of reconnection. At such structures, the frozen in flux constraint is broken in finite volumes (rather than at a single point) by a component of the electric field parallel to the magnetic field, i.e. regions where $\mathbf{E}\cdot\mathbf{B} \neq 0$. Why this occurs becomes clearer if we decompose Ohm's law into it's ideal and non-ideal parts:

$$\mathbf{E}_{ni} + \mathbf{v}_{ni} \times \mathbf{B} = \eta \mathbf{J} \tag{1.13}$$

$$\mathbf{E}_{i} + \mathbf{v}_{i} \times \mathbf{B} = 0. \tag{1.14}$$

This shows that the ideal aspect of the electric field satisfies $\mathbf{E}_i \cdot \mathbf{B} = 0$ whereas for the non-ideal part $\mathbf{E}_{ni} \cdot \mathbf{B} \neq 0$ and therefore this condition is associated with non-ideal effects. The exception, of course, is the 2D case where the geometry means that $\mathbf{E}_{ni} \cdot \mathbf{B} = 0$ but (as we saw in the previous section) connectivity change arises from the fact that $\mathbf{B}$ vanishes at a point so that $\mathbf{w}$ can not be defined there. In these localised regions where $\mathbf{E}\cdot\mathbf{B} \neq 0$ and $\mathbf{B} \neq 0$ Hornig and Schindler [1996] have shown that no unique flux transporting velocity exists. More precisely, no flux transporting velocity exists for a finite volume (D) where $\eta\mathbf{J} \neq 0$ (the 3D extension of the 2D region in the illustrative 2D example) that matches the boundary condition $\mathbf{w}_\perp = \mathbf{v}_\perp$ everywhere on the surface of D. However, if these regions contain no closed magnetic flux then this 'finite-B' reconnection can be understood by the relative mismatching of flux transporting velocities associated with the magnetic field that threads into ($\mathbf{w}_{in}$) and out of ($\mathbf{w}_{out}$) the non-ideal region (since inside it $\mathbf{w}_{in} \neq \mathbf{w}_{out}$ as it is not unique) [Hornig and Priest, 2003; Priest et al., 2003]. Figure 1.4 shows a simple cartoon to illustrate this point. As field lines are advected into the localised non-ideal region D, the flux transporting velocity associated with the end that threads into ($\mathbf{w}_{in}$) and out of ($\mathbf{w}_{out}$) the non-ideal region move at different speeds so that when one end of the field line emerges from contact with D it has 'slipped' on to a neighbouring field line. The fact that everywhere within the non-ideal region $\mathbf{w}_{in} \neq \mathbf{w}_{out}$ shows that this slippage is occurring continuously within the volume. The rate of reconnection for the whole region in this case is given by the maximum integral of $E_{\|}$ along every field line threading the domain [Hesse and Schindler, 1988].

How reconnection occurs and its interpretation when there are null points depends on how the current regions form near the null and the assumed associated change of connectivity. This leads to a variety of ways in which reconnection can take place at these structures. The main aim of this thesis is to probe more deeply the reconnection process in several of the reconnection scenarios that occur.

1.5 Magnetic Helicity

Aside from magnetic flux and reconnection rate, another important quantity related to reconnection in complex magnetic fields is magnetic helicity. Magnetic helicity is a measure of the twist (*self helicity*) and linkage or knottedness (*mutual helicity*) of a given magnetic field. Any change in the linkage (and so topology) of a magnetic field must result from the formation of new connections and so helicity is intricately linked to the process of magnetic reconnection. For a magnetic field entirely enclosed within a closed volume (i.e. the field normal to the surface enclosing the volume is zero: $\mathbf{B}\cdot\mathbf{n}=0$) helicity can be uniquely defined as

$$H=\int_V \mathbf{A}\cdot\mathbf{B}dV \tag{1.15}$$

where $\mathbf{A}$ is a vector potential such that $\mathbf{B}=\boldsymbol{\nabla}\times\mathbf{A}$ and H is gauge invariant under the assumption $\mathbf{B}\cdot\mathbf{n}=0$. The evolution of this quantity can be shown (using $\mathbf{E}=-\partial\mathbf{A}/\partial t-\boldsymbol{\nabla}\Phi$) to be

$$\frac{dH}{dt} = -2\int_V \mathbf{E}\cdot\mathbf{B}dV-\int\boldsymbol{\nabla}\cdot(\phi\mathbf{B}+\mathbf{E}\times\mathbf{A})\,dV \tag{1.16}$$

$$= -2\int_V \mathbf{E}\cdot\mathbf{B}dV-\int\mathbf{n}\cdot(\phi\mathbf{B}+\mathbf{E}\times\mathbf{A})\,dS \tag{1.17}$$

The first term on the right hand side measures internal helicity dissipation/creation and the second term represents any helicity washed into the volume through the boundary. For a system where no additional helicity is washed in through the boundaries only the term dependent upon $\mathbf{E}\cdot\mathbf{B}$ can change the helicity of the magnetic field. Therefore, during ideal evolutions and 2D reconnection ($\mathbf{E}\cdot\mathbf{B}=0$) helicity is a conserved quantity whereas fully 3D reconnection ($\mathbf{E}\cdot\mathbf{B}\neq 0$) acts as a source/sink of helicity. However, for resistive MHD (where $\mathbf{E}\cdot\mathbf{B}=\eta\mathbf{J}\cdot\mathbf{B}$) an order of magnitude comparison of the change in helicity $\sim A_0B_0L_0^3/t_0$ and the source term $\sim\eta A_0B_0L_0^3/\mu_0L_0^2$ reveals that the change in helicity is on the time scale $t_0\approx\eta_d/L_0^2=t_d$, the global diffusion time for the system. As the reconnection rates of any 3D reconnection model are typically considered to be on time scales much faster than t_d, magnetic helicity is approximately conserved during 3D reconnection. For domains where magnetic field crosses the boundary a relative helicity must be defined instead (due to the gauge dependence of H when $\mathbf{B}\cdot\mathbf{n}\neq 0$) but similar results can be shown to hold [e.g. Berger, 1984].

For complex magnetic fields helicity conservation can be a powerful tool as, given an initial magnetic field, the constraint that helicity must be conserved limits the way in which the topology of the field can change. Typically what happens is that helicity is

switched between the two forms of mutual and self helicity (twist and knottedness) in order to spread the helicity density ($\mathbf{A} \cdot \mathbf{B}$) more evenly throughout the volume. One of the first to appreciate the importance of this constraint for laboratory plasmas was Taylor [1974] who used the result of Woltjer [1958], that a field relaxing to a minimum energy state subject to helicity conservation forms a linear force free field ($\boldsymbol{\nabla} \times \mathbf{B} = \alpha \mathbf{B}$, where $\alpha = const.$), to suggest that given an initially unstable field configuration the final field could be known without the need to know the evolution between. Although not always the case in practise, this powerful idea has underpinned much laboratory plasma research ever since. The application of helicity in understanding the dynamics of the Solar Corona has also been appreciated by many authors (for a recent review see, for instance, Démoulin and Pariat [2009]). For more simple field configurations, like the isolated magnetic null points under consideration in this thesis, helicity conservation (or indeed generation over time scales as long as t_d) adds little to the understanding of how flux and energy is moved around in the system. Therefore, although helicity is an important quantity in 3D reconnection, it will not be explored further in this work. It should be noted, however, that Pontin et al. [2004] have briefly discussed helicity generation at 3D nulls subject to twisting perturbations.

1.6 3D Magnetic Null Points

1.6.1 Existence of 3D nulls

Although not the only place where reconnection can occur in complex three dimensional astrophysical fields, magnetic nulls are still important as energy release sites for magnetic reconnection. Single and multiple nulls have been observed in the reconnecting current sheet in the earth's magnetotail through *in situ* measurements from the cluster satellites [Xiao et al., 2006, 2007], as well as being inferred through fully 3D simulations in the polar cusp regions [Dorelli et al., 2007]. Their importance has also been noted in reconnection within laboratory plasmas [Gray et al., 2010]. In the context of the solar atmosphere, with the large number of mixed flux sources of opposite polarity seen in Michelson Doppler Imager (MDI) magnetograms the existence of 3D nulls is virtually guaranteed. Indeed, in the quiet Sun the number of nulls is estimated from magnetogram data to be greatest near the photosphere with a drop in number with height between an exponential [Régnier et al., 2008] and power law [Longcope and Parnell, 2009]. In more active times of the solar cycle, 3D nulls play a more important roll higher up in the solar atmosphere. The Bastille day flare, one of the most spectacular eruptive events seen on the Sun was found

(through potential field extrapolation) to have a 3D null driving the reconnection at its heart [Aulanier et al., 2000]. Other eruptive solar phenomena also believed to be linked with reconnection at 3D nulls are solar jets [Liu et al., 2011; Pariat et al., 2009], flux emergence [Török et al., 2009], flare brightening [Fletcher et al., 2001; Masson et al., 2009] and CME's (in the context of fully 3D magnetic breakout models) [Lynch et al., 2008].

1.6.2 Structure

The field topology in the vicinity of a 3D null point is defined by two structures. The *fan* (or Σ-) plane: a continuum of field lines that asymptotically recede from (or approach) the null and the *spine* (or γ-) line: two field lines that asymptotically approach (or recede from) the null (in the terminology of Priest and Titov [1996] (Lau and Finn [1990])). These structures are the equivalent of the separatrices found at 2D X-points and may be found by examining the linearised field topology around the null defined by the equation

$$\mathbf{B} = \mathcal{M} \cdot \mathbf{r}, \tag{1.18}$$

where the matrix $\mathcal{M}$ is given by the Jacobian of $\mathbf{B}$ and $\mathbf{r}$ the position vector $(x, y, z)^T$. Parnell et al. [1996] have categorised the many ways in which linear potential (ideal) and non-potential (non-ideal) nulls behave. In general, the eigenvectors of $\mathcal{M}$ (whose corresponding eigenvalues sum to zero since $\boldsymbol{\nabla} \cdot \mathbf{B} = 0$) define the spine and fan such that the two eigenvalues whose real parts have like sign lie in the fan plane with the third directed along the spine line. The fan surface is a separatrix surface between two topologically unique regions. The spine can not separate different regions being only a line but is still an important feature as changes in the symmetry within the regions separated by the fan manifest in a change in the field at or around the spine.

For potential linear nulls the off diagonal elements of the matrix $\mathcal{M}$ are zero and the magnetic field in general takes the form

$$\mathbf{B} = \frac{B_0}{L_0} \begin{bmatrix} 1 & 0 & 0 \\ 0 & p & 0 \\ 0 & 0 & -(p+1) \end{bmatrix} \begin{bmatrix} x \\ y \\ z \end{bmatrix} = \frac{B_0}{L_0}(x, py, -(p+1)z), \tag{1.19}$$

where L_0 and B_0 are some typical length scale and field strength respectively, and the dimensionless parameter p controls the degree of asymmetry of the field (see Figure 1.5). When $p \neq 1$ the field is asymmetric and the field is known as an *improper radial* null, whereas when $p = 1$ the field is symmetric and known as a *proper radial* null. In addition to the field symmetry around the null, when the field along the spine approaches the null

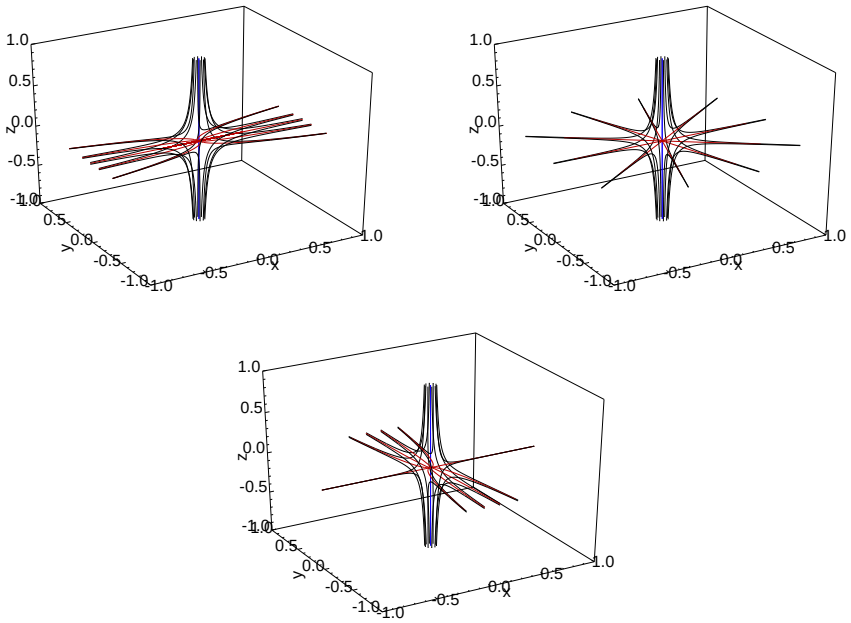

Figure 1.5: Examples of 3D potential nulls with $p = 0.5$ (top left), 1 (top right) and 2 (bottom). The fan plane is shown in red and the spine lines in blue.

($B_0 > 0$) the null is known as type A, whereas if the field recedes from the null along the spine ($B_0 < 0$) it is known as type B [Cowley, 1973].

1.6.3 Brief Summary of Previous Studies

The exact nature of the reconnection process at 3D nulls has only been explored more fully in the last two decades. The first investigation focusing on current sheet formation was conducted by Rickard and Titov [1996] in the zero β cold plasma approximation. These authors noted that depending on the manner of driving, current sheets formed either along the spine or fan or preferentially toward the null.

Following from the work of Lau and Finn [1990] early ideal models exploring the reconnective nature of 3D nulls were put forward by Priest and Titov [1996] who used the appearance of singularities in their ideal plasma flows as signatures for the breakdown of the ideal approximation and the need for non-ideal effects leading to reconnection. They found that when they imposed plasma flows across the fan plane singular flows resulted along the spine. They named this *spine* reconnection as they presumed in a non-ideal plasma a current layer must form along the spine line. Similarly when plasma was forced to cross the spine a singular swishing flow arose at the fan plane which they christened

fan reconnection.

Craig and Fabling [1996] then found exact incompressible steady state solutions for spine and fan reconnection involving semi-infinite current sheets. This was accomplished by utilising the symmetry between **B** and **v** in the steady state incompressible MHD equations to find forms of each that exactly satisfied the momentum equation. However, by the very nature of these solutions, this excluded any back reaction of the velocity field on the magnetic field through the momentum equation and so, theoretically, magnetic field could be forced to pileup at the edges of the current sheet at an unbounded rate, leading to an unbounded reconnection rate and a somewhat unrealistic plasma pressure within the current sheet. This issue was later addressed by Craig and Watson [2000] using pressure equalisation and saturation arguments to optimise these initial solutions. Several extensions sprang from these initial models to include time dependence [Craig and Fabling, 1998], a generalised Ohm's law (including particle effects in the non-ideal term **R**) [Craig and Watson, 2003] and even multiple null configurations [Craig et al., 1999].

However, in astrophysical plasmas current sheets might be expected to have a finite length and width rather than be semi-infinite. [Pontin et al., 2004, 2005] attempted to address this by solving the MHD equations in the steady state kinematic limit for a setup with a constant current density but a resistivity localised to around the null (thus localising the $\eta\mathbf{J}$ term in Ohm's law). They found that the orientation of the current at the null plays a crucial role. When the current is parallel to the spine the magnetic field is twisted and the reconnection that then occurs is in the form of a rotational slippage (much like finite-B reconnection). When the current is parallel to the fan a combination of both the spine and fan reconnection modes occur. However, due to the continuous connectivity change within the non-ideal region the new connections that form do not join up in the pairwise fashion seen in the 2D scenario.

In addition to these initial works, twisting motions near a symmetric null were also investigated numerically [Galsgaard et al., 2003a; Pontin and Galsgaard, 2007]. It was found that twisting motions around/in the spine/fan of the null lead to current build up and reconnection in the form of a rotational slippage in a disk/tube of current at the fan/spine. These regimes of reconnection were christened Torsional fan and Torsional spine respectively [Priest and Pontin, 2009].

Other numerical investigations focused on exciting both the spine and fan mode together [Galsgaard and Pontin, 2011b; Pontin et al., 2007a,b]. In general, it was found that for a compressible plasma, when either the spine or the fan are perturbed, the weak plasma pressure can not resist the Lorentz force generated by the initially planar spine or fan current sheet. This induces a local collapse of the spine on to the fan plane creating

a current sheet at an angle to both. The combination of spine and fan reconnection that occurs in this current sheet was subsequently named *spine-fan* reconnection [Priest and Pontin, 2009]. However, the strength of the collapse (and therefore the way in which flux is reconnected) is a function of many factors such as the level of plasma compressibility, the strength of the driving and the resistivity of the plasma [Pontin et al., 2007b].

Despite much progress in the studies of reconnection around 3D magnetic nulls there still remains many unanswered questions and avenues of investigation. For instance, what are the effects of a fully localised current as opposed to resistive region in terms of flux transport and reconnection in analytical models? What role does asymmetry in the current sheet dimensions play in the dynamics of 3D null point reconnection? How important is the timing of perturbations for the formation of current sheets and reconnection? Are the large flat current sheets that form across the fan plane stable? If not, what are the consequences for the system as a whole? Throughout this thesis we will visit each of these questions in an effort to understand better the process of reconnection that occurs at three dimensional magnetic null points.

1.7 On the Subject of Reconnection

Before beginning to investigate some of the reconnection scenarios that occur at 3D magnetic nulls, a brief commentary is provided on what is believed to constitute 'reconnection' in three dimensions and what differentiates it from ordinary diffusion processes. This is still a contentious issue, despite the general foundations of 3D reconnection being laid back in the 1980's through the work of Hesse and Schindler [1988] and Schindler et al. [1988]. The issue, fundamentally, comes from trying to interpret three dimensional reconnection scenarios in a similar way to 2D reconnection. However, as has been discussed above, using the concept of flux transporting velocities (and has been argued convincingly in the work of Hornig and Priest [2003]; Priest et al. [2003]) both pictures are fundamentally different and transferring the ideas of one on to the other is not easily achieved. That being said, some three dimensional reconnection scenarios do involve a hyperbolic field structure with inflows and outflows of the stagnation point type associated with 2D studies (e.g. in hyperbolic flux tubes [Galsgaard et al., 2003b; Titov et al., 2003], separator reconnection and the spine-fan reconnection mode of 3D null points) and in these instances ideas such as using the ratio of inflow to outflow speeds as a relative measure of the reconnection rate as in the 2D picture have some relevance. These scenarios are usually accepted, therefore, as 'proper' reconnection.

However, the general framework of $\mathbf{E} \cdot \mathbf{B} \neq 0$ finite-B reconnection also includes sce-

narios without hyperbolic field structures for which the name 'reconnection' does not sit as easily when viewed from the context of the 2D scenario (e.g. QSLs and the Torsional reconnection regimes of 3D nulls). Some would call this simply diffusion, whilst others refer to it as reconnection. Ultimately, what distinguishes diffusion from reconnection is the time frame over which new connections are formed and the stored energy released. In the above scenarios, this can be harder to define.

This thesis approaches the problem from the stand point of connectivity change and topology. Rather than focus on the rate of energy release, we will follow the definition of 3D reconnection in its broadest sense (as discussed in e.g. Hornig and Priest [2003]; Priest et al. [2003]; Schindler et al. [1988]) and define magnetic reconnection to have occurred when new connections are formed. More specifically, if, following an evolution of the plasma in a specific domain, the new magnetic field is not *topologically equivalent* to the initial magnetic field (i.e. the initial field can not be returned to via a smooth ideal deformation) then the new field, by definition, has a different topology and new connections are said to have been made. If this occurs as a result of isolated non-ideal regions in a predominantly ideal plasma ($Re_m \gg 1$) rather than in global current layers (with $Re_m \approx 1$) then reconnection is said to have occurred.

From the standpoint of the reconnection that occurs at 3D magnetic nulls this thesis, therefore, follows the convention of Priest and Pontin [2009] and calls both the sheared spine, fan and spine-fan modes *as well as* the twisting torsional modes reconnection. However, as this is quite an all encompassing definition, under this general umbrella a further distinction will be made in relation to the topological features of the magnetic field. To differentiate between connection changes which involve topological features and those that do not, the following terminologies will, at times, be used:

- *Topological Feature (TF) Reconnection*: scenarios where new connections are made involving a topological feature (i.e. the 3D nulls, separatrix surfaces and separators) of the magnetic field.

- *Reconnective slippage*: scenarios where new connections are made within a single topological region but no new connections form with neighbouring topological regions or with topological features such as the spines of isolated magnetic nulls.

Although perhaps a question of semantics, it is worth making the distinction between these two kinds of connection change as only scenarios exhibiting TF reconnection involve the magnetic skeleton of a given magnetic field. TF reconnection scenarios have, therefore, more of the flavour of the 2D scenario as they create new connections across separatrix

lines and surfaces in a similar way to how new connections are formed across separatrices in the 2D picture. The formation of new connections across such topological structures is often the reason that magnetic reconnection is invoked as a mechanism in the first place, so making a clear distinction is important. Under these terminologies the spine, fan and spine-fan modes of 3D magnetic null point reconnection constitute TF reconnection, whereas the torsional regimes exhibit reconnective slippage.

1.8 Outline

The objective of this thesis is to investigate the different reconnection scenarios which occur at three dimensional magnetic null points in detail, with a view to improving our understanding of the ways in which reconnection can occur at these important topological structures. A summary of the work undertaken in each chapter along with where it has been presented or published are given below.

- **Chapter 2 (Torsional Reconnection)**: In this chapter an investigation of the twisting regimes of Torsional spine and fan reconnection is presented. Using kinematic models with (for the first time) localised current layers it is shown that many scenarios are possible where reconnective slippage occurs. The rate at which the slippage occurs in each is quantified and found to be strongly dependent upon the current sheet dimensions. The work within this chapter has also been published in Wyper and Jain [2010] and Wyper and Jain [2011] and I also presented it as a talk at the National Astronomy Meeting (NAM) in Glasgow in April 2010.

- **Chapter 3 (Spine and Fan Reconnection)**: In this chapter the effect (or not) of asymmetry on the processes of spine and fan reconnection is investigated. Although asymmetry has been studied for 2D null points, this is the first investigation of asymmetrically localised current for the 3D case. Kinematic models are developed with asymmetric current sheets and it is found that asymmetry has a profound effect on the reconnection process. The work within this chapter is in preparation for submission to a journal.

- **Chapter 4 (Spine-Fan Reconnection)**: In this chapter, as a compliment to Chapter 3, asymmetric spine-fan reconnection is numerically investigated with combinations of different driving profiles. Comparisons are made with the results of Chapter 3 where possible and aspects of self consistency are addressed. It is found that, even in when the full set of MHD equations are solved, asymmetry plays an important role in the spine-fan reconnection process. Some of the work within this

chapter has been published in Wyper et al. [2012] and has also been the subject of a UK Solar Physics (UKSP) Nugget (June 2012)[1]. In addition I presented this work as talk at the US-Japan Workshop on Magnetic Reconnection (MR2012) in Princeton in May 2012 and as a poster (winning the UKSP poster prize, 2012) at the NAM in Manchester in March 2012.

- **Chapter 5 (Instability Induced Reconnection)**: In this chapter the role of instabilities in the current sheets that form at 3D magnetic nulls is considered using numerical simulations. The Kelvin-Helmholtz instability is found to readily form in the Torsional fan current sheet leading to rapid *topological feature reconnection* along with the reconnective slippage associated with the twisting motions. This is the first time, to my knowledge, that instabilities have been studied in the current sheets of 3D magnetic nulls. I presented the work contained within this chapter at the International Cambridge Workshop on Magnetic Reconnection (ICWM) in Copenhagen in August 2012 and it is currently under review for publication in the journal Physics of Plasmas.

- **Chapter 6 (Conclusions)**: This chapter gives the conclusion of the work presented in this thesis along with suggestions for further future work.

[1] which can be accessed via the link: http://www.uksolphys.org/uksp-nugget/24-asymmetric-reconnection-at-3d-magnetic-null-points/

2

Torsional Reconnection

"*Come on let's twist again like we did last summer...let's twist again, twistin' time is here.*"

Chubby Checker

2.1 Introduction

The current understanding of the Torsional spine and fan reconnection modes stems mainly from the evidence of current sheet formation and rotational reconnective slippage in the numerical investigations of Pontin and Galsgaard [2007] and Galsgaard et al. [2003a]. The reconnective slipping that occurs is, at present, only modelled analytically by the simple kinematic model of Pontin et al. [2004]. These authors exploited the fact that the non-ideal term ($\mathbf{R} = \eta\mathbf{J}$) in Ohm's law is the product of the scalar resistivity (η) and the current vector ($\mathbf{J}$) to mathematically localise the non-ideal region using the resistivity (along with a constant current). However, in typical astrophysical plasmas a non-ideal region is expected to be localised primarily by the localisation of intense current flow which is then augmented by an anomalous resistivity as a result of temperature dependent collisions [Spitzer, 1956] and microturbulence within the layer [Papadopoulos, 1977]. With η being

only a scalar, using this quantity to localise a non-ideal process is often analytically more convenient than using physically more plausible localised current layers as such layers complicate the magnetic field structure. As such, this approach is often used as a first step in kinematic investigations of three dimensional magnetic reconnection [e.g. Hornig and Priest, 2003; Pontin et al., 2004, 2005; Wilmot-Smith and Hornig, 2011].

Ideally, however, having analytical solutions involving current sheets that are qualitatively similar to those observed in numerical simulations would be preferred. Consequently, in the first section of this chapter kinematic analytical solutions using localised current sheets are developed to model the Torsional spine and fan reconnection scenarios. As a localised resistivity is also expected to play a role in typical reconnection scenarios, the second section of this chapter will consider the role of a localised resistivity in conjunction with a localised current. In particular, it is not clear how much information is lost by using just a localised resistive region in conjunction with a constant current (rather than a localised current layer) as has often been done in the past. What ultimately decides the manner of flux transport and reconnection rate in these models: the localisation of the $\eta\mathbf{J}$ term or specifically one of its constituents? Ultimately, it will be shown that the localisation of the current layer dominates over the resistivity and has a profound effect on the induced non-ideal flows and the way in which magnetic flux is reconnected.

The investigation is structured as follows. Section 2.2 introduces the analytical methodology from which the solutions are constructed. In Section 2.3 Torsional solutions are presented with (for the first time) localised current sheets. In Section 2.4 these solutions are extended to include a fully localised resistivity (i.e. zero outside of some region) and in Section 2.5 the role of anomalous resistivity (increased above a non-zero background value) is discussed. Finally, Sections 2.6 and 2.7 provide a brief summary and present some conclusions.

2.2 The Kinematic Methodology

In this chapter solutions to the MHD equations in the steady state kinematic limit are considered. In this limit, the MHD equations are given by

$$\mathbf{E} + \mathbf{v} \times \mathbf{B} = \eta \mathbf{J}, \tag{2.1}$$

$$\boldsymbol{\nabla} \times \mathbf{E} = 0, \tag{2.2}$$

$$\boldsymbol{\nabla} \times \mathbf{B} = \mu_0 \mathbf{J}, \tag{2.3}$$

$$\boldsymbol{\nabla} \cdot \mathbf{B} = 0. \tag{2.4}$$

A magnetic field ($\mathbf{B}$) is prescribed satisfying Equation (2.4) which then describes the current in the system through Equation (2.3). Parametric equations describing the magnetic field lines are then found by solving

$$\frac{dx}{B_x} = \frac{dy}{B_y} = \frac{dz}{B_z} = ds, \tag{2.5}$$

where s is related to the distance along a field line (l) through $ds = dl/|\mathbf{B}|$. Equation (2.2) allows the electric field to be written in the form of a potential Φ as

$$\mathbf{E} = -\boldsymbol{\nabla}\Phi. \tag{2.6}$$

By taking the dot product of $\mathbf{B}$ with Equation (2.1) an expression for this electric potential in terms of the prescribed magnetic field is found in the following way:

$$\begin{aligned}
\mathbf{E}\cdot\mathbf{B} &= \eta\mathbf{J}\cdot\mathbf{B} \\
-(\boldsymbol{\nabla}\Phi)\cdot\mathbf{B} &= \eta\mathbf{J}\cdot\mathbf{B} \\
(\mathbf{B}\cdot\boldsymbol{\nabla})\Phi &= -\eta\mathbf{J}\cdot\mathbf{B} \\
\frac{d\Phi}{ds} &= -\eta\mathbf{J}\cdot\mathbf{B} \\
\Phi &= -\int \eta\mathbf{J}\cdot\mathbf{B}ds + \Phi_0
\end{aligned} \tag{2.7}$$

where $\boldsymbol{\nabla}\Phi_0 \cdot \mathbf{B} = 0$. Considering that for a given magnetic field Ohm's law can be decomposed into an ideal and non-ideal part [Hornig and Priest, 2003]

$$-\boldsymbol{\nabla}\Phi_{ni} + \mathbf{v}_{ni}\times\mathbf{B} = \eta\mathbf{J} \tag{2.8}$$

$$-\boldsymbol{\nabla}\Phi_{i} + \mathbf{v}_{i}\times\mathbf{B} = 0, \tag{2.9}$$

Φ_i can be identified with the constant of integration (Φ_0) and Φ_{ni} with the integral in Equation (2.7). The induced plasma flow perpendicular to the magnetic field can then be found by taking the vector product of Equation (2.1) with $\mathbf{B}$ to yield

$$\begin{aligned}
\mathbf{v}_\perp &= \frac{(-\boldsymbol{\nabla}\Phi - \eta\mathbf{J})\times\mathbf{B}}{B^2} \\
&= -\frac{(\boldsymbol{\nabla}\Phi_{ni} + \eta\mathbf{J})\times\mathbf{B}}{B^2} - \frac{\boldsymbol{\nabla}\Phi_i\times\mathbf{B}}{B^2} \\
&= \mathbf{v}_{\perp ni} + \mathbf{v}_{\perp i}.
\end{aligned} \tag{2.10}$$

Thus, for a given magnetic field, if the integral in Equation (2.7) can be solved, then the induced perpendicular plasma flow associated with an isolated non-ideal region can be calculated. To this, any background ideal flow field that satisfies $\boldsymbol{\nabla}\Phi_i \cdot \mathbf{B} = 0$ can then be added. Solutions without a background ideal flow ($\Phi_0 = 0$) are known as *pure* solutions whereas those including one ($\Phi_0 \neq 0$) are known as *composite* solutions. The other component of the velocity $\mathbf{v}_{\parallel}$ is unspecified, but may be found by imposing an additional condition on $\mathbf{v}$. For instance, for an incompressible fluid ($\boldsymbol{\nabla}\cdot\mathbf{v} = 0$), $\mathbf{v}_{\parallel} = -|\mathbf{B}| \int \boldsymbol{\nabla} \cdot \mathbf{v}_{\perp} ds$ [Lau and Finn, 1990]. However, flows parallel to the magnetic field do not contribute to reconnection so attention is focused on the perpendicular component.

The simplicity of this methodology is that it gives an understanding of local non-ideal flows and how they can be coupled to the global field through composite solutions. In addition, by using the framework of flux transporting velocities, the difference between $\mathbf{w}_{\perp in}$ and $\mathbf{w}_{\perp out}$ can be used to qualitatively understand the manner of reconnection within a given localised non-ideal region. The obvious drawback is that the electric and magnetic fields and their associated flows lack self consistency in the absence of a momentum equation. Therefore, solutions of this nature are qualitative even though they provide a useful insight into the fully dynamic system.

2.3 Localised Current Models for Torsional Spine and Fan

To model Torsional spine and fan reconnection using this methodology it is convenient to work in cylindrical polar coordinates, so that

$$\hat{\mathbf{r}} = \cos(\phi)\hat{\mathbf{x}} + \sin(\phi)\hat{\mathbf{y}} \tag{2.11}$$

$$\hat{\boldsymbol{\phi}} = -\sin(\phi)\hat{\mathbf{x}} + \cos(\phi)\hat{\mathbf{y}}, \tag{2.12}$$

along with $r = \sqrt{x^2 + y^2}$ and $\phi = \tan^{-1}(y/x)$, and start with a background radially symmetric ($p = 1$) potential null of the form

$$\mathbf{B}_n = \frac{B_0}{L_0}(r, 0, -2z). \tag{2.13}$$

A perturbation field $\mathbf{B}_p$ is then added such that the total magnetic field is given by

$$\mathbf{B} = \mathbf{B}_n + \mathbf{B}_p.$$

To reproduce the current structures observed in the afore mentioned simulation studies the perturbation field

$$\mathbf{B}_p = \frac{B_0}{L_0} j r^\alpha z^\gamma (zr^2)^\beta e^{-\frac{1}{l^2}(a^2r^2+b^2z^2)-\frac{c^6}{l^6}(zr^2)^2}\hat{\boldsymbol{\phi}}, \tag{2.14}$$

is chosen, where α, β and γ are either zero or positive integers and a, b, c, l and j are constants. This type of perturbation leads to a twist of the field lines around the spine lines and, depending on the choice of parameters, a current disk near the fan plane or a current tube along the spine. The following subsections investigate in detail each of these types of Torsional reconnective slippage, starting initially with the pure solutions and later including background ideal flows.

2.3.1 Torsional Spine

Torsional spine reconnection can be modelled by setting $\gamma = 0$, $a = 1$ and $b = 0$ giving a total magnetic field of the form:

$$\mathbf{B} = \frac{B_0}{L_0}\left(r, j r^\alpha (zr^2)^\beta \mathrm{e}^{-\frac{r^2}{l^2}-\frac{c^6}{l^6}(zr^2)^2}, -2z\right). \tag{2.15}$$

In cylindrical coordinates the equations for the field lines become

$$\frac{dr}{B_r} = \frac{r d\phi}{B_\phi} = \frac{dz}{B_z} = ds, \tag{2.16}$$

from which the equations for r and z can be readily obtained as

$$r = r_0 e^{B_0 s/L_0} \quad \& \quad z = z_0 e^{-2B_0 s/L_0}, \tag{2.17}$$

where r_0 and z_0 are some initial position at $s = 0$. From these it can be seen that $zr^2 = z_0 r_0^2$ is a constant with respect to s. Using this property, and that $ds = dr/B_r$, the expression for ϕ is found in the following way

$$\begin{aligned} r\frac{d\phi}{ds} &= B_\phi \\ &= \frac{B_0}{L_0} j r^\alpha (zr^2)^\beta \mathrm{e}^{-\frac{r^2}{l^2}-\frac{c^6}{l^6}(zr^2)^2} \end{aligned}$$

$$
\begin{aligned}
\phi &= \frac{B_0}{L_0} j (zr^2)^\beta e^{-\frac{c^6}{l^6}(zr^2)^2} \int r^{\alpha-1} \mathrm{e}^{-\frac{r^2}{l^2}} ds + C \\
&= \frac{B_0}{L_0} j (zr^2)^\beta e^{-\frac{c^6}{l^6}(zr^2)^2} \int r^{\alpha-1} \mathrm{e}^{-\frac{r^2}{l^2}} \frac{dr}{B_r} + C \\
&= j (zr^2)^\beta e^{-\frac{c^6}{l^6}(zr^2)^2} \int r^{\alpha-2} \mathrm{e}^{-\frac{r^2}{l^2}} dr + C,
\end{aligned}
$$

leading to

$$
\phi - j (zr^2)^\beta e^{-\frac{c^6}{l^6}(zr^2)^2} F_l(r, \alpha - 1) = C, \tag{2.18}
$$

where $C(r_0, \phi_0, z_0)$ is a constant of integration and $F_l(x, A)$ is defined as

$$
F_l(x, A) = \int x^{A-1} e^{-\frac{x^2}{l^2}} dx. \tag{2.19}
$$

Using integration by parts it can be shown that $F(x, A)$ follows the recurrence relation

$$
F_l(x, A+2) = \frac{l^2}{2} \left(A F_l(x, A) - x^A e^{-\frac{x^2}{l^2}} \right), \tag{2.20}
$$

which along with

$$
F_l(x, 1) = \frac{l\sqrt{\pi}}{2} \operatorname{erf}\left(\frac{x}{l}\right) \quad \& \quad F_l(x, 2) = -\frac{l^2 e^{-\frac{x^2}{l^2}}}{2},
$$

allows solutions of the integral for integer values of $A \geq 0$. Here $\operatorname{erf}(x)$ is the *error function*. Using Equation (2.3) the components of the current are found as

$$
\begin{aligned}
J_r &= \frac{jB_0}{\mu_0 L_0} z^{-1} \left(-\beta + \frac{2c^6}{l^6}(zr^2)^2 \right) r^\alpha (zr^2)^\beta e^{-\frac{r^2}{l^2} - \frac{c^6}{l^6}(zr^2)^2} \\
J_\phi &= 0 \\
J_z &= \frac{jB_0}{\mu_0 L_0} \left((2\beta + \alpha + 1) - 2 \left(\frac{r^2}{l^2} + \frac{2c^6}{l^6}(zr^2)^2 \right) \right) r^{\alpha-1} (zr^2)^\beta e^{-\frac{r^2}{l^2} - \frac{c^6}{l^6}(zr^2)^2},
\end{aligned}
$$

which can be substituted into Equation (2.7) to yield the electric potential (see Appendix A.1)

$$
\begin{aligned}
\Phi_{ni} = \frac{j\eta_0 B_0}{\mu_0 L_0} \Bigg[& \left(\beta - \frac{2c^6}{l^6}(zr^2)^2 \right) F_l(r, \alpha+3)(zr^2)^{\beta-1} - \frac{4}{l^2} F_l(r, \alpha-1)(zr^2)^{\beta+1} \\
& + 2 \left((\alpha + 2\beta + 1) - \frac{4c^6}{l^6}(zr^2)^2 \right) F_l(r, \alpha-3)(zr^2)^{\beta+1} \Bigg] e^{-\frac{c^6}{l^6}(zr^2)^2}
\end{aligned} \tag{2.21}
$$

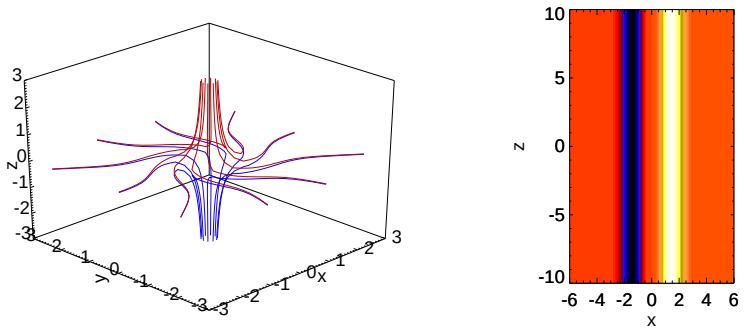

Figure 2.1: The unbounded Torsional spine case. Left: a selection of field lines. Right: the perturbation field viewed in the $y = 0$ plane where yellow indicates positive and blue negative. Plotted for $\alpha = 4, \beta = 0$ with $j = 3$ and $l = 1$. The field lines close to the spine are approaching the null and receding away from the null in the fan plane.

where $\alpha \neq 1$ or 3 (as these lead to singular electric potentials, since $F_l(r, 0)$ is singular at $r = 0$). Depending on the choices of the parameters α, β, l, c and j the background magnetic field will be perturbed differently. In the following subsections the different perturbations of the field and their induced non-ideal plasma flows are described for a variety of different cases. The rate of associated reconnective slippage that occurs for the general Torsional spine perturbation, and how it depends upon the dimensions of the non-ideal region in each case, is then discussed. Throughout each investigation the vector plots were produced using *MAPLE 15* to which a scaling of (strength/maximum)$^{1/d}$ has been applied for clarity and the constants η_0, μ_0, B_0 and L_0 are set to 1.

Equal vorticity twist

Let us start with cases where the twist applied to the field above and below the fan plane is in the same direction. To achieve this β must be even and $\alpha > 0$ in Equation (2.15) for non-singular currents.

The z independent case: $\beta = 0$, $c = 0$. Consider first the case of a perturbation that is independent of z, i.e. $\beta = 0$ and $c = 0$. In this case, the twist in the field is localised to within an unbounded tube centred on the spine. To be well represent the slippage observed in simulation studies (e.g. Galsgaard et al. [2003a]; Pontin and Galsgaard [2007]) the non-ideal region should create a relative slippage between field lines entering and leaving it, i.e. a difference between $\mathbf{w}_{in}$ and $\mathbf{w}_{out}$. The signature of such a slippage is a difference in potential along a field line threading the non-ideal region. For

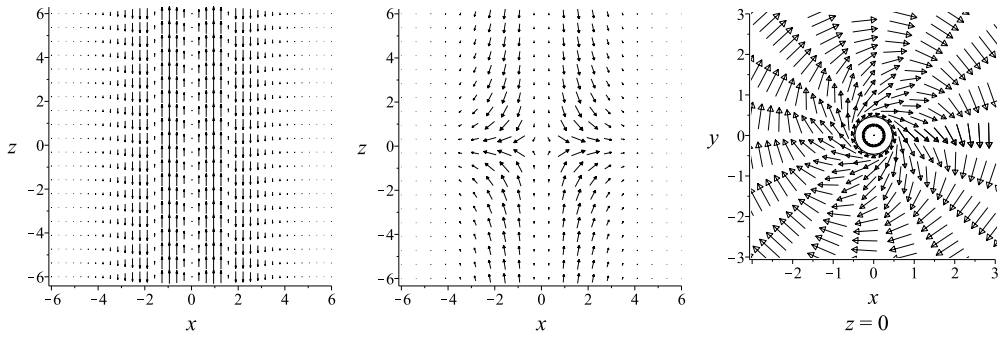

Figure 2.2: Left: Radially symmetric current flow in the $y = 0$ plane. Middle and right: perpendicular plasma flow in the $y = 0$ and $z = 0$ planes respectively. Plots for the unbounded Torsional spine case with $\alpha = 4, \beta = 0$ with $j = 3$ and $l = 1$. Here the *MAPLE* scaling is applied with $d = 3$.

odd α values both the ingoing and outgoing electric potentials are zero ($\Phi_{ni.}(r \to \infty) = 0$ and $\Phi_{ni.}(r = 0) = 0$, the limits of which are discussed in Section 2.3.1) so these solutions are therefore discounted as unlikely in practise. In addition, for $\alpha = 2$, $v_{\perp\phi}(r = 0) \neq 0$ which is non-physical. Therefore, physically plausible solutions may be found when $\alpha \geq 4$.

Choosing $\alpha = 4$ the magnetic field becomes

$$\mathbf{B} = \frac{B_0}{L_0}\left(r, jr^4 e^{-\frac{r^2}{l^2}}, -2z\right). \tag{2.22}$$

The shape of this magnetic field can be seen in Figure 2.1. Very close to the spine and at large radii the field is not twisted and so is potential. The current associated with the twist takes the form of two strong concentric tubes within the twisted region (seen as bands when viewed from the side in Figure 2.2, left panel). These tubes qualitatively match those observed by Pontin and Galsgaard [2007] at intermediate time steps in their simulations. The induced non-ideal perpendicular plasma flow is also shown in Figure 2.2. The plasma is seen to spiral down around the spine and then spiral out along the fan plane. As might be expected, the strongest flows occur within the region of greatest twist. For higher even values of α, the twist in the field is reduced (increased) where $r < l$ ($r > l$), with similar plasma and current flows.

The z dependent case: $\beta \neq 0$, $c \neq 0$. For this case, the twist in the field lines is localised to around the spine and near the fan whilst being zero in the fan plane. To observe a smooth transition from z independence to z dependence α is kept ≥ 4 for the representative choice of $\beta = 2$ along with $c \neq 0$ to maintain localisation of the current

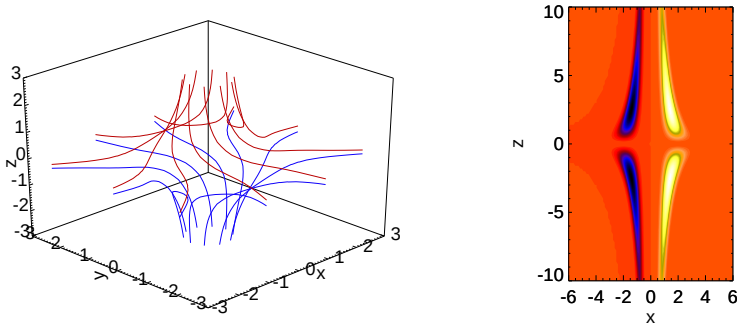

Figure 2.3: The fully localised Torsional spine case. Left: a selection of field lines. Right: the perturbation field viewed in the $y = 0$ plane where yellow indicates positive and blue negative. Plotted for $\alpha = 4, \beta = 2$ with $c = 5^{-1/3}, j = 3$ and $l = 1$. The field lines close to the spine line are approaching the null and receding away from the null in the fan plane.

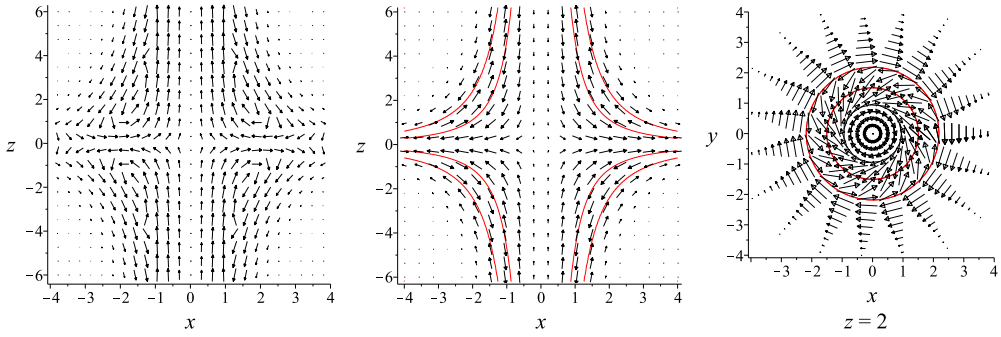

Figure 2.4: Scaled plots of the radially symmetric current flow in the $y = 0$ plane (left panel) and plasma flows in the $y = 0$ and $z = 2$ planes (middle and right panels respectively) for $\alpha = 4$, $\beta = 2$ and $c = 5^{-1/3}$ with $l = 1$ and $j = 3$. The red lines show where $v_{\perp\phi} = 0$. Here, the *MAPLE* scaling is applied with $d = 13$.

layer. This gives a magnetic field of the form

$$\mathbf{B} = \frac{B_0}{L_0}\left(r, jz^2r^8e^{-\frac{r^2}{l^2}-\frac{c^6}{l^6}(zr^2)^2}, -2z\right). \tag{2.23}$$

Figure 2.3 shows the shape of the twisted region in this case, along with a selection of field lines which pass through it. The current (as viewed in the left panel of Figure 2.4) flows in a ring within the two squashed tori either side of the fan plane. The shape of these tori follow the region of shear perpendicular to this plane (in the $\hat{\phi}$ direction) via Ampèr's law. As there is no current in the fan plane, the magnetic field in this plane is potential and therefore radial. This is a slightly unrealistic scenario as in the fully dynamic case it would be expected that the current would diffuse into the fan plane, joining the two toroidally twisted regions. However, qualitatively similar current structures were observed at intermediate time steps of the simulations of Rickard and Titov [1996] and Galsgaard et al. [2003a], except that in this case there is no current along the spine.

The induced perpendicular plasma flow (middle and right panels, Figure 2.4) show the appearance of a counter rotating region. This region results mathematically from the extra terms in Φ_{ni} when $c \neq 0$ and shows that, in general, counter rotating flows arise when the non-ideal region is localised toward both the spine and the fan. Similar counter rotational plasma flow regions were also observed in the dynamic case studied by Galsgaard et al. [2003a] when the foot points about the spine were subjected to driving of the same vorticity. Also, despite the fact that the fan plane field is unperturbed, a rotational flow is induced there by the non-ideal regions. With higher even values of α similar results are found.

Opposite vorticity twist

The other case that can be modelled within this framework is when the twist applied to the magnetic field is of opposite vorticity on either side of the fan plane. This is achieved by choosing odd values for β along with $c \neq 0$ and, for example, $\alpha = 4$. In this case the twist in the field is localised in a similar way to the previous case but the current in the $z < 0$ region switches direction. This switch in direction induces non-ideal flows of opposite vorticity on each side of the fan plane leaving a layer of static (or entirely parallel) plasma flow in the fan itself.

Reconnection Rate

To quantify the reconnection rate and indeed prove that reconnection (in the form of reconnective slippage) is taking place in these models, the framework of flux transporting velocities ($\mathbf{w}_{in}$ and $\mathbf{w}_{out}$) is used. As the spine line in the above models is ideal, field lines very close to the spine are identified as those that thread into the non-ideal current region and are associated with $\mathbf{w}_{in}$. Where these field lines then thread out of the non-ideal region is therefore associated with $\mathbf{w}_{out}$. The reconnection rate is then given by the maximum absolute potential difference between these two ideal regions: $|\Phi_{in} - \Phi_{out}|$ [Hesse and Schindler, 1988; Hornig and Priest, 2003].

To evaluate this potential difference (for the electric potential given in Equation (2.21)) note first that in the ingoing and outgoing ideal regions $\mathbf{J} = 0$ and so $\boldsymbol{\nabla}\Phi_{ni.} \cdot \mathbf{B} = \frac{d\Phi_{ni.}}{ds} = 0$ (using Ohm's law). As the system is cylindrically symmetric this means that $\Phi_{ni.}$ must be a function of $zr^2 = \epsilon$ there. Expressing the non-ideal electric potential in this new variable

$$\begin{aligned}\Phi_{ni} = \; & \frac{j\eta_0 B_0}{\mu_0 L_0}\Bigg[\left(\beta - \frac{2c^6}{l^6}\epsilon^2\right) F_l(r, \alpha+3)\epsilon^{\beta-1} - \frac{4}{l^2}F_l(r,\alpha-1)\epsilon^{\beta+1} \\ & + \; 2\left((\alpha+2\beta+1) - \frac{4c^6}{l^6}\epsilon^2\right)F_l(r,\alpha-3)\epsilon^{\beta+1}\Bigg] e^{-\frac{c^6}{l^6}\epsilon^2}, \end{aligned} \tag{2.24}$$

it is clear that the behaviour in both limits is dictated by the $F_l(x, A)$ function. Using the asymptotic values of this function as $r \to 0, \infty$ and re-expressing $\alpha = 2n + 4$ (see Appendix A.2) the general reconnection rate is found to be

$$\begin{aligned}\frac{d\Psi}{dt} = \; & \max\Bigg\{\Bigg[\left(\beta - \frac{2c^6}{l^6}\epsilon^2\right)\epsilon^{\beta-1}\left(\frac{l^2}{2}\right)^3 (2n+5)(2n+3)(2n+1) \\ & -\frac{4}{l^2}\epsilon^{\beta+1}\left(\frac{l^2}{2}\right)(2n+1) + 2\left((2n+2\beta+5) - \frac{4c^6}{l^6}\epsilon^2\right)\epsilon^{\beta+1}\Bigg] e^{-\frac{c^6}{l^6}\epsilon^2} \\ \times \; & \left(\frac{j\eta_0 B_0}{\mu_0 L_0}\right)\sqrt{\pi}\left(\frac{l^2}{2}\right)^{n+1}\prod_{m=0}^{n-1}(2(n-m)-1)\Bigg\}. \end{aligned}$$

Clearly the reconnection rate is, in general, a complicated function which depends on the geometry of the non-ideal region. In particular, the exponential damping term, which controls the length of the current tube along the spine line, has a strong impact on the maximum rate that flux is reconnected. For instance, in the simplest case of an unbounded

tube ($\beta = c = 0$ with $\alpha = 4$ ($n = 0$)) this becomes

$$\frac{d\Psi}{dt} = \frac{j\eta_0 B_0}{\mu_0 L_0}\left(-\frac{4}{l^2}\left(\frac{l^2}{2}\right) + 10\right)\sqrt{\pi}\left(\frac{l^2}{2}\right)\max\{\epsilon\},$$

which is infinite as the unbounded nature of the reconnection region allows an infinite amount of flux to be reconnected at any given instant. However, in general the reconnection region is finite and therefore, so is the reconnection rate. This reconnection rate proves that there is a rotational slippage within the non-ideal regions in agreement with what has been observed in simulation studies and previous simpler analytical models. On the other hand, it also shows the importance of the dimensions of the non-ideal region and not just its strength for reconnection in three dimensions.

2.3.2 Torsional Fan

To model the torsional fan scenario (where a disk of current sits in the fan plane) $\alpha = 1$, $a = 0$ and $b = 1$ is chosen to give a general magnetic field of the form

$$\mathbf{B} = \frac{B_0}{L_0}\left(r, jr(zr^2)^\beta z^\gamma \mathrm{e}^{-\frac{z^2}{l^2} - \frac{c^6}{l^6}(zr^2)^2}, -2z\right), \tag{2.25}$$

where β and γ are positive integers. The field line equations for r and z remain the same as before so that $zr^2 = z_0 r_0^2$. To find ϕ this time, the fact that $ds = dz/B_z$ (where $B_z = -2zB_0/L_0$) is used to solve

$$\begin{aligned}
r\frac{d\phi}{ds} &= B_\phi \\
\frac{d\phi}{ds} &= \frac{B_0}{L_0} j z^\gamma (zr^2)^\beta \mathrm{e}^{-\frac{z^2}{l^2} - \frac{c^6}{l^6}(zr^2)^2} \\
\phi &= \frac{B_0}{L_0} j (zr^2)^\beta e^{-\frac{c^6}{l^6}(zr^2)^2} \int z^\gamma \mathrm{e}^{-\frac{z^2}{l^2}} ds + C \\
&= -\frac{B_0}{L_0} j (zr^2)^\beta e^{-\frac{c^6}{l^6}(zr^2)^2} \int z^\gamma \mathrm{e}^{-\frac{z^2}{l^2}} \frac{dz}{2z}\frac{L_0}{B_0} + C \\
&= -\frac{j}{2}(zr^2)^\beta e^{-\frac{c^6}{l^6}(zr^2)^2} \int z^{\gamma-1} \mathrm{e}^{-\frac{z^2}{l^2}} dz + C,
\end{aligned}$$

leading to

$$\phi + \frac{j}{2}(zr^2)^\beta e^{-\frac{c^6}{l^6}(zr^2)^2} F_l(z, \gamma) = C, \tag{2.26}$$

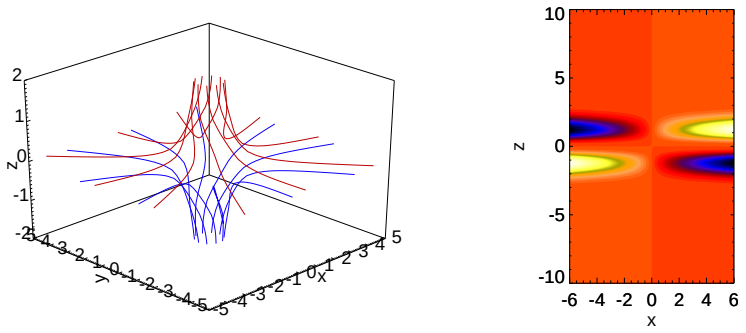

Figure 2.5: The unbounded Torsional fan case. Left: a selection of field lines. Right: the perturbation field viewed in the $y = 0$ plane where yellow indicates positive and blue negative. Plotted for $\gamma = 3$, $\beta = 0$, $j = 5$, $c = 0$ and $l = 1$. The field on the spine line is approaching the null and receding away from the null in the fan plane.

where $C(r_0, \phi_0, z_0)$. The components of current in this case are found from Equation (2.3) and given by

$$\begin{aligned} J_r &= -\frac{jB_0}{\mu_0 L_0}\left((\gamma+\beta) - 2\left(\frac{z^2}{l^2} + \frac{c^6}{l^6}(zr^2)^2\right)\right) r z^{\gamma-1}(zr^2)^\beta \mathrm{e}^{-\frac{z^2}{l^2}-\frac{c^6}{l^6}(zr^2)^2} \\ J_\phi &= 0 \\ J_z &= \frac{jB_0}{\mu_0 L_0}\left(2(1+\beta) - \frac{4c^6}{l^6}(zr^2)^2\right) z^\gamma (zr^2)^\beta \mathrm{e}^{-\frac{z^2}{l^2}-\frac{c^6}{l^6}(zr^2)^2}, \end{aligned} \tag{2.27}$$

and using Equation (2.7) the electric potential is found to be (see Appendix B.1)

$$\begin{aligned} \Phi_{ni} = -\frac{j\eta_0 B_0}{\mu_0 L_0}\Bigg[\frac{zr^2}{2}\left(\left((\gamma+\beta) - \frac{2c^6}{l^6}(zr^2)^2\right) F_l(z, \gamma-2) - \frac{2}{l^2}F_l(z,\gamma)\right) \\ + \left(2(\beta+1) - \frac{4c^6}{l^6}(zr^2)^2\right) F_l(z,\gamma+1)\Bigg] (zr^2)^\beta e^{-\frac{c^6}{l^6}(zr^2)^2}, \end{aligned} \tag{2.28}$$

where $\gamma \neq 0$ or 2. As in the Torsional spine case, there are several ways in which the system can be perturbed. As before, the following subsections systematically consider first the perturbation of the magnetic field and the induced non-ideal plasma flows for each in turn, and then the rate of reconnective slippage associated with the general perturbation. In each investigation a scaling of (strength/maximum)$^{1/d}$ has been applied to the vector plots and the constants η_0, μ_0, B_0 and L_0 set to 1.

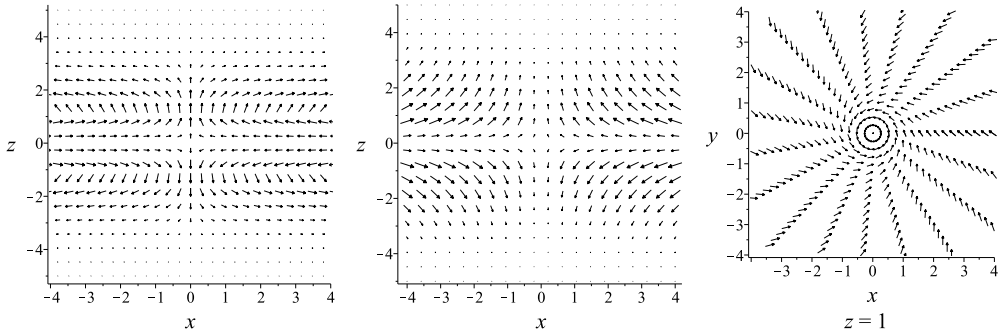

Figure 2.6: Scaled plots of the radially symmetric current flow in the $y = 0$ plane (left panel) and plasma flow in the $y = 0$ and $z = 1$ planes (middle and right panels respectively). Plotted for $\gamma = 3$ and $\beta = 0$ with $l = 1$, $c = 0$ and $j = 5$. Here the *MAPLE* scaling of $d = 3$ has been applied.

Opposite vorticity twist

The most likely scenario to occur in practice is when a strong current layer is formed at the fan plane through perturbations of opposite vorticity in each topological region. This scenario may be modelled by choosing $\gamma + \beta$ to be odd i.e. $\gamma = odd$ and $\beta = even$ or $\gamma = even$ and $\beta = odd$. Solutions with even γ values are avoided on similar grounds to when α is odd in the Torsional spine case as they produce unrealistic solutions. The investigation, therefore, focuses on when $\gamma = odd$ and $\beta = even$.

The linear (in r) perturbation: $\beta = 0$ and $c = 0$. The analogue of the z-independent torsional spine case is when the torsional fan case has an unbounded disk of current aligned to the fan plane and can be modelled by taking $\beta = 0$ and $c = 0$. When $\gamma = 1$ there exists a non-zero current in the fan plane which linearly increases with r (see Equation 2.27). This makes its behaviour slightly different from the other cases where $\gamma \geq 3$. In general, the case with non-zero current in the fan plane is less complex, so as an example, the case of $\gamma = 3$ is described with the differences to the $\gamma = 1$ case pointed out. The magnetic field when $\gamma = 3$ is given by

$$\mathbf{B} = \frac{B_0}{L_0}\left(r, jrz^3 e^{-\frac{z^2}{l^2}}, -2z\right). \tag{2.29}$$

Figure 2.5 shows the perturbation to the magnetic field along with a selection of field lines near the null and Figure 2.6 (left panel) shows the current associated with the shear region occurs in a flattened disk near the fan. These disks are qualitatively very similar to the disks of current observed in the simulations of Pontin and Galsgaard [2007]. Figure

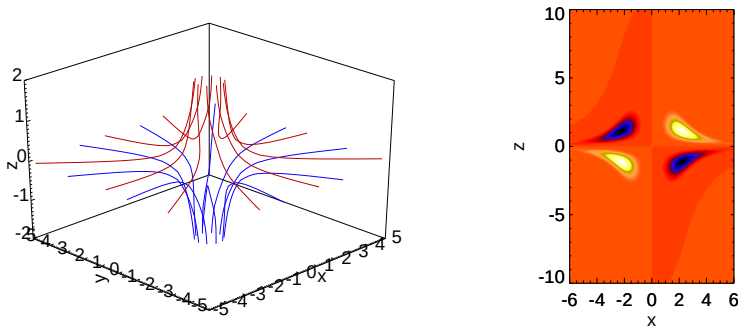

Figure 2.7: The fully localised Torsional fan case. Left: a selection of field lines. Right: the perturbation field viewed in the $y = 0$ plane where yellow indicates positive and blue negative. Plotted for $\gamma = 3$, $\beta = 2$, $j = 5$, $l = 1$ and $c = 5^{-1/3}$. The field on the spine line is approaching the null and receding away from the null in the fan plane.

2.6 (middle and right panels) shows the plasma flow. This flow counter rotates below the fan with static plasma in the fan plane separating the two regions. If the induced perpendicular rotational flows in the unbounded Torsional spine case (Figure 2.2) are compared to the rotational flows in the $z > 0$ region here, it can be seen that they are of opposite vorticity. However, when $\gamma = 1$ (where $\mathbf{J} \neq 0$ in the fan plane, Equation (2.27)) the perpendicular plasma flow switches direction and matches that of the Torsional spine case.

The nonlinear (in r) perturbation: $\beta \neq 0$ and $c \neq 0$. To consider the extra complexity brought about by an additional localisation of the non-ideal region towards the spine, γ is kept set to 3 and $\beta = 2$ is chosen along with $c \neq 0$. The magnetic field then becomes:

$$\mathbf{B} = \frac{B_0}{L_0}\left(r, jr^4z^5e^{-\frac{z^2}{l^2}-\frac{c^6}{l^6}(zr^2)^2}, -2z\right). \tag{2.30}$$

The shape of the twisted region along with a selection of field lines passing through it is shown in Figure 2.7. In a similar manner to the torsional spine case with $c \neq 0$, the twisted region has now been localised into two squashed tori near the null. However, now the bias of the localisation is toward the fan rather than the spine. It might be expected that with such a similar profile there will also be counter rotational flows. From Figure 2.8 it is clear that even more counter flows occur in distinct bands that roughly follow the shape of the background magnetic field. By comparing to cases where $c \neq 0$ and $\beta = 0$ and vice versa it is found that the counter flow near the null that spans the spine and the fan plane arises from $\beta \neq 0$, whereas the band further out is due to the exponential localisation brought

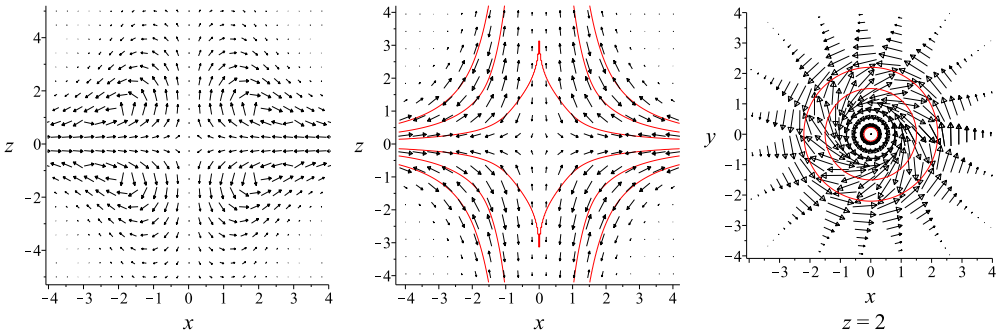

Figure 2.8: The left panel shows the scaled radially symmetric current flow in the $y = 0$ plane, the middle and right panels showing the side ($y = 0$) and top ($z = 2$) views respectively of the scaled plasma flow when $\gamma = 3$, $\beta = 2$ and $c = 5^{-1/3}$ with $l = 1$ and $j = 5$ where the scaling has been applied with $d = 13$. The red lines show where $v_{\perp\phi} = 0$.

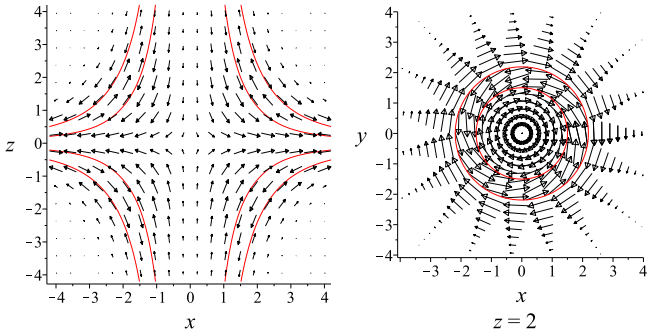

Figure 2.9: Top ($z = 2$) and side view ($y = 0$) of the scaled radially symmetric plasma flow for $\gamma = 1$, $\beta = 2$ and $c = 5^{-1/3}$ with $l = 1$ and $j = 5$ where the scaling has been applied with $d = 13$. The red lines show where $v_{\perp\phi} = 0$.

in by $c \neq 0$. These flows arise from the element of 'torsional spine-like' localisation (i.e. towards to the spine) now present in the perturbing magnetic field.

When $\gamma = 1$, the counter flow region near the null is of the same vorticity as the main flow (rather than against it when $\gamma \geq 3$), so that three distinct regions, as opposed to four, (Figure 2.9) are found to occur. However, counter flows are still prevalent.

Equal vorticity twist

$\gamma = 3$ and $\beta = 1$ is an example of when the twist applied to the field has the same vorticity on either side of the fan plane. In this case the magnetic field takes the form

$$\mathbf{B} = \frac{B_0}{L_0}\left(r, jr^3z^4e^{-\frac{z^2}{l^2}-\frac{c^2}{l^2}(zr^2)^2}, -2z\right). \tag{2.31}$$

The current ring that forms is qualitatively similar to the previous case but with the direction of current flow when $z < 0$ reversed. In general, the cases when $\gamma = 1$ and $\gamma \geq 3$ have similar features as above but the flows in both topological regions now have the same vorticity. Through symmetry, this allows for a rotational flow in the fan itself.

Reconnection rate

The reconnection rate can be found in a similar way to the Torsional spine case. In this case the limits are now taken in z rather than r. The ingoing electric potential is given by $\lim_{z\to\infty}\Phi_{ni.}$, whereas the outgoing potential is given by $\lim_{z\to 0}\Phi_{ni.}$. For the case when $\gamma = 1$ a definite reconnection rate cannot be defined as (due to the finite current in the fan plane) once the field lines enter into the current sheet they never leave. However, for $\gamma \geq 3$ a general reconnection rate may be found from the difference of the electric potentials in these limits to be (see Appendix B.2)

$$\begin{aligned}\frac{d\Psi}{dt} &= \max\Bigg\{\Bigg[\frac{\epsilon}{2}\Bigg(\left((2n+3+\beta)-\frac{2c^6}{l^6}\epsilon^2\right)-(2n+2)\Bigg)\frac{\sqrt{\pi}l^2}{2}\prod_{m=0}^{n-1}(2(n-m)-1)\\ &+ \left(2(\beta+1)-\frac{4c^6}{l^6}\epsilon^2\right)\left(\frac{l^2}{2}\right)^2\prod_{m=-1}^{n-1}(2(n-m))\Bigg]\frac{j\eta_0 B_0}{\mu_0 L_0}\left(\frac{l^2}{2}\right)^n\epsilon^\beta e^{-\frac{c^6}{l^6}\epsilon^2}\Bigg\},\end{aligned}$$

where $\epsilon = zr^2$ and $\gamma = 2n+3$. Once again, it is apparent that the rate of slippage that occurs in general for Torsional fan reconnection is very dependent upon the geometry of the the non-ideal region (i.e. upon l, c, β and n). It does, however, prove that reconnection is occurring continuously within each non-ideal region in agreement with the general theory of 3D reconnection. As in the Torsional spine case, the exponential damping term has

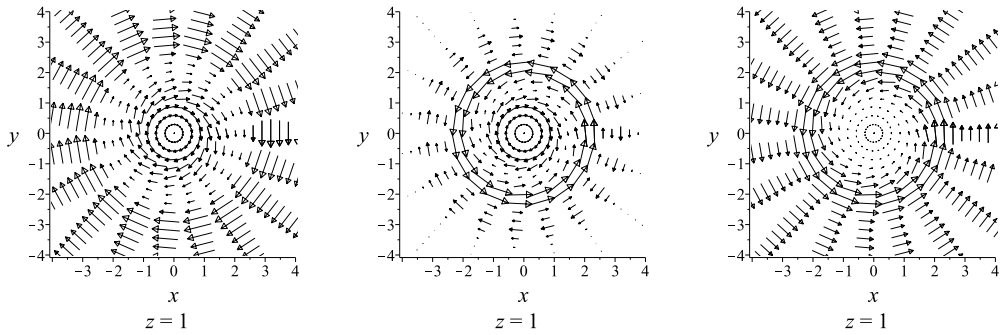

Figure 2.10: Background ideal plasma flows with $k = -700$ (left), $k = 0$ (middle) and $k = 700$ (right) added to the non-ideal solution for localised torsional spine case with $\alpha = 4$, $\beta = 0$, $l = 1$, $c = 5^{-1/3}$ and $j = 3$. No scaling has been applied to these flows ($d = 0$).

a strong effect on the maximum of this function so that when the disk is unbounded ($c = \beta = 0$), $\frac{d\Psi}{dt}$ becomes infinite.

2.3.3 Composite Solutions

How important are the ideal background plasma flows to the non-ideal solutions described above? In the dynamic simulations of Pontin and Galsgaard [2007] and Galsgaard et al. [2003a] the ideal driving flows which naturally form the current structures that lead to Torsional reconnection are rotational motions. These rotational motions are either initiated on the boundaries of the box or as perturbations present initially in the magnetic field before the system is evolved. Both approaches launch MHD waves towards the null point and it is these waves which ultimately form the current sheets within which the Torsional slippage takes place. In order to be clear of the terminology in the rest of this section and subsequent chapters a brief summary of the main features of the main MHD wave types is now given.

There are three main waves which propagate in a magnetised plasma: the shear Alfvén wave and the fast and slow magnetoacoustic wave. The Alfvén wave is a purely magnetic wave (in that it does not perturb the plasma density and pressure) which transversely perturbs the magnetic field and travels at the Alfvén speed: $c_A = B/\sqrt{\mu_0 \rho}$. The fast and slow magnetoacoustic waves are more complex as they involve a perturbation to both the plasma density and pressure as well as the magnetic field. In fact, the fast wave is characterised by an in phase relationship between the plasma and magnetic pressure perturbations, whereas for the slow wave they are out of phase. The velocities of each are

given by

$$c_{(slow,fast)} = \frac{1}{\sqrt{2}}\left(c_A^2 + c_s^2(-,+)\sqrt{(c_A^2+c_s^2)^2 - 4c_A^2c_s^2\cos^2\theta}\right)^{\frac{1}{2}},$$

where θ is the angle between the direction of wave propagation and the magnetic field and $c_s = \sqrt{\gamma P/\rho}$ is the plasma sound speed. The important points to note about the fast and slow waves are that fast waves can propagate both parallel and perpendicular to the magnetic field and that $c_{fast} \geq c_A$, whereas the slow wave can not propagate perpendicular to the magnetic field and so is predominantly longitudinal and $c_{slow} \leq c_A$. Deeper descriptions and derivations of the properties of each can be found in many astrophysics textbooks (for instance Priest [1984]).

In both of the dynamic simulations of Pontin and Galsgaard [2007] and Galsgaard et al. [2003a], when perturbations are driven slowly enough that coupling to non-linear fast waves and can be neglected, the perturbations which go on to form current sheets follow the field lines (and so are essentially torsional Alfvén waves) and only those field lines on which the perturbations begin ever feel their presence. Therefore, an ideal flow with a similar localisation to the general magnetic field perturbation is introduced:

$$\Phi_i = ke^{-\frac{c^6}{l^6}(zr^2)^2}. \tag{2.32}$$

Note, that when the background symmetric null field is unperturbed (i.e. when $j = 0$ in Equation (2.14)) this leads to a purely azimuthal plasma flow. However, with the addition of twist to the field, through the magnetic field perturbation (when $j \neq 0$), components in the z and r directions are also present. When sufficiently strong background ideal plasma flows are applied, the counter rotational bands shown in the $c \neq 0$ Torsional spine and fan non-ideal solutions may be suppressed. Depending on the direction of the ideal flow, all the plasma can be made to rotate one way or the other. Figure 2.10 shows an example of this for a localised Torsional case. The reconnection rates associated with each however remain unchanged as the ideal potential *by definition* does not vary along a magnetic field line and so is non-reconnective. The interpretation of the reconnection that occurs is still that of a relative torsional slippage but now within a globally rotating plasma field.

The weakness of the kinematic method is that we are free to choose this background flow field arbitrarily, whereas in practice, the ideal flow is likely to be coupled to the non-ideal one self consistently. However, the fact that counter rotational plasma flows have been seen in self consistent simulations suggest that these non-ideal flows can grow to dominate the ideal driving aspect. This issue will be investigated further in Chapter 5.

2.4 Localised η Models

Realising that the dimensions of the non-ideal region are important for reconnection in kinematic solutions, a fair question is how much information is lost by using only resistivity η (instead of $\mathbf{J}$) to localise the process as has often been done in the past? It might be expected that localised η solutions would be qualitatively similar to equivalent solutions with a local current; but how similar? What controls the features of the induced non-ideal flows: the resistivity or the current? Also, is the reconnection rate altered by only using a localised resistivity? Having done the hard yards by developing models with localised current sheets a simple extension of the previous solutions allows for an investigation of these questions.

2.4.1 Torsional Spine

A localised resistivity can be incorporated into the general Torsional spine solution through a choice of η with a similar form to the magnetic field perturbation

$$\mathbf{B}_p = j_0\mu_0(zr^2)^\beta r^\alpha e^{-a_1^2\frac{r^2}{l^2}-c_1^6\frac{(zr^2)^2}{l^6}}\hat{\boldsymbol{\phi}}. \tag{2.33}$$

where $j_0 = \frac{jB_0}{\mu_0 L_0}$. Thus, the resistivity takes the form

$$\eta = \eta_0(zr^2)^\delta r^\lambda e^{-a_2^2\frac{r^2}{l^2}-c_1^6\frac{(zr^2)^2}{l^6}}. \tag{2.34}$$

Note that a has been replaced with a_1 and c with c_1 in $\mathbf{B}_p$ (Equation (2.14)) to easily compare the localisation of η and $\mathbf{J}$. As η appears as a scalar multiplying quantity in the integral for Φ_{ni} it is readily found that the general non-ideal electric potential takes the form:

$$\begin{aligned}\Phi_{ni} = \; & j_0\eta_0\Bigg[\left(\beta - \frac{2c_1^6}{l^6}(zr^2)^2\right)F_q(r,\alpha+\lambda+3)(zr^2)^{-1} - \frac{4}{l^2}F_q(r,\alpha+\lambda-1)(zr^2) \\ & + \; 2\left((\alpha+2\beta+1) - \frac{4c_1^6}{l^6}(zr^2)^2\right)F_q(r,\alpha+\lambda-3)(zr^2)\Bigg](zr^2)^{\beta+\delta}e^{-\frac{c_1^6+c_2^6}{l^6}(zr^2)^2},\end{aligned}$$

where $q = \frac{l}{\sqrt{a_1^2+a_2^2}}$. Well behaved solutions now occur when $\alpha+\lambda \geq 4$ and even. From the general form of this equation it is clear that the reconnection rate will be altered by the form of η. Even if the resistivity is chosen so that the arguments of the F functions remains the same (i.e. so that $\alpha+\lambda = 4$ for $\alpha = 4,3,2,1$ with $\lambda = 0,1,2,3$ for instance)

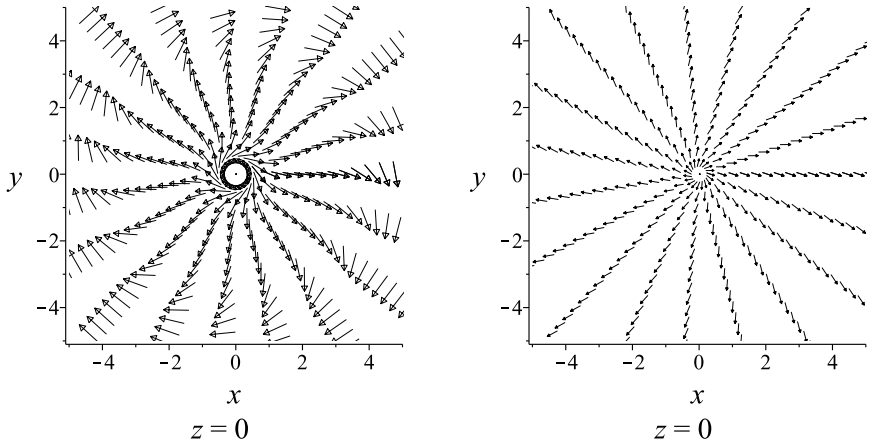

Figure 2.11: Plasma flow in the fan plane for the unbounded Torsional spine case: when $j_0 = 3, l = 1.75$ with the *MAPLE* scaling applied with $d = 11$. Left: local $\mathbf{J}$ ($\alpha = 4, a_1 = 1, \lambda = a_2 = 0$); Right: local η ($\alpha = 1, a_1 = 0, \lambda = 3, a_2 = 1$).

alterations through the α factor in the third term will lead to a different potential difference. Therefore, the reconnection rates in these models are affected when η is used to localise the non-ideal region.

A change in reconnective slippage rate suggests a change in the rate of differential rotation and so the topology of the induced perpendicular plasma flows. With many potential permutations of the above equation to explore, the attention of the following investigation of these flows is restricted to the simplest case of the unbounded current layer (when $\beta = \delta = 0$ and $c_1 = c_2 = 0$).

Direct comparison

Consider a direct comparison between plasma flows for a localised current (with η constant) and a localised η (with $\mathbf{J}$ constant). Specifically, a comparison between when $\alpha = 4, a_1 = 1, \lambda = a_2 = 0$ giving

$$\mathbf{J} = \boldsymbol{\nabla} \times \left(j_0 r^4 e^{-\frac{r^2}{l^2}} \hat{\boldsymbol{\phi}} \right), \quad \eta = \eta_0, \tag{2.35}$$

and $\alpha = 1, a_1 = 0, \lambda = 3, a_2 = 1$ giving

$$\mathbf{J} = j_0 \left(0, 0, 2\right), \quad \eta = \eta_0 r^3 e^{-\frac{r^2}{l^2}}, \tag{2.36}$$

Figure 2.11 shows the perpendicular plasma flow in the fan plane for these two cases. Both flows are rotational near the null point and have the same vorticity. However, the flows of

the local η case have a strong radial component at all values of r (excluding $r = 0$) whereas the case with the localised current only has a strong radial component for an intermediate range of r.

Why are the induced perpendicular plasma flows behaving in this way? Ultimately these differences are a geometrical effect of the changing underlying shape of the magnetic field. The strong outflow occurs where the magnetic field is strongly sheared and so has a strong ϕ-component. The differences between the two initially compared perpendicular plasma flows in Figure 2.11 are, therefore, much more easily understood by considering the shape of the magnetic field (as shown in Figure 2.12). In the case with a local $\mathbf{J}$, near to the null ($r \ll 1$) and at large radii ($r \gg 1$) the magnetic field is radial and so the induced perpendicular plasma flows in these regions are rotational.

When both η and $\mathbf{J}$ are localised, the flow topology is again dependent upon the underlying shape of the magnetic field but with the magnitude scaled down where η is reduced. It is clear, therefore, that the geometry of the field (and therefore the localisation of the current sheet) is what dictates the magnetic flux transport in solutions constructed using resistivity to localise the non-ideal region. As the associated reconnection rate is also different in models with a localised η from those derived using localised current sheets, any quantitative comparisons of these models with the local current sheets seen in simulation studies is, therefore, difficult. That being said, the manner that new connections are formed in the two approaches are the same (i.e. a rotational reconnective slippage) and so, from an understanding point of view, simple local η models provide a useful starting point of investigations into complex reconnective phenomena.

2.4.2 Torsional Fan

A similar conclusion can be drawn from the Torsional fan models. In this case a localised resistivity can be incorporated into the original Torsional fan solution via a choice of

$$\eta = \eta_0 (zr^2)^\delta z^\zeta e^{-b_2^2 \frac{z^2}{l^2} - \frac{c_2^6}{l^6}(zr^2)^2}, \quad \& \quad \mathbf{B}_p = j_0 \mu_0 r (zr^2)^\beta z^\gamma e^{-b_1^2 \frac{z^2}{l^2} - \frac{c_1^6}{l^6}(zr^2)^2} \hat{\boldsymbol{\phi}}, \tag{2.37}$$

where now b has been replaced with b_1 and c with c_1 in $\mathbf{B}_p$ (Equation (2.14)). This generalises the electric potential into

$$\begin{aligned} \Phi_{ni} = \; & -j_0 \eta_0 \left[\frac{zr^2}{2} \left(\left((\gamma + \beta) - \frac{2c_1^6}{l^6}(zr^2)^2 \right) F_q(z, \gamma + \zeta - 2) - \frac{2}{l^2} F_q(z, \gamma + \zeta) \right) \right. \\ & + \left. \left(2(\beta + 1) - \frac{4c_1^6}{l^6}(zr^2)^2 \right) F_q(z, \gamma + \zeta + 1) \right] (zr^2)^{\beta + \delta} e^{-\frac{c_1^6 + c_2^6}{l^6}(zr^2)^2}, \end{aligned} \tag{2.38}$$

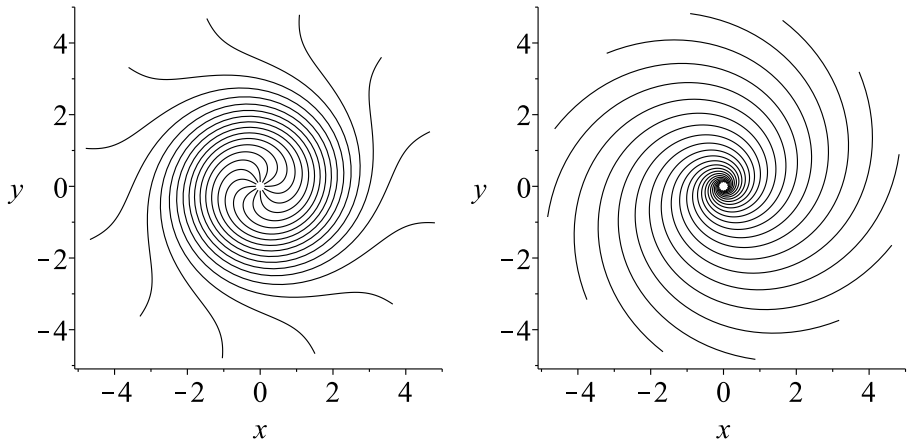

Figure 2.12: Field lines in the fan plane of the magnetic fields used in the the localised current case (left) and localised resistivity case (right) in subsection 2.4.1. Compare the shape of the field with the plasma flows in Figure 2.11.

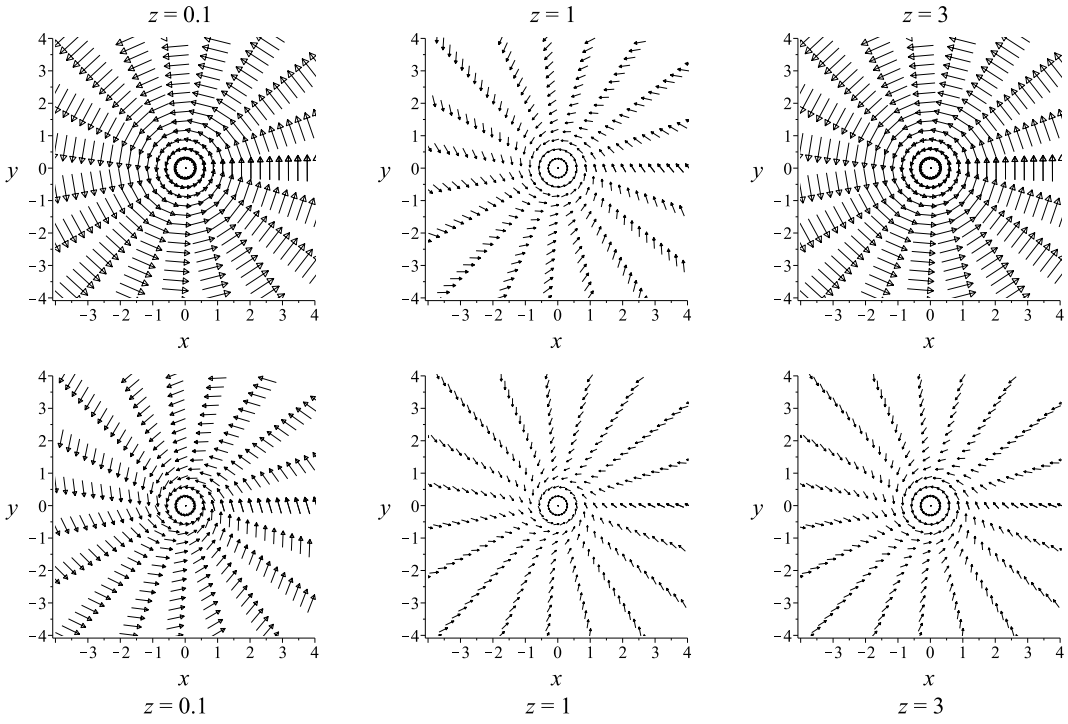

Figure 2.13: Plasma flow at various heights within the $\eta\mathbf{J}$ layer for the unbounded Torsional fan case with $j_0 = 3, l = 1$ and $d = 3$. Top row: local $\mathbf{J}$ ($\gamma = 3, \delta = 0, b_1 = 1, b_2 = 0$), bottom row: local η ($\gamma = 1, \delta = 2, b_1 = 0, b_2 = 1$).

where $j_0 = \frac{jB_0}{\mu_0 L_0}$ and $q = \frac{l}{\sqrt{b_1^2+b_2^2}}$. The non-ideal electric potential (Φ_{ni}) depends explicitly (i.e. outside of the F functions) on γ and, therefore, the reconnection rate is also expected to change when a localised resistivity is used. As in the Torsional spine case, the topology of the flows is also directly dependent upon the degree of twist in the field. However, in this case the twist varies with height (z) rather than radius. Thus, the noticeable differences between perpendicular plasma flows, induced by non-ideal regions localised by η rather than $\mathbf{J}$, become visible as the rotational flows are viewed at an increasing distance along the spine from the null.

As an example, Figure 2.13 shows the induced perpendicular plasma flows at various z values for an unbounded non-ideal region ($c_1 = c_2 = 0$ with $\beta = \delta = 0$) localised by η, where $\gamma = 1, \zeta = 2, b_1 = 0$ and $b_2 = 1$ such that

$$\mathbf{J} = j_0 \left(-r, 0, 2z\right), \quad \eta = \eta_0 z^2 e^{-\frac{z^2}{l^2}}, \tag{2.39}$$

and localised by $\mathbf{J}$, where $\gamma = 3, \zeta = 0, b_1 = 1$ and $b_2 = 0$ so that

$$\mathbf{J} = \boldsymbol{\nabla} \times \left(j_0 r z^3 e^{-\frac{z^2}{l^2}} \hat{\boldsymbol{\phi}} \right), \quad \eta = \eta_0. \tag{2.40}$$

For this choice of parameters the edge of the non-ideal region is at $|z| \approx 3$. This results in the perpendicular plasma flows in the current localised case returning to a purely azimuthal flow when $|z|$ is greater than 3, whereas the flows in the local η solution remain strongly radial.

2.5 Anomalous Resistivity and Localised Current Sheets

Finally, in this Section the physically most plausible scenario of when strong current layers are accompanied by an anomalous resistivity above some background value is briefly commented upon. In general, solutions can be constructed with a resistivity with a similar localisation to the perturbation field, i.e.

$$\mathbf{B}_p = \frac{B_0}{L_0} f(r,z) \hat{\boldsymbol{\phi}}. \quad \& \quad \eta = \eta_0 + \eta_a g(r,z), \tag{2.41}$$

where $g(r,z)$ is chosen in a similar way to the previous section to mirror the behaviour of the perturbation function. In both the Torsional spine and fan cases, on the evidence of the previous section, the non-ideal flows are not expected to be substantially modified when $\eta_a \neq 0$, but the reconnection rate would be increased noticeably. Such an increase in reconnection rate is, of course, what is needed (in addition to intense current flows)

in stellar atmospheres such as the Solar Corona (where the background value of η_0 is very small) to speed up the rate of reconnection and local ohmic heating. However, it is worth bearing in mind that the non-ideal flows and rate of reconnection are linked to the dimensions of the current sheet. In these models the dimensions are held fixed but in a fully dynamic situation the dimensions might be expected to change following the introduction of an anomalous resistivity. Indeed, in numerical studies of the Sweet-Parker [Parker, 1957; Sweet, 1958] and Petscheck [Petschek, 1964] 2D reconnection mechanisms, an anomalous resistivity has been shown to hold the length of the current sheet at a fixed (small) length and so can maintain the Petscheck (shock complimented) reconnection rate. However, with a constant resistivity the initially short Petschek current sheet lengthens to the size of the system, where reconnection then only proceeds at the Sweet-Parker rate [Scholer, 1989; Ugai, 1995]. Clearly in the 2D case an anomalous resistivity can have a dynamic effect on the current sheet dimensions. However, even if the sheet dimensions alter significantly following the introduction of an anomalous resistivity in simulations where these 3D current layers are dynamically formed, the generality of the argument above and the work within Sections 2.3 and 2.4 could still help quantify the changing flows and reconnection rates for the scenario of Torsional reconnection at symmetric 3D null points.

2.6 Summary

In this chapter steady state kinematic models were developed which describe the reconnective slipping process that occurs when twisting perturbations are applied to rotationally symmetric 3D null point magnetic fields. Thus, models were introduced for the Torsional spine and fan reconnection regimes using current sheets that are qualitatively similar to those observed in the numerical simulations of Pontin and Galsgaard [2007]. In general, it was found that the induced rotational non-ideal perpendicular flows are of opposite vorticity in the Torsional spine case compared to the Torsional fan case. Models were also introduced for more general non-linear perturbations which were localised toward both the spine and the fan plane. The current sheets in these models are qualitatively similar to those seen in the simulations of Rickard and Titov [1996] and Galsgaard et al. [2003a]. In these models (those with $c \neq 0$ and $\beta \neq 0$) competition between the two non-ideal flow types resulted in discrete bands of counter rotational magnetic flux transport. These counter rotational flows were not previously seen in the simpler kinematic model of Pontin et al. [2004], but the appearance of them agrees with flows seen in the simulations of Galsgaard et al. [2003a]. However, it was noted that these flows may be suppressed

if a sufficiently strong ideal background flow is applied on top of the non-ideal solution. When a local resistivity is used instead of a local current the induced flows are strongly dependent upon the shape of the magnetic field, with η acting only to modify slightly the current dictated flow. Lastly, the reconnection rate is found to be dependent upon the dimensions of the non-ideal region and also on whether a fully localised or anomalous resistivity is used in these models, as expected.

2.7 Conclusions

It can be concluded that, since there are many possible ways to build up current via twisting motions around rotationally symmetric 3D magnetic nulls there are a variety of ways in which connection change in the form of reconnective slippage can occur. Through the use of kinematic models, this investigation has explored some of them and confirms that the dimensions as well as the strength of the current sheet and any anomalous value of the resistivity dictates the rate of reconnective slippage that occurs. What is new is that this has been achieved using models which qualitatively match the current structures found in simulation studies. Obviously, in these models the strength and the current sheet dimensions are assumed arbitrarily as the system is not self consistent. In a fully consistent system, the dimensions (the length scale l in these models) and the strength of the current build up (j) will be functions of the plasma parameters such as the resistivity (η), the viscosity (ν) and the plasma-β (the ratio of magnetic to plasma pressure). However, it is interesting to note from the kinematic models studied in this chapter that a relatively weak but wide current sheet can reconnect just as much magnetic flux as a small but intense one.

The appearance of counter rotational flows related to the localisation of the current sheets is also a new finding. It is interesting that similar bands of counter rotational plasma flow were also seen in the fully dynamic simulations of Galsgaard et al. [2003a], although, due to their lack of self consistency, it is not clear to what extent the kinematic models developed in this chapter can be directly compared. It would be interesting to explore the physical mechanism behind such counter rotational flows in the fully self consistent case. This will be returned to again in Chapter 5.

Lastly, these models were aimed at understanding the non-ideal behaviour observed in simulation studies involving symmetric potential magnetic null points. Since these investigations and subsequent publications, Pontin et al. [2011] have investigated models with a non-symmetric magnetic null (i.e. an improper null with $p \neq 0$). They found the current sheets that form when $p \neq 1$ are elliptical with an unequal distribution of current

which depended on the degree of asymmetry (p). Such uneven current sheets then lead to a dependence of the reconnection rate upon the underlying asymmetry of the magnetic field as well as the current intensity and sheet dimensions.

3

Asymmetric Spine and Fan Reconnection

"Basic research is like shooting an arrow into the air and, where it lands, painting a target."
Homer Burton Adkins

3.1 Introduction

Typical astrophysical atmospheres rarely exhibit much long term symmetry in the active magnetic regions where reconnection is assumed to be taking place. As such, asymmetry in the reconnection process is of great physical relevance for understanding reconnection in such systems. In 2D, asymmetric reconnection at X-points has been studied both numerically and analytically (Murphy et al. [2012], Cassak and Shay [2007]) but as yet little work has been done on the problem for fully 3D null points. Because of the freedom of the third dimension, reconnection at 3D nulls can become asymmetric in one of two ways. Firstly, the null field itself may have inherent asymmetry. That is, the eigenvalues associated with the fan plane are of different values ($p \neq 1$). For the spine-fan reconnection mode (the analogue of 2D X-point reconnection at 3D nulls) this leads to asymmetric current sheet formation and a change in the reconnection rate. This has been studied

analytically and numerically by Pontin et al. [2011] and Galsgaard and Pontin [2011a]. Alternatively, the null field itself may be symmetric but, through the manner of external driving or local plasma anisotropy, the current sheet that forms at it is not. What are the consequences for the reconnection process with such asymmetry? To address this question, in this chapter, analytical solutions are developed for the spine and fan reconnection (TF reconnection) scenarios with asymmetrical current sheets.

3.2 Fan Reconnection

As in the previous chapter, solutions to the MHD equations in the steady state kinematic limit are sought so that the same methodology of finding the induced non-ideal electric potential and associated perpendicular plasma flows is followed. Again, a symmetric ($p = 1$) linear magnetic null

$$\mathbf{B}_n = \frac{B_0}{L_0}\,(x, y, -2z)\,, \tag{3.1}$$

is the starting point to which some non-ideal perturbation field is added such that the total magnetic field is then described by

$$\mathbf{B} = \mathbf{B}_n + \mathbf{B}_p.$$

A symmetric null is chosen to be the background field for these models so that only the effects of asymmetry from the perturbation field are studied.

To model fan reconnection

$$\mathbf{B}_p = f(x, z)\hat{\mathbf{y}}, \tag{3.2}$$

is chosen so that the field perturbation (and therefore the current, $\mathbf{J}$) is localised in x and z. The field line equations are then given by

$$x = x_0 e^{B_0 s/L_0}, \quad z = z_0 e^{-2B_0 s/L_0}, \quad Y = Y_0 e^{B_0 s/L_0}, \tag{3.3}$$

where $Y_0(x_0, y_0, z_0)$ is a constant of integration and

$$Y = y - e^{B_0 s/L_0} \int e^{-B_0 s/L_0} f(x, z)\,\mathrm{d}s. \tag{3.4}$$

Surfaces of field lines are described by $C_1(zx^2) = const.$ and $C_2(zY^2) = const.$, where C_1 and C_2 are arbitrary functions which are independent of s (Equation (3.3)). This useful feature will again be exploited in the localisation below.

An expression for the current is then obtained from Equation (2.3) and combined with

a resistivity localised in the y-direction

$$\eta = \eta_0 e^{-\frac{\left(zY^2\right)^2}{l^2}}, \tag{3.5}$$

completing the full localisation of the $\eta|\mathbf{J}|$ term. This is then fed into Equation (2.7) for the electric potential and subsequently Equation (2.10) giving $\mathbf{v}_\perp$.

3.2.1 The Symmetric Case

Before developing the asymmetric model, the symmetric one is first developed as a reference. In the symmetric case, closed form solutions can be achieved through the choice of

$$f(x,z) = -\frac{jB_0}{L_0} z e^{-\frac{z^2}{h^2} - \frac{(zx^2)^2}{l^6}}, \tag{3.6}$$

giving

$$\begin{aligned}
Y &= y + \frac{jB_0}{L_0} e^{B_0 s/L_0} \int e^{-B_0 s/L_0} z e^{-\frac{z^2}{h^2} - \frac{(zx^2)^2}{l^6}} ds \\
&= y + \frac{jB_0}{L_0} z^{-\frac{1}{2}} \int z^{\frac{3}{2}} e^{-\frac{z^2}{h^2} - \frac{(zx^2)^2}{l^6}} ds \\
&= y - \frac{j}{2} e^{-\frac{(zx^2)^2}{l^6}} z^{-\frac{1}{2}} \int z^{\frac{1}{2}} e^{-\frac{z^2}{h^2}} dz \\
&= y - \frac{j}{2} z^{-1} e^{-\frac{(zx^2)^2}{l^6}} I_1(z),
\end{aligned}$$

where

$$I_a(z) = z^{\frac{1}{2}} \int z^{\frac{a}{2}} e^{-\frac{z^2}{h^2}} dz.$$

Using the definition of this integral the electric potential is given by

$$\Phi_{ni} = \frac{j\eta_0 B_0}{\mu_0 L_0} x \left[\frac{1}{2} \left(1 - \frac{2}{l^6} (zx^2)^2 \right) I_{-3}(z) - \frac{1}{h^2} I_1(z) - \frac{4}{l^6} z x^2 I_3(z) \right] e^{-\frac{z^2(x^4+Y^4)}{l^6}}. \tag{3.7}$$

To arrive at the formulations above, the property that $ds = dz/B_z$ is used and that both zx^2 and zY^2 are independent of s (see Appendix C.1 for the general case). Using the solutions of each I function then gives

$$Y = y - \frac{2j}{3} \left(\frac{2}{7} \frac{z^2}{h^2} M\left(1, \frac{11}{4}, \frac{z^2}{h^2}\right) + 1 \right) z e^{-\frac{z^2}{h^2} - \frac{(zx^2)^2}{l^6}}, \tag{3.8}$$

where $M(\mu, \nu, x)$ is the *Kummer M* hypergeometric function (the properties of which are described in, for instance, Abramowitz and Stegun [1965]) and

$$\Phi_{ni} = -\frac{j\eta_0 B_0}{\mu_0 L_0}\left[a+b+c\right] x e^{-\frac{z^2}{h^2}-\frac{z^2(x^2+Y^2)}{l^6}}, \tag{3.9}$$

where

$$a = \left(1-\frac{2}{l^6}(zx^2)^2\right)(2b+1), \tag{3.10}$$

$$b = \frac{8}{21}\frac{z^4}{h^4}M\left(1,\frac{11}{4},\frac{z^2}{h^2}\right)+\frac{2}{3}\frac{z^2}{h^2}, \tag{3.11}$$

$$c = \frac{8}{5l^6}z^4x^2M\left(1,\frac{9}{4},\frac{z^2}{h^2}\right). \tag{3.12}$$

Figure 3.1 shows the localisation of the non-ideal region and current in this case. This choice of perturbation leads to a constant current in the fan plane along with a localised enhanced region of current near the null. In particular, the current flows in a ring through the null and spine. In terms of understanding the localised flux transfer near to and across the spine, this model is an improvement upon previous models using a globally constant current and localised resistivity [Pontin et al., 2005] or current sheets of an infinite extent [Craig and Fabling, 1996], as it enables the current localisation perpendicular to the direction of shear to be investigated.

As this is a pure solution (i.e. $\Phi_0 = 0$) the influence of the non-ideal region is limited to field lines within an envelope of flux that just touches the edge of the non-ideal region (Hornig and Priest [2003]). Figure 3.2 shows how, when this is the case, the flows are cyclic within this envelope and field lines are repeatedly reconnected across the spine lines. No flux, however, is reconnected across the flan plane as a result of the infinite extent of the sheet on the fan itself: the signature of fan reconnection. Thus, by localising the effects of the non-ideal region, a much more complex system of plasma flow results than in the case when *all* of the magnetic field threads into the current sheet in the fan plane [Craig and Fabling, 1996]. However, such complex flow patterns may potentially be suppressed by a strong enough background ideal flow when composite solutions are constructed.

3.2.2 The Asymmetric Case

The above solution describes well the current structures and non-ideal plasma flows of fan reconnection driven by symmetric weak perturbations of the spine line. However, general asymmetric solutions are required to give insight into the case when both spine lines are

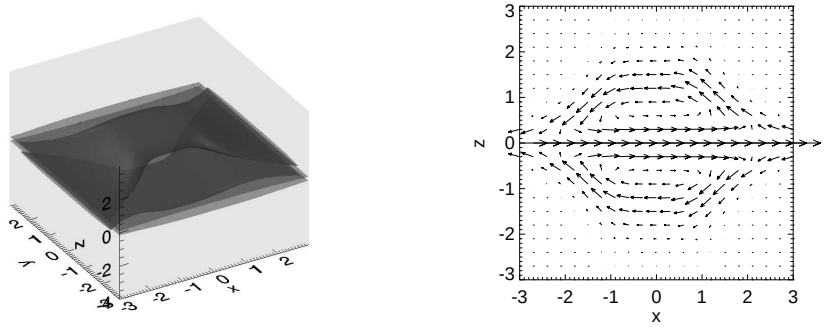

Figure 3.1: The symmetric fan case. Left: an isosurface of $\eta|\mathbf{J}|$ at 25% of the maximum, depicting the shape of the non-ideal region. Right: current flow in the $y = 0$ plane. With parameters of $B_0 = 1, L_0 = 1, \eta_0 = 1, \mu_0 = 1, j = 2, h = 1$ and $l = 2^{1/3}$.

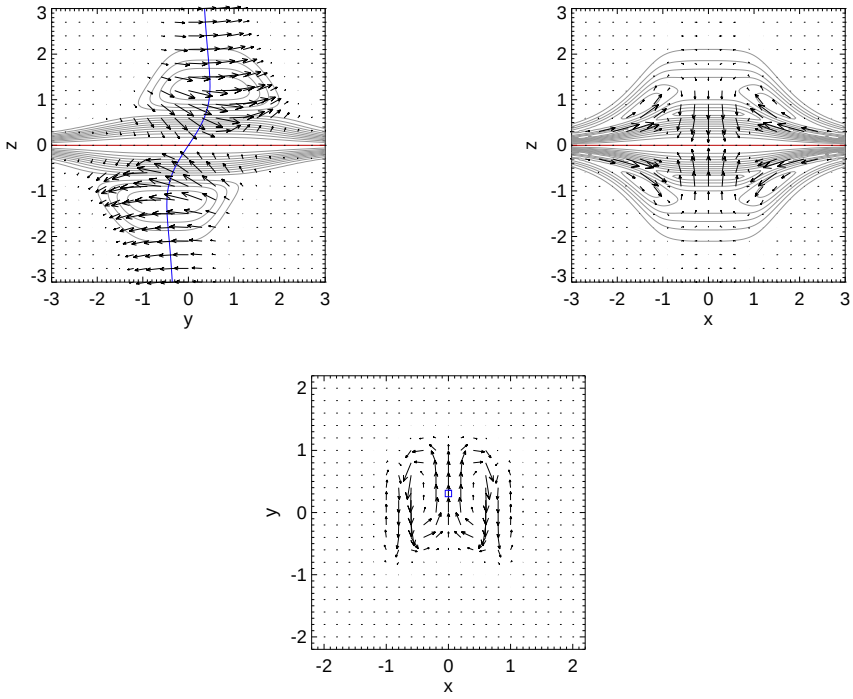

Figure 3.2: The symmetric fan case: The perpendicular plasma flow in the $x = 0$ plane (top left), $y = 0$ plane (top right), and $z = 4$ plane (bottom). The contours and arrows denote $\eta|\mathbf{J}|$ and the perpendicular plasma velocity respectively. The spine is shown in blue as a line in the $x = 0$ plane and a square in the $z = 4$ plane. The fan plane is shown in red. With the parameters given in Figure 3.1.

not symmetrically perturbed. Asymmetry can be integrated into the previous solution naturally by introducing a weighting function $g(z)$ so that in general the perturbation function takes the form

$$f(x,z) = -\frac{jB_0}{L_0} z e^{-\frac{z^2}{h^2} - \frac{(zx^2)^2}{l^6}} g(z),$$

so that now

$$Y = y - \frac{j}{2} z^{-1} e^{-\frac{(zx^2)^2}{l^6}} I_1(z),$$

where the I function has been generalised to

$$I_a(z) = z^{\frac{1}{2}} \int z^{\frac{a}{2}} e^{-\frac{z^2}{h^2}} g(z) dz.$$

The electric potential is then given by

$$\Phi_{ni} = \frac{j\eta_0 B_0}{\mu_0 L_0} x \left[\frac{1}{2} \left(1 - \frac{2}{l^6} (zx^2)^2 \right) I_{-3}(z) - \frac{1}{h^2} I_1(z) - \frac{4}{l^6} z x^2 I_3(z) + \frac{1}{2} K_{-1}(z) \right] e^{-\frac{z^2(x^4+Y^4)}{l^6}}, \tag{3.13}$$

where

$$K_a(z) = z^{\frac{1}{2}} \int z^{\frac{a}{2}} e^{-\frac{z^2}{h^2}} g'(z) dz$$

and $'$ denotes d/dz (see Appendix C.1 for details). $K_a(z)$ can be related to $I_a(z)$ using integration by parts such that

$$K_a(z) = \left(\frac{a}{2} - \frac{z^2}{h^2} \right) z^{\frac{a}{2}-1} e^{-\frac{z^2}{h^2}} g(z) - \frac{a}{2} I_{a-2}(z) + \frac{1}{h^2} I_{a+2}(z).$$

Both integrals are solutions of the system

$$\frac{dQ_a(z)}{dz} = \frac{1}{2z} Q_a(z) + z^{\frac{a+1}{2}} e^{-\frac{z^2}{h^2}} q(z), \tag{3.14}$$

where $Q_a(z) = I_a(z)$ when $q(z) = g(z)$ and $Q_a(z) = K_a(z)$ when $q(z) = g'(z)$. Therefore, both $I_a(z)$ and $K_a(z)$ have a homogeneous solution of $Az^{-\frac{1}{2}}$ which is ignored (by setting $A = 0$) as the integral is specific to the particular solution of the above equation.

To introduce asymmetry, a weighting function is chosen of the form

$$g(z) = 1 + m \operatorname{erf}\left(\frac{z}{p} \right),$$

where $\operatorname{erf}(x)$ is the error function and $0 \leq m \leq 1$. When $m = 0$ or $p \to \infty$, $g(z) = 1$ and the symmetric analytical solution above is recovered. On the other hand, when $m = 1$ and $p \to 0$, $g(z)$ is double the heavyside (unit step) function and the magnetic field

perturbation is switched off where $z < 0$. Thus, a simple measure of the degree of system asymmetry is given by the factor m/p.

This choice of $g(z)$ allows for an analytical closed form solution for $K_{-1}(z)$ given by

$$K_{-1}(z) = \frac{4m}{\sqrt{\pi}p}\left(\frac{4}{5}z^2\left(\frac{1}{h^2}+\frac{1}{p^2}\right)M\left(1,\frac{9}{4},z^2\left(\frac{1}{h^2}+\frac{1}{p^2}\right)\right)+1\right)e^{-z^2\left(\frac{1}{h^2}+\frac{1}{p^2}\right)}. \quad (3.15)$$

However, no closed form solutions exist for the $I_a(z)$ integrals and so these must be found numerically (see Appendix C.2 for details).

Figure 3.3 shows the current structure and non-ideal region when $m = p = 0.5$. It can be seen that the majority of the shear is now in the $z > 0$ region with less in the $z < 0$ region. The top and bottom regions will now be designated as the strong and the weak shear regions respectively. The strong shear region now has associated with it a stronger current ring compared with that of the weak shear region. However, the current at the null itself remains unchanged compared with the symmetric case.

The effect this asymmetry has on the plasma flows is evident in Figure 3.4. In the weak field region the perpendicular plasma flow has strengthened (below the fan plane) whereas in the strong shear region it has weakened. Most strikingly, however, it is clear that the strong flow in the weak shear region has crossed into (bottom right panel) and beyond (top left) the fan plane and flows over the top of the null. Evaluating $\mathbf{v}_\perp$ at the null gives that

$$\mathbf{v}_\perp(0,0,0) = \left(0, -\frac{2j\eta_0}{\mu_0\sqrt{\pi}}\frac{m}{p}, 0\right). \quad (3.16)$$

Thus, for asymmetric fan reconnection a bulk flow of plasma occurs across the null point which is a function of the degree of asymmetry of the system (m/p). However, there is still no flow across the fan plane as this requires a perturbation of the fan and spine reconnection. How this affects the reconnection that occurs through the two spine lines can be shown by considering two flux tubes advected by the induced flux transporting velocity $(\mathbf{w}_{\perp in})$ within the envelopes of flux that thread into the non-ideal region (along the spine from above and below the fan plane). Figure 3.5 compares this asymmetric case $(m = p = 0.5)$ with the symmetric one $(m = 0)$. In the symmetric case both flux tubes reconnect through the spine at the same rate and at the same time as would be expected. However, in the asymmetric case flux clearly reconnects at different rates across each spine line. This seems to be a generic feature of asymmetric fan reconnection brought about through the non-symmetric behaviour of the non-ideal electric potential where $z \gg h$ and $z \ll -h$.

In summary, it is found that for asymmetric fan reconnection magnetic flux is recon-

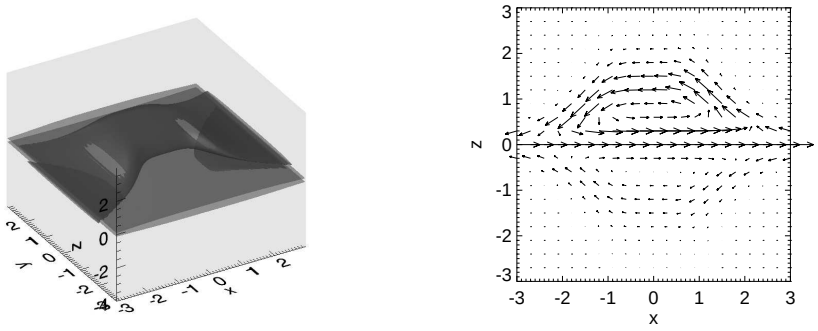

Figure 3.3: The asymmetric fan case. Left: an isosurface of $\eta|\mathbf{J}|$ at 25% of the maximum, depicting the shape of the non-ideal region. Right: current flow in the $y = 0$ plane. With the parameters given in Figure 3.1 and $m = 0.5$ and $p = 0.5$.

nected in an uneven fashion across each spine line and that the resonant surface of the shearing flow is displaced from the fan plane into the region with the stronger shear perturbation. This leads to a bulk flow of plasma through the null point which is a function of the degree of asymmetry. This picture has some similarities to the two dimensional picture of asymmetric X-point reconnection where the stagnation point of the plasma flow is also shifted from the null point [Cassak and Shay, 2007].

3.3 Spine Reconnection

In the fan reconnection scenario TF reconnection only occurs through the spine, which is itself only a line in space. This limits how much variation there can be between scenarios with asymmetric and symmetric current sheets. In the case of spine reconnection however, TF reconnection occurs across the entire fan plane surface. In the following sections several examples of how this can occur in general, and what the consequences are for the reconnection process as a whole, are presented. To create spine reconnection solutions it is more convenient to work in cylindrical coordinates so that now

$$\mathbf{B}_n = \frac{B_0}{L_0}\,(r, 0, -2z)\,. \tag{3.17}$$

To this, a perturbation function localised in r is added of the following form:

$$\mathbf{B}_p = F(r, \phi)\hat{\mathbf{z}}. \tag{3.18}$$

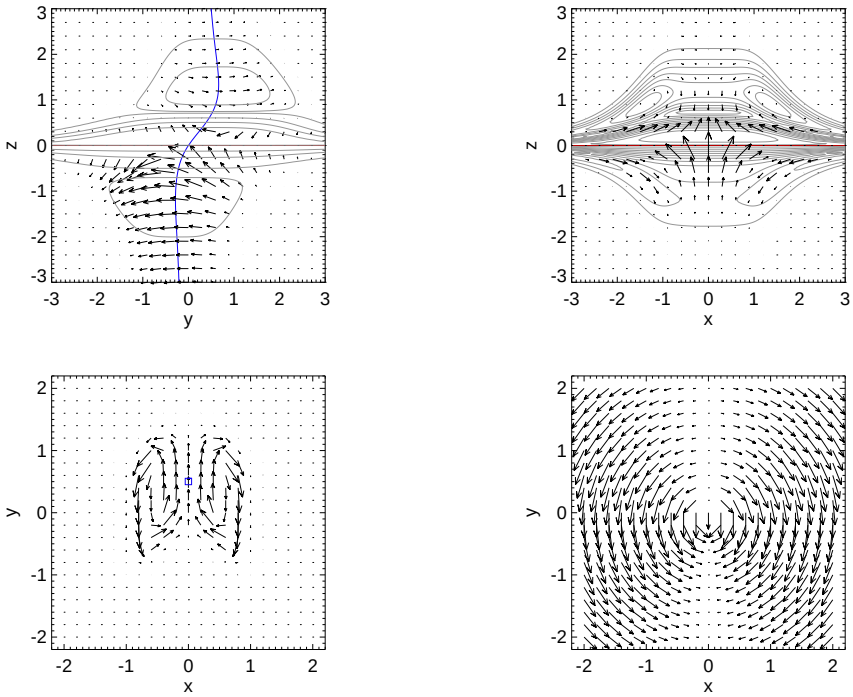

Figure 3.4: The asymmetric fan case: the perpendicular plasma flow in the $x = 0$ plane (top left), $y = 0$ plane (top right), $z = 4$ plane (bottom left) and the fan plane ($z = 0$, bottom right) for the parameters given in Figure 3.1 and $m = 0.5$ and $p = 0.5$. The contours and arrows denote $\eta|\mathbf{J}|$ and perpendicular plasma velocity respectively. The spine is shown is blue as a line in the $x = 0$ and a square in the $z = 4$ plane. The fan plane is shown in red.

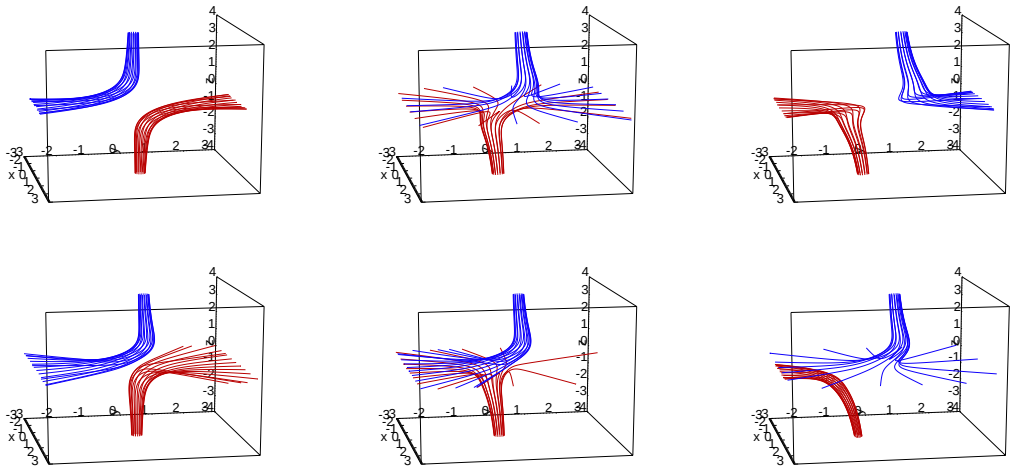

Figure 3.5: Top: evolution of flux in the symmetric fan case. Bottom: evolution of flux in the asymmetric fan case with $m = 0.5$ and $p = 0.5$.

The field line equations are then given by

$$r = r_0 e^{B_0 s/L_0}, \quad \phi = \phi_0, \quad Z = Z_0 e^{-2B_0 s/L_0}, \tag{3.19}$$

where $Z_0(r_0, \phi_0, z_0)$ is a constant of integration and

$$Z = z - e^{-2B_0 s/L_0} \int e^{2B_0 s/L_0} F(r, \phi)\, \mathrm{d}s. \tag{3.20}$$

In this case, flux surfaces are defined by $C_1(Zr^2) = const.$ and $C_2(\phi) = const.$, where C_1 and C_2 are arbitrary functions. A resistivity is then chosen of the form

$$\eta = \eta_0 e^{-\frac{(Zr^2)^2}{k^6}}, \tag{3.21}$$

to complete the localisation of the non-ideal ($\eta|\mathbf{J}|$) term. As before, an expression for the current is obtained from Equation (2.3) and fed into Equation (2.7) for the electric potential and Equation (2.10) for $\mathbf{v}_\perp$.

3.3.1 The Symmetric Case

Let us start by modelling the symmetric case which will be used as a benchmark for comparison once asymmetry is introduced. To model this a perturbation function is

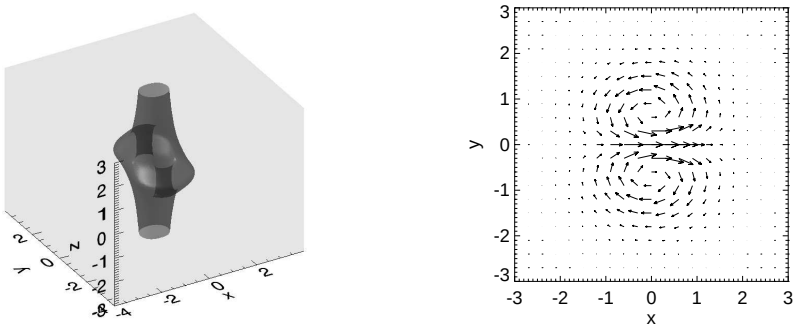

Figure 3.6: The symmetric spine case. Left: an isosurface of $\eta|\mathbf{J}|$ at 25% of the maximum, depicting the shape of the non-ideal region. Right: current flow in the $z = 0$ plane. With parameters of $B_0 = 1, L_0 = 1, \eta_0 = 1, \mu_0 = 1, j = 2, h = 1$ and $k = 1$.

chosen of the form

$$F(r,\phi) = \frac{jB_0}{L_0} f(\phi) r e^{-\frac{r^2}{h^2}}, \tag{3.22}$$

for which

$$\begin{aligned} Z &= z - \frac{jB_0}{L_0} e^{-2B_0 s/L_0} \int e^{2B_0 s/L_0} f(\phi) r e^{-\frac{r^2}{h^2}} ds \\ &= z - \frac{jB_0}{L_0} r^{-2} \int r^2 f(\phi) r e^{-\frac{r^2}{h^2}} ds \\ &= z - j f(\phi) r^{-2} \int r^2 e^{-\frac{r^2}{h^2}} dr \\ &= z + j f(\phi) \frac{h^2}{4r^2} \left(2re^{-\frac{r^2}{h^2}} - h\sqrt{\pi}\,\mathrm{erf}\left(\frac{r}{h}\right)\right). \end{aligned}$$

This gives a simple expression for the electric potential of

$$\Phi_{ni} = -\frac{j\eta_0 B_0 \sqrt{\pi} h}{2\mu_0 L_0} f'(\phi)\,\mathrm{erf}\left(\frac{r}{h}\right) e^{-\frac{(Zr^2)^2}{k^6}}, \tag{3.23}$$

where $'$ denotes $d/d\phi$. In particular, spine reconnection may be modelled by the choice of $f(\phi) = \sin(\phi)$. An exact model for spine reconnection was found by Craig and Fabling [1996] using an infinite non-ideal current region aligned to the spine. This model can be considered to be a kinematic extension of this previous one, with the spine aligned non-ideal region containing a finite amount of magnetic flux due to the localisation of η along the spine. A more general solution can be constructed with the above perturbation function as a special case (see Appendix D), however these solutions in general have no current at the null so the focus is kept upon the one above.

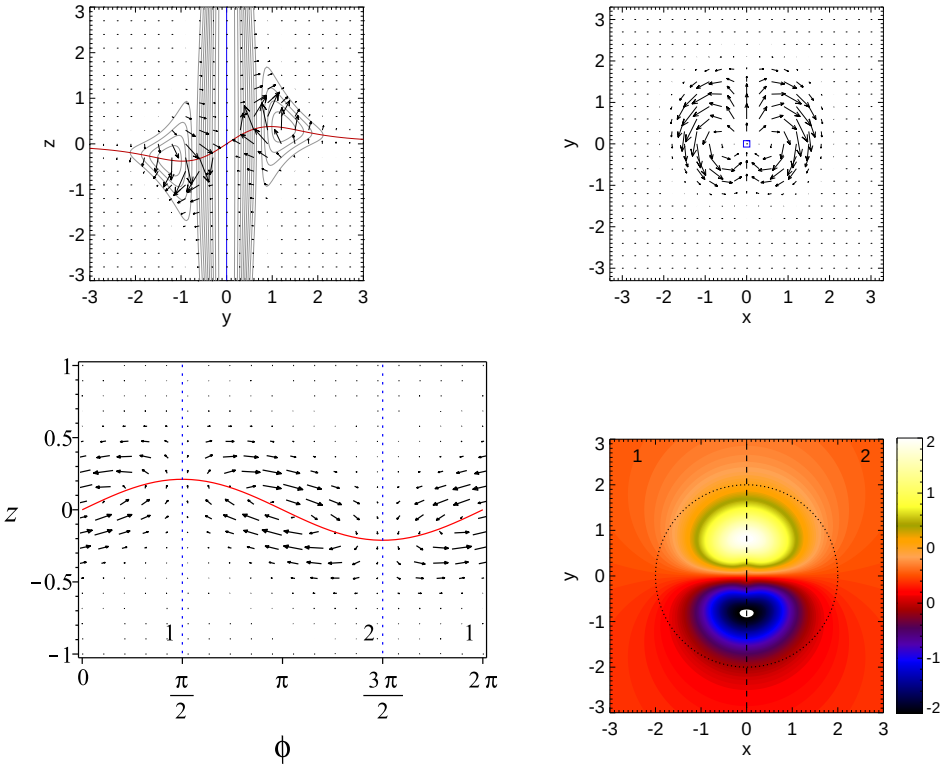

Figure 3.7: The symmetric spine case: The perpendicular plasma flow in the $x = 0$ plane (top left) and $z = 0.6$ plane (top right) with the contours denoting $\eta|\mathbf{J}|$ and the vectors perpendicular plasma velocity. Bottom right: the projection of $v_{\perp z}$ on to the fan plane. Different regions of constrained flux transport are separated by the black dashed line. Bottom left: the perpendicular plasma flow on the $r = 2$ cylindrical surface (marked with a dotted line in the bottom right panel) with the regions of constrained flux transport separated by dashed blue lines. The spine is shown is blue as a line in the $x = 0$ plane and a square in the $z = 0.6$ plane whilst the fan plane is shown in red. For the parameters given in Figure 3.6.

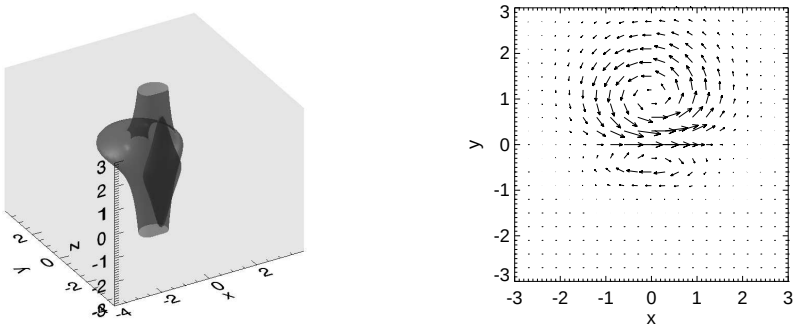

Figure 3.8: The simple asymmetric spine case with the parameters given in Figure 3.6 and $m = 0.5$ and $L = 1$. Left: an isosurface of $\eta|\mathbf{J}|$ at 25% of the maximum, depicting the shape of the non-ideal region. Right: current flow in the $z = 0$ plane.

Figure 3.6 shows the non-ideal region and current flow in the fan plane. In a similar manner to the fan reconnection scenario, the choice of perturbation leads to two current rings with the current strongest at the null between them. However, they are now aligned to the spine lines rather than the fan plane. Such a current configuration well describes symmetrical weak deformations of the fan plane in incompressible plasmas (Heerikhuisen and Craig [2004]).

As with the fan reconnection model, this is also a pure solution with its influence confined to within a flux envelope of field lines that just touch the edge of the non-ideal region. It is expected, therefore, that this will also lead to cyclic non-ideal flows. Figure 3.7 shows the resulting system of perpendicular plasma flows. In this case, flux is reconnected through one side of the fan plane, loops around either side of the spine (without passing through it), reconnects back through the fan on the opposite side, loops back around the other spine and then starts the cycle again. This leads to a circular flow around the two unperturbed field lines in the fan that lie along $y = z = 0$. Any magnetic flux that starts within one of these vortex flows remains within it for all time. This creates two distinct regions within which magnetic flux moves back and forth (denoted as regions 1 and 2 in Figure 3.7). In Section 3.5.3 how this circular flow is linked to the counter rotational flows found during finite-B reconnection is discussed. For the moment, however, let us proceed to how this flow is altered by asymmetry in the shape of the current sheet.

3.3.2 A Simple Asymmetric Case

To implement asymmetry into the above solution it might be tempting to incorporate it through the choice of $f(\phi)$. For various choices of this function it is found that any

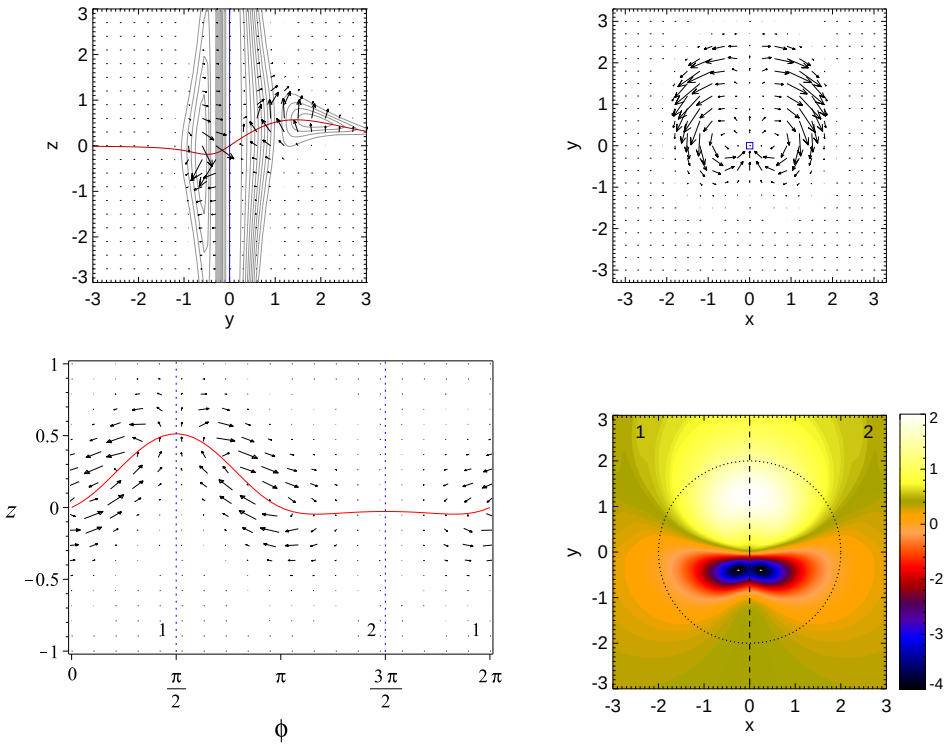

Figure 3.9: The simple asymmetric spine case with the parameters given in Figure 3.6 and $m = 0.5$ and $L = 1$. The perpendicular plasma flow in the $x = 0$ plane (top left) and $z = 0.6$ plane (top right) with the contours denoting $\eta|\mathbf{J}|$ and the vectors plasma velocity. Bottom right: the projection of $v_{\perp z}$ on to the fan plane. Different regions of constrained flux transport are separated by the black dashed line. Bottom left: the perpendicular plasma flow on the $r = 2$ cylindrical surface (marked with a dotted line in the bottom right panel) with the regions of constrained flux transport separated by dashed blue lines. The spine is shown is blue as a line in the $x = 0$ plane and a square in the $z = 0.6$ plane whilst the fan plane is shown in red.

with asymmetry are seen to produce non-linear terms which make $v_{\perp z}$ diverge as $1/z$ as $r \to 0$. Why such a naive choice does not work will become evident later. A simple and analytically tractable way to incorporate asymmetry naturally into the previous solution is through the exponential damping term in $F(r, \phi)$.

This is achieved by extending the previous model such that $h = h(\phi)$. This leads to the same form for $\mathbf{B}$, Z and η but with h replaced by $h(\phi)$. The electric potential, however, now becomes

$$\Phi_{ni} = -\frac{j\eta B_0}{\mu_0 L_0}\left[\frac{\sqrt{\pi}h(\phi)}{2}f'(\phi)\,\mathrm{erf}\left(\frac{r}{h(\phi)}\right) - 2f(\phi)\frac{h'(\phi)}{h(\phi)}\left(\frac{r}{2}e^{-\frac{r^2}{h(\phi)^2}} - \frac{h(\phi)\sqrt{\pi}}{4}\,\mathrm{erf}\left(\frac{r}{h(\phi)}\right)\right)\right]. \tag{3.24}$$

see Appendix E.1 for details. With an extra dimension of freedom compared with the fan case, there are many potential choices for h which lead to asymmetry. In Section 3.5.1 some general more complex examples of asymmetric spine reconnection are discussed. In this section, however, let us start with a plausibly simple asymmetric scenario of when the dimensions of the sheet remain approximately circular but the area over which flux is reconnected in each semi-plane ($y < 0$ and $y > 0$) is now different. To model this

$$f(\phi) = \sin(\phi) \quad \& \quad h(\phi) = L(1 + m\sin(\phi)), \tag{3.25}$$

is taken so that when $m = 0$ the symmetric case is recovered with h represented by the new length scale L. Figure 3.8 shows the current structure and non-ideal region when $m = 0.5$. The current ring in one region is now much larger and stronger than that of the other. This corresponds to a large wide deformation of the fan plane on one side and a small narrow one on the other. The wide strong current region is designated as the strong shear side and the other the weak shear side. From Figure 3.9 it can be seen that the general form of the cyclic flow remains, with plasma flowing through the fan plane on one side, looping around the spine and passing back through on the other within two distinct regions (1 and 2). However, now the axis of rotation has been shifted upward (as it is viewed in the bottom right panel of the figure) into the strong shear semi-plane. The introduction of asymmetry also alters the rate at which plasma passes through the fan plane. In the weak shear region the plasma flow across the fan is now increased relative to the symmetric case. Whereas the inverse is true of the strong shear region. So, like fan reconnection, it is found that in the asymmetric case the strongest outflows occur on the weakly deformed side. Surely the region with the stronger current should have the strongest non-ideal flow? Why is this not the case? To answer this it is convenient to first introduce the reconnection rate for the system and discuss both together.

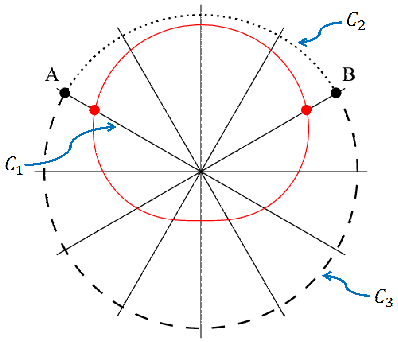

Figure 3.10: The radial black lines denote the magnetic field in the fan plane with the null at the center. The solid red line denotes the projection of the edge of a general asymmetric non-ideal region on to this plane. The points A and B lie between the positive and negative regions of flux transport across the fan plane. These two points can be connected by a path through the ideal region around the edge of the large side of the non-ideal region (C_3), around a path circuiting the small side (C_2) or though the non-ideal region and the null (C_1).

3.4 Reconnection Rate: The Simple Asymmetric Case

In symmetric spine-fan reconnection the reconnection rate is associated only with the transfer of magnetic flux across the fan plane [Pontin et al., 2005]. The flow of flux across this plane is due solely to the spine reconnection aspect of it. As such, the same methodology is applicable to pure spine reconnection. The same steps as the original are repeated here but now in the context of asymmetric spine reconnection. The rate of flux transfer in one direction across the fan plane, in the ideal region outside of the current sheet, is taken as the reconnection rate of flux in this direction through that plane. For the strong shear region this can be measured by

$$\frac{d\Psi}{dt} = -\int_{C_2} \mathbf{v} \times \mathbf{B} \cdot d\mathbf{l}, \tag{3.26}$$

where C_2 is the path shown in Figure 3.10. Since $\mathbf{E} = -\mathbf{v} \times \mathbf{B}$ in this region and the integral of the electric field is path independent (as $\mathbf{E} = -\boldsymbol{\nabla}\Phi$ is conservative) this can be found from

$$\frac{d\Psi}{dt} = \int_{C_1} E_{\parallel} dl = |\Phi_B - \Phi_A|. \tag{3.27}$$

Here A and B are points in the fan plane lying between the regions of positive and negative flux transfer (outside of the non-ideal region) about which plasma flows circulate and C_1 is the path along the radial field lines between them (see Figure 3.10). Since in steady

state the integral of electric field is path independent:

$$\int_{C_2} \mathbf{v} \times \mathbf{B} \cdot d\mathbf{l} = \int_{C_3} \mathbf{v} \times \mathbf{B} \cdot d\mathbf{l}. \tag{3.28}$$

Thus, an equal and opposite amount of flux must be transferred across the fan plane by the weak shear region. This explains why in the smaller weak field region the plasma jet is more intense than in the wider strong shear one. The strong shear region has a wider area over which to spread the same flux transfer. Therefore, asymmetric spine reconnection, in contrast to the fan case, is inherently equal and opposite in how it reconnects flux.

To measure the rate of flux transfer in one direction across the fan plane in this asymmetric model requires the asymptotic value of the non-ideal electric potential at large radii ($r \gg L$). This is given by

$$\Phi_{ni}(r \gg L) = -\frac{j\eta B_0\sqrt{\pi}}{2\mu_0 L_0}\left(h(\phi)f'(\phi) + h'(\phi)f(\phi)\right). \tag{3.29}$$

Using Equation (3.25), this becomes

$$\Phi_{ni}(r \gg L) = -\frac{j\eta B_0\sqrt{\pi}}{2\mu_0}\frac{L}{L_0}\left(1 + 2m\sin(\phi)\right)\cos\phi. \tag{3.30}$$

Depending on the value of m, this potential will change and therefore will give different reconnection rates. In particular, when $m \leq 0.5$ the reconnection rate in one direction across the fan plane is given by the difference between the maximum and minimum of this function. These are found to occur at $\phi_{max} = \phi_1$ & $\phi_{min} = \pi - \phi_1$ respectively (see Appendix E.2), where ϕ_1 is the lowest positive solution of

$$\sin\phi_1 = -\frac{1}{8m} \pm \frac{1}{2}\sqrt{\frac{1}{16m^2} + 2}. \tag{3.31}$$

The reconnection rate is then given in terms of this angle as

$$\frac{d\Psi}{dt} = \frac{j\eta_0 B_0\sqrt{\pi}}{\mu_0}\frac{L}{L_0}\left(1 + 2m\sin(\phi_1)\right)\cos(\phi_1), \tag{3.32}$$

or expressing it in terms of the reconnection rate of the symmetric case

$$\frac{d\Psi}{dt} = \left(\frac{d\Psi}{dt}\right)_{m=0}\left(1 + 2m\sin(\phi_1)\right)\cos(\phi_1). \tag{3.33}$$

Therefore, it is found that in the simplest asymmetric scenario the reconnection rate

changes depending upon the degree of asymmetry, but the manner of flux transport across the fan plane remains an equal and opposite process. When $m > 0.5$, and for more general examples of asymmetry, the picture is more complex. This is left to the discussion at the end.

Lastly, it could be argued that the need for equal and opposite flows across each side of the fan plane is only a result of the steady state condition on the system. However, consider the integral of the electric field around some closed path $\mathcal{C}$ (ABA in Figure 3.10) enclosing the entire non-ideal region in the fan plane in the general time dependent case. Then

$$\begin{aligned} \int_{\mathcal{C}} \mathbf{E} \cdot d\mathbf{l} &= \int_{\mathcal{C}} \nabla \times \mathbf{E} \cdot d\mathbf{S} \\ &= -\int_{\mathcal{C}} \frac{\partial \mathbf{B}}{\partial t} \cdot d\mathbf{S} = 0, \end{aligned} \tag{3.34}$$

where $\mathbf{S}$ is a surface on fan plane enclosed by the closed curve $\mathcal{C}$ for which $\mathbf{B} \cdot \mathbf{S} = 0$ by definition. Thus, on the fan plane

$$\int_{\mathcal{C}} \mathbf{v} \times \mathbf{B} \cdot d\mathbf{l} = 0. \tag{3.35}$$

Therefore, even in time dependent systems the reconnection of flux across the fan plane (in contrast to reconnection across the spine lines) is always an equal and opposite process. Note also, this argument relies only upon there being a localised non-ideal region in the fan plane for which $E_{\parallel} \neq 0$ and not on the non-ideal term itself (i.e. $E_{\parallel}$ can be introduced into R through other non-collisional terms such as particle inertia). Therefore, this argument applies in general beyond the confines of resistive MHD.

3.5 Discussion

Having investigated perhaps the two most plausible asymmetric scenarios of spine and fan reconnection, this section will discuss some other interesting features and extensions of the asymmetric spine case before the final concluding remarks are made.

3.5.1 Asymmetric Spine Reconnection: General Examples

Let us now consider more complex examples of asymmetric spine reconnection and generalise some of the ideas presented in the previous sections. The cases described in Section

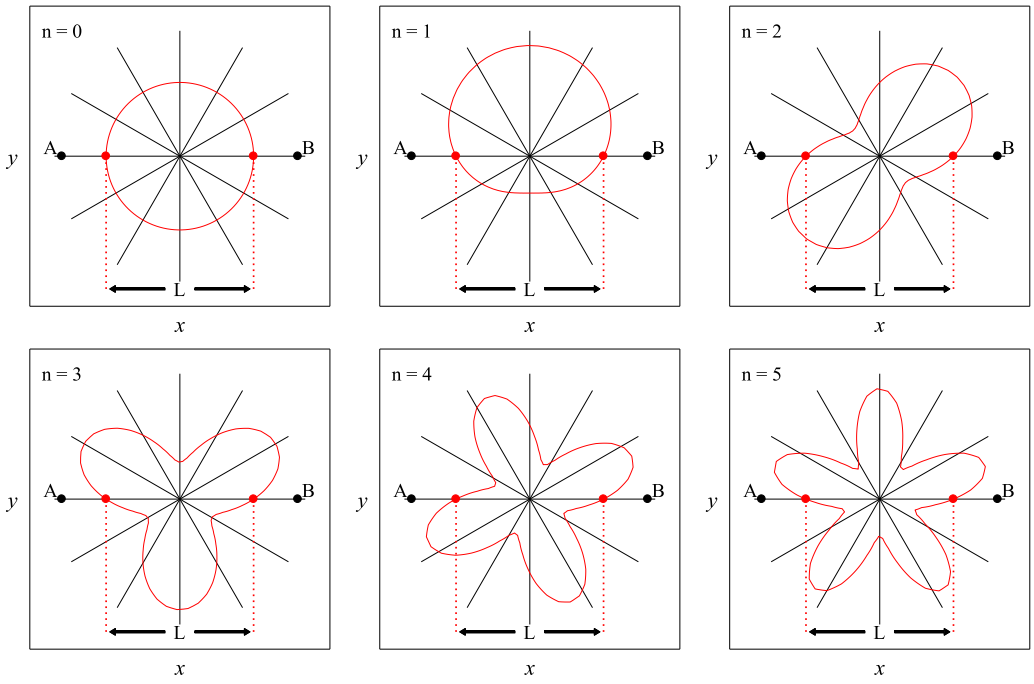

Figure 3.11: Red lines: The shape of the non-ideal regions projected on to the fan plane when $h(\phi) = L(1 + m \sin n\phi)$ with $m = 0.5$. Black lines: the magnetic field of the fan plane. The distance L indicates the length of the non-ideal region along the line AB.

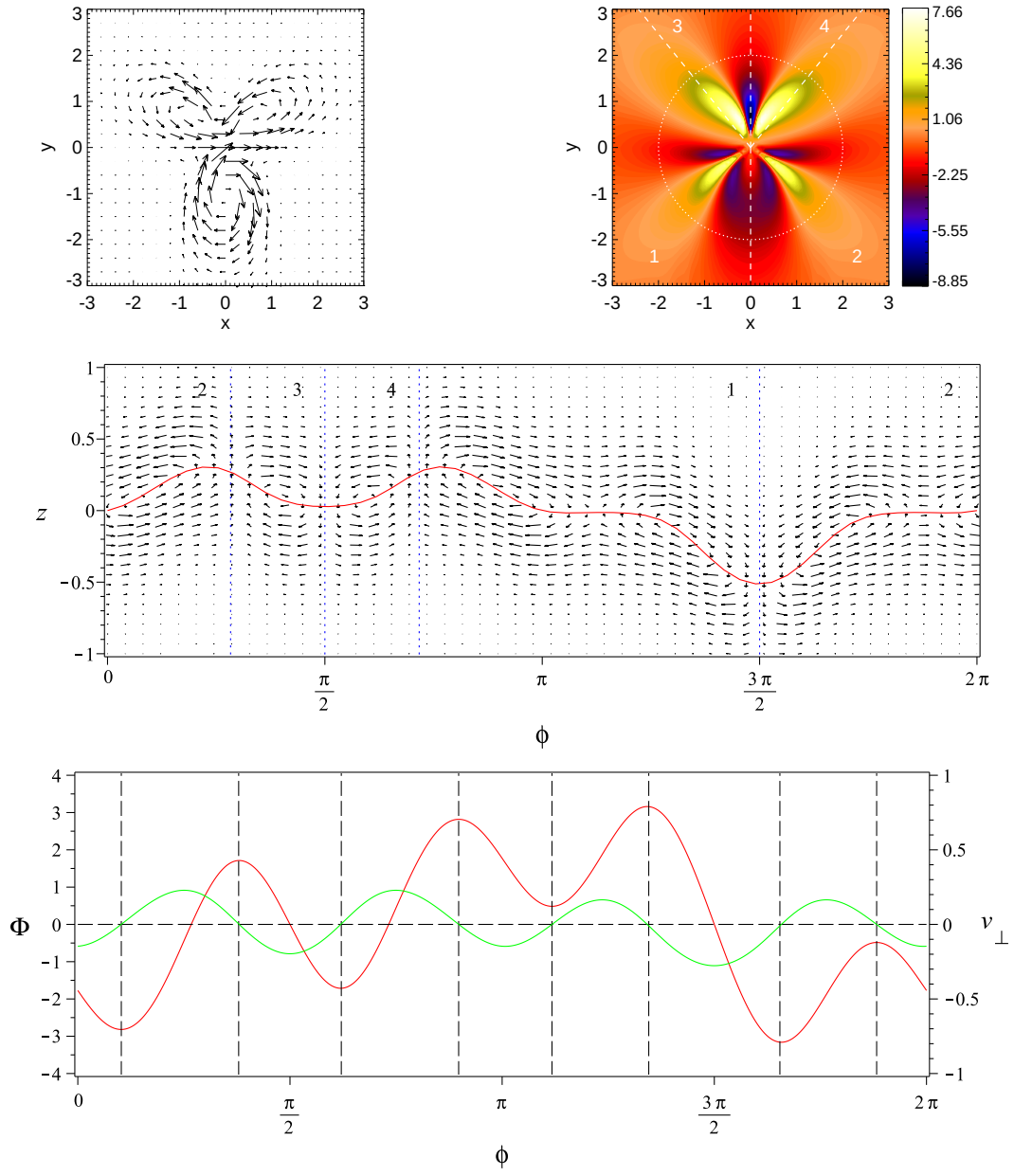

Figure 3.12: The case of general asymmetric spine reconnection with the parameters given in Figure 3.6 and $m = 0.5$ and $n = 3$. Top left: the current flow in the $z = 0$ plane. Top right: the projection on to the fan plane of $v_{\perp z}$ across it. The dashed white lines denote the edges of the trapped flux regions numbered 1 to 4. The dotted white line denotes the intersection of this plane with the $r = 2$ cylindrical surface. Middle: The perpendicular plasma flow on the $r = 2$ cylindrical surface with the fan plane shown in red and the 4 rotation regions divided by dashed blue lines. Bottom: the variation of electric potential (red) and perpendicular plasma flow (green) at $r = 4$ (outside of the non-ideal region) evaluated on the fan plane. Note that the zeros in the plasma velocity line up with the maxima and minima of the electric potential (denoted by dashed lines).

3.3 are in fact part of a family of solutions given by

$$f(\phi) = \sin(\phi) \quad h(\phi) = L(1 + m\sin(n\phi)).$$

Figure 3.11 shows the projection of the non-ideal region on to the fan plane for the first five modes. The value of n dictates how many lobe-like extensions of the non-ideal region there are. These modes are not to be mistaken for being similar to the $m > 1$ modes developed for spine reconnection by Craig and Fabling [1996], where the higher modes have no current at the null. The examples presented here all have the same current flowing through the null, but the shape of the current sheet in the fan plane is now varied. For $n \geq 2$ (and $m > 0.5$ when $n = 1$, where small lobes also appear) these lobe-like extensions produce plasma flow back and forth within each semi-plane and can considerably complicate the plasma dynamics near the fan. Figure 3.12 shows the perpendicular plasma flows for one of the simplest cases with $n = 3$.

As with all the models flux is cycled continuously, however, now distinct regions of contained flux movement occur. The top right and bottom panels show these regions of contained connectivity change. Within regions 3 and 4 a single vortex cycles magnetic flux around continuously, reconnecting it back and forth across the fan plane. In regions 1 and 2 a similar large vortex flow is present, but within in it two internal vortices coexist with a stagnation point between them. Depending upon where flux initially starts in regions 1 and 2 it will find itself either trapped to circulate around within one of these internal vortices or around the edges of both. Regions 1 and 2 are roughly speaking analogous to the two regions discussed in the previous sections when $n = 1$ and 2 as flux is, in general, brought through the fan plane in the positive direction in the $y > 0$ semi-plane and sent back through the fan in the negative direction in the $y < 0$ semi-plane. Regions 3 and 4 have no direct counter part as flux is trapped to circulate within the wedge defined by them. For higher n modes the number of these flux transport regions and the number of vortices internal to them (like the two vortices in region 1 for instance) increase.

These additional wedges and internal vortices make the definition and interpretation of the rate at which flux is reconnected across the fan plane more difficult. On the one hand, the total physical amount of flux reconnected across the fan is given by the sum of all flux cycled back and forth by every vortex flow (including those internal to each flux transport region). This quantity gives the genuine reconnection rate of the system. On the other hand, the wedges of contained flux transport and internal vortex flows that do not straddle the line $y = z = 0$ give a net zero contribution to the flux driven through the semi-plane they lie in. If the plasma flows of the non-ideal region are assumed to be

coupled to the global environment through an ideal stagnation point flow of the traditional type, i.e. one that brings in flux to be reconnected in equal and opposite directions across each semi-plane, then the internal vortices and regions of constrained flux transport do not contribute to the global rate at which flux is 'seen' to cross the fan plane by the global field. The net transfer of flux through one semi-plane is given, in this case, by the potential difference along the line $y = z = 0$ (AB, shown in Figure 3.11).

Therefore, in general, for spine reconnection two reconnection rates can be defined. A local reconnection rate given by the sum of the potential drops between adjacent maxima and minima in the electric potential, evaluated in the fan plane outside of the non-ideal region ($r \gg L$ and $Z = 0$). These maxima and minima correspond to points in the fan plane where $\mathbf{v}_\perp = 0$, so lie either in the centres of the vortices or the stagnation points between two vortices of like vorticity. As such, this potential drop gives the total flux transfer between these zero points. This can be more clearly visualised for a specific example. Figure 3.12 (bottom panel) shows the variation with ϕ of $\Phi_{ni.}$ and $\mathbf{v}_\perp$ when $Z = 0$, $r \gg L$ and $n = 3$ to demonstrate this relationship between the electric potential and the flux that is driven across the fan plane. Since around the entire non-ideal region the flux transfer is equal and opposite, this quantity can be expressed as double the sum of the difference between each maxima and the next minima ahead of it in ϕ:

$$\left(\frac{d\Psi}{dt}\right)_{local}(N) = 2\sum_{k=1}^{N}|\Phi_{max}(\phi_k) - \Phi_{min}(\phi > \phi_k)|. \tag{3.36}$$

where N is the total number of peaks in the electric potential. Alternatively, a global reconnection rate can be defined which gives the net flux through both semi-planes:

$$\left(\frac{d\Psi}{dt}\right)_{global} = 2|\Phi(\phi = 0) - \Phi(\phi = \pi)|, \tag{3.37}$$

quantifying the rate that an observer far from the null 'sees' flux reconnected at the null if the ideal flow is of a stagnation point type. The definitions of each then lead to the following properties:

$$\left(\frac{d\Psi}{dt}\right)_{local} = \left(\frac{d\Psi}{dt}\right)_{global}, \quad \text{when} \quad n = 0, \tag{3.38}$$

$$\left(\frac{d\Psi}{dt}\right)_{local} > \left(\frac{d\Psi}{dt}\right)_{global}, \quad \text{when} \quad n \geq 1, \tag{3.39}$$

$$\left(\frac{d\Psi}{dt}\right)_{local}(N+1) \geq \left(\frac{d\Psi}{dt}\right)_{local}(N). \tag{3.40}$$

Thus, this local rate will always at least equal that of the global rate. Under this new definition the reconnection rate that was found in the simple asymmetric case ($n = 1$) in Section 3.4 becomes the local rate. For modes with very large n, this local rate could comparatively dwarf the global one (see below). Such higher modes can be used to describe the situation when the edge of the current sheet is deformed by the action of an instability such as the tearing mode or Kelvin-Helmholtz instability. A comparison between these two rates would be interesting to see in the fully dynamic time dependent case.

For these choices of $f(\phi)$ and $h(\phi)$ the global rate is given by

$$\left(\frac{d\Psi}{dt}\right)_{global} = \frac{2j\eta_0 B_0\sqrt{\pi}}{\mu_0}\frac{L}{L_0}, \tag{3.41}$$

which is independent of both the degree of asymmetry (m) and the number of lobes (n). This invariance results from the fact that the length of the non-ideal region along the line AB always remains fixed as L (Figure 3.11). Thus, even in the situation when the edge of the sheet is fragmented (and if it is the net transfer that is of interest) then it is the length scale along the line AB that dictates the global reconnection rate. When this length scale is not conserved by the choice of asymmetry the global reconnection rate is simply dictated by this changing length scale (L_n):

$$\left(\frac{d\Psi}{dt}\right)_{global} = \frac{2j\eta_0 B_0\sqrt{\pi}}{\mu_0}\frac{L_n}{L_0}. \tag{3.42}$$

For example the choice of

$$f(\phi) = \sin(\phi), \quad h(\phi) = L(1 + m\cos(n\phi))$$

leads to a changing length scale of $L_n = L\,(1 + m(-1)^n)$ depending on whether two lobes are in or out of phase along the line AB. The global reconnection rate in this case, therefore, has two distinct rates.

3.5.2 Reconnection Rate vs Ohmic Dissipation

It is interesting to consider how these local and global rates of reconnection are linked to the ohmic dissipation associated with the non-ideal region. After all, in practice it is often the localised heating associated with reconnecting current layers which can be measured through observations. For simplicity, consider the case when $\eta = \eta_0$ (the limit of $k \to \infty$ in Equation (3.21)) so that the non-ideal region is invariant along the direction aligned to the spine lines (the z-direction). The ohmic dissipation per unit length in this direction is

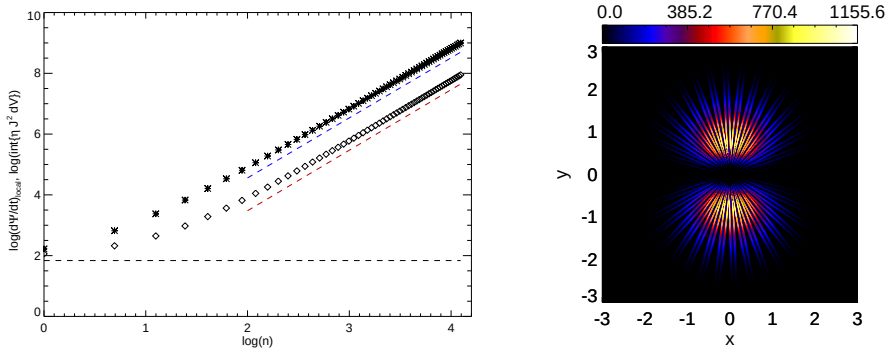

Figure 3.13: Left: Log-log plots of how the ohmic dissipation per unit length (asterisks), the local reconnection rate (diamonds) and the global reconnection rate (dashed black line) scale with n. The dashed blue and red lines denote a line of best fit between $n = 40$ and 60 (shifted down for clarity) for the ohmic dissipation and local reconnection rate respectively. Right: the current density in the xy-plane with $n = 40$. For the parameter set $(j, \eta_0, B_0, \mu_0, L_0, L) = (2, 1, 1, 1, 1, 1)$ when $f(\phi) = \sin(\phi)$ and $h(\phi) = L(1 + m\sin(n\phi))$.

then given by

$$\int \eta J^2 dV = \eta_0 \int J^2 r dr d\theta$$

and the local and global reconnection rates are still as given above (since both are evaluated on the fan plane where $\eta = \eta_0$ for all values of k). Figure 3.13 shows how each of these quantities vary as the parameter n and, therefore, the number of lobe-like extensions is increased. The global rate (black dashed line) remains fixed as n is varied, as discussed above, but for large values of n both the ohmic dissipation and the local rate increase toward the same power law dependence $\sim n^2$ (depicted by the blue and red dashed lines). This shows that, through explicit calculation, the above axioms relating to the local and global reconnection rate are adhered to and interestingly it is the local rate of reconnection that is linked to the dissipation within all of the current layers, not the global rate at which flux is seen to be transferred across the fan plane. Does that mean that ohmic dissipation and global reconnection rate are entirely unrelated quantities?

Understanding why there is such a rapid increase in ohmic dissipation with n in these models can help shed light as to why we get such a startling result. This rapid increase in ohmic dissipation is a result of the current flowing through the null point itself being invariant with n ($\mathbf{J}(x = y = 0) = \frac{jB_0}{L_0\mu_0}\hat{\mathbf{x}}$). As the perturbation field is localised, the current flows in two closed loops (see, for example, Figures 3.6 and 3.12). As n is increased, the number of lobes increase and the distance the current has to travel to loop back around to the null once more also increases. As the flow through the null itself is invariant, the

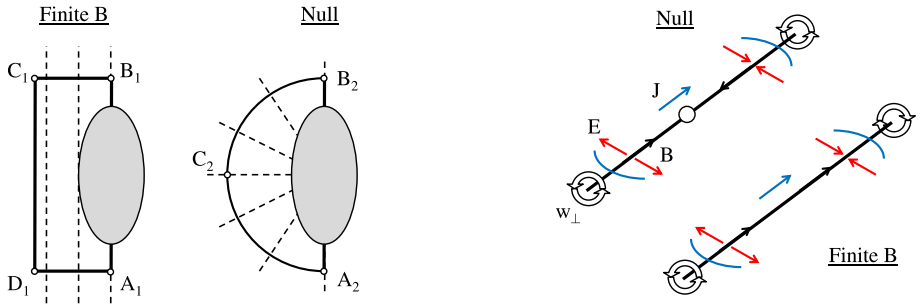

Figure 3.14: Left: Diagram showing the path integral loops that can be constructed along lines either perpendicular or parallel to the magnetic field. The field lines are shown as dashed lines and the non-ideal region in grey. Right: Diagram depicting the differences in ideal flows driven by a non-ideal region when there is a null within the region and when there is not. Hollow arrows indicate the induced ideal velocities, black arrows the direction of magnetic field, blue arrows the direction of current, red arrows the direction of electric field and the blue lines indicate the edge of the non-ideal region.

current must intensify to cover the increasing distance through all of the lobes. In addition, the width of the lobes also decreases with n and so the current is also funneled through narrower and narrower lanes. An example of the current structure for $n = 40$ is given in the right panel in Figure 3.13, note the intense current bands within each lobe.

This increase in current density cannot continue indefinitely unless the system is super conducting, i.e. $\eta_0 = 0$. When there is a finite amount of dissipation in the system ($\eta_0 \neq 0$) this intensification would eventually stall. Thus, the total current strength of the system should also be a function of n, i.e. $j = j(n)$, when j reduces with n. Therefore, the global flux transfer across the fan plane would likely be reduced in practice when n is increased as energy is expended in locally transferring flux back and forth across the fan plane.

In a self consistent system it is likely that, following say some instability which filaments the current layer as above, both effects will be observed. That is, there will be both an increase in ohmic dissipation/local reconnection rate *and* a decrease in the global rate that flux is transferred across the layer. As we shall see in Chapter 5, this actually occurs in a similar situation when the Torsional fan current sheet is fragmented via the Kelvin-Helmholtz instability.

3.5.3 Comparison between Spine and finite-B reconnection

This section now briefly discusses a general similarity between the simpler $n = 0$ and 1 modes of spine reconnection and the finite-B reconnection that occurs in the absence of null points. Finite-B reconnection is important in the context of reconnection occurring at separators and QSLs. In the case when a hyperbolic magnetic field is threaded by a guide field, a fully localised 3D non-ideal region produces a *pure* non-ideal solution with counter rotational flows on either side of it (Hornig and Priest [2003]). This flow can then be coupled to a global ideal flow (such as a stagnation point flow) that advects flux into and out of the non-ideal region and thus widens the influence of this region.

The kinematic solutions to date have been forced (in order to remove singular terms) to included such a background ideal flow to advect flux in to and then away from the non-ideal region at the null [Al-Hachami and Pontin, 2010; Pontin et al., 2005]. The pure non-ideal solution that has been found here allows a direct comparison to the pure non-ideal solution of the finite-B case.

Consider the cartoon in Figure 3.14. The left side shows the closed path integral that can be constructed around a loop of paths either parallel or perpendicular to the the magnetic field, through the non-ideal region, for the spine and finite-B cases. Paths of this nature are chosen so that potential drops along parallel paths through the non-ideal regions can be compared directly with potential drops associated with perpendicular plasma flows outside of it. Hornig and Priest [2003] showed that the potential drop around this loop in the finite-B case leads to electric fields of opposite sign along C_1B_1 and D_1A_1. Compare this to the closed path loop through the null for the spine case. This loop is the same as the one for finite-B but with the length of the line between $C_1D_1 \to 0$. Thus, the electric fields along B_2C_2 and C_2A_2 are also of opposite sign. In the finite-B case this gives oppositely directed flux transporting velocities confined to within the flux envelope of field lines that thread the non-ideal region. In the case of spine reconnection the magnetic field changes sign along the axis of plasma rotation. This sign change matches the sign change of the electric field giving rotational flows of the same vorticity all along this axis (Figure 3.14: right panel). In this case, all the field lines of the fan plane thread into the non-ideal region and so are transported by these flows.

Thus, finite-B and spine reconnection are driven by the same fundamental non-ideal process. That of a localised non-ideal region which produces *oppositely directed electric fields* on either side of itself leading to a *potential drop* across the region. The difference comes through how the underlying magnetic field structure translates these electric fields into induced non-ideal plasma flows.

3.6 Concluding Remarks

The work within this chapter has explored the effect of asymmetry on the spine and fan reconnection modes of 3D null points. In the fan case it was found that the reconnection of magnetic flux through each spine line occurs asymmetrically. A behaviour masked by the assumed symmetry of previous models [e.g. Craig and Fabling, 1996; Pontin et al., 2005; Priest and Titov, 1996]. A bulk flow of plasma through the null point is also found in a similar way to the asymmetric 2D picture. In contrast to the fan case, spine reconnection is found to be inherently equal and opposite in how flux is reconnected across the fan, with no plasma flow at the null. However, with an extra degree of freedom, asymmetric spine reconnection is considerably more complex. In the simplest asymmetric case, asymmetric outflow jets were formed within the vicinity of the null but globally an equal and opposite amount of magnetic flux is driven through both sides of the fan plane. Higher modes were also found where constrained regions of flux transport were localised to within wedges in each semi-plane. In this more complex situation, two definitions for reconnection rate became appropriate: a local reconnection rate that measures how much flux is genuinely reconnected across the fan plane and, on the assumption that the non-ideal region has been created through some large background ideal stagnation point flow, a global rate that measures the net amount of flux that is driven across each semi-plane. Obviously the choice of background ideal flow used to advect flux into and away from the non-ideal region is crucial for the interpretation of the reconnection rate. Therefore, different composite solutions could potentially give rise to different reconnection rates depending upon how much of the flux transfer within each vortex flow can be accessed by the global ideal flow field. An investigation of the composite solutions would be interesting to pursue in the future.

Conceptually, it was also shown that the simple spine reconnection scenario is fundamentally the same process as finite-B reconnection but with a different knock on effect in terms of flux transport (facilitated by the local magnetic field structure). This ties in nicely with the recent work of Wilmot-Smith and Hornig [2011] on separator reconnection. In their pure non-ideal model they showed how the finite-B reconnection that occurs between two nulls joined by a single separator leads to cyclic spine reconnection at each adjoining null point. The cyclic spine reconnection that they see matches that of the symmetric model in Section 3.3, except in their model there is no current sheet enveloping the null and so they have singular flows there. They point out that for separator reconnection to occur such non-ideal flows are always necessary at the end nulls. Thus, the spine mode (and likely also the spine-fan mode) can act as a key to unleashing strong

nearby reconnection when there are multiple null points. For strong deformations these authors also found the existence of multiple separators in accordance with those found in numerical simulations (Parnell et al. [2010]). One could postulate that the wedges of constrained flux transport contained in the higher modes ($n \geq 2$) of spine reconnection studied in Section 3.5.1 could be associated with where each of the multiple separators approach and rejoin at the null. This would also be something interesting to pursue in the future.

Lastly, by necessity, these models ignore time dependent effects and also lack a degree of self consistency. In the fully time dependent scenario might we not expect the position of the null point to move with time? And how might such asymmetric current structures form in the first place? Presumably the manner of current sheet formation is very dependent upon the manner of the external driving. In the following chapter we will investigate some of these questions.

4

Asymmetric Spine-Fan Reconnection

"There's something that doesn't make sense. Let's go and poke it with a stick."

Matt Smith (11th Doctor),
Amy's Choice

4.1 Introduction

In this chapter a series of numerical experiments are presented which investigate more deeply the role of asymmetric current sheets in the reconnection process of three dimensional magnetic null points. The focus is now on the case of spine-fan reconnection (where both the spine and fan reconnection regimes occur together) as this is more likely to occur, in general, in a fully dynamic scenario. The aim of this chapter is to compliment and extend the results presented in Chapter 3 by investigating aspects such as the self consistent formation and time dependent behaviour of asymmetric spine-fan current sheets, which the kinematic models could not address. In particular, a generalisation of the numerical investigation of Pontin et al. [2007a] (where spine-fan reconnection was driven by symmetric perturbations of the spine foot points, hereafter referred to as PBG07) to cases where

the driving pulses are applied asynchronously is presented.

In Sections 4.2 and 4.3 the numerical code and simulation setup are introduced. In Section 4.4 a detailed comparison of the differences between the spine-fan collapse driven by a single pulse compared to by two symmetrically introduced oppositely directed pulses is presented. Particular attention is paid to the differences in the sheet dimensions, connectivity change, scaling relations and time dependent effects between the two. Section 4.5 gives an extension to when two pulses drive spine-fan reconnection asynchronously. Sections 4.6 and 4.7 discuss the later phases of the reconnection process and whether the plasma flow is similar to what was shown in Chapter 3. In Section 4.8 the dependence upon the driving spatial scale is also discussed and finally Section 4.9 presents a summary and discussion of the results.

4.2 The Numerical Code

The investigation is conducted using a three dimensional MHD numerical code which solves the compressive resistive MHD equations in the following form

$$\begin{aligned}
\frac{\partial \rho}{\partial t} &= -\boldsymbol{\nabla}\cdot(\rho\mathbf{v}),\\
\frac{\partial \mathbf{B}}{\partial t} &= -\boldsymbol{\nabla}\times\mathbf{E},\\
\mathbf{E} &= -\mathbf{v}\times\mathbf{B}+\eta\mathbf{J},\\
\mathbf{J} &= \boldsymbol{\nabla}\times\mathbf{B},\\
\frac{\partial(\rho\mathbf{v})}{\partial t} &= -\boldsymbol{\nabla}\cdot(\rho\mathbf{v}\mathbf{v}+\underline{\underline{\tau}})-\boldsymbol{\nabla}P+\mathbf{J}\times\mathbf{B},\\
\frac{\partial e}{\partial t} &= -\boldsymbol{\nabla}\cdot(e\mathbf{v})-P\boldsymbol{\nabla}\cdot\mathbf{v}+\eta J^2+Q_{visc},
\end{aligned} \tag{4.1}$$

where ρ is the plasma density, $\mathbf{v}$ the plasma velocity, $\mathbf{B}$ the magnetic field, $\mathbf{E}$ the electric field, η the plasma resistivity, $\mathbf{J}$ the electric current, $\underline{\underline{\tau}}$ the viscous stress tensor, e the internal energy and Q_{visc} the viscous dissipation. The plasma is assumed to be an ideal gas so that $P=(\gamma-1)e$ and throughout this chapter we take $\gamma=5/3$. The above equations have been non-dimensionalised by setting the magnetic permeability $\mu_0=1$ and the gas constant (R) equal to the mean molecular weight (M). This results in one time unit in the code being equivalent to the travel time of an Alfvén wave over a unit distance through a plasma with unit density and unit magnetic field ($\rho=1, |\mathbf{B}|=1$). Under this non-dimensionalisation the magnetic diffusivity (η_d) is equal to magnetic resistivity (η) and takes the form of an inverse magnetic Reynolds number $\eta=\frac{\eta_{dim}}{L_0V_0}=Re_m^{-1}$ (where η_{dim} is the dimensional resistivity and L_0 and V_0 are some typical length scale and velocity).

The viscous stress tensor in this version of the code is made up of artificial viscous diffusion operators which are carefully chosen to be negligible over large scales (where they are not needed) but 'switch on' at scales comparable to the grid scale to damp out numerical errors. As numerical errors can never be fully eradicated, such diffusion operators are standard practice in many numerical codes as they help ensure numerical stability, and therefore as accurate a representation of the modelled physical system as possible. By using operators of this kind, the contribution to dissipation from viscosity is negligible compared to resistive dissipation within the volume except when the length scale of any structure reaches near the grid scale, where numerical artefacts must be dealt with. Each simulation is set up to avoid reaching these length scales and so in general the plasma can be considered inviscid. Full details of these operators and of the non-dimensionalisation can be found in Galsgaard and Nordlund [1997].

The equations are solved on a Cartesian staggered mesh where, with respect to a unit cube, ρ and e are evaluated at the center of the cube, $\mathbf{B}$ and $\rho\mathbf{v}$ in the centres of the cube faces and $\mathbf{E}$ and $\mathbf{J}$ at the centres of the edges between these faces. This configuration has the advantage that through constrained transport [Evans and Hawley, 1988] the divergence of the magnetic field is preserved to within machine accuracy. The partial derivatives are evaluated using a sixth order accurate *central difference* method (which uses the three adjacent grid points on either side) to return a value for the partial derivative shifted half a grid point with respect to the initial grid position of the quantity it is operated on. Often this is where the partial derivative is required to be known. An example of the derivative in the x direction is given by

$$\begin{aligned}\partial^{+}_{,x}(f_{i,j,k}) &= f'_{i+\frac{1}{2},j,k} \\ &= \frac{a}{\Delta x}(f_{i,j,k}+f_{i+1,j,k})+\frac{b}{\Delta x}(f_{i-1,j,k}+f_{i+2,j,k})+\frac{c}{\Delta x}(f_{i-2,j,k}+f_{i+3,j,k}),\end{aligned}$$

where

$$a=\frac{1}{2}-b-c, \quad b=-\frac{1}{16}-3c, \quad c=\frac{3}{256}. \tag{4.2}$$

The other operators can be found from a permutation of the indices in the above equation. When the values of a physical quantity are required at a different position in the grid, a fifth order accurate interpolation operator is applied to give the value of the quantity at the desired point. For instance, the operator which interpolates a physical quantity up

half a grid point in the x direction is given by

$$\begin{aligned} T_x^+(f_{i,j,k}) &= f_{i+\frac{1}{2},j,k} \\ &= a(f_{i,j,k} + f_{i+1,j,k}) + b(f_{i-1,j,k} + f_{i+2,j,k}) + c(f_{i-2,j,k} + f_{i+3,j,k}), \end{aligned}$$

where

$$a = 1 - 3b + 5c, \quad b = -\frac{1}{24} - 5c, \quad c = \frac{3}{640}, \tag{4.3}$$

and again the other 'shifting' operators may be found through permutations of the indices.

Lastly, the time stepping is handled through a third order *predictor corrector* method which is an extension of the one proposed by Hyman [1979] to include a variable time step. The predictor step is given by

$$f_{n+1}^{(*)} = a_1 f_{n-1} + (1 - a_1) f_n + b_1 \dot{f}_n, \tag{4.4}$$

and the corrector is

$$f_{n+1} = a_2 f_{n-1} + (1 - a_2) f_n + b_2 \dot{f}_n + c_2 \dot{f}_{n+1}^*, \tag{4.5}$$

where

$$\begin{aligned} a_1 &= r^2, \\ b_1 &= \Delta t_{n+1/2}(1 + r), \\ a_2 &= 2(1 + r)/(2 + 3r), \\ b_2 &= \Delta t_{n+1/2}(1 + r^2)/(2 + 3r), \\ c_2 &= \Delta t_{n+1/2}(1 + r)/(2 + 3r), \\ r &= \Delta t_{n+1/2}/\Delta t_{n-1/2}. \end{aligned}$$

The choices of these operators were based on numerical tests performed by the authors of the code. Greater detail on the employed methodology and implementation of the numerical methods in this code can be found in Galsgaard and Nordlund [1997] and on http://www.astro.ku.dk/∼kg.

4.3 Simulation Setup

A similar simulation setup is used to that in PBG07. An isolated linear null point with magnetic field $\mathbf{B} = B_0(-2x, y, z)$ is placed in the center of a numerical box of size

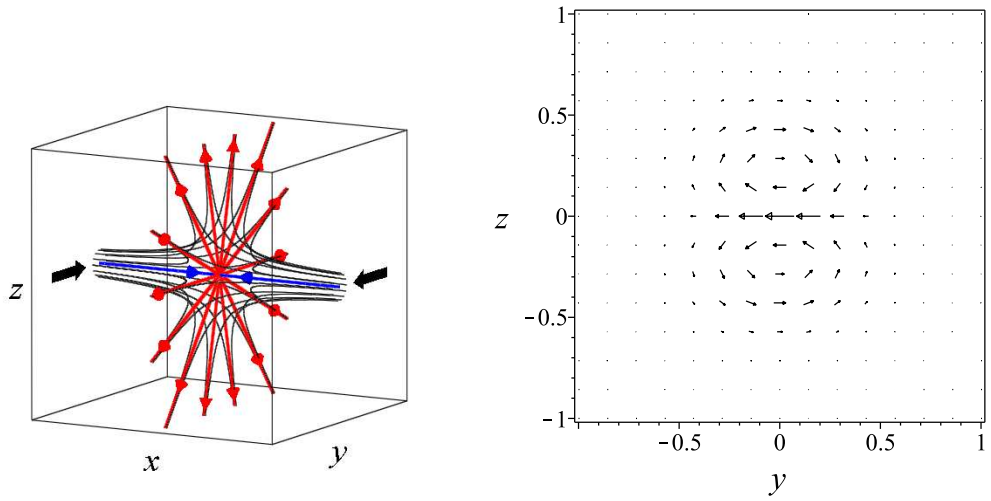

Figure 4.1: Left: The initial magnetic field configuration. The spine (in blue) lies along the x-axis and the fan (in red) lies in the $x = 0$ plane. Coloured arrows indicated the field direction. The black arrows show the direction of shear applied by the driver at the boundaries. Right: The driving profile applied to the x-boundaries with $A_d = 80$. Wyper et al. [2012] reproduced with permission ©ESO.

$[\pm X_l, \pm Y_l, \pm Z_l]$. The plasma is initially in equilibrium with density $\rho = 1$ and internal energy $e = 5\beta^*/2$. Here β^* is a parameter that controls the plasma-β, the ratio of plasma pressure to magnetic pressure: $P/(B^2/2\mu_0) = (1-\gamma)e/(B^2/2\mu_0) = 10\beta^*/3B^2$. The plasma-$\beta$ is infinite at the null where $B = 0$, with the rate of its reduction away from the null controlled by β^*. β^* is set to 0.05, $B_0 = 1$ and $\eta = 5 \times 10^{-4}$ for the majority of the simulations so that the surface where the plasma-$\beta = 1$ is given by a rotationally symmetric ellipsoid (or oblate spheroid) with minor axis along the spine of length 0.2 and major axis in the fan plane of radius 0.4. If the typical length scale (L_0) and speed (V_0) within the simulation box are taken as the distance between the driving (x) boundaries and the Alfvén speed at the spine foot points (in the manner of Galsgaard and Pontin [2011b]) then this value of η corresponds to a magnetic Reynolds number of $Re_m = L_0 V_0/\eta = 1/(5 \times 10^{-4}) = 2000$. Therefore, in these simulations the plasma within the box is essentially ideal so that the frozen in flux condition is only broken when small length scale regions of intense current form.

At the beginning of each simulation, the fan plane sits on the $x = 0$ surface and the spine lies along the x-axis and connects with the boundaries at $[\pm X_l, 0, 0]$ (see Figure 4.1, left panel). Boundary shearing is then applied in opposite directions to the x-boundaries which advect the spine foot points. The driven boundaries are linetied, i.e. the foot points

of the magnetic field are fixed so that they move at the prescribed velocity (tangential to this boundary), whereas on the non-driven boundaries the magnetic field is free to move. All boundaries are closed so that no mass flux enters or leaves the numerical box and a thin damping region is applied to the non-driven boundaries which linearly removes momentum in a way that reduces reflection of waves back into the domain. This damping region also strongly damps any motion of the free moving magnetic field footpoints on the non-driven boundaries. The driving velocity is divergence free with the stream function

$$\varphi = V_0(t)\cos^2\left(\frac{\pi y_1}{2}\right)\sin(\pi z_1)e^{-A_d(y_1^2+z_1^2)}, \tag{4.6}$$

where $y_1 = y/Y_l$ and $z_1 = z/Z_l$ and A_d controls the spatial extent of the driving patch. This driver advects the spine in the $\pm\hat{\mathbf{y}}$ direction with return flows at a larger radius (Figure 4.1). Throughout the simulations Y_l and Z_l are set to 3 and $X_l = 0.5$ with a resolution of 128^3 (although test runs were performs at 256^3 to check that the results were qualitatively similar). The grid is also stretched to include more points near the null ($\delta x \sim 0.005$ and $\delta y, \delta z \sim 0.025$) to better resolve structures there.

In order to study the self consistent formation of asymmetric current sheets a time variation is chosen of the form

$$V_0(t) = v_0 \tanh^2\left(\frac{t}{0.1}\right)\begin{cases} e^{-0.2(t-\tau)^6}, & x = -0.5 \\ e^{-0.2(t-\tau-t_{lag})^6}, & x = 0.5 \end{cases}, \tag{4.7}$$

when the reconnection is driven by two pulses. The plasma velocity on the $x = -0.5$ boundary is driven by a pulse that peaks in magnitude at $t = \tau$ and drops to near zero by $t = 2\tau$. A second pulse is then initiated at the $x = 0.5$ boundary but offset in time by t_{lag}. When the spine-fan collapse is driven by only one pulse $V_0(t)$ is set to 0 on the $x = 0.5$ boundary.

4.4 Asymmetric Driving: One Pulse vs Two Simultaneous Pulses

4.4.1 Current and Plasma Flow Evolution

Let us begin by describing the differences in the current sheet formation and induced plasma flows between when spine-fan collapse is driven by a single pulse or by two equal and opposite pulses sent simultaneously ($t_{lag} = 0$). In both sets of experiments $\tau = 1.8$, $A_d = 80$ and $\eta = 5 \times 10^{-4}$. When there are two pulses they both propagate essentially

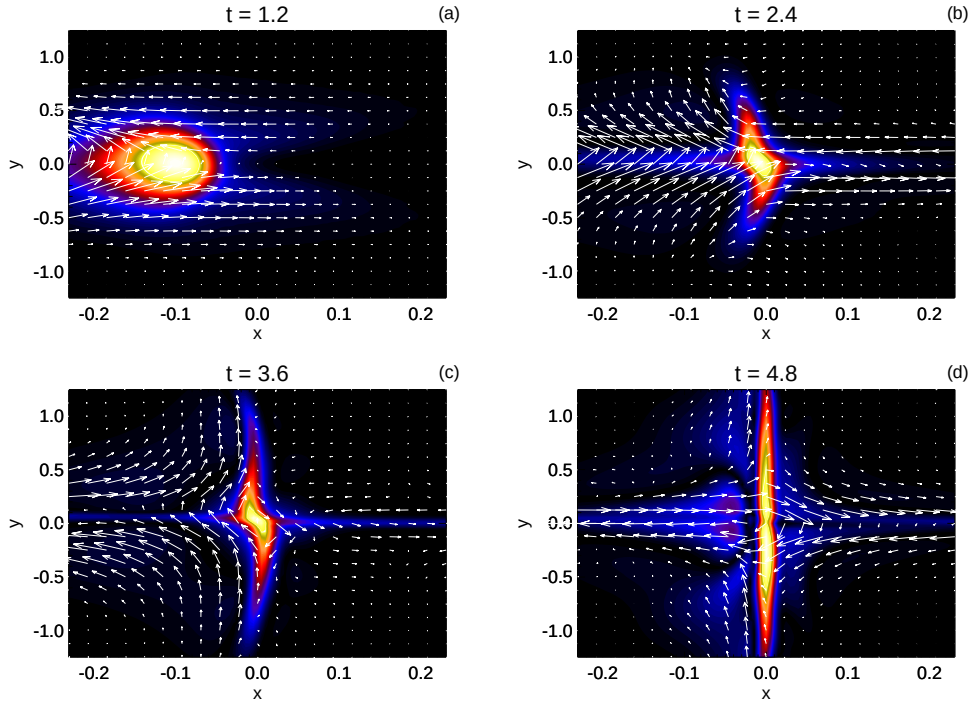

Figure 4.2: Build up of current at the null with a single pulse. Shaded contours show $|\mathbf{J}|$ (scaled to the maximum of each snapshot with yellow depicting regions where the current density is strong and blue regions where it is weak), while the arrows depict the plasma flow. Initially the null is at the origin with the spine along $y = 0$ and the fan along $x = 0$. For the case of $v_0 = 0.01$. Wyper et al. [2012] reproduced with permission ©ESO.

Alfvénically away from the boundaries at the same time, i.e. both pulses follow the magnetic field as they propagate into the domain. Note that, in general, a perturbation to a magnetic field produces two pulses which propagate away from where the perturbation is applied in both directions along the field. In this case, as the perturbation is applied on the boundaries, the outgoing wave is outside of the domain of interest. The fact that the pulses under discussion are inwardly propagating is now taken to be understood. As the pulses reach the null, the shear of the wave front steepens generating strong electric currents. Near the null, where the Alfvén velocity drops to zero, the disturbance couples to acoustic wave modes and focuses on the null itself [for a review of the properties of MHD waves in the vicinity of magnetic nulls see for example McLaughlin et al., 2011]. A strong current sheet then forms at the null, with the null location remaining fixed at the origin for all time. This case was described in detail in PBG07.

To clearly visualise the process when there is only one pulse it is useful to study the evolution of the current density in the $z = 0$ plane (i.e. the plane of shear containing both the spine and fan). Figure 4.2 shows a typical case when $v_0 = 0.01$. The pulse propagates (from the $x = -0.5$ boundary) into the volume and follows the field lines toward the null (Figure 4.2 (a)). As there is no symmetric pulse from the opposite boundary, when the pulse arrives at the null, the position of the null point shifts in the direction of shear; the extent of this shift depends upon ideal and non-ideal effects (discussed later in Section 4.4.5). By the time of Figure 4.2 (b), the null point position (following the direction of shear) is shifting in the positive y-direction. At this time, it can be seen that a weak flow has been induced on the undriven side in the opposite direction to that of the driving pulse so that, in the vicinity of the null point, the plasma flow takes on a stagnation point structure. This shows that, even in the presence of asymmetric driving, flow across the spine line and fan plane are ubiquitous in the early stages of spine-fan collapse. At the null itself, a non-zero plasma flow is also found to occur (discussed in greater detail in Section 4.7). The system then begins to relax after the driving ceases and the null reaches its maximum displacement (Figure 4.2 (c)). After this time the electric current sheet slowly spreads out across the fan plane (Figure 4.2 (d)) as the system enters the relaxation phase of the process ($t > 5$, Section 4.6).

Figure 4.3 (left panel) shows the variation of the maximum in current modulus within the volume ($|\mathbf{J}|_{max}$, occurring at the null in both cases) with time for one pulse (green) and two pulses (from opposite boundaries) sent together (black) over the period of current sheet formation. As in PBG07, and in accordance with the analytical models of the previous chapter, it is found that the current in the direction perpendicular to the direction of shear (the z-component) dominates the components in the other two directions (x and y). From

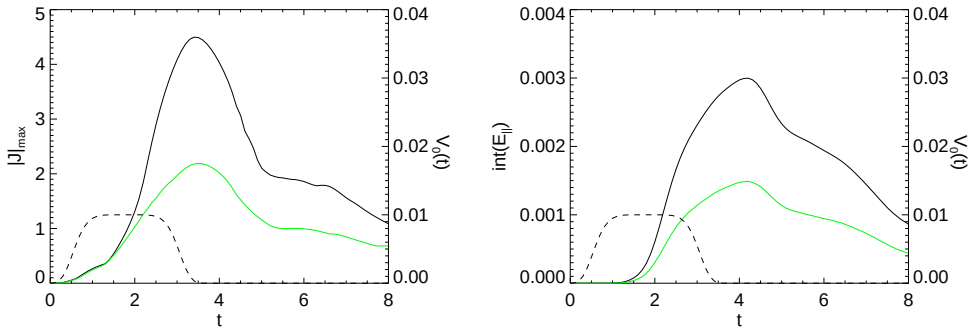

Figure 4.3: Solid lines (left panel): $|\mathbf{J}|_{max}$ plotted against t. Solid lines (right panel): $\int E_{\|} dl$ plotted against t. Black: two simultaneous pulses ($t_{lag} = 0$), green: one single pulse. The dashed lines indicate the driving amplitude of the second pulse in the two pulse case. For cases with $v_0 = 0.01$ and $\eta = 5 \times 10^{-4}$.

Figure 4.3 it is clear that during the formation of the current sheet ($t < 5$) the temporal evolution for one pulse follows closely that of the $t_{lag} = 0$ case with two pulses (except at a lower amplitude) with both curves reaching their maximum at the same time, at the point where the pulses reach the null. The build up of this current results from the local collapse between the spine and fan in the weak field region near the null point, with the degree of this collapse dictated by the plasma properties and the perturbations applied to the spine lines due to the arriving pulses. The one pulse case applies half the stress to the field near the null but with the same variation in time as the two pulse case and so the curves closely match but with the one pulse case at a reduced amplitude. Once the current maximum is reached, the magnetic stress in the field reduces as the current sheet spreads out across the fan plane and the null point returns to its initial position.

4.4.2 Magnetic Connectivity

From previous symmetric studies [e.g. Galsgaard and Pontin, 2011b; Pontin et al., 2007a] it is known that spine-fan reconnection involves reconnection of field lines across both the spine line and the fan surface. How is connectivity change affected by the asymmetry of the spine-fan current sheet that forms in response to the asymmetric foot point driving? As the non-ideal region is three dimensional, the general theory states that connection change within the current sheet will be continuous and field lines threading into and out of the current sheet will slip on to new connections. By considering field lines which enter and leave the current sheet, and which are initially connected, the formation of these new connections can be shown.

The top panels of Figure 4.4 shows this for the symmetric two pulse case. Initially ($t = 0$: left panel) two flux tubes are present. The red field lines thread into the current sheet and are connected to the gold field lines which thread out. Similarly, the green field lines thread in and are connected to the blue field lines which thread out. Once the current sheet forms, as a result of the applied driving (middle panel), the red and green field lines slip through/around the spine (in the manner of fan reconnection) and the gold and blue field lines reconnect across the fan plane (in the manner of spine reconnection). Once the driving has ceased (far right panel), the gold field lines are connected now to the region where the green field lines are and the blue to the region where the red ones are. However, the new connections which have been made are clearly not one to one in the manner of 2D reconnection.

The bottom panels in Figure 4.4 show how the evolution of the single pulse case differs. The driving is now applied only to the foot points of the red field lines, which slip through/around the spine as before. The green field line foot points are not driven and are anchored by the line tying on the boundary. However, the movement of the null point and the induced stagnation point flow in the vicinity of the null create new connections on this side of the fan plane and move the spine foot point forward (into the green flux tube) as the spine tries to straighten up, in line with the new null point position. Thus, flux is reconnected across both spines but, as is clear from the bottom middle and right panels, the rate at which it crosses each spine line is different in the asymmetric case in agreement with what was shown in Chapter 3. It is also clear that the green and gold field lines reconnect across the fan plane in a very similar way to the two pulse case as a result of the equal and opposite nature of flux transfer across the fan plane, also discussed in Chapter 3. Therefore, the resulting new connections following the end of the driving are asymmetric compared to the symmetric two pulse case but still follow a similar pattern of connection change.

4.4.3 Reconnection Rate and $E_{\parallel}$

The signature of reconnection in 3D is an electric field component parallel to the magnetic field ($E_{\parallel}$). Pontin et al. [2005] showed in the case of a symmetrically perturbed null point that, for the spine-fan reconnection mode and in the geometry of this set up, the rate that flux is transferred across the fan plane (taken as the reconnection rate) can be found from

$$\frac{d\Psi}{dt} = \int_{x=y=0} E_{\parallel} dz. \tag{4.8}$$

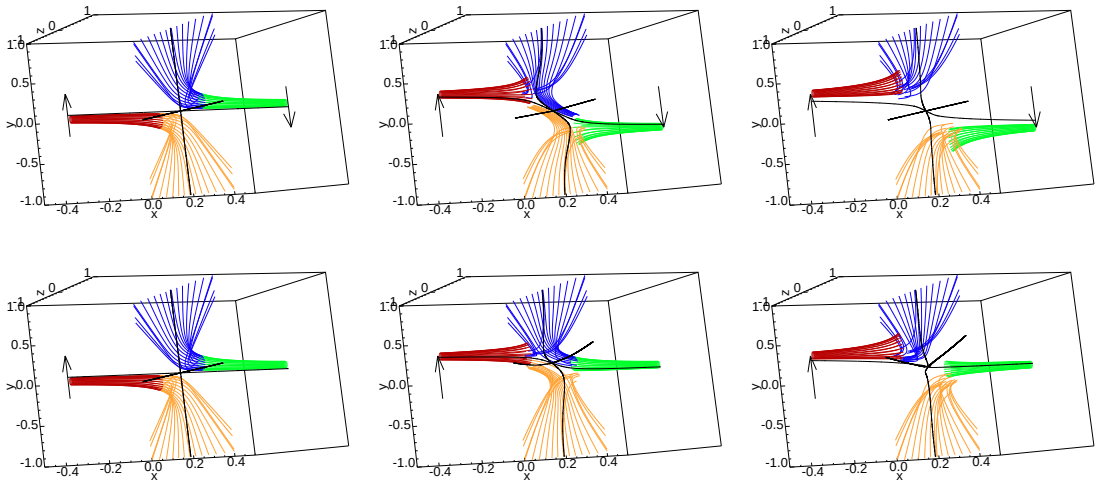

Figure 4.4: The change in connectivity with two simultaneous pulses (top) one pulse applied on the $x = -0.5$ boundary (bottom) and when $v_0 = 0.04$, $A_d = 80$ and $\eta = 5{\times}10^{-4}$. Arrows indicate the direction of boundary driving and black field lines depict the shape of the fan plane and spine lines. The panels in the two pulse case correspond to $t = 0$ (left), $t = 3$ (middle) and $t = 5$ (right). The panels in the single pulse case correspond to $t = 0$ (left), $t = 3$ (middle) and $t = 6$ (right).

In the symmetric case ($t_{lag} = 0$) $x = y = 0$ is the path along which the strongest parallel electric field lies.

As was discussed in Chapter 3, the TF reconnection rate for spine reconnection is formally equivalent to the above method of measuring the reconnection rate for the spine-fan reconnection mode. This arises since the above definition ignores any contribution to reconnection from new connections made across the spine lines and so quantifies only how much flux is reconnected across the fan plane. However, with no currently accepted way to incorporate the rate at which new connections form across the spine lines into the general spine-fan reconnection rate, this investigation will focus on quantifying the rate based solely on flux transfer across the fan plane (calling this the reconnection rate). The insight gained from the simple asymmetric spine models in Chapter 3 can then be used to understand how to measure this rate in the asymmetric numerical models.

In the simple asymmetric spine case the path along which the integral of $E_{\|}$ is maximum was found to be the true measure of this flux transfer rate. In the simulations with one pulse the null point position moves and so the z-axis is no longer coincident with the magnetic field lines along which the integral of $E_{\|}$ is maximum (see Figure 4.5). To find these field lines (and therefore the correct flux transfer rate) in such single pulse cases,

integrals along several field lines in the fan plane from starting positions just above and below the null (in z) as far as the edge of the current sheet (i.e. where $|\mathbf{J}| = 0$) are taken. The reconnection rate is then given by the sum of the maximum integrals for z positive and negative with an additional term including a contribution from $\mathbf{E} = (0, 0, -\eta j_z)$ across the null i.e.

$$\begin{aligned} \frac{d\Psi}{dt} &= \max\left\{ \int_{(x_0,y_0,z_0)}^{(x_1,y_1,z_1)} E_\parallel dl + \int_{(x_1,y_1,-z_1)}^{(x_0,y_0,-z_0)} E_\parallel dl \right\} \\ &\quad + \text{null contribution} \\ &= \max\left\{ \int_{(x_1,y_1,-z_1)}^{(x_1,y_1,z_1)} E_\parallel dl \right\}, \end{aligned} \tag{4.9}$$

where $(x_0, y_0, \pm z_0)$ is the starting point near the null and $(x_1, y_1, \pm z_1)$ is the edge of the current sheet. Note that $(x_1, y_1, \pm z_1)$ varies with time as the shape of the current sheet changes. For these simulations $z_0 = 0.05$ is chosen. Any smaller choices of z_0 may result in the magnetic field line being traced increasingly inaccurately. On the other hand, for a larger choice of z_0 the null contribution becomes increasingly inaccurate. Thus, $z_0 = \pm 0.05$ is chosen for the many starting points on either side of the null point to give the best balance between both of these errors. Lastly, to give starting points close to the position of the null, the changing position of the null point in time must be known. To find this, it was noted that the null remains in the $z = 0$ plane (through the symmetry in the applied driving profile) allowing the use of a 2D Newton-Raphson root finding scheme to track the approximate position of the root of $B_y = B_x = 0$ with time.

Figure 4.3 (right panel) shows the variation of the reconnection rate with t during the formation of the current sheet ($t < 5$) for one pulse (green: measured using Equation (4.9)) and two pulses sent simultaneously from opposite boundaries (black: measured using Equation (4.8)) with no time lag, i.e. $t_{lag} = 0$. Similar to the current density (left panel), the reconnection rate for one pulse closely matches the temporal behaviour of the case of two pulses sent at the same time but at a reduced amplitude. Unlike in two dimensions, where the peak in current and reconnection rate coincide since the reconnection rate of flux (over a unit distance out of the plane) is given directly by the electric field at the null ($\mathbf{E}_{null} = -\eta \mathbf{J}_{null}$), it can be seen that in 3D the reconnection rate peaks after the current. This is due to the reconnection rate, as it is defined here, being the integral through the whole sheet which widens after the current peaks, compensating for the reduced current at the null itself. This is an interesting aspect of the 3D reconnection process occurring within the spine-fan current sheet, and shows that a weak but wide current sheet can

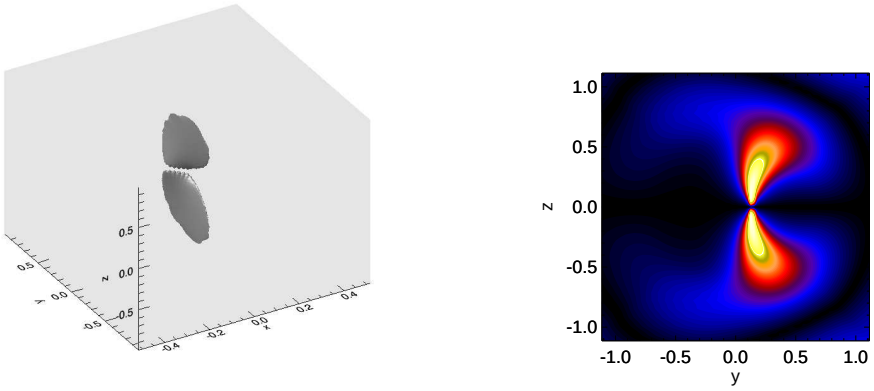

Figure 4.5: Left: an iso-surface (at 50% of maximum) of $|E_{\parallel}|$. Right: a contour plot of $|E_{\parallel}|$ in the $x = -0.005$ plane (containing the null point). For the case of one pulse with $v_0 = 0.04$ and $\tau = 1.8$. Taken at the point where the null is most displaced from its initial position. Note the asymmetrical shape (in the y-direction) of the strong $E_{\parallel}$ regions near the null point. Wyper et al. [2012] reproduced with permission ©ESO.

sometimes transfer more flux across the fan plane than an intense but narrow one.

4.4.4 Qualitative Trends with Driving Amplitude

The trends in quantitative behaviour of current sheet formation driven by only one pulse and two pulses sent together are now compared. For two pulses sent at the same time ($t_{lag} = 0$) from opposite boundaries and for only one pulse, simulations with varied driving strength (v_0) were carried out with $\tau = 1.8$, $A_d = 80$ and $\eta = 5 \times 10^{-4}$. As the aim is to extend the results of PBG07, the focus will be on the peak current (occurring at the null even when it is advected) and the peak reconnection rate, calculated as described earlier. Similarly, the sheet dimensions in the x-, y- and z-directions (L_x, L_y and L_z respectively), taken as the full width at half maximum of the current sheet and measured at the time of maximum current are also considered.

As the driving is not sustained, it is expected that the flux pileup at the onset of the current sheet does not saturate due to the finite speed of reconnection within the current layer. Therefore, the peak reconnection rate and current should scale linearly with driving velocity (compared to the non-linear relations observed in the continuously driven case [Galsgaard and Pontin, 2011b]). Indeed, Figure 4.6 (top panels) shows that both the two pulse and one pulse driving cases increase linearly with v_0 and that the gradient of the line described by the single pulse case is half of that described by cases with two pulses. Clearly,

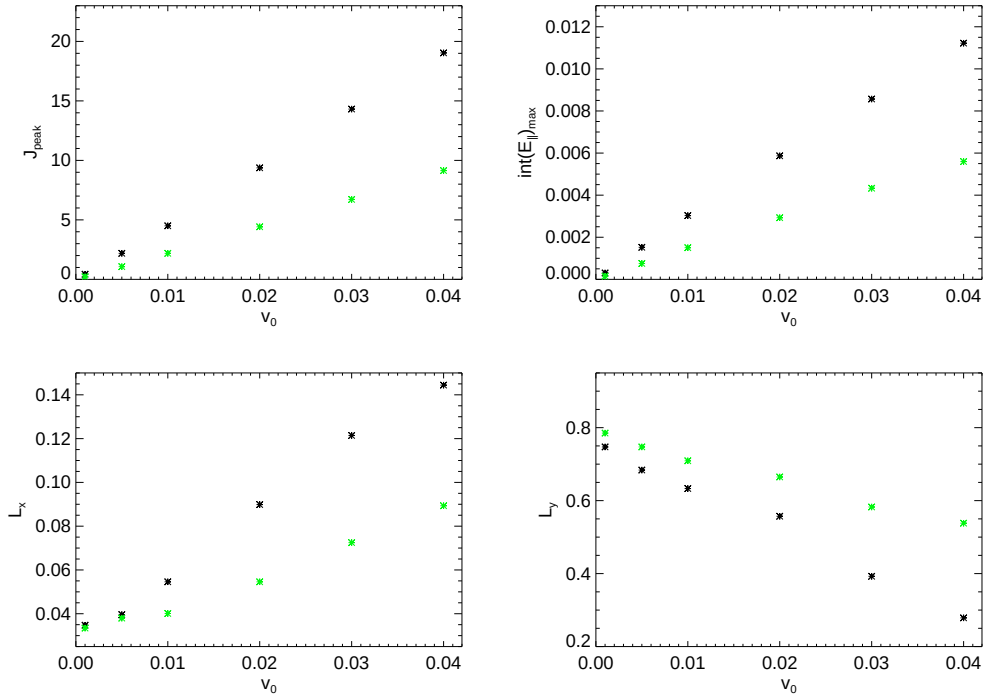

Figure 4.6: Scaling of the absolute value of the driving velocity with peak current $|\mathbf{J}|_{peak}$, peak reconnection rate $\int E_{\|} dl$ and sheet dimensions in the x and y directions (L_x, L_y) taken as the full width at half maximum and measured at the time of peak current within the sheet. Here runs for one pulse are in green and with two are in black ($t_{lag} = 0$) when $\tau = 1.8$, $A_d = 80$ and $\eta = 5 \times 10^{-4}$.

despite the non-linear movement of the null point (and the differing plasma dynamics near the null) what is important in the present case of non-continuous driving, is the amount of available free energy within the perturbations driving the spine-fan collapse and the timing of when this energy is applied at the null point.

The current sheet dimensions are dictated by the strength of the spine-fan collapse which increases when the current (and therefore the Lorentz force) in the sheet increases. This manifests in the increase in L_x and decrease in L_y as v_0 increases (Figure 4.6, bottom panels). Compared with the two pulse case, the one pulse case creates less total stress in the magnetic field at the fan plane. Therefore, it is natural that the spine-fan collapse be reduced at the point of peak current as the Lorentz force which is generated is weaker compared to the induced pressure gradient it must overcome to force the collapse. Thus, the sheet is spread more widely across the fan plane (reducing L_x and increasing L_y in Figure 4.6).

As with the case of $t_{lag} = 0$ studied in PBG07, the interpretation of L_x and L_y varies with the changes in current sheet morphology since they are a direct measure of the dimensions of the current sheet in the x- and y- directions but the shape of the sheet itself changes. When the driving is very weak the current sheet is almost planar across the fan plane (large L_y and small L_x). When the driving strength is increased, the current sheet forms an S-shape with some collapse of the spine and fan (reduced L_y and slightly increased L_x). With the driving further increased the current forms into a planar sheet spanning both spine and fan at an angle to both (reducing L_y and increasing L_x further). In the case of only one pulse and the cases discussed in Section 4.5 where $t_{lag} \neq 0$ the current sheet becomes asymmetrical but in general the same qualitative interpretation of the sheet dimensions discussed above for $t_{lag} = 0$ applies, i.e. stronger driving equals a stronger spine-fan collapse and a tendency of the current sheet to form at an angle to the fan plane.

4.4.5 Null Displacement

In this section the physics behind the initial displacement of the null point in the case of one driving pulse are described. There are two dominant competing effects that govern the rate of null point movement: the ideal asymmetric spine-fan collapse and the non-ideal reconnection of flux into the collapsed regions.

The ideal collapse of the spine on to the fan plane occurs as the disturbance reaches the null (see Figure 4.7). During this collapse the balance of Lorentz and pressure gradient forces in the two outflow regions become unequal and so magnetic flux and plasma are more rapidly expelled in one outflow region than the other. This shifts the null point (being the

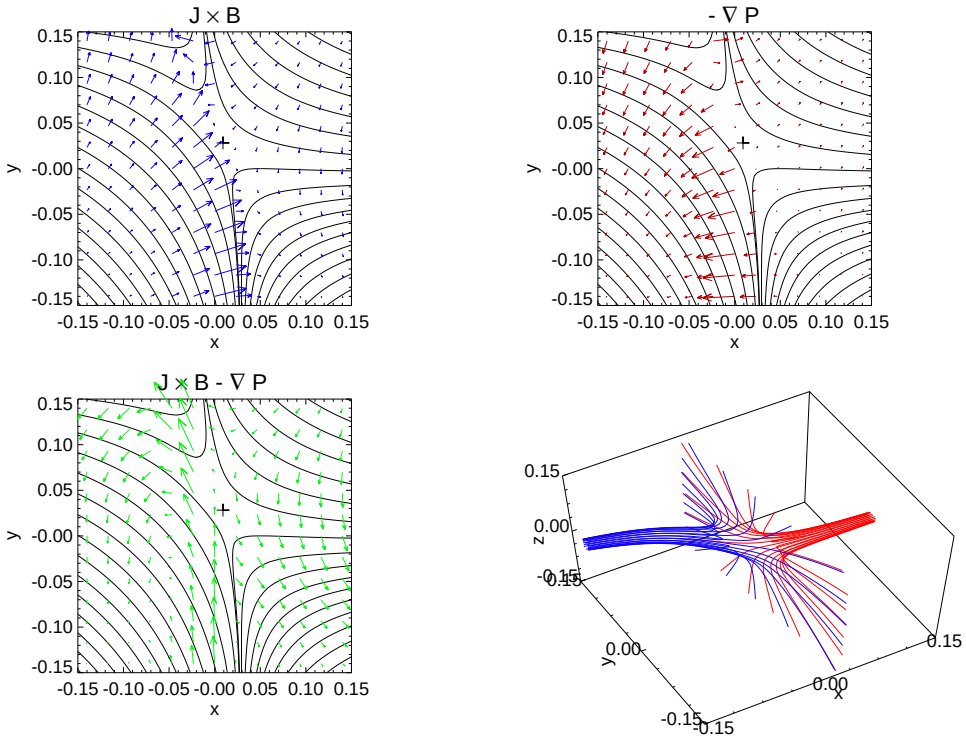

Figure 4.7: Arrows depict Lorentz (top left: blue) and pressure forces (top right: red) in the $z = 0$ plane. Bottom left: the combination of Lorentz and pressure forces (green). The solid black lines show a selection of field lines and the '+' sign indicates the null point position. Bottom right: field lines traced from around the null in 3D. Taken at $t = 2.0$ for the case of one pulse with $v_0 = 0.04$, $\tau = 1.8$, $A_d = 80$ and $\eta = 5 \times 10^{-4}$. Wyper et al. [2012] reproduced with permission ©ESO.

absence of field) toward the more collapsed region with the current sheet following (as it is centred on the null). However, as the collapse increases the current in the collapsed region intensifies which in turn increases the importance of the non-ideal term ($\eta\mathbf{J}$) in Ohm's law. When this term becomes important, magnetic flux can be reconnected (through the spine and fan) into the collapsed region, reducing the displacement of the null point from its initial position and the degree of spine-fan collapse.

For a given external perturbation, the value of the resistivity in the plasma dictates how intense the current in the collapsed region can become before reconnection of flux into the collapsed region can reduce the displacement of the null point. Therefore, with all other parameters fixed, the null point displacement should be related to the plasma resistivity (η). As the null remains in the $z = 0$ plane through the symmetry of the driving profile, the displacement of the null can be defined as $d = \sqrt{x_{null}^2 + y_{null}^2}$, where $(x_{null}, y_{null}, 0)$ is the displaced position of the null from the origin (found using the 2D Newton-Raphson method to solve $B_x \approx B_y \approx 0$). Figure 4.8 (top left panel) shows the dependency of the maximum displacement (d_{max}) with η for two values of v_0 when $A_d = 80$ and $\tau = 1.8$. As expected, with stronger driving and a reduction in resistivity (leading to a more severe asymmetric spine-fan collapse) the null is displaced further. For the values chosen, the null displacement most closely follows an exponential increase with a reduction in η, with relationships given by

$$d_{max} = \begin{cases} 0.075e^{-59.5\eta} & \text{for} \quad v_0 = 0.02 \\ 0.038e^{-61.6\eta} & \text{for} \quad v_0 = 0.01 \end{cases}.$$

It should be noted, though, that with such small values of d_{max} an exponential and a linear fit are rather similar, with the above exponential fit being only marginally better than a linear one. In any case, regardless of the exact relationship, when η is smaller the asymmetric collapse of the spine and fan is greater and the null moves position more rapidly. The maximum displacement of the null also depends linearly on the driving associated with the pulse (Figure 4.8: top right panel) in agreement with the linear dependence of $|\mathbf{J}|_{peak}$ in Figure 4.12.

Lastly, in plasmas near the limit of incompressibility Pontin et al. [2007b] have shown that (with all other parameters fixed) the spine-fan collapse is inhibited by the greater ability of the plasma pressure gradient across the current sheet to resist the Lorentz force which drives the collapse. The resulting current sheet is much more planar in nature and spread out across the fan plane. As the movement of the null clearly depends upon the degree of spine-fan collapse, this suggests that the maximum displacement of the null will

also be dependent upon the background plasma pressure and, therefore, the plasma-β (i.e. the relative strength of the plasma to magnetic pressure gradients). To check this, several more experiments were conducted where the plasma-β was varied through the parameter β^* (recall that in these simulations the plasma-β $= 10\beta^*/3B^2$). It is found that the dependence of the maximum displacement on the β^* scaling parameter is nicely fitted by a logarithmic relationship (Figure 4.8: bottom panel) given by

$$d_{max} = -0.0043 \ln \beta^* + 0.025, \tag{4.10}$$

showing that in the limit of high plasma-β (i.e. when plasma pressure dominates over magnetic effects) the null displacement is indeed reduced in line with the reduction in spine-fan collapse. For plasmas with very small plasma-β's the magnetic field dominates the plasma pressure and the spine-fan collapse is much greater. The logarithmic relationship shows that the null will be rapidly displaced in this case. However, geometrical factors such as the spatial scale of the driver and the line tying of the magnetic field would then be expected to limit the null movement.

An intriguing question is does this rapid change of position of the null change the scalings associated with the reconnection rate and current? Recently Lukin and Linton [2011] discussed reconnection at a 3D magnetic null moving parallel to the direction of current passing through it (compared to the case discussed here where the null moves perpendicular to the direction of current). In their setup the null has the ability to move out of the plane containing the outflow from the reconnection site. This hints at the possibility of fast reconnection, as the rate at which flux is reconnected may not be dependent upon the rate at which the outflow can expel newly connected flux from the current sheet (the so called Sweet-Parker bottle neck). In the present study will the ability of the null to move increase or decrease such a bottleneck effect? Figure 4.9 shows the scalings with η of peak reconnection rate and current density with one pulse (green points) and two pulses (black points). It can be seen that the trends of both quantities are in excellent agreement, with the average power law dependencies for each quantity given by

$$\left[\int E_{\parallel} dl\right]_{max} \propto \eta^{0.15} \quad \& \quad |\mathbf{J}|_{peak} \propto \eta^{-0.65}. \tag{4.11}$$

Therefore, it can be concluded that there is no evidence to suggest that the movement of the null perpendicular to the direction of current affects the reconnection rate and current scalings. The delivery of energy from the driving pulses and the value of resistivity appear to be more important.

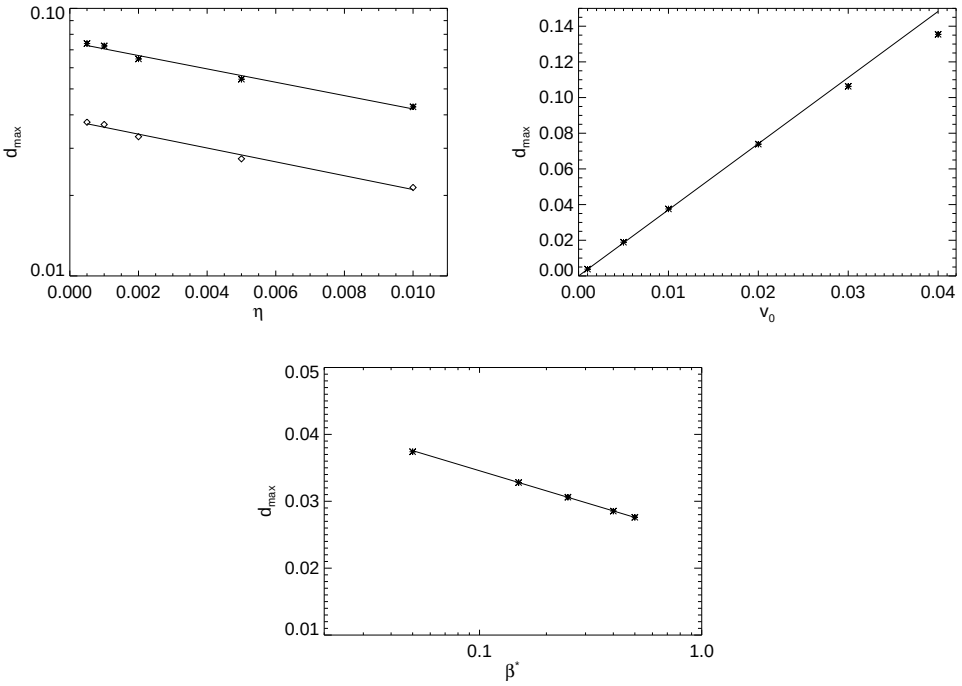

Figure 4.8: For the case of spine-fan reconnection driven by a single pulse. Top left panel: maximum displacement $\left(d = \sqrt{x_{null}^2 + y_{null}^2}\right)$ of the null point from its initial position plotted against η. Diamonds: $v_0 = 0.01$, asterisks: $v_0 = 0.02$. Bottom panel: d_{max} plotted against β^* with $\eta = 5 \times 10^{-4}$ and $v_0 = 0.01$. Top right panel: maximum displacement of the null point plotted against v_0 with $\eta = 5 \times 10^{-4}$. Note, the null remains in the $z = 0$ plane through the symmetry inherent in the driver. Solid lines depict the line of best fit in each case. Wyper et al. [2012] reproduced with permission ©ESO.

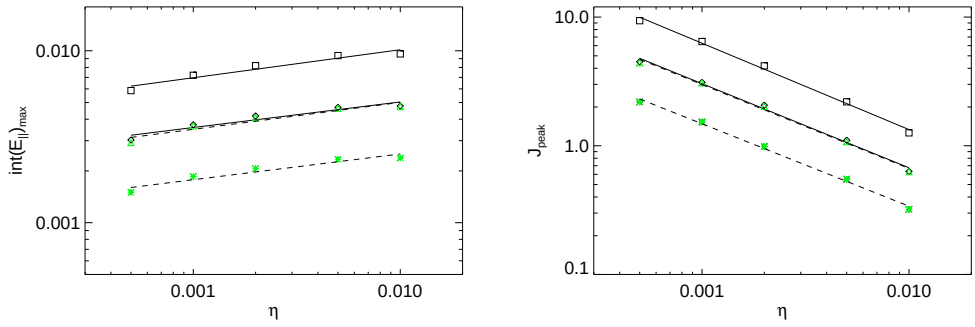

Figure 4.9: Log-log plots of peak reconnection rate (left panel) and peak current (right panel) against η. Black points: two pulses sent at the same time (diamonds: $v_0 = 0.01$, squares: $v_0 = 0.02$). Green points: one pulse (asterisks: $v_0 = 0.01$, triangles: $v_0 = 0.02$). The lines depict the lines of best fit for two pulses sent at the same time (solid) and one pulse (dashed) in each case. Wyper et al. [2012] reproduced with permission ©ESO.

Lastly, how do these resistivity scalings compare with those of previous symmetric studies? The transient driving that has been considered is on the cusp between truly wave driven reconnection, which in the linear regime gives rise to oscillatory reconnection and scaling relations which depend upon $\log \eta$ [Craig and McClymont, 1991], and driven flux pileup reconnection which scales as a power law. An initial investigation by Priest and Pontin [2009] found a power law fit for $|\mathbf{J}|_{peak}$ and somewhere between a power law and logarithmic scaling for reconnection rate. Here a power law appears to fit best for both. Comparing to the flux pileup regimes, the power law scaling for peak current ($\eta^{-0.65}$) is comparable with those of the dynamic incompressible fan solutions of Craig and Fabling [1998]: $\eta^{-3/4}$ and those found empirically for the continuously driven case: $\eta^{-0.6} \sim \eta^{-0.8}$ [Galsgaard and Pontin, 2011b]. The reconnection rate, however, scales slightly faster compared to the $\eta^{0.25}$ scaling found in the other two studies [Craig and Fabling, 1998; Galsgaard and Pontin, 2011b]. A highly accurate scaling analysis covering many orders of magnitude of resistivity is needed to fully determine the scaling behaviour of the transient case. However, in the context of the present investigation, it can confidently be said that the behaviour of the symmetric case at values of resistivity which are realistic of astrophysical plasmas will be mirrored by that of the more complex asymmetrically driven cases.

4.5 Asymmetric Driving: Two Pulses With a Lag Between

4.5.1 Current, Reconnection Rate and Plasma Flow Evolution

In the two preceding cases (two pulses with $t_{lag} = 0$ and one pulse) the disturbances applied on the boundaries arrive at the null at the same time in each scenario. Therefore, it should not be surprising that there are similarities in the early temporal evolutions of current or reconnection rate between the cases with a single pulse and two sent simultaneously. What happens if the second pulse is applied at a later time? How important is the subsequent overlap to the reconnection process? To investigate this two more sets of simulations were performed with two pulses with lag periods between them. In particular $t_{lag} = 0.9$ and $t_{lag} = 1.8$ are investigated for $\tau = 1.8$, $A_d = 80$ and $\eta = 5 \times 10^{-4}$.

Figure 4.10 shows the current evolution in the $z = 0$ plane (the plane containing both spine and fan) for the $v_0 = 0.01$ and $t_{lag} = 1.8$ case taken at the same times as in Figure 4.2. The early evolution (Figure 4.10 (a) and (b)) of the system is the same as that seen in the case with one pulse. The first pulse generates an asymmetric current sheet at the null which is displaced in the direction of shear. From the point of view of the null point, the flow near it is a stagnation point flow.

The second pulse (sent from the $x = 0.5$ boundary at $t_{lag} = 1.8$) then arrives around $t = 3.6$ and shifts the null back toward and then past its initial position (Figures 4.10 (c) and 4.13: top left panel). This increases the contortion of the current sheet into an S-shape which then stretches along the fan plane once both pulses start to dissipate (Figure 4.10 (d)). At this point the driving flow in the y-direction starts to dominate.

For the $t_{lag} = 0.9$ case, the same morphology of the wave fronts and current sheet occurs but (with the second pulse arriving sooner) the null travels less distance when displaced and the shear from the first pulse is less dissipated when the second pulse arrives.

Figure 4.11 shows the variation of maximum current modulus within the volume ($|\mathbf{J}|_{max}$) and reconnection rate with time for the two cases ($t_{lag} = 0.9$: red and 1.8: blue, calculated using Equation (4.9)) compared against the symmetrically driven case ($t_{lag} = 0$: black) and the one pulse case (green). As the lag period between the pulses increases ($t_{lag} = 0 \rightarrow 1.8$) the latent shear associated with the first pulse is reduced by the time the second pulse arrives. This reduces the maximum current attained which in both cases occurs shortly after the second pulse reaches the null, at which time the null point (along with the entire current sheet) is shifting in the direction of the shear from the second pulse.

Similar to the peak current density, the maximum reconnection rate is slightly reduced

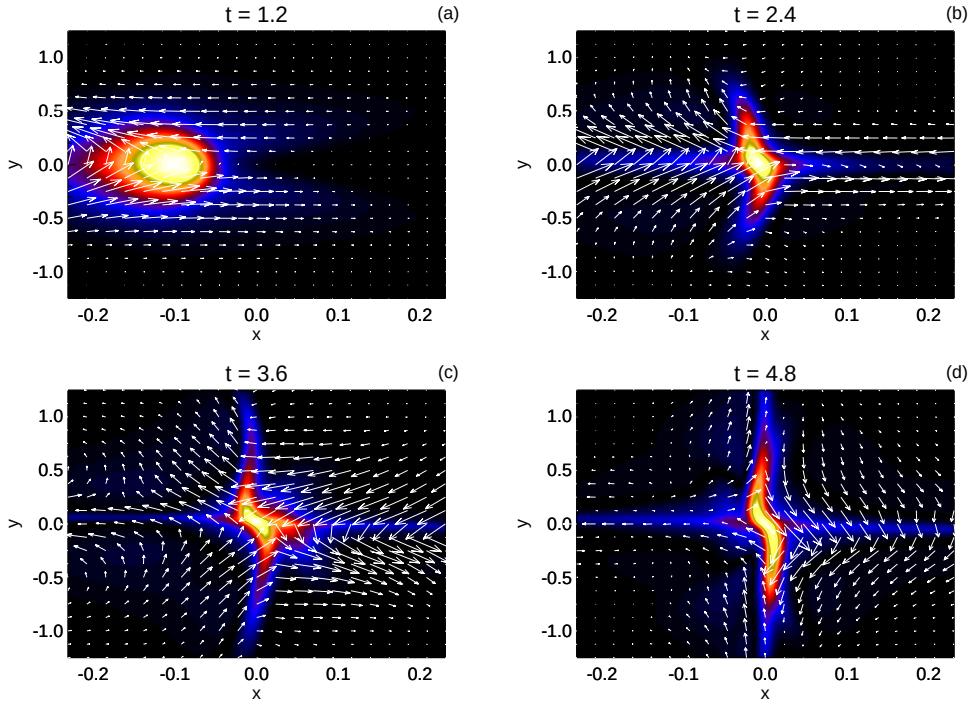

Figure 4.10: Shaded contours show $|\mathbf{J}|$ (scaled to the maximum of each snapshot with yellow depicting regions where the current density is strong and blue regions where it is weak), while the arrows depict the plasma flow. Initially the null is at the origin with the spine along $y = 0$ and the fan along $x = 0$. For the case of $v_0 = 0.01$ and $t_{lag} = 1.8$. Wyper et al. [2012] reproduced with permission ©ESO.

and occurs at a later time for the drivers with a longer lag between the pulses. In the case of $t_{lag} = 1.8$ (see blue solid lines) there are two peaks as the second pulse arrives late enough that the flux transfer from the first pulse has started to slow down.

4.5.2 Qualitative Trends

So far in this section, the dynamics of current sheet formation and early null displacement due to a late second pulse have been investigated. Might the linear increase in peak reconnection rate and current with driving velocity that was found in the simpler cases in Section 4.4 still be expected? To investigate this the above analysis was repeated for several other values of v_0. Surprisingly the peak reconnection rate and current *do* still depend linearly upon driving velocity, despite the increased complexity of the situation (Figure 4.12, red: $t_{lag} = 0.8$, blue: $t_{lag} = 1.8$). In fact, the one pulse case and the $t_{lag} = 0$ symmetric two pulse case provide upper and lower bounds for the peak current

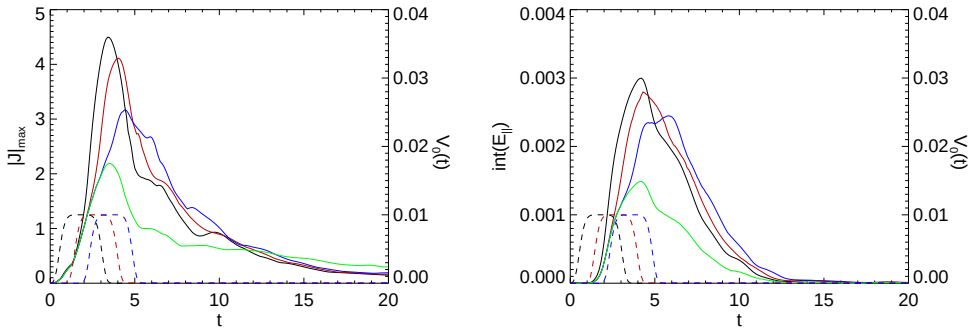

Figure 4.11: Solid lines (left panel): $|\mathbf{J}|_{max}$ plotted against t. Solid lines (right panel): $\int E_{\parallel} dl$ plotted against t. For the cases with two pulses the dashed lines indicate the driving amplitude of the second pulse. Black: $t_{lag} = 0$, red: $t_{lag} = 0.9$ and blue: $t_{lag} = 1.8$. The solid green line is with only one pulse. For the case of $v_0 = 0.01$. Wyper et al. [2012] reproduced with permission ©ESO.

and reconnection rate within which the asynchronous two pulse simulations (when all other parameters are fixed) fall.

The spine-fan collapse (and therefore the sheet dimensions) follows the same trend as the single and symmetric double pulse cases, in that it increases with driving velocity as a result of a stronger perturbation of the spine lines initiating a more severe Lorentz force driven collapse. This gives an increased L_x and decreased L_y as v_0 is raised. The sheet dimensions themselves are measured at the time of peak current, which occurs progressively later as the time between pulses increases (see Figure 4.11). As such, the stress in the field from the first pulse would be expected to have spread out further across the fan plane by arrival at the null of the second pulse. This is demonstrated in Figure 4.12 as an increase in L_y and decrease in L_x for increasing t_{lag}.

The naturally wider and weaker current sheets that occur as the gap between the pulses increases leads to a subtle difference between the trends in the peak values of reconnection rate and current. The peak reconnection rate is affected slightly less than the peak current (staying closer to the values obtained when $t_{lag} = 0$) by the increasing gap between the two pulses ($t_{lag} = 0 \rightarrow 1.8$). As the reconnection rate is defined as the integral of the parallel electric field across the whole sheet, the spread of the current sheet compensates somewhat for the reduced maximum strength of current within it.

In summary, the initial current sheet morphology is complicated by the introduction of a second pulse sent at a later time. Clearly the timing of the pulses plays an important roll in the values obtained for peak reconnection rate and current. However, the relationships developed in the symmetric case remain valid despite the extra complexity in the dynamics.

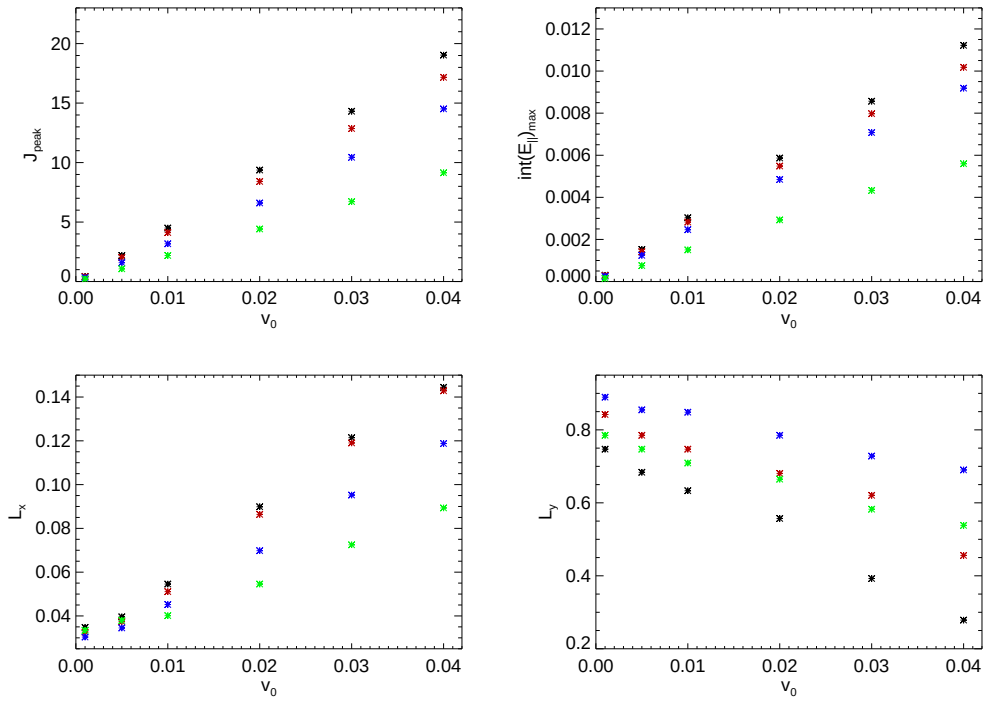

Figure 4.12: Scaling of the absolute value of the driving velocity with peak current $|\mathbf{J}|_{max}$, peak reconnection rate $\int E_{\|} dl$ and sheet dimensions in the x and y directions (L_x, L_y) taken as the full width at half maximum. Here runs for one pulse are in green and with two are in black ($t_{lag} = 0$), red $t_{lag} = 0.9$ and blue $t_{lag} = 1.8$ when $\tau = 1.8$, $A_d = 80$ and $\eta = 5 \times 10^{-4}$. Wyper et al. [2012] reproduced with permission ©ESO.

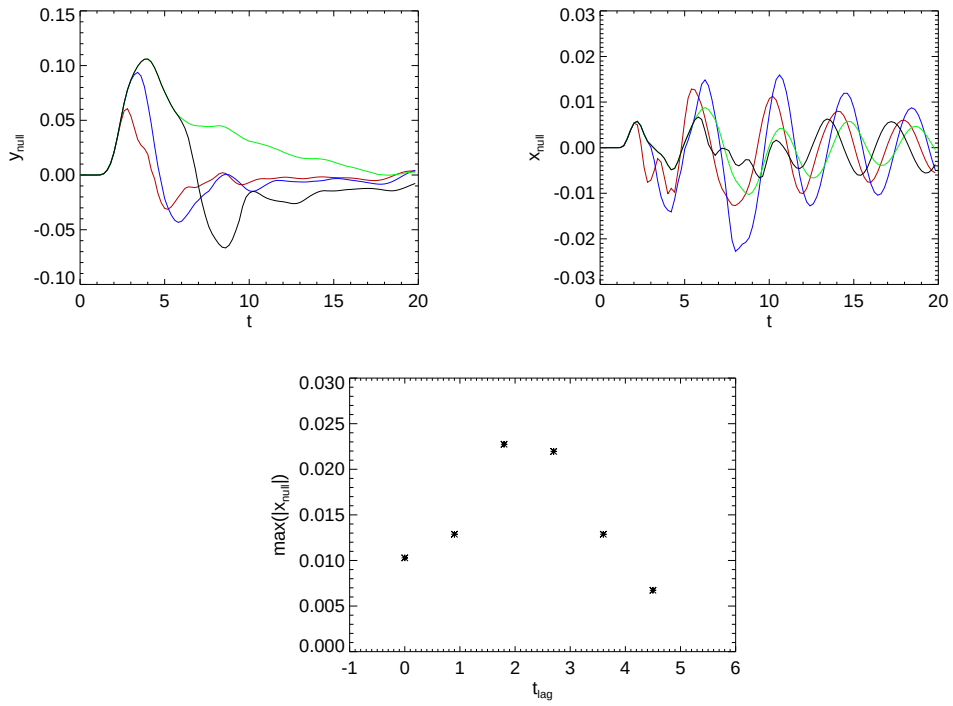

Figure 4.13: The x- and y-components of the null position $(x_{null}, y_{null}, 0)$ plotted against t. Top left: y_{null} and right: x_{null}. For one pulse (green) and two asynchronous pulses with $t_{lag} = 0.9$ (red), 1.8 (blue) and 4.5 (black). Bottom panel: $max(|x_{null}|)$ for various t_{lag} cases. Each case has $v_0 = 0.03$, $\eta = 5 \times 10^{-4}$ and $A_d = 80$.

4.6 Asymmetric Driving: Relaxation Phase

In this section a brief investigation of the longer term behaviour of the system beyond the initial peak in current density and reconnection rate is presented. This relaxation phase is defined as the time period once the reconnection rate begins to decline. To show this phase, the experiments for several values of t_{lag} and one pulse at driving velocities of $v_0 = 0.01$ and 0.03 (with $\eta = 5 \times 10^{-4}$ and $A_d = 80$) were carried out well beyond their peaks in reconnection rate. Once each case enters this phase of reconnection the spine-fan collapse reduces, the current sheet spreads out across the fan plane and the null point returns toward its initial position (in the cases where it has been displaced). However, in these cases the displaced null does not simply slowly make its way to the origin. During the null's initial displacement the acoustic aspect of the wave disturbance washes over the null point and creates an uneven distribution of mass in each topological region. The inertial overshoot associated with the equalisation of this distribution leads to an oscillation in the x-direction of the null point position and the surrounding fan plane (discussed further in Section 4.7). Thus, the null oscillates perpendicular to the fan plane (in x: Figure 4.13, top right panel) as it slowly moves back in y toward $y = 0$ (top left panel).

The amplitude of the null oscillation depends upon whether the arrival of the second pulse amplifies or cancels with the oscillation excited by the first. For the experiment with $t_{lag} = 1.8$ it can be seen from the blue lines in the right panel of Figure 4.13 that both pulses have combined constructively whereas when $t_{lag} = 4.5$ (black lines) the oscillatory effect is slightly cancelled out. A simple measure of the degree of constructive/destructive interaction between the pulses is given $(|x_{null}|)_{max}$, shown in the bottom panel of Figure 4.13, from which it can be seen that the null oscillation for this particular system is best amplified when t_{lag} is chosen to be around 1.8. Also, recall that the initial displacement of the null depends upon the driving velocity and resistivity (see Figure 4.8) indicating that an increase (decrease) in velocity (resistivity) will also lead to bigger oscillations. Comparing the oscillations seen in the experiments with $v_0 = 0.01$ to the those above confirms this for v_0.

The current and reconnection rate evolutions when $v_0 = 0.03$ follow a similar evolution to those of the $v_0 = 0.01$ case. Therefore, comparing Figures 4.11 and 4.13 it is clear that this induced oscillatory behaviour is non-reconnective (under the definition of reconnection rate used here) as it continues well beyond the time ($t > 14$) when the reconnection ceases. At this point, there is still significant current in the system which slowly reduces through magnetic diffusion. Such fan plane perturbations (and the associated plasma flows through the null: Section 4.7) are reminiscent of the radially symmetric non-reconnecting $m = 0$

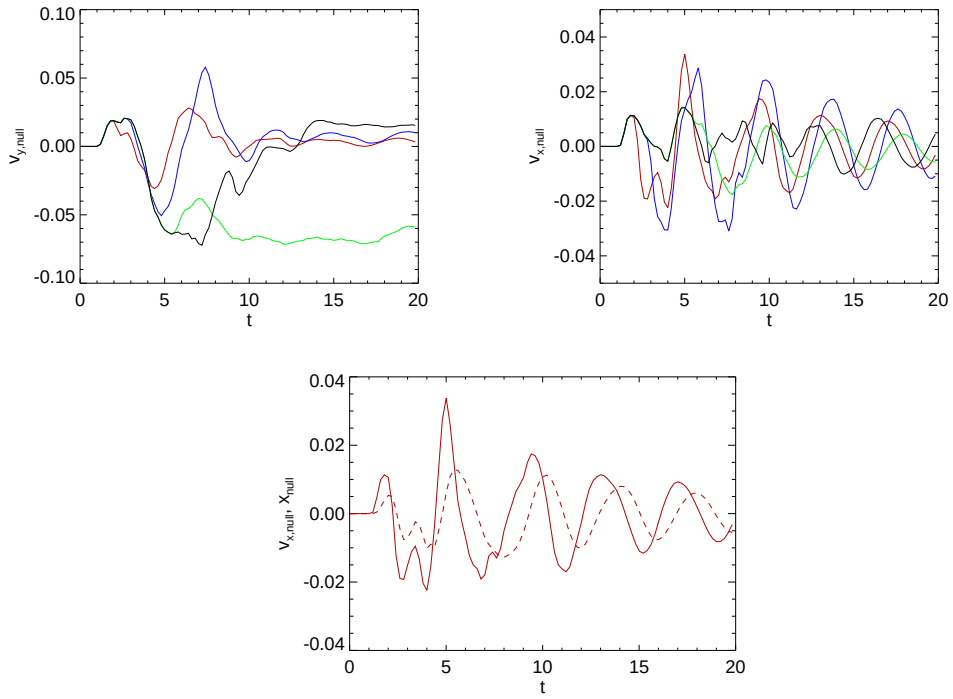

Figure 4.14: The components of the plasma velocity at the null point $(v_{x,null}, v_{y,null}, 0)$ plotted against t. Top left: $v_{y,null}$ and top right: $v_{x,null}$. For the same cases as in Figure 4.13 with one pulse (green) and two asynchronous pulses with $t_{lag} = 0.9$ (red), 1.8 (blue) and 4.5 (black). Bottom: comparison of $v_{x,null}$ (solid) and x_{null} (dashed) for the case with $t_{lag} = 0.9$.

spine mode of Craig and Fabling [1996], hinting that such solutions could be utilized to analyse such oscillations in the future. For much longer time frames this oscillatory motion will damp out (which begins to occur around $t = 10$ in Figure 4.13, bottom panel) leaving the null back at the origin and a current sheet in force balance between the plasma pressure gradient and Lorentz force.

Lastly, is should be noted that the current in the system perturbed by a single pulse decays more slowly than the cases perturbed by two pulses (green line, Figure 4.12: left panel). When perturbed by two pulses (symmetric or otherwise) much of the stress applied by the first pulse to the magnetic field on one side of the fan plane is matched by the second on the other side. As the field relaxes both combine to bring the field toward a potential field configuration faster than when the stress applied is uneven as in the case of a single pulse.

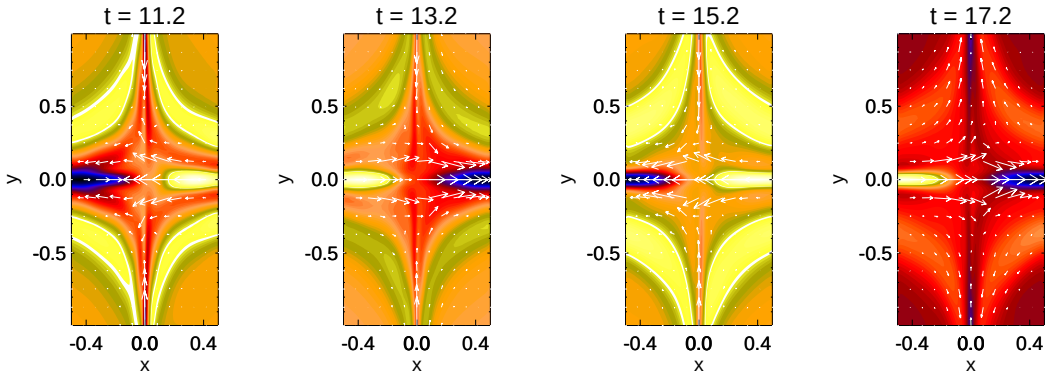

Figure 4.15: Oscillating plasma flows across the fan plane in the $y = 0$ plane at different times during the relaxation phase. Arrows show plasma velocity and the contours show plasma pressure (scaled to the maximum in each frame with high pressure shown as yellow and low as blue). For the asynchronous case with $t_{lag} = 1.8$, $v_0 = 0.03$, $\eta = 5 \times 10{-}4$ and $A_d = 80$.

4.7 Plasma Flow at the Null Point

In Chapter 3 it was found that asymmetric fan current sheets gave rise to a non-zero plasma flow through the null point. It seems likely therefore that there will be flow through the null in the asymmetric spine-fan scenario also. Figure 4.14 (top panels) shows the components of plasma velocity at the null as a function of time for the same four cases as plotted in Figure 4.13. These plots show clearly that there is a non-zero plasma flow and that both components have a different distinct behaviour.

The y-component ($v_{y,null}$) of the plasma flow through the null point is equivalent to the plasma flow at the null that was seen in the asymmetric analytical fan model in Chapter 3. Consider first the case with one driving pulse (shown in green). As in Chapter 3, if the side where the spine line is perturbed (in this case by the driving pulse) is denoted the strong shear side then the analytical model predicts that the flow from the weak side should have encroached into the strong shear region (as in Figure 3.4). As the field on the strong shear side is perturbed in the *positive* y-direction, this should mean that the y-component of the flow through the null point should be in the *negative* y-direction. From the left panel of Figure 4.14 it can be seen that in the one pulse case that the quasi-steady flow which forms as the null point slowly moves back to its initial position does indeed have a y-component in the negative direction. In the other cases (with two pulses) the second pulse shifts the null back to the origin more quickly so that this component of the flow rapidly reduces to zero (black, blue and red lines: Figure 4.14).

The x-component ($v_{x,null}$, Figure 4.14: right panel) is linked to the oscillation of the null position. Initially, the plasma flow through the null in the x-direction is driven by the acoustic aspect of the magnetoacoustic driving wave pulse as it reaches the null point. This leads to a net difference in plasma density between the two topological regions separated by the fan plane. Recall that (as was also shown in Chapter 3) the spine-fan mode reconnects an equal and opposite amount of flux across the fan plane so should not contribute much to the net difference in density. This difference in density, driven by the associated pressure gradient, slows the plasma transfer through the null in the x-direction from the initial pulse and eventually reverses the direction of plasma flow so that mass passes back through the null in the opposite x-direction. This sets up the oscillation of the flow through the null in this direction, as each time the plasma flow reverses it overshoots it's equilibrium state and builds a reverse pressure gradient once more (see Figure 4.15). This oscillation of the plasma flow is what drives the oscillatory motion of the null in the x-direction which can be seen by the way that the plasma flow oscillation ($v_{x,null}$) leads the oscillation of the null position (x_{null}) in Figure 4.14 (bottom panel). The constructive and destructive interference which occurs in cases with two asynchronous pulses can then be understood in terms of how the initial density drop is built up by the combination of the two pulses.

Interestingly, the period of oscillation is nearly the same in the four cases ($t_{period} \approx 4$ Alfvén times) suggesting that there is a unique frequency of oscillation that must depend upon the plasma parameters and the size of the numerical box. An interesting avenue of investigation would be to explore this time dependent behaviour further and to see firstly how the oscillation period depends upon the system parameters and secondly how important these parameters are to the value of t_{lag} which produces the resonant oscillation of x_{null} and $v_{x,null}$. Such an investigation is, however, beyond the current scope of this investigation which focuses on the early stages of the spine-fan process.

In summary, plasma flows through the null point seem to be ubiquitous to the asymmetric spine-fan scenario, although the direction of this flow can be very time dependent. However, the presence of the plasma flow in the y-direction which qualitatively matches to the flow predicted by the kinematic model shows that, in certain circumstances, the kinematic methodology can reproduce the behaviour of solutions to the fully dynamic MHD equations.

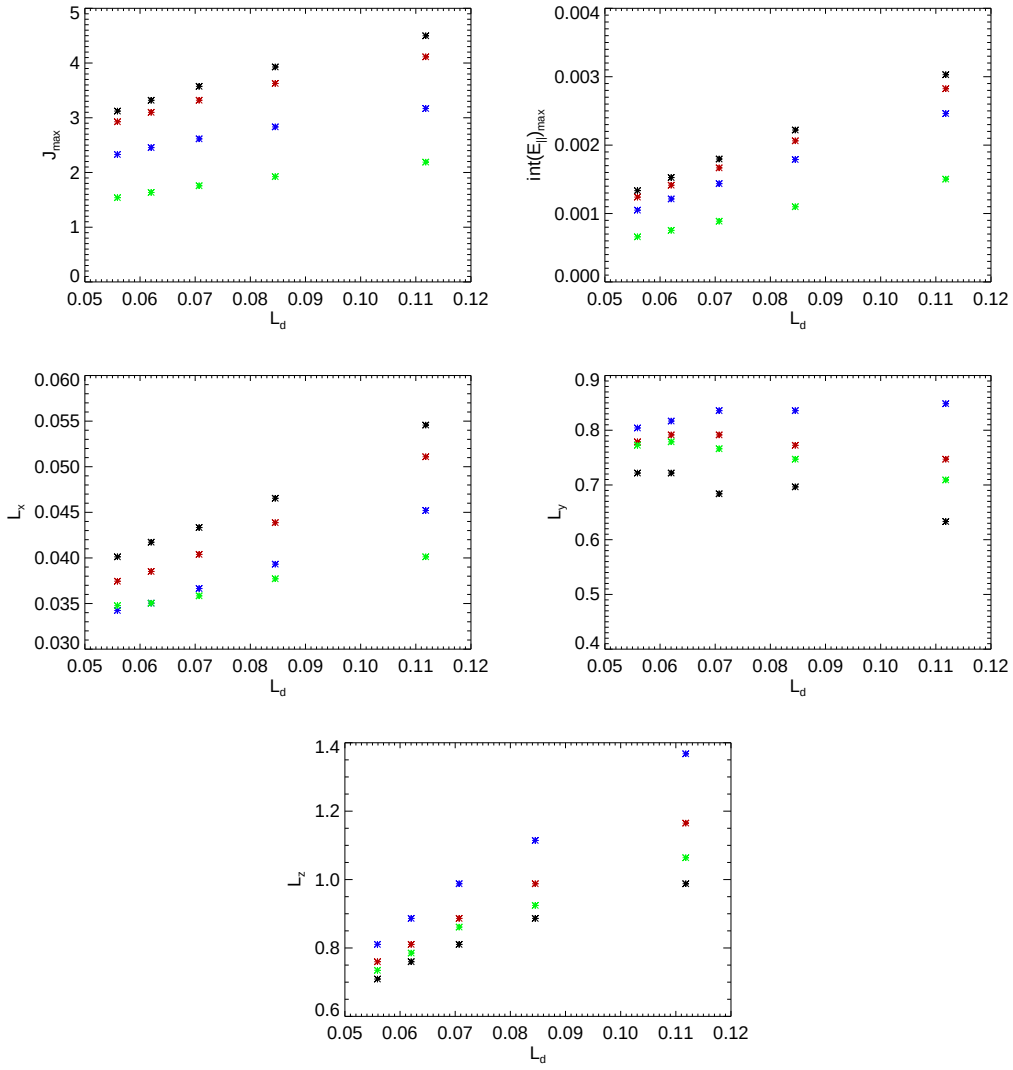

Figure 4.16: Peak current $|\mathbf{J}|_{max}$, peak reconnection rate $\int E_{\|} dl$ and the sheet dimensions in the x, y and z directions (L_x, L_y and L_z) taken as the full width at half maximum plotted against the driving patch length scale L_d. Here runs for one pulse are in green and with two are in black ($t_{lag} = 0$), red $t_{lag} = 0.9$ and blue $t_{lag} = 1.8$ when $\tau = 1.8$, $v_0 = 0.01$ and $\eta = 5 \times 10^{-4}$. Wyper et al. [2012] reproduced with permission ©ESO.

4.8 Spatial Variation

In Chapter 3, an investigation of the role of asymmetric current sheets and their dimensions in the spine and fan models was presented. Within this chapter it has been shown that an asymmetry in the driving pulses can give rise to similarly asymmetrically shaped current sheets and altered reconnection rates when the MHD equations are evolved self consistently. However, drivers of different spatial dimensions would also be expected to alter the dimensions and reconnection rates of the induced current sheets. Indeed, due to the complex surface flow topology in the Sun and the effective line-tying at the solar photosphere, driving motions could often be constrained in size. In this section the effect of spatially varying foot point displacements on current growth and reconnection rate is, therefore, investigated. To achieve this, simulations for varied driving patch sizes were performed with $v_0 = 0.1$, $\tau = 1.8$ and $\eta = 5 \times 10^{-4}$. The patch length scale, $L_d = A_d^{-1/2}$, is doubled by varying A_d from 320 to 80 (see Equation (4.6)). For increased generality simulations with varied L_d were also repeated for two pulses with temporal variation, $t_{lag} = \tau/2$ and τ and for a single driving pulse.

What should be expected? With a larger driving patch the spine should be displaced more during the driving and therefore the current sheet formed at the null should be stronger. Indeed, it is found that the relation of peak values for current and reconnection rate with L_d (and therefore spine displacement) is linear (Figure 4.16, top panels) indicating that for transient driving the width over which the perturbation occurs also plays an important role in the dynamics of current sheet formation.

With an increase in current within the sheet an increase in spine-fan collapse through the stronger Lorentz force is expected. This is seen as an increase in L_x in Figure 4.16. The sheet length along the direction of shear however appears to be less altered, with a variation $\approx 10\%$ compared with $\approx 30\%$ in L_x. The sheet is actually lengthening along the fan plane in the y-direction, however the angle that the sheet makes to the fan is also increasing, reducing L_y in the way it is measured here. Lastly, out of the xy-plane, with an increase in the width of the driver (L_d), a linear increase in current sheet width (L_z) would be expected. What is found is a near linear curve as the increase in current at the null (due to the increased spine displacement) slightly reduces the width between the half maximum points.

4.9 Summary and Discussion

The investigations within this chapter have explored the nature of spine-fan reconnection driven by asymmetric perturbations. It was found that any degree of asymmetry in the driving produces an asymmetric spine-fan collapse and a displacement of the null itself. This suggests that in practice a solar coronal null will be constantly moving. Indeed, that the displacement of the null increases with reducing η and plasma-β suggests that at realistic coronal values a 3D null will be severely rattled around by buffeting driving flows. This rapid movement could be a potential mechanism to crash together nulls of opposite type (A ($B_0 > 0$) or B ($B_0 < 0$), Greene [1988]) leading to the null cancellation observed in the null clusters that connect large scale reconnecting separators [Dorelli et al., 2007; Maclean et al., 2009; Parnell et al., 2010].

In light of this rapid movement of the null, the scaling laws associated with the reconnection rate and current build up were tested to see how robust they were with the additional complexity of asymmetric current sheets, plasma flow through the null and asymmetric outflow jets. What is encouraging, considering the complexity of the flows in the solar atmosphere, is that despite these extra dynamical effects the scaling relationships established in the idealised cases with symmetric driving remain robust (at least for the weak perturbations studied here).

An interesting finding from these transiently driven cases is that unlike in the two dimensional case [Craig and McClymont, 1991; McLaughlin et al., 2009] there is no evidence of oscillatory reconnection of the traditional type during the relaxation phase (i.e. no change in sign of $\int E_{\parallel} dl$, Figure 4.11). In the 2D case, the inertial overshoot of plasma into the outflow regions from the X-point collapse builds up enough that: the *collapsed* regions *open out* and the *opened out* regions *collapse* together. This reverses the direction of the reconnection. Why we do not see something similar could be a result of the line tied boundary conditions and the proximity of the box to the regions where the spine-fan collapse occurs. Were the boundaries further away perhaps the spine lines could move more freely and create the oscillating scissor effect (between the spine and fan in this case) that is characteristic of the 2D oscillatory scenario. However, another possible reason why this kind of oscillatory reconnection is not seen is that in the 2D case the inertial overshoot that is created by the reconnection has nowhere else to go *but* back across the separatrices. In this case, the mismatch can escape into the 3rd dimension (i.e. out of the $z = 0$ plane containing the spine and fan) and slowly flow back around the spine to equalise the build up (in the manner of the $n = 1$ pure spine solution in Chapter 3). It is, therefore, likely a question of time scales between these two effects as to why there is no reversal of the

reconnection direction. In the future, it would be interesting to see if it is the rate at which plasma escapes into the third dimension or the rigidity of the boundary conditions which suppresses oscillatory reconnection in this setup.

What was found instead was the generation of a different kind of oscillatory behaviour involving inertial overshoot. This resulted in plasma flow through the null point and an oscillation of the null point position (perpendicular to the fan plane). It was noted, however, that this oscillation is likely to be very dependent upon the dimensions of the simulation box and other plasma parameters. It seems likely that both behaviours will occur together in the relaxation phase of asymmetric spine-fan reconnection with the manner of perturbation and the local plasma parameters playing an important part in deciding which of the two dominates. An investigation of this would be interesting to undertake in the future.

What is found in these transiently driven simulations, in common with those of McLaughlin et al. [2009], is that the system relaxes towards a non-potential intermediate state in force balance through plasma pressure. This state indicates that even small perturbations of the spine or fan will lead to a non-potential fan plane magnetic field and preferential heating there. This seems in agreement with the heating observed at domed fan structures observed in solar jets [e.g. Liu et al., 2011; Török et al., 2009]. For much longer time scales (beyond what is practical to run these simulations for) the current in the sheets would be expected to diffuse away leaving a potential magnetic field in a plasma of constant pressure.

Another result worth highlighting is that a plasma flow at the null point appears to be ubiquitous to asymmetric spine-fan reconnection and that it has two distinct components: one oscillatory flow related to the wave-like motion of the null perpendicular to the fan plane and another more slowly varying component associated with the subsequent slow return of the null toward its initial position. In particular, this second flow component qualitatively matches what was predicted by the asymmetric kinematic steady state model for fan reconnection in Chapter 3 and shows that under certain circumstances kinematic solutions give a good description of the fully self consistent time dependent reconnection scenario.

Lastly, the importance of the current build-up and sheet dimensions on the length scale on the driver were briefly considered. A linear correlation between driving length scale and peak reconnection rate and current was found along with a noticeable change in the current sheet dimensions. This suggests that, in line-tied systems, a limited driving spatial scale can have a detrimental effect on the efficiency of the reconnection process. This highlights that, although line-tied photospheric motions are often used as the catalysts for

generating non-ideal regions and reconnection [e.g. magnetic breakout, Antiochos et al., 1999], depending on the magnetic topology they can also limit the ultimate reconnection rate.

5

Kelvin-Helmholtz Induced Reconnection in the Torsional Fan Current-Vortex Sheet

"*Success consists of going from failure to failure without loss of enthusiasm.*"

Winston Churchill

"*This aint no technological breakdown. Oh no, this is the road to hell.*"

Chris Rea,
The road to hell (Part II)

5.1 Introduction

The work within this chapter will consider the role of instabilities in driving or altering the reconnection processes which occur at 3D magnetic null points. From previous studies [e.g. Pontin and Galsgaard, 2007; Pontin et al., 2007a] and the work presented in Chapters 2 and 3 it is known that in the cases of externally driven fan and Torsional fan reconnection the current layer that forms at the fan separatrix surface includes both a sheared

Figure 5.1: Kelvin-Helmholtz instability in the cloud formation over Mount Shasta, California. Photo ©Beverly Shannon. *Photo only available in the printed version to comply with copyright laws.*

magnetic and velocity field component. Numerical studies of both regimes until now have focused purely on the formation of these smooth current layers. However, such a shear layer configuration (known as a current-vortex sheet) is know to be unstable to shear flow and resistive instabilities, leading to fragmentation of the current layer and multiple reconnection sites [e.g. Chen and Morrison, 1990; Einaudi and Rubini, 1986]. Such instabilities have perhaps been suppressed in these previous numerical studies owing to the use of relatively large resistivity and viscosity in the simulations and the shorter time scales over which the boundary driving velocities were imposed. This chapter investigates, for the first time, an instability of a Kelvin-Helmholtz-like (KH-like) nature occurring in a fully three-dimensional current-vortex sheet formed at the fan plane of a 3D null point.

The KH instability is fascinating in its own right and has been the subject of much attention over many decades of research. In general, the KH instability is an instability of the boundary layer between two fluid streams moving at different rates. When a velocity shear layer is KH unstable, any small perturbation perpendicular to the boundary layer draws energy from each flow stream and creates a ripple of the layer which grows in time. These ripples, given the right conditions, grow into vortices which straddle a region between the two streams and mix the two fluids. In the early (linear) phase of the instability, the perturbed quantities can be expressed in terms of a Fourier decomposition, i.e. $\epsilon = Ae^{-i\omega t + i\mathbf{k}\cdot\mathbf{x}}$ where ϵ is some perturbed quantity, $\mathbf{k}$ is the wave vector and ω the angular frequency. If, for a given shear layer, ω has and imaginary part so that $\omega = \omega_{r.} + i\omega_{im.}$ then this imaginary part gives rise to an exponentially growing perturbation for which the growth rate $\Gamma = \omega_{im.}$. In the simplest two dimensional case of two unmagnetised, incom-

pressible, inviscid fluids of constant and equal density, separated by a layer of infinitesimal width, the linear growth rate is given by $\Gamma = \Delta v k/2$, where Δv is the velocity difference across the layer (see, for instance, Chandrasekhar [1961]; Choudhuri [1998]). Therefore, larger wave numbers (or smaller wave lengths (λ) as $k = 2\pi/\lambda$) are the fastest growing in this simple case. However, the inclusion of viscosity, surface tension, compressibility and other effects all act to restrict the growth of the KH instability at different wave numbers in the hydrodynamic (HD) case [see for instance Blumen, 1970; Chandrasekhar, 1961].

When a magnetic field is introduced the linear and non-linear dynamics of the KH instability are also strongly affected. A uniform magnetic field component aligned with the shear flow (or 'parallel field') is known to be a stabilising influence, due to the associated magnetic tension force [e.g. Chandrasekhar, 1961; Miura and Pritchett, 1982]. Specifically, the KH instability is linearly stabilised when $\Delta v/c_A < 2$, where c_A is the Alfvén speed. On the other hand, a magnetic field component perpendicular to the shear layer ('transverse field') does not affect the stability, but modifies the growth rate of a given mode [e.g. Miura and Pritchett, 1982]. At later times during the non-linear evolution, a parallel field inhibits the inverse cascade of energy from small to large scales seen in the HD case and forces energy to be dissipated at small scales [e.g. Frank et al., 1996; Malagoli et al., 1996], whereas a transverse field is simply advected by the plasma.

In the numerical experiments described within this chapter, in the fan plane where the instability occurs, there exists a strong transverse magnetic field component (the radial field B_r associated with the potential field defining the null), as well as a sheared in-plane component that reverses sign at the same location as the flow (the azimuthal field B_θ associated with the current layer that forms at the fan in response to the boundary driving). The stability of such a current-vortex sheet (where the magnetic and velocity shear layers coincide) has been studied in 2 and 2.5 dimensions in several investigations [e.g. Dahlburg and Einaudi, 2002; Dahlburg et al., 1997; Einaudi and Rubini, 1986; Keppens et al., 1999; Landi and Bettarini, 2011]. Einaudi and Rubini [1986] showed that, in the incompressible limit, a transition between a tearing-like regime and a KH-like regime occurs when $\Lambda = \left(\frac{L_b}{L_v}\right)\left(\frac{\Delta v}{c_A}\right)^{2/3} = 1$. Here L_b and L_v are the widths of the magnetic and velocity shear layers, Δv is the velocity difference across the layer and c_A the Alfvén speed far from the layer. When $\Lambda < 1$, a tearing unstable regime is found as the magnetic shear strongly outweighs the velocity shear and the current sheet is fragmented into many magnetic islands [Furth et al., 1963]. Conversely, when $\Lambda > 1$ the velocity shear dominates the layer, and the linear phase of the instability is ideal, and of a Kelvin-Helmholtz nature. This transition has also been shown to hold in weakly compressible [Dahlburg and Einaudi, 2000] and viscous plasmas [Einaudi and Rubini, 1989]. By considering the stresses involved Dahlburg

et al. [1997] argue that even when $\Lambda > 1$ the presence of the magnetic shear fundamentally alters the nature of the KH-type instability by allowing magnetic reconnection to become important, and that, therefore, the instabilities of the current-vortex sheet should not be considered as a simple mix of tearing and Kelvin-Helmholtz modes.

As shear flows are prevalent in many astrophysical and geophysical situations the KH instability is important in a wide range of contexts. Obvious terrestrial examples include wind driven water waves and billowed cloud formation (a nice example of which is shown in Figure 5.1). There have also been numerous observations of KH signatures on the magnetopauses of various planets [e.g. Masters et al., 2010; Sundberg et al., 2012] as well as our own [Hasegawa et al., 2004; Nykyri et al., 2006], where the instability is thought to play a crucial role in mixing the plasmas of the planetary magnetosphere and the solar wind. The KH instability is also crucial in the disruption of astrophysical jets, emanating for example from young stellar objects and active galactic nuclei [Ferrari, 1998]. In the solar corona there are recent direct observations of KH instabilities in regions of strong flow shear associated with eruptions [Foullon et al., 2011; Ofman and Thompson, 2011]. This work highlights that, in addition to these fast flows, magnetic separatrices are prime locations for the formation of current-vortex sheets in the complex topology of magnetic fields such as the corona. In the work within Chapter 2, as well as in other studies [e.g. Priest et al., 2005], these separatrix surfaces have already been proposed as preferential sites of plasma heating in the corona. This heating could be significantly enhanced by instabilities such as that studied herein.

The work presented within this chapter will investigate the self consistent formation and stability of the current-vortex sheet created by twisting motions around the spine foot points of a linear, rotationally symmetric 3D magnetic null. The focus is restricted to the KH unstable regime ($\Lambda > 1$), leaving the tearing-type regime for future study. It should be noted, however, that in the tearing unstable regime the growth of the instability would be expected to be slow as a velocity shear flow is known to damp the tearing mode growth rate [Chen and Morrison, 1990]. It should also be noted that in the numerical experiments within this chapter, the geometry of the problem is much more complex than that of the studies discussed above. In particular, the widths of the shear layers (L_B and L_v) vary along the transverse (radial) direction, and are set in a self-consistent manner by a balance between the driving flow and the dissipation in the system, rather than being fixed by the initial conditions.

The investigation is structured as follows: Section 5.2 introduces the numerical setup. Section 5.3 discusses the self consistent formation of the current vortex layer whilst Section 5.4 investigates the growth and development of the instability. Finally, Section 5.5

summarises the findings and presents some conclusions.

5.2 Numerical Setup

The investigation was carried out numerically using the same code as described in the previous chapter. However, in this case, as the KH instability is strongly dependent upon small scale dynamics, the artificial viscosity operators were replaced with a physically meaningful constant viscosity such that the equations being solved in the code now take the form

$$\frac{\partial \mathbf{B}}{\partial t} = \boldsymbol{\nabla} \times (\mathbf{v} \times \mathbf{B}) + \eta \nabla^2 \mathbf{B} \tag{5.1}$$

$$\frac{\partial (\rho \mathbf{v})}{\partial t} = -\boldsymbol{\nabla} \cdot (\rho \mathbf{v}\mathbf{v}) - \boldsymbol{\nabla} P + \mathbf{J} \times \mathbf{B} + \mu \left(\nabla^2 \mathbf{v} + \frac{1}{3} \boldsymbol{\nabla} (\boldsymbol{\nabla} \cdot \mathbf{v}) \right) \tag{5.2}$$

$$\frac{\partial e}{\partial t} = -\boldsymbol{\nabla} \cdot (e \mathbf{v}) - P \boldsymbol{\nabla} \cdot \mathbf{v} + \eta J^2 + Q_{visc} \tag{5.3}$$

$$\frac{\partial \rho}{\partial t} = -\boldsymbol{\nabla} \cdot (\rho \mathbf{v}) \tag{5.4}$$

$$\mathbf{J} = \boldsymbol{\nabla} \times \mathbf{B} \tag{5.5}$$

$$\nabla \cdot \mathbf{B} = 0 \tag{5.6}$$

where the viscous heating term is given by

$$Q_{visc} = \mu \left(\frac{\partial v_i}{\partial x_j} \frac{\partial v_i}{\partial x_j} + \frac{\partial v_j}{\partial x_i} \frac{\partial v_i}{\partial x_j} - \frac{2}{3} (\boldsymbol{\nabla} \cdot \mathbf{v})^2 \right),$$

using the convention of summation over repeated indices. Note that this form of viscosity is appropriate for weak magnetic fields, being the form taken in the Navier-Stokes equations, but in general when the magnetic field is non-negligible the viscous stress tensor is considerably more complex due to the anisotropy of charged particle motions relative to the field [Braginskii, 1965; Hollweg, 1986]. The above form is chosen for simplicity. In most of the experiments a prescribed, spatially-uniform η and μ are used. Under the non-dimensionalisation of the above equations, in a similar way to the resistivity (which takes the form of an inverse magnetic Reynolds number $\eta = \frac{\eta_{dim}}{L V_0} = Re_m^{-1}$ (see Chapter 4)), the introduced constant kinematic viscosity ($\nu = \mu/\rho$) takes the form of an inverse plasma Reynolds number $\nu = \frac{\nu_{dim}}{L_0 V_0} = Re^{-1}$, where L_0 and V_0 are some typical length scale and velocity.

To investigate the properties of the current-vortex sheet created through twisting motions around the spine, a similar initial setup to that used in the previous chapter is used.

A rotationally symmetric linear null point with magnetic field $\mathbf{B} = B_0(-2x, y, z)$ is placed in the centre of a Cartesian box of size $\pm[0.25, 3.5, 3.5]$. Again, the grid is stretched to include more points near to the spine and fan of the null to improve the resolution of structures there. As before the plasma is assumed to be an ideal gas ($\gamma = 5/3$) which is initially at rest with a density of 1 and thermal energy $e = 5\beta^*/2$. In this case, $B_0 = 1$ is again taken but β^* increased to 0.5 to reduce compressional effects during the evolution of the KH instability (the ramifications of which will be discussed at the end). In setting $\rho = 1$ initially, the kinematic viscosity becomes the same as the dynamic viscosity ($\nu = \mu/\rho = \mu$) and so the magnetic Prandtl number (the ratio of the rates of magnetic and viscous diffusion) may be found from $Pr = \mu/\eta$.

Because of the cylindrical symmetry of this system it is convenient to define a new cylindrical coordinate system

$$\begin{aligned} \hat{\mathbf{r}} &= r\cos\theta\hat{\mathbf{y}} + r\sin\theta\hat{\mathbf{z}} \\ \hat{\boldsymbol{\theta}} &= -r\sin\theta\hat{\mathbf{y}} + r\cos\theta\hat{\mathbf{z}} \\ \hat{\mathbf{x}} &= \hat{\mathbf{x}}, \end{aligned}$$

where $r = \sqrt{y^2 + z^2}$ and $\theta = \tan^{-1}\left(\frac{z}{y}\right)$. The $\hat{\mathbf{r}}$ and $\hat{\boldsymbol{\theta}}$ directions are referred to as the radial direction and azimuthal directions respectively. In these coordinates the magnetic field becomes $\mathbf{B} = r\hat{\mathbf{r}} - 2x\hat{\mathbf{x}}$. Rotational driving on the boundaries is applied in opposite senses around each spine foot point of the form

$$v_\theta(x = \mp 0.25) = \pm V_0(t) r \left(1 + \tanh\left((1 - 36r^2)\right)\right) \tag{5.7}$$

and is ramped up from zero to a constant level through a temporal variation given by

$$V_0(t) = v_0 \tanh^2\left(\frac{t}{\tau}\right). \tag{5.8}$$

$\tau = 0.25$ is chosen to smoothly ramp the driving up from zero as a near discontinuous increase in driving has been shown to generate fast waves (in addition to the main torsional Alfvén wave) which focus on to the null [Galsgaard et al., 2003a]. As this investigation is interested in the longer term behaviour of the system the driving is ramped up slowly to avoid these effects.

Lastly, the driving (x) boundaries are again closed and line tied, whereas the side boundaries are merely closed. As this is a cylindrically symmetric system a cylindrical damping region is imposed beyond $r = 2.8$ which removes momentum in a way which

increases linearly with radius (r) to reduced reflection of waves at the boundary back into the domain. Thus, if the side boundary is taken as the edge of the damping region ($r = 2.8$) this boundary can be considered quasi-open.

Table 5.1: Summary of simulations

Case	v_0	η	μ	$Pr = \nu/\eta$	Resolution	Stable/Unstable
1	0.25	5×10^{-4}	1×10^{-4}	0.2	160^3	S
2	0.5	5×10^{-4}	1×10^{-4}	0.2	160^3	S
3	1.0	5×10^{-4}	1×10^{-4}	0.2	160^3	S
4	0.5	2×10^{-4}	1×10^{-4}	0.5	160^3	S
5	0.5	1×10^{-3}	1×10^{-4}	0.1	160^3	S
6	0.5	5×10^{-4}	1×10^{-3}	2.0	160^3	S
7	0.5	5×10^{-4}	5×10^{-4}	1.0	160^3	S
8	0.5	2×10^{-4}	1×10^{-5}	0.05	320^3	U
9	0.5	5×10^{-4}	1×10^{-5}	0.02	320^3	U
10	0.5	1×10^{-3}	1×10^{-5}	0.01	320^3	U
11	0.5	2×10^{-4}	numerical	-	320^3	U
12	0.5	5×10^{-4}	numerical	-	320^3	U
13	0.5	1×10^{-3}	numerical	-	320^3	U

5.3 Formation of the current-vortex sheet

5.3.1 Qualitative Behaviour

In this section the formation of the current-vortex sheet and its structure are discussed. As discussed in Chapter 3, several previous investigations have observed the formation of a current layer focused on the fan plane in response to rotational driving motions [Galsgaard et al., 2003a; McLaughlin et al., 2008; Pontin and Galsgaard, 2007; Pontin et al., 2011; Rickard and Titov, 1996]. In particular, Galsgaard et al. [2003a] presented linear analytical wave solutions for the torsional Alfvén and fast waves that propagate near to the null point. In general, the early stages of the simulations proceed as follows: once the driving begins a torsional Alfvén wave is launched from each boundary which spreads out as it follows the hyperbolic shape of the field toward the null. The current in the wave front increases as the length scale (perpendicular to the fan) of the wave front decreases. Once both wave fronts get close to the fan, the current diffuses into the fan plane itself creating a strong current layer. Of the studies cited above, only Galsgaard et al. [2003a] maintained the driving for long enough to see the appearance of counter rotating (i.e. against the direction of the driver) flow regions near the null. However, the focus of that investigation

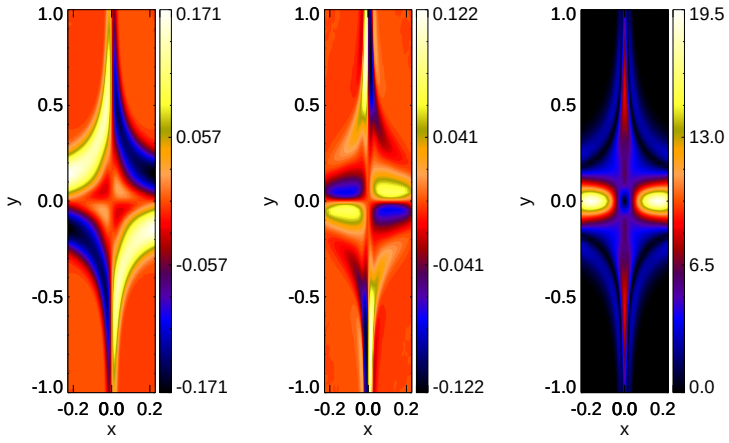

Figure 5.2: Plots viewed at $t = 2.0$ in the $z = 0$ plane for case 3. The null is at the origin, the spine along $y = 0$ and the fan at $x = 0$. Left: the velocity out of the plane (note the counter flow regions near the null), middle: the Lorentz force out of the plane, right: the current density in the plane.

was on the wave dynamics so this was not deeply investigated and no physical reason was put forward for the appearance of these flows. As these counter flows become important for the stability of the current-vortex sheet, their properties are now investigated.

5.3.2 The Counter flow

To investigate these flows a series of simulations were performed at a resolution of 160^3 for various plasma and driving profile parameters to observe the early dynamics of the system (see Table 5.1, cases 1 to 7 for details). The viscosity in these cases is chosen to be large enough that the fan plane current-vortex sheet remains stable, allowing us to focus on the formation of the counter flow regions. Figure 5.2 shows an example of the counter rotational flow that begins to form around $t = 1.8$ for case 3 (see Table 5.1). These counter rotating regions locally inhibit the velocity shear across the fan plane and produce what will be termed as a 'hole' in the vorticity layer around the null (Figure 5.3, left panel). Despite the drop in velocity shear in this region there still exists a strong shear in the magnetic field across the fan as can be seen by the strength of the current (Figure 5.3, right panel).

The formation of this vortex hole arises from the interplay of forces in the vicinity of the null. As the system is rotationally symmetric the accelerating force leading to the counter flow regions cannot come from the plasma pressure or magnetic pressure

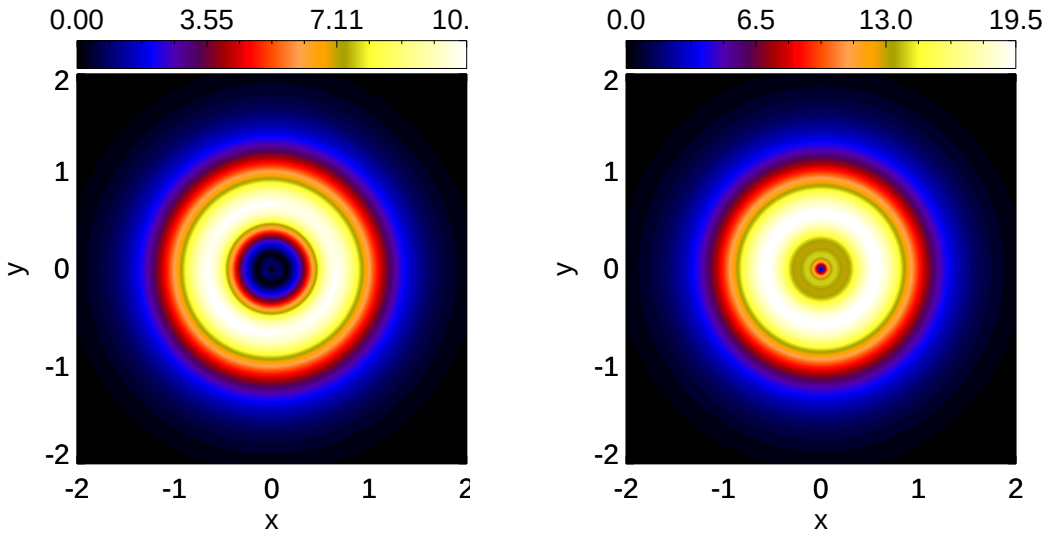

Figure 5.3: Vorticity density (left) and current density (right) in the fan plane ($x = 0$) at $t = 2.2$ for case 3.

gradients. Nor is it likely to be from viscosity terms, which act to damp plasma flows rather than accelerate them. Therefore, it must be through magnetic tension that the counter rotational acceleration of the plasma arises. Comparing the Lorentz force (identical to the magnetic tension in the observed plane) and velocity plots in Figure 5.2, it can be seen that the counter flowing plasma regions are indeed matched by similarly signed regions of magnetic tension associated with the two regions of strong current along the spine and in the fan plane (Figure 5.2, right panel).

Why such a pattern develops in the observed tension force is not clear but is likely a result of the manner in which magnetic slippage occurs within the two current regions. Certainly, as the tension force is opposite in each current concentration, it appears that a typical magnetic field line can be considered as being effectively anchored in the ideal region between the two current concentrations, with this point acting as a pivot about which the field lines want to straighten (Figure 5.4: left panel). This suggests that the foot points of field lines on the driving boundaries have become partially detached from the boundary as a result of the connection change within the strong current concentration near the spine. Were these foot points still strongly attached to the field in the volume then the magnetic field would be expected to straighten around the foot points themselves (Figure 5.4: right panel), resulting in a unidirectional tension force between the foot points and the fan plane. In any case, it is clear that the current concentration along the spine has a profound effect on the plasma dynamics near the fan plane.

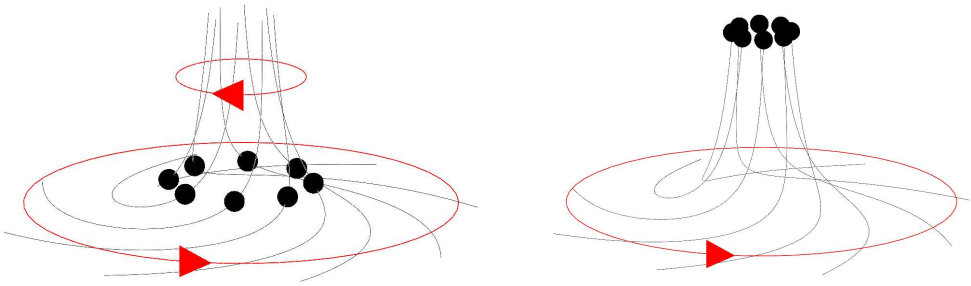

Figure 5.4: Left: Cartoon of how the different behaviour of the magnetic tension in different regions can be translated as the magnetic field trying to straighten (red arrows) about a point (black dots) along each field line that lies between the two non-ideal regions (near the spine and fan). Right: cartoon of how the field would be expected to try and straighten out were the foot points of the field lines frozen to the driving boundary.

It is found that with stronger driving (cases 1 to 3) or for lower values of resistivity (cases 2, 4 and 5) that the current build up near the spine (and therefore the magnetic tension force in this region) increases. Thus, the strength of counter flow, and therefore the size of the 'hole' in the vorticity, also increase. In addition, when η is reduced the thinning of the fan current layer combined with the hyperbolic shape of the magnetic field also widen the vorticity hole. A reduction in viscosity (cases 6 and 7) also increases the strength of the counter flows by reducing drag between the shear layers. Lastly, it should be noted that the strength of the current regions near the driving boundaries are strongly dependent upon the chosen driving profile and that other choices of rotational driving will results in different degrees of counter flow. As will be shown later, for this particular driving profile, the counter flow region plays a key role in determining the initial region of instability.

5.4 KH Instability of the Current-Vortex Sheet

5.4.1 The Shear Layer

Having discussed the formation of the current-vortex sheet at the fan surface, let us now proceed to explore its stability to the KH-type instability. Two sets of simulations were performed at a 320^3 grid resolution, see Table 5.1. For one set (cases 8 to 10) μ was set to zero and therefore viscosity is handled through numerical diffusion. This gives the least damping of any KH fluctuations for the chosen resolution and provides a benchmark against the second set (cases 11 to 13) where $\mu = 1 \times 10^{-5}$.

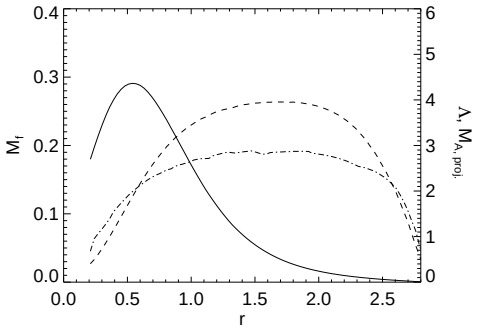

Figure 5.5: Azimuthally symmetric shear layer quantities for case 9 at $t = 5$. Solid line: the fast mode Mach number ($M_f = \Delta v/\sqrt{c_s^2 + c_A^2}$); dashed line: the projected Alfvén Mach number ($M_{A,\,proj.} = \Delta v\sqrt{\rho\mu_0}/\Delta B$) and dot-dashed line: Λ.

Within the fan plane current-vortex sheet the velocity shear is essentially azimuthal. Relative to this flow the magnetic field has two components: a strong transverse guide field component B_r associated with the initial potential null point field, and a sheared component parallel to the plasma flow (associated with the current in the layer formed in response to the boundary driving). Related to these two components can be defined two radially varying but rotationally symmetric Mach numbers:

$$M_f = \frac{\Delta v}{\sqrt{c_s^2 + c_A^2}} \quad \& \quad M_{A,\,proj.} = \frac{\Delta v\sqrt{\rho\mu_0}}{\Delta B}, \tag{5.9}$$

where Δv and ΔB are the total velocity and magnetic shear across the layer and $c_s = \sqrt{\gamma P/\rho}$ and $c_A = B/\sqrt{\rho\mu_0}$ are the radially varying sound and Alfvén speeds respectively. M_f is the fast mode Mach number related to the velocity shear and $M_{A,\,proj.}$ is the projected Alfvén Mach number associated with the sheared magnetic field component. For the KH instability, in the case of a constant perpendicular guide field, the instability is linearly stabilized at all wave numbers when $M_f > 2$ [Miura and Pritchett, 1982]. Also, using the above definition of the projected Alfvén Mach number, the transition from the tearing-type to the KH-type instability should occur around $\Lambda = \left(\frac{L_b}{L_v}\right) M_{A,\,proj.}^{2/3} = 1$ [Einaudi and Rubini, 1986]. Therefore, to excite the KH instability the driving and plasma parameters are chosen so that the layer is super-Alfvénic (in a projected sense) but sub-magnetosonic.

Figure 5.5 shows both Mach numbers along with Λ for case 9 at $t = 5$ just before any instability arises, which it can be seen falls into this category at almost all values

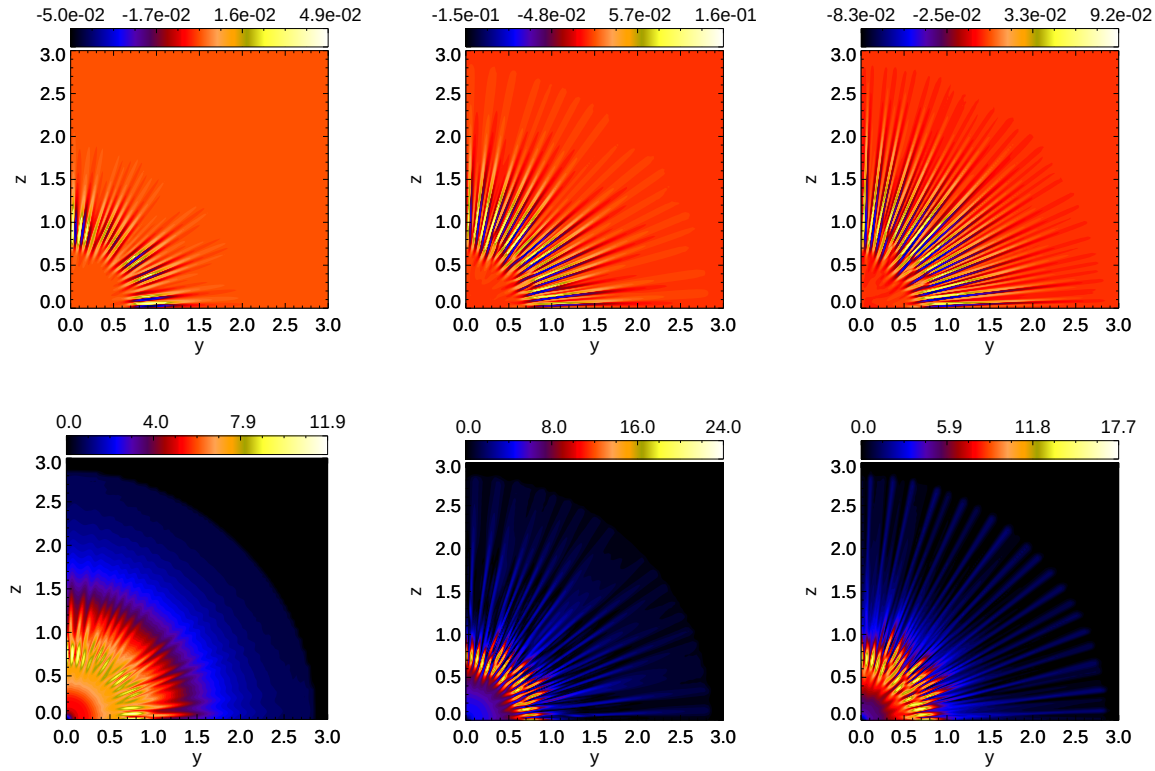

Figure 5.6: Development of the KH instability in the current sheet in case 9. Top: the velocity out of the plane ($v_x(x = 0)$). Bottom: the current density in the plane ($|\mathbf{J}|(x = 0)$). The contours are scaled to the maximum in each frame. For times $t = 7.0$ (left), 8.0 (middle) and 9.0 (right).

of r. It should be noted that the reduction in Λ beyond $r = 2.0$ is in part due to the boundary damping at $r = 2.8$, however the instability begins well away from this edge and so the boundaries affect the main evolution little. The following sections begin by first describing the growth and evolution of the KH instability in the fan plane current-vortex sheet, before briefly investigating the dependence of the shear layer and its stability on the value of resistivity.

5.4.2 Nature and Evolution of the Sheet Breakup

In this section the results of simulation 9 are described as they are representative of the general evolution of the instability in the various simulations. Generally speaking, the instability involves a filamentation of the current layer, with the formation of vortical flows in the plane of the velocity shear.

Figure 5.6 (top panels) shows the development of the KH vortices by plotting the

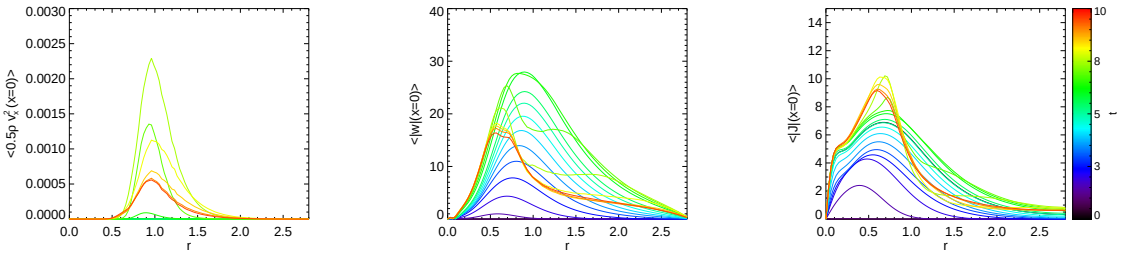

Figure 5.7: Azimuthally averaged quantities plotted as a function r in the plane $x = 0$ (the initial position of the fan plane) at different t. Left: the average perpendicular kinetic energy ($< \rho v_x^2(x = 0) >$), middle: the average vorticity density ($< |\mathbf{w}|(x = 0) >$), right: the average current density ($< |\mathbf{J}|(x = 0) >$), where $< .. >$ denotes an average over the azimuthal angle $\theta = \tan^{-1}(z/y)$.

associated component of velocity perpendicular to the $x = 0$ plane. In Figure 5.7 (left panel) this is quantified by plotting the azimuthally averaged value of $\rho v_x^2/2$ at $x = 0$ (the original position of the fan plane). From both figures it is evident that the instability initially develops at around $r = 0.9$. The vortex tubes form aligned to the radial magnetic field, thus reducing the damping effects of magnetic tension. Analysing Figure 5.7 (middle panel) it is clear that $r = 0.9$ coincides with the radial peak in vorticity. Thus, the size of the vortex hole in the fan plane (discussed above) dictates the starting point of the KH instability growth. At later times, the development of the instability then depletes the net vorticity within the current-vortex layer as the stress in the velocity flow field is dispersed by the formation of the vortical flows.

Following the guiding influence of the radial magnetic field, the vortex tubes spread outwards and inwards from the initial radius of formation. As they spread outward from the null they encounter a longer (in the $\hat{\boldsymbol{\theta}}$ direction) and thinner (in the $\hat{\mathbf{x}}$ direction) shear layer and so branch off in order to maintain a diameter approximately equal to the width of the shear layer (Figure 5.6, top right). Conversely, as they spread inwards toward the null they coalesce. Once out of the linear growth phase the KH vortices saturate as they reach the width of the shear layer and a new slowly varying state is reached.

Figure 5.8 shows how the development of the instability affects the structure of the current sheet. The instability results in a rippling or kinking of the shear layer, in the same way as described by Dahlburg et al. [1997]. In the strongly sheared stagnation point flow between each vortex a strong current layer forms. This fragments the main current sheet into filaments that lie between each of the branched off vortex tubes and appear as fingers of current in Figure 5.6 (bottom panels). This additional localisation of the current layer in the azimuthal direction naturally leads to the formation of twisted magnetic field

structures (through Ampère's law) along each current filament (Figure 5.8, bottom right panel). The circular component of these fields is, however, small in comparison with the radial guide field resulting in only a small deformation of the fan plane (black dashed line, Figure 5.8). Similar circular magnetic field structures have been observed to form between the plasma vortices in two dimensional simulations with comparatively better resolution of the shear layer (for example: Antognetti et al. [2002]; Keppens et al. [1999]). However, in the 2D scenario the magnetic tension of the field in the flow vortex leads to additional circular magnetic fields co-aligned with the vortices which is not seen here, perhaps as a result of the strong transverse field that is present.

As a result of the formation of the flow vortices, the kinetic energy within the volume is more efficiently converted to local twist within the shear layer and dissipated through ohmic heating than prior to the onset of the instability. Figure 5.10 shows this for case 9 as a drop in the volumetric kinetic energy and viscous dissipation along with an increase in ohmic dissipation during the non-linear phase (beginning around $t = 7.5$). Considering the total dissipation within the volume, it is clear that the onset of the instability has lead to a increase in the localised heating of the plasma around the fan plane.

Once the instability saturates, the layer settles down toward a new slowly changing state. In this slowly varying state no secondary instabilities of the current filaments arise but some filaments are seen to begin to coalesce through the 'zipping up' of two adjacent current branches. It was conjectured by Dahlburg and Einaudi [2002], and subsequently confirmed by Onofri et al. [2004], that a strong guide field stabilises secondary kinking instabilities, leaving a state in which the coalescence instability is the dominant mode. These results imply that this is still the case when there is a strong shear flow present. Comparing the averaged shear layer widths and strengths from before and after the onset of the instability the layer has become widened and the shear reduced (Figure 5.9). Thus, the KH instability acts as a key to the relaxation (on average) of the stress across the fan plane by allowing the system to transition to a state with a steady sharing of flux between the two topologically distinct regions.

5.4.3 Connection Change

Before going into the details of how to measure the reconnection rate in the layer it is instructive to consider whether such small scale fluctuations of the current-vortex layer actually have any effect on the global connectivity of the field around the null. Before the instability sets off, the connection change that occurs in the volume is in the form of the Torsional reconnective slippage investigated in Chapter 2. Figure 5.11 shows the manner in which this occurs. Initially the blue flux tubes (plotted from foot points on the driving

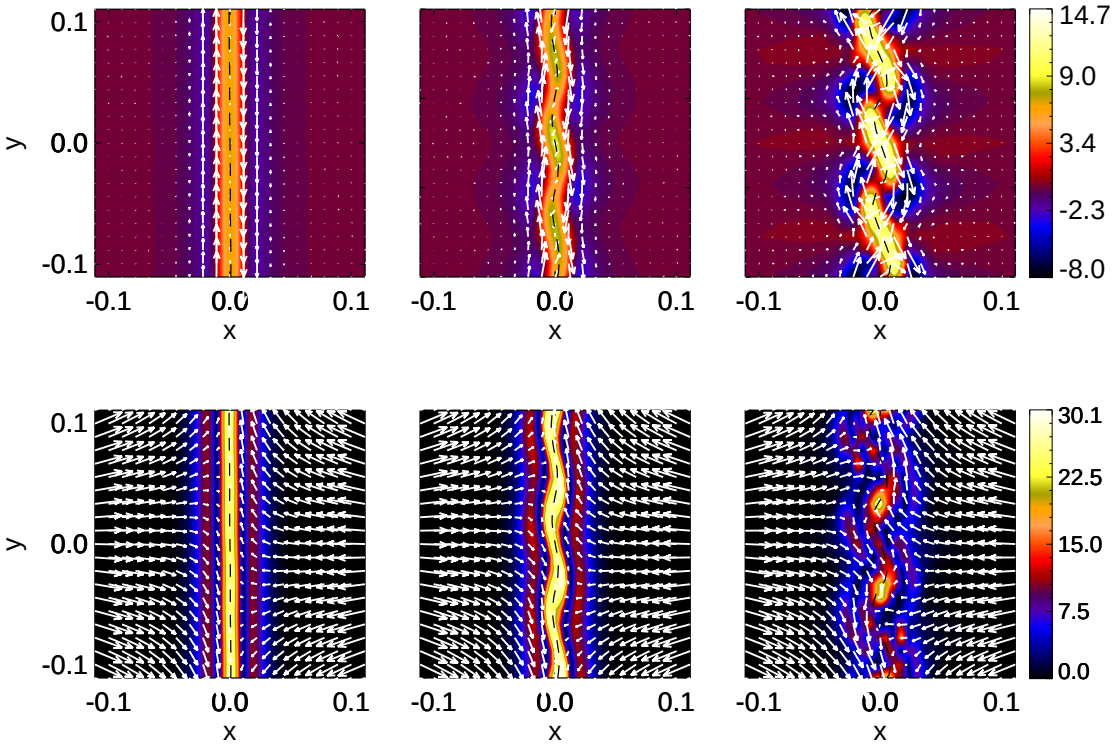

Figure 5.8: Development of the instability in the current-vortex sheet. Top: contours indicate the current out of the plane and vectors show the plasma velocity. Bottom: contours indicate vorticity density and vectors the magnetic field components in the plane. Dashed line shows the fan plane position. Taken in the plane $z = 0.85$ at $t = 6$ (left), 7 (middle) and 8 (right) for case 9.

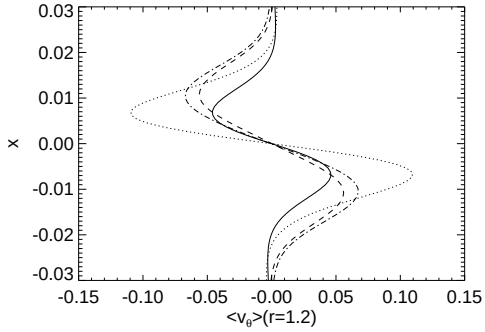

Figure 5.9: $< v_\theta >$ evaluated at $r = 1.2$ for case 8 showing the relaxation (on average) of the shear layer after the onset of the instability. Solid line: $t = 3$; dotted line: $t = 6$, dot-dashed: $t = 9$, dashed: $t = 12$. Note the reduction in shear strength and widening of the layer after the instability sets in around $t = 6$.

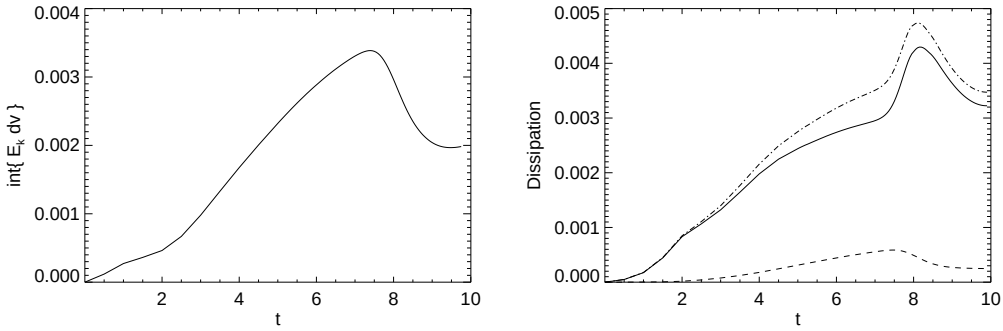

Figure 5.10: Left: $\int E_k dv$; kinetic energy integrated over the volume of the box as a function of t. Right: energy dissipation through ηJ^2 (solid) and Q_{visc} (dashed) and $\eta J^2 + Q_{visc}$ (dot-dashed) as a function of t. Both for case 9 (with $\eta = 5 \times 10^{-4}$ and $\mu = 1 \times 10^{-5}$).

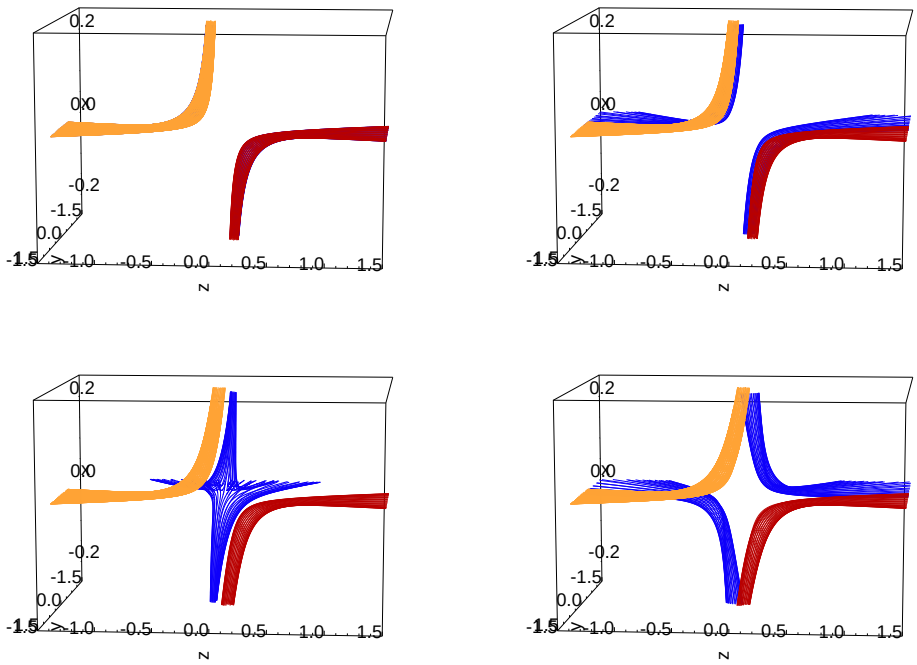

Figure 5.11: At $t = 0$ (top left) two flux tubes (red and yellow) which connect the driving boundary to the side boundaries of the numerical box are shown. At progressively later times ($t = 0.5$ (top right), $t = 1.0$ (bottom left) and $t = 1.5$ (bottom right)) the foot points of the field lines on the driving boundary are advected by the rotational driving profile and slip on to nearby field lines in a circular manner, connecting now to the blue field lines describing two different flux tubes. Note: the null is at the origin and the spine lies along the line $y = z = 0$.

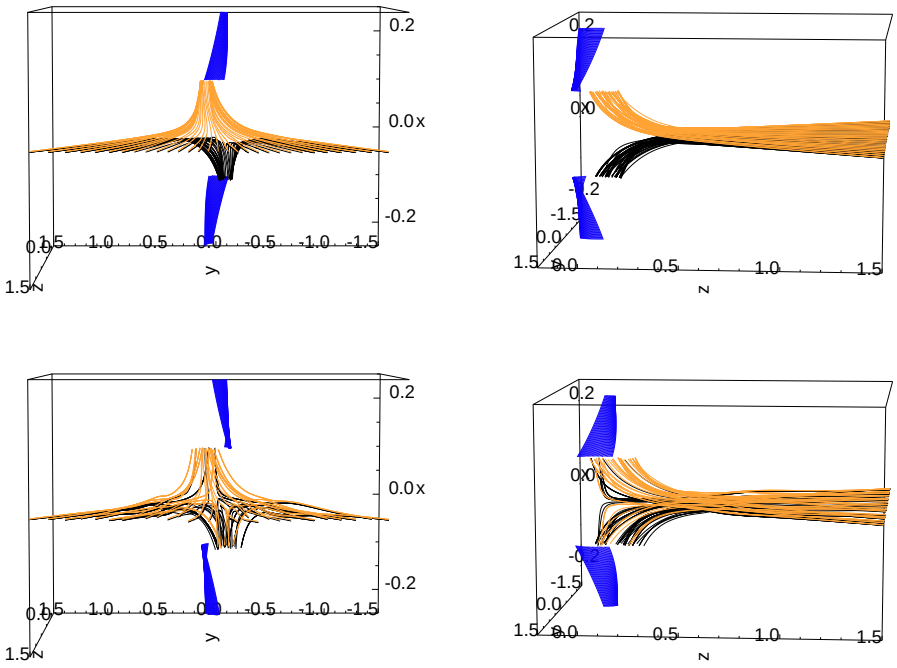

Figure 5.12: A selection of field lines traced from the boundaries of the box before (top panels: $t = 7$) and after (bottom panels: $t = 8.0$) the onset of the instability. At $t = 0$ the blue field lines are connected to the yellow/black field lines in the $x > 0/x < 0$ region but rotationally slip from them once the main current sheets form. Through the action of the KH instability many new connections are formed across the fan plane (lower panels).

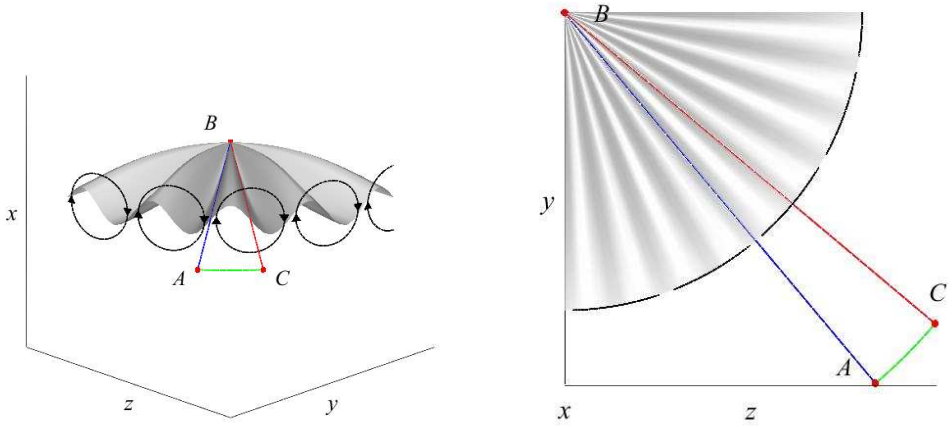

Figure 5.13: Sketch of the paths considered in Equations (5.11, 5.12) The grey isosurface shows the perturbed fan plane and the black streamlines the plasma flow. The null point sits at position B.

boundaries) are connected to the yellow and red flux tubes (plotted from the foot points on the side boundaries). Once the driving begins, the foot points of the blue field lines are advected and as the current in the associated Alfvén wave intensifies these field lines begin to slip on to their nearest neighbours in a circular manner. During this phase of the evolution no new connections are made between the topological regions separated by the fan plane, i.e. no *topological feature* reconnection occurs.

Once the instability begins, are there new connections formed between the two topological regions? Figure 5.12 shows a selection of field lines near to the fan plane just before and after the onset of the KH instability. From the bottom panels it is evident that numerous new connections *have* been made. That is, flux has been exchanged between the two topologically distinct regions. Also, the blue field lines which connect to the driving boundaries (and were initially connected to the yellow and black field lines) continue to slip on to their nearest neighbour showing that after the onset of the KH instability there is both Torsional reconnective slippage and TF reconnection across the fan plane occurring together. How do we evaluate and interpret the reconnection rate of the system in this case?

5.4.4 Reconnection Rate

To evaluate the rate that connections are changed across the fan plane it was noted that the KH vortices are very similar to the vortices that were found to occur in the general asymmetric spine reconnection examples discussed in Chapter 3. As such, a similar

approach can be utilised to quantify the rate at which flux is reconnected across the fan plane. Recall from Chapter 3 that the condition

$$\int_{\mathcal{C}} \mathbf{v} \times \mathbf{B} \cdot d\mathbf{l} = 0, \tag{5.10}$$

where $\mathcal{C}$ is some closed curve in the fan plane around the non-ideal region, implies that flux is reconnected across the fan plane in an equal and opposite manner. The interpretation of this condition in this case is that the net transfer of flux across the fan plane (as seen by the global magnetic field) is zero since each vortex flow reconnects and equal amount of magnetic flux in both directions across the fan. To quantify the *total* rate at which flux is transferred (giving the genuine rate of reconnection) the *gross* rate of flux transfer across the fan from all of the KH vortices must be evaluated. Considering one half of a given KH vortex, the rate that flux is driven across the fan plane can be found by exploiting the path independence of $\mathbf{E}$ on the fan surface (implied by Equation (5.10)) and considering the path depicted in Figure 5.13. The rate at which flux is driven across the fan plane in the ideal region by half of this vortex can be written as

$$-\int_{AC} \mathbf{v} \times \mathbf{B} \cdot d\mathbf{l} = \int_{AC} \mathbf{E} \cdot d\mathbf{l} = \int_{ABC} \mathbf{E} \cdot d\mathbf{l}, \tag{5.11}$$

where AB and BC are field lines lying in the fan surface, and so the rate of change of flux associated with half of a KH vortex, $(d\Psi/dt)_{KH}$, is given by

$$\left(\frac{d\Psi}{dt}\right)_{KH} = \int_{AB} E_{\parallel} dl - \int_{CB} E_{\parallel} dl. \tag{5.12}$$

Therefore, the reconnection rate associated with one vortex tube is double the difference between the integral of $E_{\parallel}$ along the strong current lane between two adjacent tubes (AB) and the integral of $E_{\parallel}$ through the weak current along the tube centre (CB). For the total gross rate of flux transfer across the fan plane this must then be summed over all of the vortex tubes. In the terminology of Chapter 3, this sum total quantity is the 'local' reconnection rate associated with the layer whereas the 'global' rate in this case is zero (implied by Equation (5.10)).

To evaluate this total reconnection rate in practice for each snapshot in time, $E_{\parallel}$ is integrated along a large number ($1800 \sim 3600$) of field lines in the fan plane. Each integral is evaluate between $r = 0.05$ (since field tracing at the null is numerically problematic) and $r = 2.8$ (the edge of the boundary damping region). The data is then binned to remove long wavelength modes resulting from the Cartesian grid, after which the difference

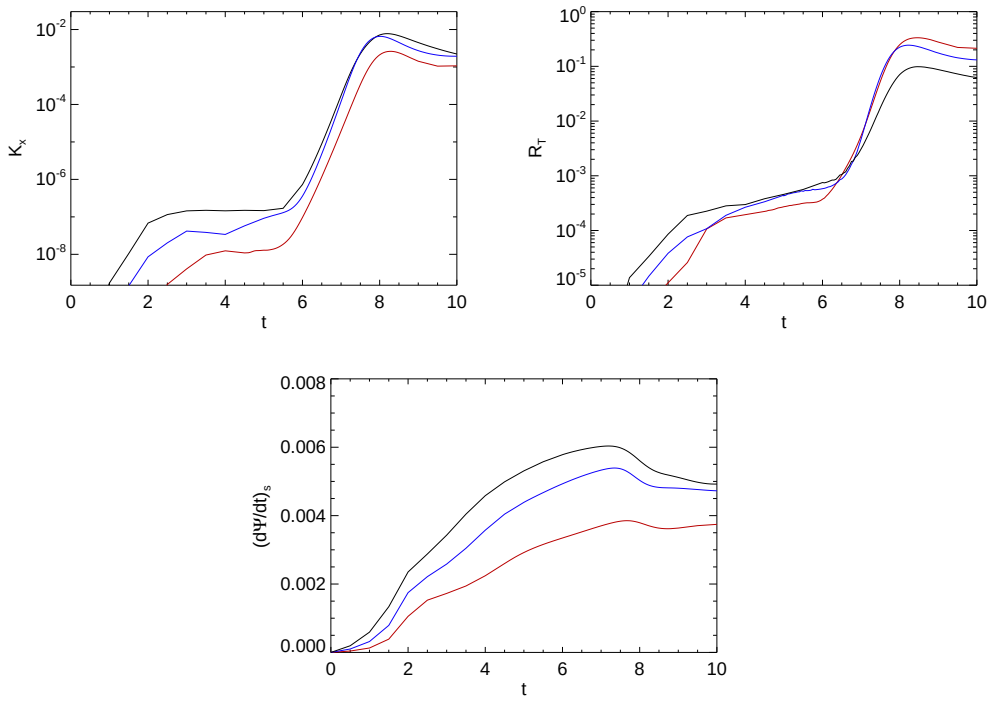

Figure 5.14: Log plots of the kinetic energy (top left panel) and the total local KH induced reconnection rate (top right panel) as a function of time. Bottom panel: the average rate of Torsional slippage ($\left(\frac{d\Psi}{dt}\right)_s$) plotted against time. For simulation runs with $\mu = 1 \times 10^{-5}$ and $\eta = 2 \times 10^{-4}$ (red), 5×10^{-4} (blue) and 1×10^{-3} (black).

between peaks and troughs is summed over the entire angular distribution. This gives an approximation to the total rate of flux transfer across the fan plane

$$R_T = \left\{ \left(\frac{d\Psi}{dt} \right)_{KH} \right\}_{total}. \tag{5.13}$$

Consider now the rate of rotational slippage occurring in the volume associated with the Torsional fan reconnection that occurs even in the absence of the instability. Prior to the instability (when the current sheets are smooth and rotationally symmetric) it was shown in Chapter 2 that the Torsional slippage rate is given by the maximum of the integral of $E_\parallel$ along all field lines threading the non-ideal current regions

$$\left(\frac{d\Psi}{dt} \right)_s = \left(\int E_\parallel dl \right)_{max}. \tag{5.14}$$

If the cylindrical symmetry of the driving is taken advantage of, the rate of rotational

reconnective slippage occurring once the fan plane current sheet has fragmented can be found. Due to this symmetry, despite the small scale fluctuations in the fan plane current-vortex sheet, the driven foot points are still smoothly rotating and thus, on average, the magnetic field must change connections in a symmetric manner to preserve this overall symmetry. Therefore, the rate of rotational slippage can be defined as the maximum of the azimuthal average of the integral of $E_{\parallel}$, i.e.

$$\left(\frac{d\Psi}{dt}\right)_s = \left(\left\langle \int E_{\parallel} dl \right\rangle\right)_{max}, \tag{5.15}$$

where $< .. >$ denotes an average over the azimuthal angle. In practice, this occurs along field lines lying asymptotically close to the spine and fan. It should be noted that this defines an overall reconnection rate, including rotational slippage both within the fan current sheet, and the large-scale current concentrations around the spine. Using these definitions the change in how flux is reconnected can be quantified as various parameters of the system are varied.

In general, in each simulation, $(d\Psi/dt)_s$ grows steadily under the action of the continued boundary driving until, at some point, the KH instability in the fan plane current-vortex layer fragments the current sheet, decreasing $(d\Psi/dt)_s$ as R_T grows rapidly. Figure 5.14 (bottom and right panels) shows this for cases 8-10 where it is clear that R_T (the local rate) rapidly grows to dwarf $(d\Psi/dt)_s$ (the global slippage rate) as a result of the recursive nature of the KH induced connection change and the large number of reconnection sites in the fan plane. Such a result should indeed be expected on the basis of the relationship between the local and global rates of the similar scenario of general asymmetric spine reconnection discussed in Chapter 3. Following the saturation of the instability, both rates of reconnection then level out as the system reaches a new equilibrium.

5.4.5 Quantitative Properties of the System

This Subsection briefly explores how the behaviour described above changes as the resistivity and viscosity of the plasma are varied. As the resistivity of astrophysical plasmas such as the solar corona is incredibly small (and therefore impossible to simulate numerically) it is important to understand how any simulated reconnecting system behaves as the resistivity is reduced. Typically, this involves finding scaling laws for parameters such as the growth rate of the instability or the peak reconnection rate. A full scaling analysis is impractical in this case, given the size of the data sets and computational power required, but a preliminary investigation of how the evolution changes as η is reduced is now presented.

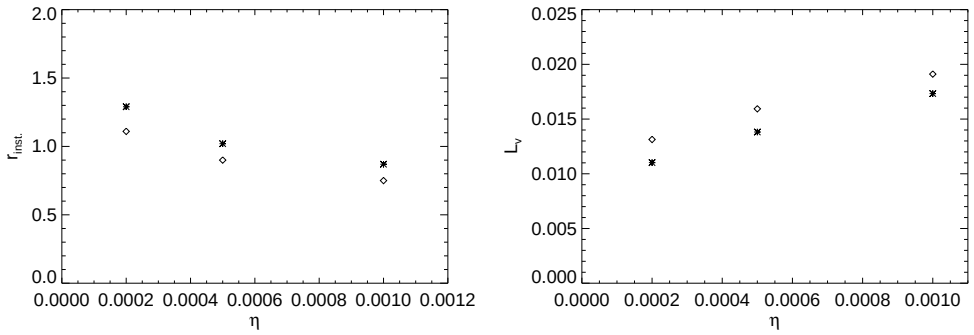

Figure 5.15: Left: the radius of initial instability growth ($r_{inst.}$). Right: the average width of the velocity shear layer between $r = 0.6$ and 2.8 (taken to be where the shear layer is well formed). Asterisks: with numerical viscosity (cases 8 to 10). Squares: $\mu = 1 \times 10^{-5}$ (cases 11 to 13).

The Current-Vortex Sheet

Let us start by considering how the properties of the current-vortex sheet change as η is varied. As η is reduced the current layer, and thus the velocity shear layer, becomes thinner. This can be seen in Figure 5.15 (right panel) which shows the mean velocity layer thickness (L_v) between $0.6 \leq r \leq 2.8$ in cases 8 to 13 at $t = 4$. As the shear layer thins, the vorticity hole becomes wider (due to the hyperbolic shape of the field) and the KH instability sets in initially at a larger radius (Figure 5.15, left panel). This suggests that at realistic coronal parameters the instability of the sheet will occur at large distances from the null but, through the spreading of its influence described in earlier sections, will still dominate a significant portion of the fan plane current-vortex sheet. In competition with the above effect, the increase in viscosity between cases 8 to 10 and 11 to 13 clearly widens the shear layer so that in more viscous fluids the vortices form closer to the null.

An important consequence of the formation of a thinner shear layer is that the number of vortices that form greatly increases (Figure 5.16). This suggests that as η is reduced and the layer thins, the associated gross flux transfer across the fan plane may increase. This will be explored further below. Lastly, at larger values of η plasma may slip through the magnetic field more readily than at lower values. Thus, as η is lowered so the relative velocity shear to magnetic shear ($M_{A,\,proj.}$) decreases. This is shown in Figure 5.17 which also shows the increasing current and vorticity density as a result of the thinning of the layer.

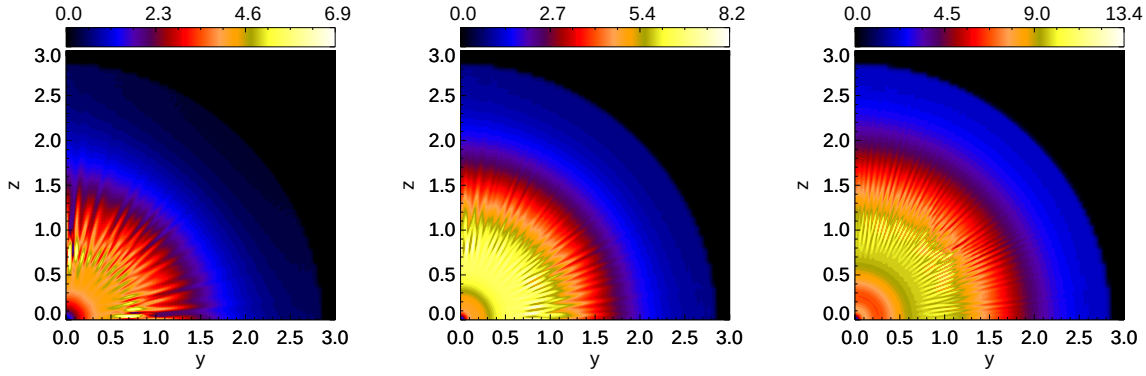

Figure 5.16: Current density in the $x = 0$ plane for cases 11 (left, at $t = 6.5$), 12 (middle, at $t = 7.0$) and 13 (right, at $t = 7.5$).

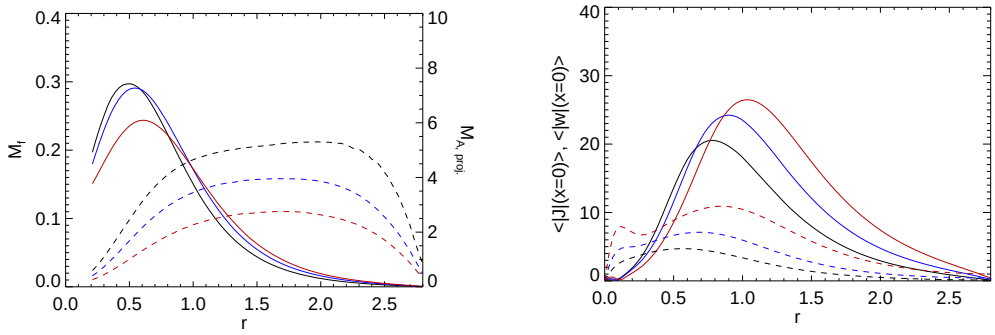

Figure 5.17: Left: how the Mach numbers vary with η (M_f: solid, $M_{A,\,proj.}$: dashed). Right: the changing vorticity (solid) and current (dashed) densities with η. For cases 8 (red), 9 (blue) and 10 (black) when $t = 4$ (prior to the instability).

The Instability: Linear Phase

Let us now consider the dependence of the properties of the instability on η and ν. From the results of previous studies [e.g. Dahlburg et al., 1997], it should be noted that the KH-type instability is expected to have no dependence upon η in the linear phase (as this phase of the evolution is ideal). However, there is an indirect influence due to the varying properties of the shear layer that forms, as discussed above. Moreover, the properties of the instability as it non-linearly saturates *will* be expected to depend upon the dissipation parameters as discussed below.

The evolution and growth of the instability of the current-vortex layer can be quantified by integrating the kinetic energy associated with the component of the flow perpendicular to the $x = 0$ plane, i.e.

$$K_x = \iint \frac{1}{2}\rho v_x^2 dy dz, \tag{5.16}$$

in the plane ($x = 0$). This can be compared with the gross rate of flux transfer across the fan surface (R_T: Equation (5.13)). As shown in Figure 5.14, both quantities exhibit an exponential growth phase during the early stages of the instability. The increase in R_T lags behind the growth of K_x as expected for a KH-type instability, since the linear phase of the instability is ideal, and initially the kinetic energy of each vortex is expended in ideally deforming the fan surface (dashed black line, Figure 5.8).

By assuming that the growth phase approximates $\sim e^{\Gamma t}$ and normalising against the Alfvén travel time across the width of the simulation box (using the Alfvén speed at the spine foot points and the distance between the x-boundaries: $t_A \approx L/c_A(x = 0.25) = 0.5/0.5 = 1$) the growth rates of K_x and R_T (Γ: kinetic energy, Γ_{R_T}: reconnection rate) relative to a typical time scale for the whole system can be compared. It should be noted, however, that as these growth rates are global quantities they inherently include many different effects (such as different dominant wave numbers, shear layer widths, Alfvén Mach numbers and magnetic and plasma Reynolds numbers between each shear layer) that can affect the growth rate of the KH instability.

Figure 5.18 (left panel) shows the growth rate of K_x for the different cases that were studied. In general, the growth rate of the instability is seen to increase as η is reduced. The exception being case 8 (with $\mu = 1 \times 10^{-5}$ and $\eta = 2 \times 10^{-4}$) where the wavelength of the dominant wave mode has likely become comparable to the viscous length scale. The growth rates of R_T follow a similar trend, but at the lowest values of η are reduced as a likely result of increased numerical diffusion leading to an underestimation of the value of η.

One of the factors affecting the growth of the instability that can be normalised against

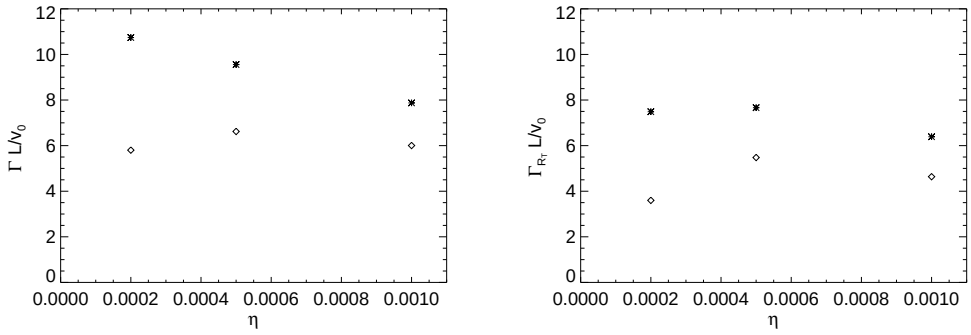

Figure 5.18: Growth rates of K_x and R_T normalised by the Alfvén travel time between the x-boundaries of the simulation box ($t_A \approx L/c_A(x = 0.25) = 0.5/0.5 = 1$) plotted against η. Asterisks: with numerical viscosity (cases 8 to 10). Squares: $\mu = 1 \times 10^{-5}$ (cases 11 to 13).

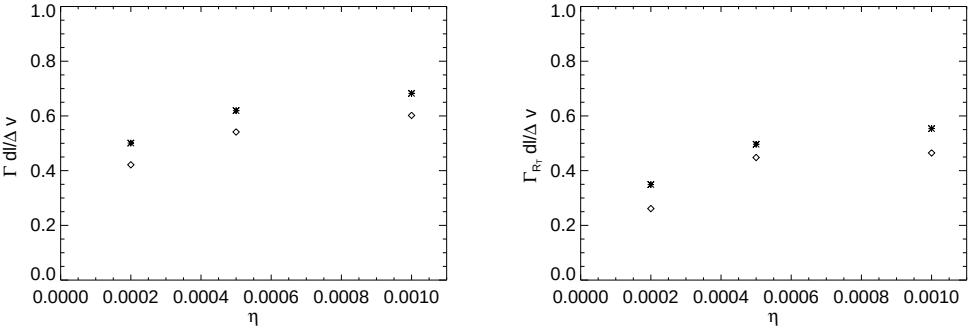

Figure 5.19: Growth rates of K_x (left) and R_T (right) normalised by the minimum travel time across the shear layer ($(L_v/dl)_{min}$) plotted against η. Asterisks: with numerical viscosity, squares: $\mu = 1 \times 10^{-5}$.

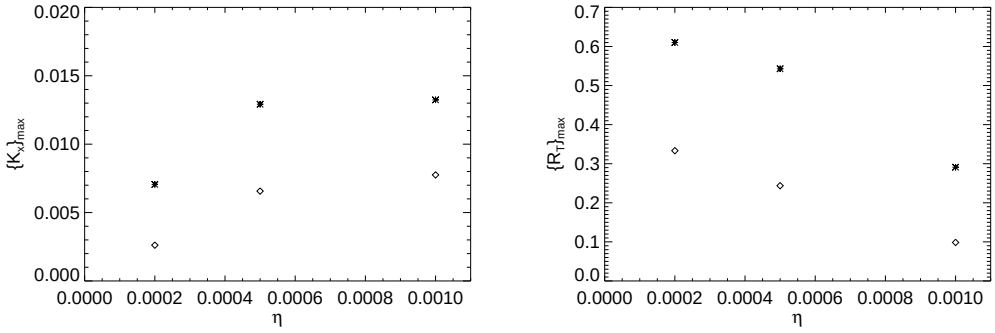

Figure 5.20: Peak values at saturation K_x (left) and R_T (right) against η. Asterisks: with numerical viscosity, squares: $\mu = 1 \times 10^{-5}$.

is the changing thickness of the shear layer. Specifically, the increase in growth rate associated with a thinner shear layer can be removed by normalising against the minimum travel time across the vortex sheet ($(L_v/\Delta v)_{min}$), taken before the onset of the instability (at $t = 4$). Figure 5.19 shows the same growth rates as in Figure 5.18 with the effect of the thinning shear layer removed. In this case, the growth rates of both quantities now decrease with decreasing η. This shows that the dominant factor in the increase in the global growth of the KH instability as η is reduced is the thinning of the shear layer. What is clear from these results is that the growth rates of both K_x and R_T are linked and that the relative strength of resistivity to viscosity (i.e. the magnetic Prandtl number) plays an important role in setting up the initial layer, and thus how fast the KH instability of the layer grows.

The Instability: Non-linear Phase

When the vortices grow to be comparable to the width of the shear layer they leave the linear phase, non-linearly saturate and reduce in amplitude. At this point both K_x and R_T peak before reaching a new steady level. Figure 5.20 shows the peak values attained. There appears to be a reduction in the peak value of K_x with decreasing η, although this may not be systematic and may be partly due to an under-resolution of the vortex structures in v_x at the smallest values of η. It could also be that the maximum energy content of the perturbation flow associated with the vortices is reduced as the non-linear phase is entered earlier with a reduction in the width of the shear layer. By contrast, the peak reconnection rate R_T increases approximately linearly as η is reduced. This surprising result arises because as η is reduced there are many extra vortex tubes produced as the shear layer thins.

Lastly, it should be noted that small scale near turbulent reconnection events around the edge of the flow vortices have been seen in 2D simulations (e.g. Keppens et al. [1999]) with $L_b \ll L_v$ to help drive the plasma circulation and alter the growth rate and saturation values of the instability. This effect is beyond what is currently available to study at the resolution of these simulations, but could also play an important role in the dynamics of the current-vortex sheet.

5.5 Summary and Discussion

In this chapter an investigation of the Torsional fan current-vortex sheet of a rotationally symmetric 3D magnetic null is presented. The aim was to study the self consistent formation of the sheet and how stable the layer was to the Kelvin-Helmholtz instability. It was

found that the formation of the current-vortex layer is complex, with local non-ideal effects brought about by strong current regions that form along the spine lines. This strongly affects the initial region of KH growth when the layer is KH unstable.

When the layer was KH unstable, the formation of the instability leads to the breakup of the planar current layer at the fan, into vortex structures in the plane of the flow and magnetic shears, consistent with earlier studies of 2 and 2.5 dimensional current-vortex sheets. Due to a combination of the field geometry and resistive and viscous diffusion, the unstable region with highly sheared magnetic and velocity fields is confined at intermediate radii from the null point. The widths and magnitudes of the current and vorticity shear layers are consistent with a KH-type instability according to the previous theory [Einaudi and Rubini, 1986]. There are a number of aspects of these simulations that point to the observed instability being of a KH-type. First, the growth of the reconnected flux (R_T) lags behind the growth of the kinetic energy of the perturbation (K_x), suggesting that in the early stages the instability is predominantly an ideal one. Furthermore, the instability is associated with a rippling or kinking of the shear layer, consistent with the KH-dominated regime in 2D as discussed by Dahlburg et al. [1997]. One new effect that was found was a 'branching' of the vortex tubes / current filaments in the direction transverse to the shear. This is an effect that arises due to the fully 3D nature of the system, in that the layer gets longer (in the azimuthal direction of the shear flow) and thinner as one moves away from the null in this transverse direction.

Once formed, it was found that the instability quickly grows to dominate the majority of the current-vortex sheet. The strong current lanes between the 'branched' vortex tubes more efficiently heat the plasma in the layer and enable a rapid recursive sharing of magnetic connections between the two previously separate topological regions. The associated connectivity change dominates over the reconnective slippage associated with the global driving flow. This shows how, subject to a smooth deformation, instabilities in the fan plane current layer of 3D null points can lead to a sudden burst of *TF* connectivity change from a system previously exhibiting only reconnective slippage. Such recursive reconnection is also a feature of reconnection between nulls connected by multiple separators [Parnell et al., 2010], however in that case there are several topological domains which come and go with time. Previous studies [e.g. Priest et al., 2005] as well as the work described in Chapter 4 have stressed the importance of separatrix surfaces as preferential sites of heating in the solar corona. The work within this chapter suggests that such heating could be significantly enhanced by the instabilities of the current-vortex sheets which form at these surfaces as described herein.

As the instability of the current-vortex sheet is strongly dependent on the driving

and plasma parameters the investigation was focused on only a small parameter range to best optimize the available resolution. Attention was concentrated on the importance of viscosity and resistivity in the dynamics of the layer. Deep investigation was hampered by the difficulty in resolving the fine scale structure following the formation of the layer, however what became clear is that both the resistivity and the viscosity of the plasma have a strong effect on the initial position, growth rate and saturation level of the KH instability in the fan plane current-vortex sheet. This is perhaps counter-intuitive since the KH instability is an ideal one, but the key point is that the properties of the shear layer itself are strongly dependent on η and ν, which means that the growth rate of the instability also is, albeit indirectly. In addition, changing other parameters would also affect the layer. For instance in 2D it is known that increasing the role of compressional effects in the plasma (by, for example, changing the plasma-β via the scaling parameter β^* or the driving speed, v_0) so that $M_f \geq 1.3$ produces shocks where the plasma is accelerated by the vortices [Miura, 1984; Shen et al., 2000]. It is not clear how these shocks would form in the fully 3D situation and what effect they would have on the reconnection process in the layer.

It should also be noted that for continued driving beyond the end of these simulations the kink instability may set in around the spine lines which would destroy the formation of the current-vortex shear layer. The growth of this instability would lead instead to a shifting of the null position and patchy reconnection across the fan plane [Pariat et al., 2009]. It is expected that the kink instability would set in sooner for systems which are more strongly driven or less resistive as more twist may build up around the spine of the null point field. This suggests that the there may only be a window in time for which the KH instability forms in the fan plane current-vortex sheet before the kink instability destroys the shear layer. It remains to be seen if at more realistic coronal parameters this window is too short for the KH instability, under these driving conditions, to be a realistic means for sudden energy release.

5.6 Conclusions

In conclusion the fragmentation via the KH instability of the Torsional fan current-vortex sheet could provide a rapid mechanism for energy release and connectivity change between the two topologically distinct regions separated by the fan separatrix surface. However, the conditions under which it occurs are rather specific and could potentially be destroyed by other instabilities. Further work is needed to determine if this mechanism is a realistic candidate for sudden energy release in parameter spaces typical of astrophysical plasmas.

However, as noted earlier the fan reconnection scenario also forms, under certain conditions, a current-vortex layer. This scenario is arguably more realistic and is not effected by the kink instability. Thus, it may be a good candidate for rapid energy release through either the tearing or KH instabilities. It is hoped that the techniques and understanding developed in this work could be used to probe this scenario more deeply in the future.

6

Summary and Future Work

"I may not have gone where I intended to go, but I think I have ended up where I needed to be."

Douglas Adams,
Dirk Gently's Holistic
Detective Agency

6.1 Summary

Three dimensional magnetic null points are now accepted as important topological features where magnetic reconnection occurs. In the last 15 years or so the theory of 3D null point reconnection has begun to be developed, although the physical understanding of the processes involved is still far behind the well developed field of 2D X-point reconnection. Therefore, the aim of this thesis was to present realistic extensions of the known ways in which 3D null point reconnection occurs to further drive our understanding of this complex subject.

As reconnection in 3D is expected to occur in regions of intense current in conjunction with locally enhanced resistivity, Chapter 2 presented an in depth investigation of the Torsional reconnection scenario using kinematic models with (for the first time) localised

current sheets in addition to locally enhanced regions of resistivity. A wealth of different reconnection scenarios were found to occur, some of which qualitatively matched what have been seen in previous numerical studies. Key findings were the appearance of counter rotational non-ideal flows, not previously seen in other analytical investigations, and a clear dependence of the reconnection rate upon the dimensions of the non-ideal regions in addition to their intensity.

Symmetric magnetic reconnection configurations are unlikely to be maintained during reconnection in astrophysical plasmas (e.g. in flaring active regions on the Sun). Therefore, the work within Chapter 3 focused on the role of asymmetry in the topological feature reconnection modes of spine and fan reconnection. When the fan reconnection current sheet is asymmetric, it was found that flux reconnects asymmetrically across the spine lines, along with a non-zero plasma flow through the null point. In contrast, for asymmetric spine reconnection there is no flow through the null point and flux is constrained to reconnect in an equal and opposite way across the fan plane. With the fan plane being a surface, the ways in which this could occur were varied and so two new definitions of reconnection rate were introduced for spine reconnection:

- *The local rate*: describing the *actual* rate at which new connections are formed across the fan plane.
- *The global rate*: describing the manner in which the global field 'sees' the new connections that have been formed.

As a compliment to Chapter 3, Chapter 4 then investigated the self consistent formation of such asymmetric current structures in the more generic case of spine-fan reconnection (when both spine and fan reconnection occur together). Time dependent effects such as the displacement of the null point and the asymmetrical spine-fan collapse were studied. By using the understanding developed in Chapter 3, the reconnection rate could also be evaluated. Two key conclusions were drawn. Firstly, that through asymmetrical spine-fan collapse, 3D magnetic null points are likely to be continually moving around in realistic astrophysical plasmas. Secondly, despite all of the dynamical effects described therein, the resistive scalings developed in the idealised symmetrically driven cases are robust (at least for weakly driven perturbations). Thus, we can be more confident of their use in interpreting reconnection in more complex magnetic topologies typical of reconnecting astrophysical plasmas.

Finally, as instabilities are thought to play a crucial role in the reconnection dynamics of complex astrophysical plasmas, Chapter 5 presented the first investigation of its kind into the self consistent formation and subsequent instability of a current-vortex sheet at

the fan plane of a 3D magnetic null. Both the formation of the layer and the time evolution of the instability were found to be complex and very situation dependent. Expanding upon the ideas developed in Chapter 3, a local reconnection rate associated with the instability was also defined. The results of this investigation show that separatrix surfaces are great potential sites for current-vortex sheet formation and therefore the additional heating and topological feature connection change associated with the subsequent instability of this layer.

In general, the work within this thesis shows the variety of connection changing scenarios afforded by the three dimensional nature of 3D magnetic null points. Fundamentally, as was highlighted towards the end of Chapter 3, each situation, be it fragmented current regions in the fan or a smooth twisted current tube along the spine, are all expressions of the same process. That is, a continuous change of connectivity, within a localised non-ideal region, as a result of a *difference in potential* along field lines threading the region. What makes 3D nulls particularly important, is the fact that their hyperbolic field shape naturally develops such non-ideal regions much more readily than most other field configurations and that their topology facilitates the formation of new connections across topological magnetic structures, which is, after all one, one of the most important aspects of reconnection in the first place.

6.2 Future Work

Although the work within this thesis has investigated the way in which reconnection occurs at 3D magnetic null points, there still remain many avenues of investigation to explore and unanswered questions to address.

Further extensions of the work presented in Chapters 2 and 3 may also provide further insight into the reconnective processes occurring at 3D nulls. For instance, a further extension of the Torsional spine solutions is permitted where the perturbation field takes the form $\mathbf{B}_p = \frac{B_0}{L_0}(0, f(r), g(r))$, which adds a symmetric shear to the fan plane field giving a component of current aligned to the azimuthal direction (along the direction of applied twist). Such a solution, along with a simulation study, could be used to study how different modes of reconnection non-linearly interact in the vicinity of 3D null points. Also, the solutions presented in Chapter 3 could be complimented by an asymmetric analytical spine-fan study using a localised resistivity of a similar form to that given by Pontin et al. [2005], with a perturbation field of the form $\mathbf{B}_p = -j(z + z^2)B_0/L_0$. Although the solutions presented in this chapter use localised currents and are therefore more realistic, the development of such a simple model might allow the study of how both asymmetric

spine and fan scenarios occur together. In addition, the development of composite solutions for the spine and fan models presented in Chapter 3 might also provide interesting new results.

The self consistent investigation, solving the full set of resistive MHD equations, presented in Chapter 4 could be extended to search for the oscillatory reconnection scenario that has been seen to occur in 2D studies. Certainly, as the reconnection rate in linear models for this process depend logarithmically on η and are therefore considered as 'fast' [Craig and McClymont, 1991], this would be an important study in the framework of 3D MHD.

There are many potential extensions of the investigation of the current-vortex sheet presented in Chapter 5 which should be considered. Firstly, the symmetry in the driving profile or the initial magnetic field should be relaxed as this is likely to have a profound effect upon the stability and formation of the current-vortex layer. The investigation of the development of turbulence and its role in the plasma heating should also be considered, although this will likely require a different numerical method, perhaps in conjunction with larger scale simulations of the layer formation. Also, in preliminary experiments it has been found that the spine-fan mode, when driven weakly, exhibits a similar instability near the null. Although the lack of symmetry in the geometry of that system leads to a considerably more complex evolution than that seen in these Torsional experiments. However, the spine-fan mode is arguably more realistic as it is less reliant upon symmetry and so the understanding gained from this study should be applied to the spine-fan case in future. Lastly, the range of parameters associated with the tearing-type regime could also be studied in both the Torsional and spine-fan cases.

Throughout all of the investigations within this thesis, the ideal evolution was broken solely through the collisional term in Ohm's law: $\eta\mathbf{J}$. Extensions of the studies within each chapter which should also be considered are to include non-ideal particle terms in Ohm's law, such as the Hall effect or electron inertia. This is particularly important as a next step, as in some astrophysical plasmas these terms actually dominate the contribution from resistive collisions and would be expected to alter the evolution and steady state configurations of both the analytical and numerical models presented herein.

Finally, the models developed in each chapter are ideally suited to be used as the starting configurations for test particle investigations of particle acceleration in the manner of Dalla and Browning [2005]. In particular, it would be interesting to see how the symmetric jets of particles found using previously symmetric spine and fan models are altered by current sheet asymmetry. Assuming that the accelerated jets of particles also exhibit a degree of asymmetry, this could help provide an understanding of the 'asymmetry in the

acceleration process in the corona' that is sometimes cited (along with other effects such as magnetic mirroring) as a means to explain the observations of asymmetric Hard X-ray (HXR) foot points in solar flares [e.g. as discussed in Yang et al., 2012].

A

Torsional Spine

A.1 Φ_{ni}

The proof for the electric potential is as follows:

$$\begin{aligned} \Phi_{ni} &= -\int \eta \mathbf{J} \cdot \mathbf{B} ds \\ &= -\eta_0 \int (J_r B_r + J_z B_z) ds \\ &= -\eta_0 (A_1 + A_2). \end{aligned} \tag{A.1}$$

Concentrating on the first term and using $zr^2 = const.$ and $ds = dr/B_r$ where $B_r = B_0 r/L_0$:

$$\begin{aligned}
A_1 &= \int J_r B_r ds \\
&= \int \frac{jB_0}{\mu_0 L_0} z^{-1} \left(-\beta + \frac{2c^6}{l^6}(zr^2)^2\right) r^\alpha (zr^2)^\beta e^{-\frac{r^2}{l^2} - \frac{c^6}{l^6}(zr^2)^2} \frac{B_0 r}{L_0} ds \\
&= \frac{jB_0^2}{\mu_0 L_0^2}(zr^2)^\beta e^{-\frac{c^6}{l^6}(zr^2)^2} \int z^{-1} \left(-\beta + \frac{2c^6}{l^6}(zr^2)^2\right) r^{\alpha+1} e^{-\frac{r^2}{l^2}} ds \\
&= \frac{jB_0^2}{\mu_0 L_0^2}(zr^2)^\beta e^{-\frac{c^6}{l^6}(zr^2)^2} \int \left(-\beta + \frac{2c^6}{l^6}(zr^2)^2\right) (zr^2)^{-1} r^{\alpha+3} e^{-\frac{r^2}{l^2}} ds \\
&= \frac{jB_0^2}{\mu_0 L_0^2}(zr^2)^{\beta-1} e^{-\frac{c^6}{l^6}(zr^2)^2} \left(-\beta + \frac{2c^6}{l^6}(zr^2)^2\right) \int r^{\alpha+3} e^{-\frac{r^2}{l^2}} ds \\
&= \frac{jB_0}{\mu_0 L_0}(zr^2)^{\beta-1} e^{-\frac{c^6}{l^6}(zr^2)^2} \left(-\beta + \frac{2c^6}{l^6}(zr^2)^2\right) \int r^{\alpha+2} e^{-\frac{r^2}{l^2}} dr \\
&= \frac{jB_0}{\mu_0 L_0}(zr^2)^{\beta-1} e^{-\frac{c^6}{l^6}(zr^2)^2} \left(-\beta + \frac{2c^6}{l^6}(zr^2)^2\right) F_l(r, \alpha+3),
\end{aligned}$$

where $F_l(x, A)$ is defined in the text. The second part is found in a similar way:

$$\begin{aligned}
A_2 &= \int J_z B_z ds \\
&= -\frac{2jB_0^2}{\mu_0 L_0^2} \int \left[(2\beta + \alpha + 1) - 2\left(\frac{r^2}{l^2} + \frac{2c^6}{l^6}(zr^2)^2\right)\right] r^{\alpha-1} (zr^2)^\beta e^{-\frac{r^2}{l^2} - \frac{c^6}{l^6}(zr^2)^2} z ds \\
&= -\frac{2jB_0^2}{\mu_0 L_0^2}(zr^2)^{\beta+1} e^{-\frac{c^6}{l^6}(zr^2)^2} \int \left[(2\beta + \alpha + 1) - 2\left(\frac{r^2}{l^2} + \frac{2c^6}{l^6}(zr^2)^2\right)\right] r^{\alpha-3} e^{-\frac{r^2}{l^2}} ds \\
&= -\frac{2jB_0}{\mu_0 L_0}(zr^2)^{\beta+1} e^{-\frac{c^6}{l^6}(zr^2)^2} \int \left[(2\beta + \alpha + 1) - 2\left(\frac{r^2}{l^2} + \frac{2c^6}{l^6}(zr^2)^2\right)\right] r^{\alpha-4} e^{-\frac{r^2}{l^2}} dr \\
&= -\frac{2jB_0}{\mu_0 L_0}(zr^2)^{\beta+1} e^{-\frac{c^6}{l^6}(zr^2)^2} \int \left[\left((2\beta + \alpha + 1) - \frac{4c^6}{l^6}(zr^2)^2\right) - 2\left(\frac{r^2}{l^2}\right)\right] r^{\alpha-4} e^{-\frac{r^2}{l^2}} dr \\
&= -\frac{2jB_0}{\mu_0 L_0}(zr^2)^{\beta+1} e^{-\frac{c^6}{l^6}(zr^2)^2} \left[\left((2\beta + \alpha + 1) - \frac{4c^6}{l^6}(zr^2)^2\right) F_l(r, \alpha-3) - \frac{2}{l^2} F_l(r, \alpha-1)\right],
\end{aligned}$$

which when combined in Equation (A.1) gives the non-ideal electric potential

$$\Phi_{ni} = \frac{j\eta_0 B_0}{\mu_0 L_0}\Bigg[\left(\beta - \frac{2c^6}{l^6}(zr^2)^2\right)F_l(r,\alpha+3)(zr^2)^{\beta-1} - \frac{4}{l^2}F_l(r,\alpha-1)(zr^2)^{\beta+1} + 2\left((\alpha+2\beta+1) - \frac{4c^6}{l^6}(zr^2)^2\right)F_l(r,\alpha-3)(zr^2)^{\beta+1}\Bigg]e^{-\frac{c^6}{l^6}(zr^2)^2}. \quad \text{(A.2)}$$

A.2 Reconnection Rate

To find the reconnection rate requiers the electric potentials evaluated at $r = 0$ and $r \to \infty$. Using the new variable $\epsilon = zr^2$ they are given by

$$\Phi_{in,out} = \Phi_{ni.}(r \to 0, \infty) = \frac{j\eta_0 B_0}{\mu_0 L_0}\Bigg[\left(\beta - \frac{2c^6}{l^6}\epsilon^2\right)C_1\epsilon^{\beta-1} - \frac{4}{l^2}C_2\epsilon^{\beta+1} + 2\left((\alpha+2\beta+1) - \frac{4c^6}{l^6}\epsilon^2\right)C_3\epsilon^{\beta+1}\Bigg]e^{-\frac{c^6}{l^6}\epsilon^2}, \quad \text{(A.3)}$$

where

$$C_1 = \lim_{r\to 0,\infty} F_l(r,\alpha+3) \quad \& \quad C_2 = \lim_{r\to 0,\infty} F_l(r,\alpha-1) \quad \& \quad C_3 = \lim_{r\to 0,\infty} F_l(r,\alpha-3). \quad \text{(A.4)}$$

To evaluate each of these requieres the knowledge of the behaviour of the $F_l(x,A)$ function as $x \to 0$ and ∞. In general this function follows the recurrence relation

$$F_l(x,A+2) = \frac{l^2}{2}\left(AF_l(x,A) - x^A e^{-\frac{x^2}{l^2}}\right). \quad \text{(A.5)}$$

In the both limits this becomes

$$F_l(x,A+2) = \frac{l^2}{2}AF_l(x,A). \quad \text{(A.6)}$$

Using this, C_1 and C_2 can be expressed in terms of C_3 as

$$C_1 = \left(\frac{l^2}{2}\right)^3(\alpha+1)(\alpha-1)(\alpha-3)C_3 \quad \& \quad C_2 = \frac{l^2}{2}(\alpha-3)C_3. \quad \text{(A.7)}$$

When the argument of $F_l(x, A)$ is odd it can be iterated to find a general relationship as follows:

$$\begin{aligned} F_l(x, 2n+1) &= \frac{l^2}{2}(2n-1)F_l(x, 2n-1) \\ &= \left(\frac{l^2}{2}\right)^2 (2n-1)(2n-3)F_l(x, 2n-3) \\ &= \left(\frac{l^2}{2}\right)^3 (2n-1)(2n-3)(2n-5)F_l(x, 2n-5) \\ &\vdots \\ F_l(x, 2n+1) &= \left(\frac{l^2}{2}\right)^n \prod_{m=0}^{n-1} (2(n-m)-1)F_l(1). \end{aligned} \tag{A.8}$$

Along with the asymptotic value of $F(1)$ as $x \to 0$ and ∞ this becomes

$$F_l(x, 2n+1) = \begin{cases} \sqrt{\pi}\left(\frac{l^2}{2}\right)^{n+1} \prod_{m=0}^{n-1}(2(n-m)-1), & x \to \infty \\ 0, & x \to 0 \end{cases}. \tag{A.9}$$

The reconnection rate in general is given by the maximum in ϵ of $|\Phi_{in} - \Phi_{out}|$. Using the above expressions and defining $\alpha = 2n + 4$ this then becomes in general

$$\begin{aligned} \frac{d\Psi}{dt} &= \max\Bigg\{\Bigg[\left(\beta - \frac{2c^6}{l^6}\epsilon^2\right)\epsilon^{\beta-1}\left(\frac{l^2}{2}\right)^3 (2n+5)(2n+3)(2n+1) \\ &\quad -\frac{4}{l^2}\epsilon^{\beta+1}\left(\frac{l^2}{2}\right)(2n+1) + 2\left((2n+2\beta+5) - \frac{4c^6}{l^6}\epsilon^2\right)\epsilon^{\beta+1}\Bigg] e^{-\frac{c^6}{l^6}\epsilon^2} \\ &\times \quad \left(\frac{j\eta_0 B_0}{\mu_0 L_0}\right)\sqrt{\pi}\left(\frac{l^2}{2}\right)^{n+1}\prod_{m=0}^{n-1}(2(n-m)-1)\Bigg\}. \end{aligned} \tag{A.10}$$

B

Torsional Fan

B.1 Φ_{ni}

The proof for the electric potential is as follows:

$$\begin{aligned} \Phi_{ni} &= -\int \eta \mathbf{J} \cdot \mathbf{B} ds \\ &= -\eta_0 \int (J_r B_r + J_z B_z) ds \\ &= -\eta_0 (A_1 + A_2). \end{aligned} \tag{B.1}$$

Concentrating on the first term and using $zr^2 = const.$ and $ds = dz/B_z$ where $B_z = -2B_0 z/L_0$:

$$\begin{aligned}
A_1 &= \int J_r B_r ds \\
&= -\int \frac{jB_0}{\mu_0 L_0}\left((\gamma+\beta) - 2\left(\frac{z^2}{l^2} + \frac{c^6}{l^6}(zr^2)^2\right)\right) r z^{\gamma-1}(zr^2)^\beta \mathrm{e}^{-\frac{z^2}{l^2}-\frac{c^6}{l^6}(zr^2)^2}\frac{B_0 r}{L_0} ds \\
&= -\frac{jB_0^2}{\mu_0 L_0^2}(zr^2)^\beta \mathrm{e}^{-\frac{c^6}{l^6}(zr^2)^2}\int\left((\gamma+\beta) - 2\left(\frac{z^2}{l^2} + \frac{c^6}{l^6}(zr^2)^2\right)\right) r^2 z^{\gamma-1}\mathrm{e}^{-\frac{z^2}{l^2}} ds \\
&= -\frac{jB_0^2}{\mu_0 L_0^2}(zr^2)^{\beta+1} \mathrm{e}^{-\frac{c^6}{l^6}(zr^2)^2}\int\left((\gamma+\beta) - 2\left(\frac{z^2}{l^2} + \frac{c^6}{l^6}(zr^2)^2\right)\right) z^{\gamma-2}\mathrm{e}^{-\frac{z^2}{l^2}} ds \\
&= \frac{jB_0}{2\mu_0 L_0}(zr^2)^{\beta+1} \mathrm{e}^{-\frac{c^6}{l^6}(zr^2)^2}\int\left((\gamma+\beta) - 2\left(\frac{z^2}{l^2} + \frac{c^6}{l^6}(zr^2)^2\right)\right) z^{\gamma-3}\mathrm{e}^{-\frac{z^2}{l^2}} dz \\
&= \frac{jB_0}{2\mu_0 L_0}(zr^2)^{\beta+1} \mathrm{e}^{-\frac{c^6}{l^6}(zr^2)^2}\int\left(\left((\gamma+\beta) - \frac{2c^6}{l^6}(zr^2)^2\right) - \frac{2z^2}{l^2}\right) z^{\gamma-3}\mathrm{e}^{-\frac{z^2}{l^2}} dz \\
&= \frac{jB_0}{2\mu_0 L_0}(zr^2)^{\beta+1} \mathrm{e}^{-\frac{c^6}{l^6}(zr^2)^2}\left(\left((\gamma+\beta) - \frac{2c^6}{l^6}(zr^2)^2\right) F_l(z,\gamma-2) - \frac{2}{l^2}F_l(z,\gamma)\right),
\end{aligned}$$

where $G(A)$ is defined in the text. The second part is found in a similar way:

$$\begin{aligned}
A_2 &= \int J_z B_z ds \\
&= -\frac{2jB_0^2}{\mu_0 L_0^2}\int\left(2(1+\beta) - \frac{4c^6}{l^6}(zr^2)^2\right) z^\gamma (zr^2)^\beta \mathrm{e}^{-\frac{z^2}{l^2}-\frac{c^6}{l^6}(zr^2)^2} z ds \\
&= -\frac{2jB_0^2}{\mu_0 L_0^2}(zr^2)^\beta \mathrm{e}^{-\frac{c^6}{l^6}(zr^2)^2}\int\left(2(1+\beta) - \frac{4c^6}{l^6}(zr^2)^2\right) z^{\gamma+1}\mathrm{e}^{-\frac{z^2}{l^2}} ds \\
&= \frac{jB_0}{\mu_0 L_0}(zr^2)^\beta \mathrm{e}^{-\frac{c^6}{l^6}(zr^2)^2}\int\left(2(1+\beta) - \frac{4c^6}{l^6}(zr^2)^2\right) z^\gamma \mathrm{e}^{-\frac{z^2}{l^2}} dz \\
&= \frac{jB_0}{\mu_0 L_0}(zr^2)^\beta \mathrm{e}^{-\frac{c^6}{l^6}(zr^2)^2}\left(2(1+\beta) - \frac{4c^6}{l^6}(zr^2)^2\right) F_l(z,\gamma+1).
\end{aligned}$$

Both combined lead to

$$\begin{aligned}
\Phi_{ni} = -\frac{j\eta_0 B_0}{\mu_0 L_0}\Bigg[&\frac{zr^2}{2}\left(\left((\gamma+\beta) - \frac{2c^6}{l^6}(zr^2)^2\right) F_l(z,\gamma-2) - \frac{2}{l^2}F_l(z,\gamma)\right) \\
&+ \left(2(\beta+1) - \frac{4c^6}{l^6}(zr^2)^2\right) F_l(z,\gamma+1)\Bigg](zr^2)^\beta e^{-\frac{c^6}{l^6}(zr^2)^2}. \qquad \text{(B.2)}
\end{aligned}$$

B.2 Reconnection Rate

To find the reconnection rate for torsional fan, in addition to the limit of $F(x,A)$ as $x \to \infty, 0$ when A is odd, the behaviour when A is even is requiered.

$$\begin{aligned} F_l(x,2n+2) &= \frac{l^2}{2}(2n)F_l(x,2n) \\ &= \left(\frac{l^2}{2}\right)^2 (2n)(2(n-1))F_l(x,2(n-1)) \\ &= \left(\frac{l^2}{2}\right)^3 (2n)(2(n-1))(2(n-2))F_l(x,2(n-2)) \\ &\vdots \\ F_l(x,2n+2) &= \left(\frac{l^2}{2}\right)^n \prod_{m=0}^{n-1}(2(n-m))F_l(2). \end{aligned} \tag{B.3}$$

Along with the asymptotic values of $F(x,2)$ in the limits $x \to 0$ and ∞ this becomes

$$F_l(x,2n+2) = \begin{cases} 0, & x \to \infty \\ -\left(\frac{l^2}{2}\right)^{n+1} \prod_{m=0}^{n-1}(2(n-m)), & x \to 0 \end{cases}. \tag{B.4}$$

The ingoing and outgoing potentials are found in the limits $z \to \infty$ and 0 respectively. Using the variable $\epsilon = zr^2$ and re-expressing γ as $2n+3$ these can be expressed as

$$\begin{aligned} \Phi_{in,out} = \;& \Phi_{ni.}(z \to \infty, 0) \\ &= -\frac{j\eta_0 B_0}{\mu_0 L_0}\left[\frac{\epsilon}{2}\left(\left((2n+3+\beta) - \frac{2c^6}{l^6}\epsilon^2\right)C_1 - \frac{2}{l^2}C_2\right)\right. \\ &\quad + \left.\left(2(\beta+1) - \frac{4c^6}{l^6}\epsilon^2\right)C_3\right]\epsilon^\beta e^{-\frac{c^6}{l^6}\epsilon^2}, \end{aligned} \tag{B.5}$$

where

$$C_1 = \lim_{z\to 0,\infty} F_l(z,2n+1) \quad \& \quad C_2 = \lim_{z\to 0,\infty} F_l(z,2n+3) \quad \& \quad C_3 = \lim_{z\to 0,\infty} F_l(z,2n+4). \tag{B.6}$$

Using the recurrance relation in these limits when A is odd (defined in Appendix A.2) C_2 can be expressed in terms of C_1 as

$$C_2 = \frac{l^2}{2}(2n+2)C_1. \tag{B.7}$$

Using this and the asymtotic values of $F(x,A)$ when A is both even and odd gives

$$\begin{aligned}
\Phi_{in} &= -\frac{j\eta_0 B_0}{\mu_0 L_0}\left[\frac{\epsilon}{2}\left(\left((2n+3+\beta)-\frac{2c^6}{l^6}\epsilon^2\right)-(2n+2)\right)\right]\epsilon^\beta e^{-\frac{c^6}{l^6}\epsilon^2} \\
&\quad\times\quad \sqrt{\pi}\left(\frac{l^2}{2}\right)^{n+1}\prod_{m=0}^{n-1}(2(n-m)-1) \\
\Phi_{out} &= \frac{j\eta_0 B_0}{\mu_0 L_0}\left(2(\beta+1)-\frac{4c^6}{l^6}\epsilon^2\right)\epsilon^\beta e^{-\frac{c^6}{l^6}\epsilon^2}\left(\frac{l^2}{2}\right)(2n+2)\left[\left(\frac{l^2}{2}\right)^{n+1}\prod_{m=0}^{n-1}(2(n-m))\right] \\
&= \frac{j\eta_0 B_0}{\mu_0 L_0}\left(2(\beta+1)-\frac{4c^6}{l^6}\epsilon^2\right)\epsilon^\beta e^{-\frac{c^6}{l^6}\epsilon^2}\left(\frac{l^2}{2}\right)^{n+2}\prod_{m=-1}^{n-1}(2(n-m)),
\end{aligned} \tag{B.8}$$

from which the reconnection rate is given by $|\Phi_{out}-\Phi_{in}|_{max}$.

$$\begin{aligned}
\frac{d\Psi}{dt} &= \max\Bigg\{\left[\frac{\epsilon}{2}\left(\left((2n+3+\beta)-\frac{2c^6}{l^6}\epsilon^2\right)-(2n+2)\right)\frac{\sqrt{\pi}l^2}{2}\prod_{m=0}^{n-1}(2(n-m)-1)\right. \\
&\quad+\quad\left.\left(2(\beta+1)-\frac{4c^6}{l^6}\epsilon^2\right)\left(\frac{l^2}{2}\right)^2\prod_{m=-1}^{n-1}(2(n-m))\right]\frac{j\eta_0 B_0}{\mu_0 L_0}\left(\frac{l^2}{2}\right)^n\epsilon^\beta e^{-\frac{c^6}{l^6}\epsilon^2}\Bigg\}.
\end{aligned}$$

C

Asymmetric Fan

C.1 $\Phi_{ni.}$

The magnetic field perurbation in the general asymmetric case is given by

$$f(x,z) = -\frac{jB_0}{L_0} z e^{-\frac{z^2}{h^2} - \frac{(zx^2)^2}{l^6}} g(z). \tag{C.1}$$

Using equation 2.3 the current associated with this field is given by

$$J_x = \frac{jB_0}{L_0\mu_0}\left(\left(1-\frac{z^2}{h^2}-\frac{(zx^2)^2}{l^6}\right)g(z)+zg'(z)\right)e^{-\frac{z^2}{h^2}-\frac{(zx^2)^2}{l^6}} \tag{C.2}$$

$$J_y = 0 \tag{C.3}$$

$$J_z = \frac{jB_0}{L_0\mu_0}\left(\frac{4(zx^2)^2}{l^6}zx^{-1}g(z)\right)e^{-\frac{z^2}{h^2}-\frac{(zx^2)^2}{l^6}}. \tag{C.4}$$

Along with the magnetic field this is fed into Equation (2.7) to find the non-ideal electric potential by using that $ds = dz/B_z$ where $B_z = -2B_0z/L_0$ and that $zx^2 = z_0x_0^2$ and $zY^2 = z_0Y_0^2$ as follows:

$$\begin{aligned}\Phi_{ni} &= -\int \eta\mathbf{J}\cdot\mathbf{B}ds \\ &= -\eta_0\int e^{-\frac{\left(zY^2\right)^2}{l^2}}(J_xB_x+J_zB_z)ds \\ &= -\eta_0 e^{-\frac{\left(zY^2\right)^2}{l^2}}\int (J_xB_x+J_zB_z)ds \\ &= -\eta(A_1+A_2).\end{aligned} \tag{C.5}$$

Starting with the first term gives

$$\begin{aligned}A_1 &= \int J_xB_xds \\ &= \int \frac{jB_0}{L_0\mu_0}\left(\left(1-\frac{z^2}{h^2}-\frac{(zx^2)^2}{l^6}\right)g(z)+zg'(z)\right)e^{-\frac{z^2}{h^2}-\frac{(zx^2)^2}{l^6}}\frac{B_0x}{L_0}ds \\ &= -\frac{jB_0}{L_0\mu_0}\int\left(\left(1-\frac{z^2}{h^2}-\frac{(zx^2)^2}{l^6}\right)g(z)+zg'(z)\right)e^{-\frac{z^2}{h^2}-\frac{(zx^2)^2}{l^6}}x\frac{dz}{2z} \\ &= -\frac{jB_0}{L_0\mu_0}\int\left(\left(1-\frac{z^2}{h^2}-\frac{(zx^2)^2}{l^6}\right)g(z)+zg'(z)\right)e^{-\frac{z^2}{h^2}-\frac{(zx^2)^2}{l^6}}\frac{(zx^2)^{\frac{1}{2}}}{2}z^{-\frac{3}{2}}dz \\ &= -\frac{jB_0}{L_0\mu_0}\frac{(zx^2)^{\frac{1}{2}}}{2}e^{-\frac{(zx^2)^2}{l^6}}\int\left(\left(1-\frac{z^2}{h^2}-\frac{(zx^2)^2}{l^6}\right)g(z)+zg'(z)\right)z^{-\frac{3}{2}}e^{-\frac{z^2}{h^2}}dz \\ &= -\frac{jB_0}{L_0\mu_0}\frac{xz^{\frac{1}{2}}}{2}e^{-\frac{(zx^2)^2}{l^6}}\int\left(\left(1-\frac{(zx^2)^2}{l^6}-\frac{z^2}{h^2}\right)g(z)+zg'(z)\right)z^{-\frac{3}{2}}e^{-\frac{z^2}{h^2}}dz \\ &= -\frac{jB_0}{L_0\mu_0}\frac{x}{2}e^{-\frac{(zx^2)^2}{l^6}}\left(\left(1-\frac{(zx^2)^2}{l^6}\right)I_{-3}(z)-\frac{1}{h^2}I_1(z)+K_{-1}(z)\right),\end{aligned}$$

where

$$I_a(z) = z^{\frac{1}{2}} \int z^{\frac{a}{2}} e^{-\frac{z^2}{h^2}} g(z) dz \quad \& \quad K_a(z) = z^{\frac{1}{2}} \int z^{\frac{a}{2}} e^{-\frac{z^2}{h^2}} g'(z) dz. \tag{C.6}$$

Similarly, the second term gives

$$\begin{aligned}
A_2 &= \int J_z B_z ds \\
&= \int \frac{jB_0}{L_0\mu_0} \left(\frac{4(zx^2)^2}{l^6} zx^{-1} g(z) \right) e^{-\frac{z^2}{h^2} - \frac{(zx^2)^2}{l^6}} \frac{-2B_0 z}{L_0} ds \\
&= -2\frac{jB_0^2}{L_0^2\mu_0} \int \left(\frac{4(zx^2)^2}{l^6} zx^{-1} g(z) \right) e^{-\frac{z^2}{h^2} - \frac{(zx^2)^2}{l^6}} z ds \\
&= -8\frac{jB_0^2}{L_0^2\mu_0} \frac{(zx^2)^2}{l^6} e^{-\frac{(zx^2)^2}{l^6}} \int zx^{-1} g(z) e^{-\frac{z^2}{h^2}} z ds \\
&= -8\frac{jB_0^2}{L_0^2\mu_0} \frac{(zx^2)^2}{l^6} e^{-\frac{(zx^2)^2}{l^6}} \int z^{\frac{3}{2}} (zx^2)^{-\frac{1}{2}} g(z) e^{-\frac{z^2}{h^2}} z ds \\
&= -8\frac{jB_0^2}{L_0^2\mu_0} \frac{(zx^2)^{\frac{3}{2}}}{l^6} e^{-\frac{(zx^2)^2}{l^6}} \int z^{\frac{3}{2}} g(z) e^{-\frac{z^2}{h^2}} z \frac{dz}{-2z} \frac{L_0}{B_0} \\
&= 4\frac{jB_0}{L_0\mu_0} \frac{(zx^2)^{\frac{3}{2}}}{l^6} e^{-\frac{(zx^2)^2}{l^6}} \int z^{\frac{3}{2}} g(z) e^{-\frac{z^2}{h^2}} dz \\
&= 4\frac{jB_0}{L_0\mu_0} \frac{zx^3}{l^6} e^{-\frac{(zx^2)^2}{l^6}} I_3(z).
\end{aligned}$$

Combining all of the above gives the general asymmetric non-ideal electric potential

$$\Phi_{ni} = \frac{j\eta_0 B_0}{\mu_0 L_0} x \left[\frac{1}{2} \left(1 - \frac{2}{l^6}(zx^2)^2 \right) I_{-3}(z) - \frac{1}{h^2} I_1(z) - \frac{4}{l^6} zx^2 I_3(z) + \frac{1}{2} K_{-1}(z) \right] e^{-\frac{z^2(x^4+Y^4)}{l^6}}. \tag{C.7}$$

In the symmetric case $g(z) = 1$ so that $g'(z) = 0$ and therefore $K_{-1}(z) = 0$. In this case the integrals can be solved analytically to give

$$\Phi_{ni} = -\frac{j\eta_0 B_0}{\mu_0 L_0} [a + b + c] x e^{-\frac{z^2}{h^2} - \frac{z^2(x^2+Y^2)}{l^6}}, \tag{C.8}$$

where

$$a = \left(1 - \frac{2}{l^6}(zx^2)^2\right)(2b+1), \tag{C.9}$$

$$b = \frac{8}{21}\frac{z^4}{h^4}M\left(1, \frac{11}{4}, \frac{z^2}{h^2}\right) + \frac{2}{3}\frac{z^2}{h^2}, \tag{C.10}$$

$$c = \frac{8}{5l^6}z^4x^2M\left(1, \frac{9}{4}, \frac{z^2}{h^2}\right). \tag{C.11}$$

C.2 Numerical Solutions for $I_a(z)$

To find the numerical solutions of $I_{-3}(z)$, $I_1(z)$ and $I_3(z)$ when

$$g(z) = 1 + m\,\mathrm{erf}\left(\frac{z}{p}\right), \tag{C.12}$$

we note that near $z = 0$, $g(z) \approx 1 + \frac{2mz}{\sqrt{\pi}p}$. Using this form for $g(z)$ an analytical solution for each of the I functions can be found that is valid in the vicinity of $z = 0$. From these it is found that there is no contribution at $z = 0$ to the symmetric ($m = 0$) solutions from the error function in $g(z)$. Therefore, the values of our unknown functions at $z = 0$ are given by each $m = 0$ solution evaluated at this point:

$$I_{-3}(0) = -2, \quad I_1(0) = 0, \quad I_3(0) = 0. \tag{C.13}$$

The domain is then discretised over $z \in [-3, 3]$ and each value is used as the initial value for a fourth order Runge-Kutta scheme which intergrates out in both the positive and negative directions to obtain the function over the entire domain.

This is straightforward for the integrals $I_1(z)$ and $I_3(z)$, however, for $I_{-3}(z)$ the singular nature of the $z^{\frac{a+1}{2}}$ term in Equation (3.14) makes numerical solutions near $z = 0$ difficult to obtain. In this case the transform $z = 1/t$ is used so that the system to be solved in this case becomes

$$\frac{dI_{-3}(t)}{dt} = -\frac{1}{2t}I_{-3}(t) - \frac{1}{t}e^{-\frac{1}{t^2l^2}}\left(1 + m\,\mathrm{erf}\left(\frac{1}{tp}\right)\right), \tag{C.14}$$

which is solved over the domain $t \in [-200, 1/3] \cup [1/3, 200]$ with the initial condition applied on $t = \pm 200$ (equivalent to $z = \pm 0.005$ which is taken to be suitably close to

$z = 0$ to apply the boundary condition, since the function varies slowly in this region). The singular region of this equation now lies outside the domain of interest (at $t = 0$, equivalent to $z = \pm\infty$) and so can be numerically evaluated where we desire it. This is then inverted to give $I_{-3}(z)$.

D

General Solution for Symmetric Spine

In general solutions may be constructed with the choice of

$$F(r,\phi) = jf(\phi)r^{\alpha/2}e^{-r^{\alpha}/h^{\alpha}}. \tag{D.1}$$

In this case

$$Z = z - \frac{j}{B_0}\frac{f(\phi)}{r^2}\int r^{\frac{\alpha}{2}+1}e^{-\frac{r^{\alpha}}{l^{\alpha}}}dr, \tag{D.2}$$

and the electric potential is given by

$$\Phi = -\frac{j\eta_0\sqrt{\pi}h^{\frac{\alpha}{2}}}{\alpha\mu_0}f^{'}(\phi)\,\mathrm{erf}\left(\frac{r^{\frac{\alpha}{2}}}{h^{\frac{\alpha}{2}}}\right)e^{-\frac{(Zr^2)^2}{k^6}}. \tag{D.3}$$

This general model may also be extended in a similar way to general asymmetric cases through setting $h = h(\phi)$. The choice of $\alpha = 2$ gives a constant current at the null and is the one that is choosen to be investigated further in the text. Choices of $\alpha < 2$ result in singular currents and so are non-physical, whereas choices of $\alpha > 2$ have zero current at the null. These solutions are better suited to modeling higher mode spine solutions such as with $f(\phi) = \sin(m\phi)$ where $m = 2, 3, 4....$ These solutions can be considered the kinematic extension of the higher m mode exact solutions of Craig and Fabling [1996] to include a localised resistivity. As these modes have no current at the null they are generally considered less likely in practise and so these solutions are not pursued further.

E

Asymmetric Spine

E.1 $\Phi_{ni.}$

The proof for the non-ideal electric potential is as follows: the magnetic field perturbation for the general asymmetric spine case is given by

$$F(r,\phi) = \frac{jB_0}{L_0} f(\phi) r e^{-\frac{r^2}{h(\phi)^2}}, \tag{E.1}$$

from which the current components are found from Equation (2.3) as

$$J_r = \frac{jB_0}{L_0\mu_0}\left(f'(\phi)+2r^2f(\phi)\frac{h'(\phi)}{h(\phi)^3}\right)e^{-\frac{r^2}{h(\phi)^2}} \tag{E.2}$$

$$J_\phi = -\frac{jB_0}{L_0\mu_0}f(\phi)\left(1-2\frac{r^2}{h(\phi)^2}\right)e^{-\frac{r^2}{h(\phi)^2}} \tag{E.3}$$

$$J_z = 0. \tag{E.4}$$

This is fed into Equation (2.7) to give

$$\begin{aligned}
\Phi_{ni} &= -\int \eta\mathbf{J}\cdot\mathbf{B}ds \\
&= -\eta_0 e^{-\frac{(Zr^2)^2}{k^6}}\int J_rB_rds \\
&= -\eta\int J_rdr \\
&= -\eta\int\frac{jB_0}{L_0\mu_0}\left(f'(\phi)+2r^2f(\phi)\frac{h'(\phi)}{h(\phi)^3}\right)e^{-\frac{r^2}{h(\phi)^2}}dr \\
&= -\frac{jB_0\eta}{L_0\mu_0}\int\left(f'(\phi_0)+2r^2f(\phi_0)\frac{h'(\phi_0)}{h(\phi_0)^3}\right)e^{-\frac{r^2}{h(\phi_0)^2}}dr \\
&= -\frac{jB_0\eta}{L_0\mu_0}\left(f'(\phi_0)\int e^{-\frac{r^2}{h(\phi_0)^2}}dr+2f(\phi_0)\frac{h'(\phi_0)}{h(\phi_0)^3}\int r^2e^{-\frac{r^2}{h(\phi_0)^2}}dr\right) \\
&= -\frac{j\eta B_0}{\mu_0L_0}\left[\frac{\sqrt{\pi}h(\phi_0)}{2}f'(\phi_0)\,\mathrm{erf}\left(\frac{r}{h(\phi_0)}\right)\right. \\
&\quad + \left. 2f(\phi_0)\frac{h'(\phi_0)}{h(\phi_0)}\left(-\frac{r}{2}e^{-\frac{r^2}{h(\phi_0)^2}}+\frac{h(\phi_0)\sqrt{\pi}}{4}\,\mathrm{erf}\left(\frac{r}{h(\phi_0)}\right)\right)\right],
\end{aligned}$$

which then gives the non-ideal electric potential as

$$\begin{aligned}
\Phi_{ni} &= -\frac{j\eta B_0}{\mu_0L_0}\left[\frac{\sqrt{\pi}h(\phi)}{2}f'(\phi)\,\mathrm{erf}\left(\frac{r}{h(\phi)}\right)\right. \\
&\quad - \left. 2f(\phi)\frac{h'(\phi)}{h(\phi)}\left(\frac{r}{2}e^{-\frac{r^2}{h(\phi)^2}}-\frac{h(\phi)\sqrt{\pi}}{4}\,\mathrm{erf}\left(\frac{r}{h(\phi)}\right)\right)\right].
\end{aligned} \tag{E.5}$$

E.2 Reconnection Rate

The non-ideal electric potential in the limit of $r \gg L$ is given by:

$$\Phi_{ni} = -\frac{j\eta B_0\sqrt{\pi}}{2\mu_0}\frac{L}{L_0}\left(1 + 2m\sin(\phi)\right)\cos\phi. \tag{E.6}$$

To find the reconnection rate the values of all maxima and minima of this function are requiered. These occur where

$$\begin{aligned}
0 &= \frac{d}{d\phi}\left[(1 + 2m\sin(\phi))\cos\phi\right] \\
&= \frac{d}{d\phi}\left(\cos\phi + m\sin(2\phi)\right) \\
&= -\sin\phi + 2m\cos(2\phi) \\
&= -\sin\phi + 2m(1 - 2\sin^2(\phi)) \\
&= -\sin\phi + 2m - 4m\sin^2(\phi) \\
&= 4m\sin^2(\phi) + \sin\phi - 2m.
\end{aligned}$$

The solution of which is given by solving

$$\sin\phi = -\frac{1}{8m} \pm \frac{1}{2}\sqrt{\frac{1}{16m^2} + 2}. \tag{E.7}$$

When $m = 0$ this reduces to $\sin\phi = 0, -\infty$ and therefore $\phi = 0, \pi$ (giving the maximum and minimum respectively) as is expected from the symmetric case. As m is increased from 0, two real solutions exist of the form $\phi = \phi_1, \pi - \phi_1$ up to $m = 0.5$ (when $\phi_1 = \pi/6$) where a thrid solution arises at $\phi = 3\pi/2$ which is a point of inflection. Beyond $m = 0.5$ a bifurcation developes from this point of inflection creating an additional maxima and minima in the electric potential and two new flux transfer regions. In general, when $m \leq 0.5$ the reconnection rate is then found from the difference of the non-ideal potentials

evaluated at the maximum and mimimum

$$(\Phi_{ni})_{max} = -\frac{j\eta B_0\sqrt{\pi}}{2\mu_0}\frac{L}{L_0}\left(1+2m\sin(\phi_1)\right)\cos\phi_1 \tag{E.8}$$

$$\begin{aligned}(\Phi_{ni})_{min} &= -\frac{j\eta B_0\sqrt{\pi}}{2\mu_0}\frac{L}{L_0}\left(1+2m\sin(\pi-\phi_1)\right)\cos(\pi-\phi_1)\\ &= \frac{j\eta B_0\sqrt{\pi}}{2\mu_0}\frac{L}{L_0}\left(1+2m\sin(\phi_1)\right)\cos\phi_1,\end{aligned} \tag{E.9}$$

giving

$$\frac{d\Psi}{dt} = \frac{j\eta_0 B_0\sqrt{\pi}}{\mu_0}\frac{L}{L_0}\left(1+2m\sin(\phi_1)\right)\cos\phi_1, \tag{E.10}$$

with ϕ_1 the smallest positive solution of

$$\sin\phi_1 = -\frac{1}{8m} \pm \frac{1}{2}\sqrt{\frac{1}{16m^2}+2.} \tag{E.11}$$

References

M. Abramowitz and I. A. Stegun. *Handbook of mathematical functions with formulas, graphs, and mathematical tables*. Dover, 1965. 52

A. K. Al-Hachami and D. I. Pontin. Magnetic reconnection at 3D null points: effect of magnetic field asymmetry. *A&A*, 512:A84, March 2010. doi: 10.1051/0004-6361/200913002. 74

H. Alfvén. Existence of Electromagnetic-Hydrodynamic Waves. *Nature*, 150:405–406, October 1942. doi: 10.1038/150405d0. 5

V. Angelopoulos, J. McFadden, D. Larson, C. Carlson, S. Mende, H. Frey, T. Phan, D. Sibeck, K. Glassmeier, U. Auster, E. Donovan, I. Mann, J. Rae, C. Russell, A. Runov, X. Zhou, and L. Kepko. Tail Reconnection Triggering Substorm Onset. *AGU Fall Meeting Abstracts*, page C3, December 2008. 3

S. K. Antiochos, C. R. DeVore, and J. A. Klimchuk. A Model for Solar Coronal Mass Ejections. *ApJ.*, 510:485–493, January 1999. doi: 10.1086/306563. 2, 110

A. Antognetti, G. Einaudi, and R. B. Dahlburg. Transonic and subsonic dynamics of the current-vortex sheet. *Physics of Plasmas*, 9:1575–1583, May 2002. doi: 10.1063/1.1460881. 124

V. Archontis and A. W. Hood. Formation of Ellerman bombs due to 3D flux emergence. *A&A*, 508:1469–1483, December 2009. doi: 10.1051/0004-6361/200912455. 2

G. Aulanier, E. E. DeLuca, S. K. Antiochos, R. A. McMullen, and L. Golub. The Topology and Evolution of the Bastille Day Flare. *ApJ.*, 540:1126–1142, September 2000. doi: 10.1086/309376. 13

D. N. Baker, T. I. Pulkkinen, V. Angelopoulos, W. Baumjohann, and R. L. McPherron. Neutral line model of substorms: Past results and present view. *J. Geophys. Res.*, 101: 12975–13010, June 1996. doi: 10.1029/95JA03753. 3

M. A. Berger. Rigorous new limits on magnetic helicity dissipation in the solar corona. *Geophysical and Astrophysical Fluid Dynamics*, 30:79–104, September 1984. doi: 10.1080/03091928408210078. 11

W. Blumen. Shear layer instability of an inviscid compressible fluid. *Journal of Fluid Mechanics*, 40:769–781, 1970. doi: 10.1017/S0022112070000435. 112

S. I. Braginskii. Transport Processes in a Plasma. *Reviews of Plasma Physics*, 1:205, 1965. 115

D. S. Brown, C. E. Parnell, E. E. Deluca, L. Golub, and R. A. McMullen. The Magnetic Structure of a Coronal X-Ray Bright Point. *Sol. Phys.*, 201:305–321, July 2001. doi: 10.1023/A:1017907406350. 2

T. N. Bungey, V. S. Titov, and E. R. Priest. Basic topological elements of coronal magnetic fields. *A&A*, 308:233–247, April 1996. 9

H. Carmichael. A Process for Flares. *NASA Special Publication*, 50:451, 1964. 2

P. A. Cassak and M. A. Shay. Scaling of asymmetric magnetic reconnection: General theory and collisional simulations. *Phys. of Plasmas*, 14:102114–+, 2007. doi: 10.1063/1.2795630. 49, 56

S. Chandrasekhar. *Hydrodynamic and hydromagnetic stability*. Clarendon Press, Oxford, 1961. 112

X. L. Chen and P. J. Morrison. Resistive tearing instability with equilibrium shear flow. *Physics of Fluids B*, 2:495–507, March 1990. doi: 10.1063/1.859339. 112, 114

A.R. Choudhuri. *The physics of fluids and plasmas: an introduction for astrophysicists*. Cambridge University Press, 1998. 3, 112

S. W. H. Cowley. A qualitative study of the reconnection between the Earth's magnetic field and an interplanetary field of arbitrary orientation. *Radio Science*, 8:903, 1973. doi: 10.1029/RS008i011p00903. 14

I. J. D. Craig and R. B. Fabling. Exact Solutions for Steady State, Spine, and Fan Magnetic Reconnection. *ApJ.*, 462:969, May 1996. doi: 10.1086/177210. 15, 52, 59, 69, 75, 103, 162

I. J. D. Craig and R. B. Fabling. Dynamic magnetic reconnection in three space dimensions: Fan current solutions. *Phys. of Plasmas*, 5:635–644, March 1998. doi: 10.1063/1.872754. 15, 96

I. J. D. Craig and A. N. McClymont. Dynamic magnetic reconnection at an X-type neutral point. *Astrophys. J. Lett*, 371:L41–L44, April 1991. doi: 10.1086/185997. 96, 108, 144

I. J. D. Craig and P. G. Watson. Optimized magnetic reconnection solutions in three dimensions. *Sol. Phys.*, 194:251–268, June 2000. 15

I. J. D. Craig and P. G. Watson. Magnetic Reconnection Solutions Based on a Generalized Ohm's law. *Sol. Phys.*, 214:131–150, May 2003. 15

I. J. D. Craig, R. B. Fabling, J. Heerikhuisen, and P. G. Watson. Magnetic Reconnection Solutions in the Presence of Multiple Nulls. *ApJ.*, 523:838–848, October 1999. doi: 10.1086/307750. 15

R. B. Dahlburg and G. Einaudi. The compressible plane current-vortex sheet. *Physics of Plasmas*, 7:1356–1365, May 2000. doi: 10.1063/1.873952. 113

R. B. Dahlburg and G. Einaudi. MHD unstable modes in the 3D evolution of 2D MHD structures and the diminished role of coalescence instabilities. *Physics Letters A*, 294: 101–107, February 2002. doi: 10.1016/S0375-9601(02)00027-0. 113, 124

R. B. Dahlburg, P. Boncinelli, and G. Einaudi. The evolution of plane current-vortex sheets. *Physics of Plasmas*, 4:1213–1226, May 1997. doi: 10.1063/1.872301. 113, 123, 134, 137

S. Dalla and P. K. Browning. Particle acceleration at a three-dimensional reconnection site in the solar corona. *A&A*, 436:1103–1111, June 2005. doi: 10.1051/0004-6361:20042589. 144

E. M. de Gouveia dal Pino and A. Lazarian. Production of the large scale superluminal ejections of the microquasar GRS 1915+105 by violent magnetic reconnection. *A&A*, 441:845–853, October 2005. doi: 10.1051/0004-6361:20042590. 3

P. Démoulin and E. Pariat. Modelling and observations of photospheric magnetic helicity. *Advances in Space Research*, 43:1013–1031, April 2009. doi: 10.1016/j.asr.2008.12.004. 12

J. C. Dorelli, A. Bhattacharjee, and J. Raeder. Separator reconnection at Earth's dayside magnetopause under generic northward interplanetary magnetic field conditions. *J. Geophys. Res.*, 112:A02202, February 2007. doi: 10.1029/2006JA011877. 12, 108

J.W. Dungey. Lxxvi. conditions for the occurrence of electrical discharges in astrophysical systems. *Philosophical Magazine Series 7*, 44(354):725–738, 1953. doi: 10.1080/14786440708521050. URL http://www.tandfonline.com/doi/abs/10.1080/14786440708521050. 7

G. Einaudi and F. Rubini. Resistive instabilities in a flowing plasma. I - Inviscid case. *Physics of Fluids*, 29:2563–2568, August 1986. doi: 10.1063/1.865548. 112, 113, 121, 137

G. Einaudi and F. Rubini. Resistive instabilities in a flowing plasma. II - Effects of viscosity. *Physics of Fluids B*, 1:2224–2228, November 1989. doi: 10.1063/1.859038. 113

C. R. Evans and J. F. Hawley. Simulation of magnetohydrodynamic flows - A constrained transport method. *ApJ.*, 332:659–677, September 1988. doi: 10.1086/166684. 79

A. Ferrari. Modeling Extragalactic Jets. *Ann. Rev. Astron. Astrophys.*, 36:539–598, 1998. doi: 10.1146/annurev.astro.36.1.539. 114

L. Fletcher, T. R. Metcalf, D. Alexander, D. S. Brown, and L. A. Ryder. Evidence for the Flare Trigger Site and Three-Dimensional Reconnection in Multiwavelength Observations of a Solar Flare. *ApJ.*, 554:451–463, June 2001. doi: 10.1086/321377. 13

T. G. Forbes. Reconnection Theory for Flares (Invited). In R. D. Bentley and J. T. Mariska, editors, *Magnetic Reconnection in the Solar Atmosphere*, volume 111 of *Astronomical Society of the Pacific Conference Series*, page 259, 1997. 2

C. Foullon, E. Verwichte, V. M. Nakariakov, K. Nykyri, and C. J. Farrugia. Magnetic Kelvin-Helmholtz Instability at the Sun. *Astrophys. J. Lett.*, 729:L8, 2011. doi: 10.1088/2041-8205/729/1/L8. 114

A. Frank, T. W. Jones, D. Ryu, and J. B. Gaalaas. The Magnetohydrodynamic Kelvin-Helmholtz Instability: A Two-dimensional Numerical Study. *ApJ.*, 460:777, April 1996. doi: 10.1086/177009. 113

H. P. Furth, J. Killeen, and M. N. Rosenbluth. Finite-Resistivity Instabilities of a Sheet Pinch. *Physics of Fluids*, 6:459–484, 1963. doi: 10.1063/1.1706761. 113

K. Galsgaard and Å. Nordlund. Heating and activity of the solar corona. 3. Dynamics of a low beta plasma with three-dimensional null points. *J. Geophys. Res.*, 102:231–248, January 1997. doi: 10.1029/96JA02680. 79, 80

K. Galsgaard and D. I. Pontin. Current accumulation at an asymmetric 3D null point caused by generic shearing motions. *A&A*, 534:A2, October 2011a. doi: 10.1051/0004-6361/201117532. 50

K. Galsgaard and D. I. Pontin. Steady state reconnection at a single 3D magnetic null point. *A&A*, 529:A20, May 2011b. doi: 10.1051/0004-6361/201014359. 15, 81, 85, 89, 96

K. Galsgaard, E. R. Priest, and V. S. Titov. Numerical experiments on wave propagation towards a 3D null point due to rotational motions. *J. Geophys. Res.*, 108:1042, January 2003a. doi: 10.1029/2002JA009393. 15, 21, 27, 30, 38, 39, 45, 46, 116, 117

K. Galsgaard, V. S. Titov, and T. Neukirch. Magnetic Pinching of Hyperbolic Flux Tubes. II. Dynamic Numerical Model. *ApJ.*, 595:506–516, September 2003b. doi: 10.1086/377258. 16

C. Gontikakis, V. Archontis, and K. Tsinganos. Observations and 3D MHD simulations of a solar active region jet. *A&A*, 506:L45–L48, November 2009. doi: 10.1051/0004-6361/200913026. 2

T. Gray, V.S. Lukin, M.R. Brown, and C. D. Cothran. Three-dimensional reconnection and relaxation of merging spheromak plasmas. *Phys. of Plasmas*, 17:102106, 2010. 12

J. M. Greene. Geometrical properties of three-dimensional reconnecting magnetic fields with nulls. *J. Geophys. Res.*, 93:8583–8590, August 1988. doi: 10.1029/JA093iA08p08583. 108

H. Hasegawa, M. Fujimoto, T.-D. Phan, H. Rème, A. Balogh, M. W. Dunlop, C. Hashimoto, and R. TanDokoro. Transport of solar wind into Earth's magnetosphere through rolled-up Kelvin-Helmholtz vortices. *Nature*, 430:755–758, 2004. doi: 10.1038/nature02799. 113

R. J. Hastie. Sawtooth Instability in Tokamak Plasmas. *Astrophys. Space Sci.*, 256:177–204, 1997. 3

J. Heerikhuisen and I. J. D. Craig. Magnetic Reconnection in Three Dimensions - Spine, Fan and Separator Solutions. *Sol. Phys.*, 222:95–114, July 2004. doi: 10.1023/B:SOLA.0000036878.13759.68. 61

M. Hesse and K. Schindler. A theoretical foundation of general magnetic reconnection. *J. Geophys. Res.*, 93:5559–5567, June 1988. doi: 10.1029/JA093iA06p05559. 10, 16, 31

T. Hirayama. Theoretical Model of Flares and Prominences. I: Evaporating Flare Model. *Sol. Phys.*, 34:323–338, February 1974. doi: 10.1007/BF00153671. 2

J. V. Hollweg. Viscosity and the Chew-Goldberger-Low equations in the solar corona. *ApJ.*, 306:730–739, July 1986. doi: 10.1086/164382. 115

G. Hornig and E. Priest. Evolution of magnetic flux in an isolated reconnection process. *Physics of Plasmas*, 10:2712–2721, July 2003. doi: 10.1063/1.1580120. 10, 16, 17, 22, 23, 31, 52, 74

G. Hornig and K. Schindler. Magnetic topology and the problem of its invariant definition. *Physics of Plasmas*, 3:781–791, March 1996. doi: 10.1063/1.871778. 7, 10

J M Hyman. A method of lines approach to the numerical solution of conservation laws. In *Advances in Computer Methods for Partial Differential Equations III, R. Vichnevetsky and R.S. Stepleman (Eds), IMACS*, 1979. 80

R. Keppens, G. Tóth, R. H. J. Westermann, and J. P. Goedbloed. Growth and saturation of the Kelvin-Helmholtz instability with parallel and antiparallel magnetic fields. *Journal of Plasma Physics*, 61:1–19, January 1999. doi: 10.1017/S0022377898007223. 113, 124, 136

R. A. Kopp and G. W. Pneuman. Magnetic reconnection in the corona and the loop prominence phenomenon. *Sol. Phys.*, 50:85–98, October 1976. doi: 10.1007/BF00206193. 2

S. Landi and L. Bettarini. Three-Dimensional Simulations of Magnetic Reconnection with or Without Velocity Shears. *Space Science Rev.*, page 295, October 2011. doi: 10.1007/s11214-011-9824-6. 113

Y. T. Lau and J. M. Finn. Three-dimensional kinematic reconnection in the presence of field nulls and closed field lines. *ApJ.*, 350:672–691, February 1990. doi: 10.1086/168419. 13, 14, 24

W. Liu, T. E. Berger, A. M. Title, T. D. Tarbell, and B. C. Low. Chromospheric Jet and Growing "Loop" Observed by Hinode: New Evidence of Fan-spine Magnetic Topology Resulting from Flux Emergence. *ApJ.*, 728:103, February 2011. doi: 10.1088/0004-637X/728/2/103. 13, 109

D. W. Longcope. Topological Methods for the Analysis of Solar Magnetic Fields. *Living Reviews in Solar Physics*, 2:7, November 2005. 9

D. W. Longcope and C. E. Parnell. The Number of Magnetic Null Points in the Quiet Sun Corona. *Sol. Phys.*, 254:51–75, January 2009. doi: 10.1007/s11207-008-9281-x. 12

V. S. Lukin and M. G. Linton. Three-dimensional magnetic reconnection through a moving magnetic null. *Nonlinear Processes in Geophys.*, 18(6):871–882, 2011. doi: 10.5194/npg-18-871-2011. 94

B. J. Lynch, S. K. Antiochos, C. R. DeVore, J. G. Luhmann, and T. H. Zurbuchen. Topological Evolution of a Fast Magnetic Breakout CME in Three Dimensions. *ApJ.*, 683:1192–1206, August 2008. doi: 10.1086/589738. 13

R. C. Maclean, C. E. Parnell, and K. Galsgaard. Is Null-Point Reconnection Important for Solar Flux Emergence? *Sol. Phys.*, 260:299–320, December 2009. doi: 10.1007/s11207-009-9458-y. 108

A. Malagoli, G. Bodo, and R. Rosner. On the Nonlinear Evolution of Magnetohydrodynamic Kelvin-Helmholtz Instabilities. *ApJ.*, 456:708, January 1996. doi: 10.1086/176691. 113

S. Masson, E. Pariat, G. Aulanier, and C. J. Schrijver. The Nature of Flare Ribbons in Coronal Null-Point Topology. *ApJ.*, 700:559–578, July 2009. doi: 10.1088/0004-637X/700/1/559. 13

A. Masters, N. Achilleos, M. G. Kivelson, N. Sergis, M. K. Dougherty, M. F. Thomsen, C. S. Arridge, S. M. Krimigis, H. J. McAndrews, S. J. Kanani, N. Krupp, and A. J. Coates. Cassini observations of a Kelvin-Helmholtz vortex in Saturn's outer magnetosphere. *J. Geophys. Res. (Space Phys)*, 115:A07225, 2010. doi: 10.1029/2010JA015351. 113

J. A. McLaughlin, J. S. L. Ferguson, and A. W. Hood. 3D MHD Coronal Oscillations about a Magnetic Null Point: Application of WKB Theory. *Solar Phys.*, 251:563–587, 2008. doi: 10.1007/s11207-007-9107-2. 117

J. A. McLaughlin, I. De Moortel, A. W. Hood, and C. S. Brady. Nonlinear fast magnetoacoustic wave propagation in the neighbourhood of a 2D magnetic X-point: oscillatory reconnection. *A&A*, 493:227–240, January 2009. doi: 10.1051/0004-6361:200810465. 108, 109

J. A. McLaughlin, I. de Moortel, and A. W. Hood. Phase mixing of nonlinear visco-resistive Alfvén waves. *A&A*, 527:A149, March 2011. doi: 10.1051/0004-6361/201015552. 84

A. Miura. Anomalous transport by magnetohydrodynamic Kelvin-Helmholtz instabilities in the solar wind-magnetosphere interaction. *J. Geophys. Res.*, 89:801–818, February 1984. doi: 10.1029/JA089iA02p00801. 3, 138

A. Miura and P. L. Pritchett. Nonlocal stability analysis of the MHD Kelvin-Helmholtz instability in a compressible plasma. *J. Geophys. Res.*, 87:7431–7444, September 1982. doi: 10.1029/JA087iA09p07431. 112, 113, 121

N. A. Murphy, M. P. Miralles, C. L. Pope, J. C. Raymond, H. D. Winter, K. K. Reeves, D. B. Seaton, A. A. van Ballegooijen, and J. Lin. Asymmetric Magnetic Reconnection in Solar Flare and Coronal Mass Ejection Current Sheets. *ApJ.*, 751:56, May 2012. doi: 10.1088/0004-637X/751/1/56. 49

K. Nykyri, A. Otto, B. Lavraud, C. Mouikis, L. M. Kistler, A. Balogh, and H. Rème. Cluster observations of reconnection due to the Kelvin-Helmholtz instability at the dawnside magnetospheric flank. *Annales Geophysicae*, 24:2619–2643, October 2006. doi: 10.5194/angeo-24-2619-2006. 3, 113

L. Ofman and B. J. Thompson. SDO/AIA Observation of Kelvin-Helmholtz Instability in the Solar Corona. *Astrophy. J. Lett.*, 734:L11, 2011. doi: 10.1088/2041-8205/734/1/L11. 114

M. Onofri, L. Primavera, F. Malara, and P. Veltri. Three-dimensional simulations of magnetic reconnection in slab geometry. *Physics of Plasmas*, 11:4837–4846, October 2004. doi: 10.1063/1.1791638. 124

K. Papadopoulos. A review of anomalous resistivity for the ionosphere. *Reviews of Geophysics and Space Physics*, 15:113–127, 1977. 21

E. Pariat, G. Aulanier, B. Schmieder, M. K. Georgoulis, D. M. Rust, and P. N. Bernasconi. Resistive Emergence of Undulatory Flux Tubes. *ApJ.*, 614:1099–1112, October 2004. doi: 10.1086/423891. 2

E. Pariat, S. K. Antiochos, and C. R. DeVore. A Model for Solar Polar Jets. *ApJ.*, 691: 61–74, January 2009. doi: 10.1088/0004-637X/691/1/61. 13, 138

E. N. Parker. Sweet's Mechanism for Merging Magnetic Fields in Conducting Fluids. *J. Geophys. Res.*, 62:509–520, December 1957. doi: 10.1029/JZ062i004p00509. 8, 45

E. N. Parker. Nanoflares and the solar X-ray corona. *ApJ.*, 330:474–479, July 1988. doi: 10.1086/166485. 2

C. E. Parnell, J. M. Smith, T. Neukirch, and E. R. Priest. The structure of three-dimensional magnetic neutral points. *Physics of Plasmas*, 3:759–770, March 1996. doi: 10.1063/1.871810. 13

C. E. Parnell, R. C. Maclean, and A. L. Haynes. The detection of numerous magnetic separators in a three-dimensional magnetohydrodynamic model of solar emerging flux. *Astrophys. J. Lett*, 725(2):L214, 2010. 76, 108, 137

H. E. Petschek. Magnetic Field Annihilation. *NASA Special Publication*, 50:425, 1964. 8, 45

D. I. Pontin and I. J. D. Craig. Current singularities at finitely compressible three-dimensional magnetic null points. *Physics of Plasmas*, 12(7):072112, July 2005. doi: 10.1063/1.1987379. 7

D. I. Pontin and K. Galsgaard. Current amplification and magnetic reconnection at a three-dimensional null point: Physical characteristics. *J. Geophys. Res.*, 112:A03103, March 2007. doi: 10.1029/2006JA011848. 15, 21, 27, 28, 34, 38, 39, 45, 111, 117

D. I. Pontin, G. Hornig, and E. R. Priest. Kinematic reconnection at a magnetic null point: spine-aligned current. *Geophysical and Astrophysical Fluid Dynamics*, 98:407–428, May 2004. doi: 10.1080/0309192042000272324. 12, 15, 21, 22, 45

D. I. Pontin, G. Hornig, and E. R. Priest. Kinematic reconnection at a magnetic null point: fan-aligned current. *Geophys. & Astrophys. Fluid Dynamics*, 99:77–93, January 2005. doi: 10.1080/03091920512331328071. 15, 22, 52, 64, 74, 75, 86, 143

D. I. Pontin, A. Bhattacharjee, and K. Galsgaard. Current sheet formation and nonideal behavior at three-dimensional magnetic null points. *Phys. of Plasmas*, 14(5):052106–+, May 2007a. doi: 10.1063/1.2722300. 15, 77, 85, 111

D. I. Pontin, A. Bhattacharjee, and K. Galsgaard. Current sheets at three-dimensional magnetic nulls: Effect of compressibility. *Phys. of Plasmas*, 14(5):052109, May 2007b. doi: 10.1063/1.2734949. 15, 16, 93

D. I. Pontin, A. K. Al-Hachami, and K. Galsgaard. Generalised models for torsional spine and fan magnetic reconnection. *A&A*, 533:A78, September 2011. doi: 10.1051/0004-6361/201117250. 46, 50, 117

E. Priest and T. Forbes. *Magnetic Reconnection*. Cambridge University Press, June 2000. 4

E. R. Priest. *Solar magneto-hydrodynamics*. Kluwer Academic, 1984. 3, 39

E. R. Priest and P. Démoulin. Three-dimensional magnetic reconnection without null points. 1. Basic theory of magnetic flipping. *J. Geophys. Res.*, 100:23443–23464, December 1995. doi: 10.1029/95JA02740. 9

E. R. Priest and D. I. Pontin. 3D Null Point Reconnection Regimes. *Phys. of Plasmas*, 16:122101–+, 2009. doi: 10.1063/1.3257901. 15, 16, 17, 96

E. R. Priest and V. S. Titov. Magnetic Reconnection at Three-Dimensional Null Points. *Royal Society of London Proceedings Series A*, 354:2951–2992, December 1996. 13, 14, 75

E. R. Priest, T. N. Bungey, and V. S. Titov. The 3D topology and interaction of complex magnetic flux systems. *Geophysical and Astrophysical Fluid Dynamics*, 84:127–163, 1997. doi: 10.1080/03091929708208976. 9

E. R. Priest, G. Hornig, and D. I. Pontin. On the nature of three-dimensional magnetic reconnection. *J. Geophys. Res.*, 108:1285–+, July 2003. doi: 10.1029/2002JA009812. 7, 10, 16, 17

E. R. Priest, D. W. Longcope, and J. F. Heyvaerts. Coronal heating at separators and separatrices. *Astrophys. J.*, 624:1057–1071, 2005. 114, 137

S. Régnier, C. E. Parnell, and A. L. Haynes. A new view of quiet-Sun topology from Hinode/SOT. *A&A*, 484:L47–L50, June 2008. doi: 10.1051/0004-6361:200809826. 12

G. J. Rickard and V. S. Titov. Current Accumulation at a Three-dimensional Magnetic Null. *ApJ.*, 472:840, December 1996. doi: 10.1086/178114. 14, 30, 45, 117

J. Sarff, A. Almagri, J. Anderson, D. Brower, D. Craig, B. Deng, D. den Hartog, W. Ding, G. Fiksel, C. Forest, V. Mirnov, S. Prager, and V. Svidzinski. Magnetic reconnection and self-organization in Reversed Field Pinch laboratory plasmas. In K. T. Chyzy, K. Otmianowska-Mazur, M. Soida, and R.-J. Dettmar, editors, *The Magnetized Plasma in Galaxy Evolution*, pages 48–55, June 2005. 3

K. Schindler, M. Hesse, and J. Birn. General magnetic reconnection, parallel electric fields, and helicity. *J. Geophys. Res.*, 93:5547–5557, June 1988. doi: 10.1029/JA093iA06p05547. 16, 17

M. Scholer. Undriven magnetic reconnection in an isolated current sheet. *J. Geophys. Res.*, 94:8805–8812, July 1989. doi: 10.1029/JA094iA07p08805. 45

C. Shen, Z. X. Liu, and T. S. Huang. Shocks associated with the Kelvin-Helmholtz-resistive instability. *Physics of Plasmas*, 7:2842–2848, July 2000. doi: 10.1063/1.874133. 138

J. C. Shi, Q. S. Lin, Z. W. Hu, H. B. Zhao, and Y. H. Ma. The Disconnection Event of Comet Lulin. *Acta Astronomica Sinica*, 52:136–144, March 2011. 3

L. Spitzer. *Physics of Fully Ionized Gases*. Interscience, 1956. 21

P. A. Sturrock. Model of the High-Energy Phase of Solar Flares. *Nature*, 211:695–697, August 1966. doi: 10.1038/211695a0. 2

T. Sundberg, S. A. Boardsen, J. A. Slavin, B. J. Anderson, H. Korth, T. H. Zurbuchen, J. M. Raines, and S. C. Solomon. MESSENGER orbital observations of large-amplitude Kelvin-Helmholtz waves at Mercury's magnetopause. *J. Geophys. Res. (Space Phys)*, 117:A04216, 2012. doi: 10.1029/2011JA017268. 113

P. A. Sweet. The Neutral Point Theory of Solar Flares. In B. Lehnert, editor, *Electromagnetic Phenomena in Cosmical Physics*, volume 6 of *IAU Symposium*, page 123, 1958. 8, 45

J. B. Taylor. Relaxation of Toroidal Plasma and Generation of Reverse Magnetic Fields. *Physical Review Letters*, 33:1139–1141, November 1974. doi: 10.1103/PhysRevLett.33.1139. 12

V. S. Titov, K. Galsgaard, and T. Neukirch. Magnetic Pinching of Hyperbolic Flux Tubes. I. Basic Estimations. *ApJ.*, 582:1172–1189, January 2003. doi: 10.1086/344799. 16

T. Török, G. Aulanier, B. Schmieder, K. K. Reeves, and L. Golub. Fan-Spine Topology Formation Through Two-Step Reconnection Driven by Twisted Flux Emergence. *ApJ.*, 704:485–495, October 2009. doi: 10.1088/0004-637X/704/1/485. 13, 109

M. Ugai. Computer studies on powerful magnetic energy conversion by the spontaneous fast reconnection mechanism. *Physics of Plasmas*, 2:388–397, February 1995. doi: 10.1063/1.870965. 45

M. Volwerk, M. Delva, Y. Futaana, A. Retinò, Z. Vörös, T. L. Zhang, W. Baumjohann, and S. Barabash. Substorm activity in Venus's magnetotail. *Annales Geophysicae*, 27:2321–2330, June 2009. doi: 10.5194/angeo-27-2321-2009. 3

A. Vourlidas, C. J. Davis, C. J. Eyles, S. R. Crothers, R. A. Harrison, R. A. Howard, J. D. Moses, and D. G. Socker. First Direct Observation of the Interaction between a Comet and a Coronal Mass Ejection Leading to a Complete Plasma Tail Disconnection. *Astrophys. J. Lett*, 668:L79–L82, October 2007. doi: 10.1086/522587. 3

A. L. Wilmot-Smith and G. Hornig. A Time-dependent Model for Magnetic Reconnection in the Presence of a Separator. *ApJ.*, 740:89, October 2011. doi: 10.1088/0004-637X/740/2/89. 2, 22, 75

L. Woltjer. A Theorem on Force-Free Magnetic Fields. *Proceedings of the National Academy of Science*, 44:489–491, June 1958. doi: 10.1073/pnas.44.6.489. 12

P. F. Wyper and R. Jain. Torsional magnetic reconnection at three dimensional null points: A phenomenological study. *Phys. of Plasmas*, 17:092902–+, 2010. doi: 10.1063/1.3480639. 18

P. F. Wyper and R. Jain. Torsional magnetic reconnection: The effects of localizing the non-ideal (ηJ) term. *Journal of Plasma Physics*, 77:843–855, December 2011. doi: 10.1017/S0022377811000262. 18

P. F. Wyper, R. Jain, and D. I. Pontin. Spine-fan reconnection. The influence of temporal and spatial variation in the driver. *A&A*, 545:A78, September 2012. doi: 10.1051/0004-6361/201219281. 19, 81, 83, 89, 92, 95, 96, 98, 99, 100, 106

C. J. Xiao, X. G. Wang, Z. Y. Pu, H. Zhao, J. X. Wang, Z. W. Ma, S. Y. Fu, M. G. Kivelson, Z. X. Liu, Q. G. Zong, K. H. Glassmeier, A. Balogh, A. Korth, H. Reme, and C. P. Escoubet. In situ evidence for the structure of the magnetic null in a 3D reconnection event in the Earth's magnetotail. *Nature Physics*, 2:478–483, July 2006. doi: 10.1038/nphys342. 12

C. J. Xiao, X. G. Wang, Z. Y. Pu, Z. W. Ma, H. Zhao, G. P. Zhou, J. X. Wang, M. G. Kivelson, S. Y. Fu, Z. X. Liu, Q. G. Zong, M. W. Dunlop, K.-H. Glassmeier, E. Lucek, H. Reme, I. Dandouras, and C. P. Escoubet. Satellite observations of separator-line geometry of three-dimensional magnetic reconnection. *Nature Physics*, 3:609–613, September 2007. doi: 10.1038/nphys650. 12

Ya-Hui Yang, C. Z. Cheng, Sm Krucker, Min-Shiu Hsieh, and Nai-Hwa Chen. Asymmetry of hard x-ray emissions at conjugate footpoints in solar flares. *The Astrophysical Journal*, 756(1):42, 2012. 145

E. G. Zweibel and M. Yamada. Magnetic Reconnection in Astrophysical and Laboratory Plasmas. *Annual Review of Astronomy & Astrophys.*, 47:291–332, September 2009. doi: 10.1146/annurev-astro-082708-101726. 8